

**King Khalid University**



**جامعة الملك خالد**

***Proceedings of***

**14<sup>TH</sup>**

**ANNUAL  
RESEARCH  
DAY**

**Organized by**

**Deanship of Scientific Research  
and  
College of Engineering Research Center**

**Building (B) Auditorium (6)  
Thursday 4<sup>th</sup> April 2019**

## Message from the Dean

The world is changing rapidly and it is facing challenges in many areas such as energy, water, food, health and environment. The Challenges creates opportunities for faculty members to tackle them in research. In the research day the college of Engineering develops solutions with innovative approach to tackle these challenges for a better and sustainable world. The starting point of any innovation is the laboratory apparatus and the outcome of development is the production plant. The up-to-date information about the process of development can be obtained not only from patent and published literature but also from conferences and discussed scientific meetings.

In this regard, the College of Engineering is collaborating with the Deanship of Scientific Research on an annual basis in organizing the 'Annual Research Day' event.

I hope the research day will offer an attractive platform for discussing emerging technologies that would result in multidisciplinary network, collaboration and high quality research outcomes.

My sincere appreciation to all of those behind the preparation of the research day especially the head of the research center in the college of Engineering; Dr. Ihab Shiqidi. I extend my thanks to the heroes of the research day, those who participate by presenting their research and allow for interactive thorough discussions.

*Dr. Ibrahim Idris A Falqi*

# 14<sup>th</sup> Annual Research Day

Organised by the Deanship of Scientific Research in collaboration with the College of Engineering  
Research Centre  
4<sup>th</sup> April 2019

## Contents

Sl No.	Title	First Author	Dep.	Page No.
1	Apply sustainable development on the architecture, planning and infrastructure of Abha to be the first eco-city in the Middle East	Dr.Wael A. Aboneama	Architecture	3
2	A review on bioclimatic Architecture for improving the residential building environment in hot dry regions of Saudi Arabia	Mr. Farhat Ali		14
3	Creating a unique sustainable rating system for Saudi Arabia to achieve environmental assessment and 2030 Vision	Dr.Wael A. Aboneama		20
4	Comparative study of Salvia Officinal essential oil from different countries geographic areas	Dr. Atef El Jery	Chemical	32
5	Effect of Structure and Chemical Activation on the Adsorption Properties of Green Clay Minerals for the Removal of Cationic Dye	Dr. Abdelfattah Amari		41
6	Synthesis, Characterization and Application of Ferrochrome slag/polyaniline Nanocomposite as Corrosion Protection Coatings for Carbon Steel	Dr. Mohammad Ilyas Khan		57
7	The Graphene/Gold @Polyaniline nanocomposite for the Removal of Methylene Blue and Its Thermal Electrical Stability Studies	Dr. Mudassir Hassan		65
8	Application of Saudi Building Code Recommendations to Design Shear Critical Concrete Members	Dr. Mohd. Ahmed	Civil	68
9	A smart tower crane to improve safety in Masjid Al-Haram of Mecca	Dr. Mohamed Hechmi El Ouni		73
10	Investigation of Geology and Hydro-geophysical Features Using Electromagnetic and Vertical Sounding Methods for Abu Zabad Area, Western Kordofan State, Sudan	Dr. Elhag A. B		79
11	Linear Crack Simulation in Concrete Beam Using Finite Element Modelling	Dr. Sivakumar Anandan		86
12	Non-Linear Analysis of Floating Structures	Dr. Mohammed Jameel		92
13	Rock slope stability analysis by empirical and numerical methods: case study	Dr. Abdelkader HOUAM	103	
14	Analysis of Airborne Dust Effects on Terrestrial Microwave Propagation in Arid Area	Dr. Elfaih A. A. Elsheikh	Electric al	108

# 14<sup>th</sup> Annual Research Day

Organised by the Deanship of Scientific Research in collaboration with the College of Engineering  
Research Centre  
4<sup>th</sup> April 2019

15	A Novel Parallel Hardware Architecture for filter module in HEVC	Dr. Hassan Loukil		116
16	Design of 8b Multiplying Digital to Analog Converter in Current mode using Glitch Reduction Technique	Mr. Mohammed Abdul Muqet		123
17	DMA communications and Photonic in chip multiprocessors: a Review	Dr. F. M. Suliman		128
18	Energy and Throughput of Data collection in Wireless Sensor Networks	Dr. Shamimul Qamar		135
19	Energy Efficiency mechanism for Wireless Sensor Networks	Dr. Monji Zaidi		139
20	Estimation of Carrier Frequency Offsets and Channel for SC-FDMA Uplink Systems	Dr. Muneer Parayangat		148
21	Logic Based Approach for Analysis of Nucleotide Sequences in Typical Case	Dr. M. Abbas		152
22	Control Strategies for Liquid Level Control in Twin Tank System	Dr. Mohammad Fazle Azeem		160
23	Nonlinear Transformation for Improving Noise Robustness of Chaotic Signals	Dr. Thafasal Ijyas V. P		170
24	Ratio of High-Extinction and Low Based Silica In Relation To Strictly Non-Blocking High Density Switches: a Review	Dr. Fakher Eldin M Suliman		174
25	Evaluating Flexible Manufacturing System using Combinatorial Approach	Dr. Mohamed Rafik Noor Mohamed Qureshi	Industrial	181
26	Gripping Task Performance Evaluation by Varying Grip Span and Stroke Rotation	Dr. Zulqarnain Mallick		182
27	Application of Phase Change Materials in Transportation of Temperature Sensitive Products	Dr. C Ahamed Saleel	Mechanical	194
28	Strain Rate Sensitivity of a superelastic NiTi Shape Memory Alloy after Hydrogen Immersion	Dr. FEHMI GAMAOUN		200
29	Strengthening Mechanisms of Metal Matrix Composites	Dr. VINEET TIRTH		206

# 14<sup>th</sup> Annual Research Day

Organised by the Deanship of Scientific Research in collaboration with the College of Engineering  
Research Centre  
4<sup>th</sup> April 2019

---

## Apply sustainable development on the architecture, planning and infrastructure of Abha to be the first eco-city in the Middle East

Dr. Wael A. Aboneama

<sup>1</sup>Department of Architecture & Planning, College of Engineering, King Khalid University,  
PO Box 394, Abha 61411 KSA.

E-mail address: waboneama@kku.edu.sa – Mob: (+966) 539 193 501

**Abstract:** Sustainability improvement in Saudi Arabia and the whole Middle East is focused on only buildings and small projects. However, the history of architecture in the Middle East starting from 7th century to the end of 19th century was the real beginning of sustainable design and development. Nowadays, there is no wide planning to take a step forward towards sustainable city. Abha in Saudi Arabia could be one of the best inceptions as a sustainable city. Its climate puts Abha in the first places to be selected for applying sustainable development. Abha is the biggest city in Asir territory and the capital of tourism in Saudi Arabia. It is located 2,200 meters above the sea level with a prolific soil on the mountains of southwestern Saudi Arabia (Hoiberg D. H., 2010). All over the year, the temperature moves from its lowest level around 7 C° to its maximum of 28 C° (Weather spark, n.d.). The average rainfall is 278 mm, which means that it is enough for human use and irrigation.

**Keywords:** Abha, Eco-city, Sustainable development, Architecture, Planning and infrastructure.

---

### 1. Introduction:

First, we should be more familiar and closer to the definition of sustainable cities and the difference between them against normal cities. Many cities such as Copenhagen, Amsterdam, Stockholm, Vancouver, London and more achieved the level of eco-cities. Those cities are enjoying living in high quality of healthy life, less energy and water consumption, better land-use, and economic returns (Rigester, 2008). Most of Middle East cities are suffering from several environmental, economic, social, and land-use problems. The sample of Masdar city in UAE fig (1) as a sustainable city could be adequate for new urban development, but it is not convenient for existing old cities, which is the case of most of Middle East cities. Abha is the biggest city in Asir territory Fig. (2). It has a big potential to be a sustainable city. Its weather, rainfall average and surrounding environment are motivations to

select Abha as one of the best cities for living in the Middle East. It was selected as the capital of Arab tourism in 2017 (Abdallah, 2017).



**Figure (1)** Masdar city, UAE (Willmott, 2014)

The summer is long, warm, arid, and partly cloudy and the winter is short, cool, dry, and

# 14<sup>th</sup> Annual Research Day

Organised by the Deanship of Scientific Research in collaboration with the College of Engineering Research Centre

4<sup>th</sup> April 2019

mostly clear. On the other hand, the Middle East region is thirsty for sustainable development in particular the Arabian Peninsula. The common weather is very hot and the use of renewable energy is not compatible with the available solar and wind powers. In addition, potable water resources are scarce. Table (1) describes that the fossil fuels are the most important source of energy in Saudi Arabia. The rest of the countries in Arabian Peninsula are not much better. The most important measure in the energy balance of Saudi Arabia is the total consumption of 292.80 billion kWh of electric energy per year. Per capita, this is an average of 9,072 kWh. The electricity consumption in Saudi Arabia increased from 219.66 terawatt in 2011 to 287.44 terawatt in 2016, which means 30% in only five years.



**Figure (2)** Abha city, Saudi Arabia (Abir, 2015)

**Table 1:** Describes the energy sources in Saudi Arabia compared with Europe in 2014. (saudi-arabia/energy-consumption, n.d.)

Energy source	Total in Saudi Arabia	percentage in Saudi Arabia	percentage in Europe	per capita in Saudi Arabia	per capita in Europe
Fossil fuels	604.27 bn kWh	99,9 %	48,9 %	18,722.24 kWh	7,994.86 kWh
Nuclear power	0.00 kWh	0,0 %	7,2 %	0.00 kWh	1,185.87 kWh
Water power	0.00 kWh	0,0 %	23,4 %	0.00 kWh	3,829.91 kWh
Renewable energy	604.88 m kWh	0,1 %	16,2 %	18.74 kWh	2,655.34 kWh
Other energy sources	0.00 kWh	0,0 %	4,3 %	0.00 kWh	696.17 kWh
Total production capacity	604.88 bn kWh	100,0 %	100,0 %	18,740.98 kWh	16,362.15 kWh

## 2. Literature review:

### 2.1 Sustainable cities (Eco-Cities)

Sustainable city, urban sustainability and eco-city are several terminologies of considering the three principles, which are ecology, people, and economy without any negative impact of future generation's natural resources. These cities are inhabited by people whom are dedicated towards minimization of required inputs of energy, water, food, waste, output of heat, air pollution - CO<sub>2</sub>, methane, and water pollution (en.wikipedia.org, 2008) 1987 was the first time for the term of "eco-city" written by Richard Register in his book "Eco-city Berkeley: Building Cities for a Healthy Future". Eco-city defines as the design and planning on the synergy and interdependence of ecological and economic sustainability, and their fundamental ability to reinforce each other in the urban context (Hiroaki Suzuki, 2010)

### 2.2 Eco- city models in the world

The Global Green Economy Index (GGEI) 4th edition with a deep study of more than 60 countries and 70 cities which passed through a long path of environmentally friendly economies with actual performance. Copenhagen, Amsterdam, Stockholm, Vancouver, London, Berlin, New York, Singapore, Helsinki, and Oslo are selected in order as the top ten eco-cities in the world. (Pantsios, 2014).



**Figure (3)** Copenhagen, Denmark (vacationidea, 2016)

# 14<sup>th</sup> Annual Research Day

Organised by the Deanship of Scientific Research in collaboration with the College of Engineering Research Centre

4<sup>th</sup> April 2019

On the other hand, Xuzhou is another sample of the three eco-cities in China fig. (4). The transforming of this city was based on sustainable development of health, social, solid and waste water, traffic and transportation, energy, urban function, economic development, primary, secondary and tertiary industry. One obstacle faced this city, was that the frameworks have not been developed bottom-up in a local participation process. Xuzhou clarifies the importance of cooperation between the different city departments responsible for energy, water, and transportation (Liu, Wennersten, Luo, Jiang, & Dong, 2016)



**Figure (4)** Xuzhou eco-city 2030, China (Liu, Wennersten, Luo, Jiang, & Dong, 2016)

## 2.3 The World Bank and ecological cities

The World Bank motivates Ecological Cities, as an integral part of its Urban and Local Government Strategy, to help cities in developing countries achieve greater ecological and economic sustainability (Hiroaki Suzuki, 2010). The World Bank's interest of eco-cities is a great advantage for any country to start working hard to transform its cities to be sustainable cities.

## 2.4 The transportation in Abha

The main mean of transportation in Abha city is the private cars. Unfortunately, there is no public transportation in Abha such as buses, tram, or

trolley bus. However, the planning of the city and the neighbouring city Khamis Mushait based on highway and ring roads connecting most of the attraction points. Fig (5) & (6). This leads to two outcomes. First one, fuel consumption and carbon emissions now at the worst level compared to the population. Secondly, developing a sustainable public transportation plan using all possible means of sustainable transportation is much easier than any other city based on its planning and kingdom vision 2030.



**Figure (5)** Illustrates Abha city roads & streets. (By researcher using Google Earth)

## 2.5 Sources of potable water in Abha and Asir province

The Saudi Arabia is a very arid country with little rainfall and no permanent freshwater sources such as rivers or lakes (watersaving - Switzerland, 2014). Three quarters of Saudi Arabia's freshwater comes from non-renewable groundwater. Contrariwise, Asir province has an average rainfall of 278 mm, which means that it is enough for human use and irrigation. Many projects of dam's construction took place in the territory of Asir. For example, dam rainfall in the city of Abha fig (7). Tens of dams has been constructed and planned more than this number in KSA vision 2030. All these projects give advantages to Abha city to be selected as eco-city



# 14<sup>th</sup> Annual Research Day

Organised by the Deanship of Scientific Research in collaboration with the College of Engineering Research Centre

4<sup>th</sup> April 2019

**Figure (6)** Abha streets, (feedyeti, 2018)



**Figure (7)** Dam rainfall, Abha, (Titi, 2016)

## 2.6 Generating renewable energy in Saudi Arabia

Saudi Arabia is seeking investment of up to \$7 billion of investment in the coming year to build about 4,000MW of renewable energy capacity, as part of its plan to supply 9,500MW, or 10% of its power demand, from renewable sources by 2023. (Scott, 2018). Saudi, the world's largest oil producer, is looking to generate more energy from renewable sources, in part to reduce its greenhouse gas emissions, but also to allow it to sell oil abroad at full price rather than use it domestically where it is heavily subsidised. Developing a renewable energy industry is also part of its Vision 2030. In a sign of how rapidly the kingdom's renewable energy sector is developing, it will tender for 3,200MW of solar power and 800MW of wind, this year, compared to 700MW in 2017. It will also look at other sources of power, including concentrated solar power (CSP) and waste-to-energy. (Scott, 2018)

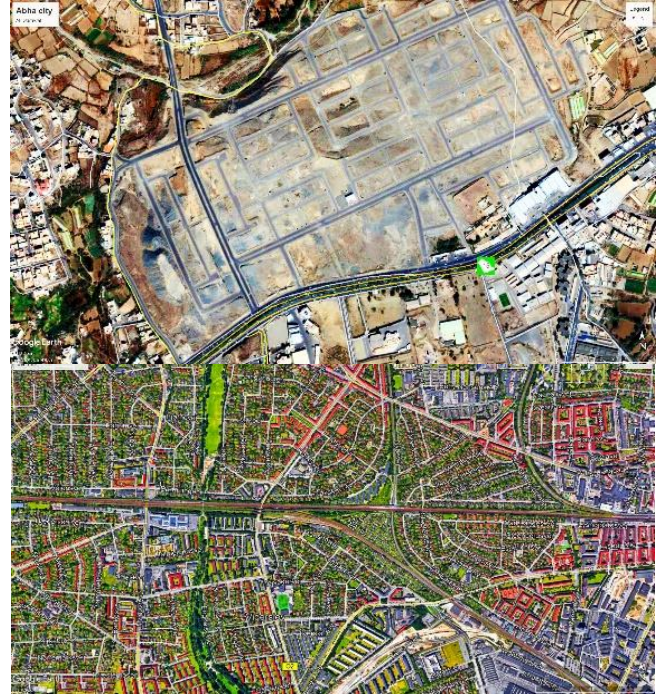


**Figure (8)** Illustrates Al-Mansak & Al-Mwazafeen districts in Abha without green areas. Bottom Copenhagen, Denmark and the mixed-use developments (By researcher using Google Earth)

## 2.7 Urban developments in Abha

The urban development growth in Abha is running very fast, meanwhile urban development should be controlled by a sustainable planning and that encourage integration between green space, sustainable transportation system, and mixed-use development. In addition, policymakers, developers, and contractors should support sustainable site planning and construction techniques that reduce pollution. They should ensure the balance between ecology and buildings (American society of landscape architects, 2018). In fig (8), we can see the difference between existing situations of urban development in Abha against Copenhagen. There is no protection or development of green areas. The main interest is getting more plots for building to convoy the

# 14<sup>th</sup> Annual Research Day

Organised by the Deanship of Scientific Research in collaboration with the College of Engineering Research Centre

4<sup>th</sup> April 2019

urban sprawl of the city. The concept does not change even for new urban development fig (9).



**Figure (9)** New urban development El-Sarawat, Abha (By researcher using Google Earth)

## 2.8 Asir architectural heritage and ecology

Villages in Asir has architectural heritage that respects the environment and human scale, use, culture, and taste. Every mountain village in Asir has a unique character. Asir province architectural heritage has different colour some are towering terraced houses clinging to the cliff faces, while others look cakes decorated with icing (SCTA, 2010) fig (10) & (11). There is no sustainable development without respecting and searching for people heritage. It is obvious the beauty of buildings respecting mountain levels. Unfortunately, nowadays developers and contractors demolish the mountains and produce one level to can start construction. Asir arts like (El-Got El-Asiri) fig (11) which is accredited by Ionesco and produced by ladies in their homes in the past is not used anymore unless for exhibitions and forums.



**Figure (10)** both photos in Rijal Almaa village architectural heritage, Asir (Reda, 2018)



**Figure (11)** Al-Got Al-Asiri, Asir (Al-Almaeyi, 2018)

## 2.8 Building Materials in Abha's heritage

Using local materials for building construction in Asir heritage protects the indoor environmental quality for human use. These materials require little processing or transporting, the environmental and economic costs are low (Green home building, 2001). Local building materials are defined by individual characteristics such as VOC levels or recyclability. Bricks and tiles are absolutely free of pollutants and allergens. By specifying regional materials, however, a product's sustainability profile will extend to

# 14<sup>th</sup> Annual Research Day

Organised by the Deanship of Scientific Research in collaboration with the College of Engineering Research Centre

4<sup>th</sup> April 2019

extraction, manufacturing, and transportation practices (Morton, 2013).

### 3. Methodology steps for Abha to be an eco-city:

#### 3.1 Developing sustainable transportation plan for Abha & Khamis Mushait cities

Abha city does not have any kind of public transportation unless very few number of taxi drivers and few buses for university female students. The main mean of transportation is private cars, which cost the environment and the economy of the country a huge bill of pollution, carbon emissions, and losing fossil fuel. In addition, Khamis Mushait acts as a market and serving city for Abha. It has low-income houses and huge number of people living in Khamis Mushait are working in Abha. In addition, it has lot of commercial shops and most of Asir trading done in Khamis Mushait. Then, we cannot study the transportation plan of Abha ignoring connection and the transportation inside Khamis Mushait city.

The first step towards sustainable city is creating a full transportation plan based on using sustainable means of transportation. Traditional transportation have their bad impact on the environment, around 20% to 25% of world energy consumption and Carbon emissions (Jeon & Amekudzi, 2005). In the following, some types of suitable means of sustainable transportation could be used in Abha and Khamis Mushait cities.

##### 3.1.1 Installing trolleybus

Trolleybus is an electric bus that draws its electricity from overhead using spring-loaded trolley poles fig (12). Currently, around 300 trolleybus systems are in operation, in cities and towns in 43 countries. It has electric engine providing torque in the start-up with rubber tires

not need underneath infrastructure. New models have gas engine for any failure (wikipedia, 2008).



**Figure (12)** on left trolleybus, (Skoda, 2018), on right electric bus (Ptacek, 2018), Bottom, hybrid bus (FuelCellsWorks, 2018).

##### 3.1.2 Installing zero emission buses & Fuel Cell Hybrid Bus Fleet

The Zero Emission Urban Bus System aims to be the main activity to extend the fully electric solution to the core part of the urban bus. Hybrid buses produce only water vapor: no smog forming nitrogen oxides. Fig (12) (Aboneama, 2015)

##### 3.1.3 Installing new tram lines between Abha and Khamis Mushait

The distance between Abha and Khamis Mushait is around 25 km. King Fahd road with its five lanes for each direction can include a tramline connecting both cities. This tram lane will cover a huge percentage from daily traffic between both cities fig (13). Rabat in Morocco and Athens development in 2004 for Olympic Games are samples. (Aboneama, 2015). The

# 14<sup>th</sup> Annual Research Day

Organised by the Deanship of Scientific Research in collaboration with the College of Engineering Research Centre

4<sup>th</sup> April 2019

A monorail is a railway in which the track consists of a single rail, typically elevated. The interesting issue about monorail is its ability to be installed inside an old crowded city.



**Figure (13)** on top tram, (govnews, 2015), In the Middle monorail (globalrailnews, 2018), below, zero emission car “electric car” (Carter, 2014)

### 3.1.4 Zero emission vehicles

A green vehicle produces less harmful impacts to the environment than normal cars. Policy makers can encourage the people to buy these kind of cars in Saudi Arabia by eliminating any taxes or customs for this kind of cars, and provide stations for car charging or alternative fuel supply (wikipedia, 2009)

### 3.2 Improving pedestrian lanes and bicycles

A bikeway is a lane, route, way or path, which in some manner is specifically designed and /or

designated for bicycle travel. Roads often have a designated footpath for pedestrian traffic, called the sidewalk. Regular walking is important both for human health and for the natural environment (Schmitt, 2013)



**Figure (14)** Pedestrian lanes and bicycles (Schmitt, 2013)

### 3.3 Generating energy from renewable energy sources

As the energy, consumption per capita reflects the level of living in the country and in most countries reflects the needs of energy for industrial needs. Unfortunately, as illustrated in the below map that Saudi Arabia is one of the highest country for energy consumption. Generating energy from renewable sources has become a mandatory. Using wind turbines, solar energy, hydro energy that is very suitable in Asir province, geo-thermal, and bio energy is not an option for energy production



# 14<sup>th</sup> Annual Research Day

Organised by the Deanship of Scientific Research in collaboration with the College of Engineering Research Centre

4<sup>th</sup> April 2019

**Figure (15)** Energy consumption per person by country (burn an energy journal, 2010)

### 3.4 New sustainable agriculture techniques

Studying the new sustainable agriculture techniques and applying the suitable from them to intended ecology. It will save water resources and increase the agriculture production. In addition, sustainable techniques will prevent using harmful components such as bad chemical pesticides or fertilizers in people food.

### 3.5 Apply passive design criteria for building designs

Unfortunately, all buildings inside Abha city are very different with Asir architectural heritage. They are all boxes with grey or white colors without any sense of Asir heritage. Local building materials, orientation, construction techniques, aesthetics, and people culture do not have any impact on buildings. As illustrated in fig (16) the whole kingdom houses have the same view.

Meanwhile, the architectural history of Asir province and the whole Middle East have abundant techniques for passive and environmental design such as courtyards, mashrabia, takhtaboosh, and orientation techniques fig (17). Passive design criteria is focusing on reduction of air-conditioning usage, and moves towards natural lighting and ventilation systems. Trying to achieve or get closer to zero-energy buildings



**Figure (16)** Abha building's character (Manea, 2010)

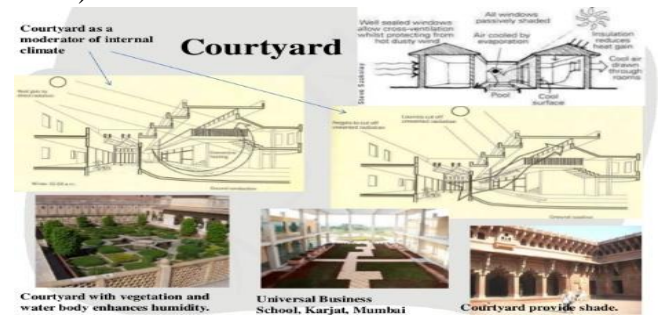


**Figure (17)** Passive design (Jain, 2013)

### 3.6 Developing the whole city drainage systems

It is divided into two branches. First, is focusing on separating the main city infrastructure and buildings drainage systems for grey and black water. The existing systems in most of the cities now depend on mixing both types of waters. We can recycle and re-use grey water in flush tanks and irrigation to save potable water use. Secondly, to ensure separate or at least do not mix storm water harvesting with black water drainage system. Better to be totally separated or at least for economic reasons to combine it with grey water drainage system.

### 3.7 Xeriscaping - garden and landscape design for water conservation

To reduce the excessive use of water for maintaining landscapes, planners and planters are encouraged to adopt Xeriscape landscaping. This concept conserves water and protects the environment. Xeriscape landscapes need not be cactus and rock gardens. They can be cool, green landscapes full of beautiful plants maintained with water-efficient practices. The seven water-saving principles of xeriscape landscaping are; start with a plan, analyze and prepare the soil, be practical with turf areas, select appropriate plants, conserve moisture with mulches, use good maintenance practices, and use one of the following irrigation systems (sprinkler irrigation or drip irrigation) (Douglas F. Welsh, 2001).

# 14<sup>th</sup> Annual Research Day

Organised by the Deanship of Scientific Research in collaboration with the College of Engineering  
Research Centre

4<sup>th</sup> April 2019

---

## 4. Results and Discussion

We can conclude from this research that we have an excellent opportunity to have Abha as a sustainable city in the Middle East, which has an optimal weather conditions and rainfall average. Abha needs development in several ways such as transportation, urban planning, buildings architectural design, landscape, developing its drainage systems, enhance storm water harvesting, and searching for new resources of generating energy to achieve this goal.

## 5. Discussion and analysis:

Sustainable urban development, creating transportation plan with sustainable means, generating energy from renewable resources, applying passive design criteria on buildings, developing new water strategies and drainage systems based on sustainable and recycling principals require long term planning and should defined in 2030 vision of Saudi Arabia. Future planning will be divided into short, five-year stages to be able to confront all those serious challenges and solve all obstacles. Transforming Abha to be an eco-city is magnificent solution and guide way for many cities in the Middle East that have same challenges.

## 6. Conclusion and recommendations:

Transforming Abha to eco-city should be studied by governmental authorities in co-operation with practical experiments and getting the experience from other countries and cities that achieve this goal. Saudi Arabia institutions and authorities should work together in the highest level of amity. Solving problems in the shortest time is the only key words for this step. Implementing sustainable urban growth based on the potential of renewable energy production, developing sewage systems, applying passive design techniques on buildings, developing landscape

strategies, sustainable agriculture techniques will create a new era for the Saudi Arabian economy and living standards

## Acknowledgement & Note

This paper published in European Journal of Sustainable Development – Volume 7, NO4 – September 2018, Rome,

Italy (European Center of Sustainable Development)

ISSN 2239-5938 (Print)

ISSN 2239-6101 (Online)

<https://ecsdev.org/ojs/index.php/ejsd/article/view/702>

## BIBLIOGRAPHY

Abdallah, A.-H. (2017, Jan 6). *أبها عاصمة السياحة العربية 2017*. Retrieved from al-jazirah: <http://www.al-jazirah.com/2017/20170106/ew1.htm>

Abir. (2015, Sep. 28). *Abha photos*. Retrieved from 3bir: <https://v.3bir.net/345832/>

Aboneama, W. (2015). Installing various means of sustainable transportation to achieve sustainable urban development and Cairo vision 2050. *Future north Africa transportation summit* (pp. 11-12). Cairo: IQPC.

Al-Almaey, I. (2018). *abotalal40041*. Retrieved from Twitter: <https://twitter.com/abotalal40041>

American society of landscape architects. (2018). *sustainable urban development*. Retrieved from [www.asla.org](http://www.asla.org):

<https://www.asla.org/sustainableurbandevlopment.aspx>

burn an energy journal. (2010). *MAP: How much energy is the world using?* Retrieved from [burnanenergyjournal.com](http://burnanenergyjournal.com):

<http://burnanenergyjournal.com/how-much-energy-are-we-using/>

Carter, M. (2014, June 4). *Eight US States Form Alliance to Put 3.3 Million Zero Emission Vehicles on the Road by 2025*. Retrieved from

# 14<sup>th</sup> Annual Research Day

Organised by the Deanship of Scientific Research in collaboration with the College of Engineering  
Research Centre

4<sup>th</sup> April 2019

---

inhabitat.com: <https://inhabitat.com/eight-us-states-form-alliance-to-put-3-3-million-zero-emission-vehicles-on-the-road-by-2025/>

Douglas F. Welsh, W. C. (2001). *Xeriscape Landscape Water Conservation*. Texas: Texas agriculture extension service.

en.wikipedia.org. (2008). *Sustainable city*. Retrieved from Wikipedia: [https://en.wikipedia.org/wiki/Sustainable\\_city](https://en.wikipedia.org/wiki/Sustainable_city)

feedyeti. (2018). *Abha*. Retrieved from feedyeti.com: <https://feedyeti.com/hashtag.php?q=abha>

FuelCellsWorks. (2018, April 14). *zero-emission-buses*. Retrieved from fuelcellsworks.com: <https://fuelcellsworks.com/news/zero-emission-buses-equipped-with-freudenberg-seals-set-durability-milestone>

globalrailnews. (2018, June 2). *CRRC tests suspended monorail called the 'Sky Train'*. Retrieved from globalrailnews.com: <https://www.globalrailnews.com/2017/07/27/crrc-tests-suspended-monorail-vehicle/>

govnews. (2015, Nov). *Victoria taps Bombardier for new \$274 mil E-Class trams*. Retrieved from govnews.com.au: <http://www.govnews.com.au/victoria-taps-bombardier-for-new-274-mil-e-class-trams/>

Green home building. (2001). *Local materials*. Retrieved from greenhomebuilding.com: <http://www.greenhomebuilding.com/localmaterial.htm>

Hiroaki Suzuki, W. B. (2010). *Ecological cities as economic cities*. (ISBN 978-0-8213-8046-8): Synopsis.

Hoiberg, D. H. (2010). *Encyclopædia Britannica* (Vol. 15th ed). A-ak Bayes.

Jain, A. (2013, Nov 29). *passive techniques*. Retrieved from slideshare.net:

<https://www.slideshare.net/anvitajain3/passive-techniques>

Jeon, C. M., & Amekudzi. (2005). *Sustainable transport*. Retrieved from en.wikipedia.org: [https://en.wikipedia.org/wiki/Sustainable\\_transport](https://en.wikipedia.org/wiki/Sustainable_transport)

Liu, H., Wennersten, R., Luo, P., Jiang, L., & Dong, a. W. (2016). Conceptual Sustainability Framework for Eco-City Development in the City Core of Xuzhou. *Journal of Urban Planning and Development*, Volume 142, Issue 4. Retrieved from ascelibrary.org: <https://ascelibrary.org/doi/10.1061/%28ASCE%29UP.1943-5444.0000319>

Manea, M. (2010, Dec 28). *Teenagers bother Al-Mansek district with drifting*. Retrieved from alwatan.com.sa: [http://www.alwatan.com.sa/Politics/News\\_Detail.aspx?ArticleID=34996](http://www.alwatan.com.sa/Politics/News_Detail.aspx?ArticleID=34996)

Morton, J. (2013, Jan 25). *Regional Materials: Benefits and Advantages*. Retrieved from buildings.com: <https://www.buildings.com/article-details/articleid/15165/title/regional-materials-benefits-and-advantages/viewall/true>

Pantsios, A. (2014, Oct. 24). *top-10-greenest-cities-in-the-world*. Retrieved from ecowatch.com: <https://www.ecowatch.com/top-10-greenest-cities-in-the-world-1881963132.html>

Ptacek, K. (2018, Jan 10). *zero-emission-all-electric-buses*. Retrieved from dartdallas.dart.org: <http://dartdallas.dart.org/2018/01/10/dart-demos-new-proterra-zero-emission-all-electric-buses/>

Reda, A. (2018). *rijal-alma-heritage-village-located-assir-region*. Retrieved from dreamstime.com: <https://www.dreamstime.com/rijal-alma-heritage-village-located-assir-region-capital-almaa->

# 14<sup>th</sup> Annual Research Day

Organised by the Deanship of Scientific Research in collaboration with the College of Engineering  
Research Centre

4<sup>th</sup> April 2019

---

province-was-natural-corridor-linking-  
image107226437

Rigester, R. (2008). *advantages-and-disadvantages*. Retrieved from ecocitiescatq3rene: <https://ecocitiescatq3rene.weebly.com/advantages-and-disadvantages.html>

*saudi-arabia/energy-consumption*. (n.d.). Retrieved from World Data: <https://www.worlddata.info/asia/saudi-arabia/energy-consumption.php>

Schmitt, A. (2013, July 31). *The Rise of The North American Protected Bike Lane*. Retrieved from [momentummag.com](https://momentummag.com): <https://momentummag.com/the-rise-of-the-north-american-protected-bike-lane/>

Scott, M. (2018, Jan 18). *Saudi Arabia Plans To Source 10% Of Its Power From Renewable Energy Within 5 Years*. Retrieved from [forbes.com](https://www.forbes.com): <https://www.forbes.com/sites/mikescott/2018/01/18/saudi-arabia-plans-to-source-10-of-its-power-from-renewable-energy-within-5-years/#3fb41fd9485f>

SCTA. (2010). *Asir-Mountain-Villages*. Retrieved from [arriyadh.com](http://www.arriyadh.com): [http://www.arriyadh.com/Eng/Tourism/Left/KSA/Attract/Asir/Asir-Mountain-Villages.doc\\_cvt.htm](http://www.arriyadh.com/Eng/Tourism/Left/KSA/Attract/Asir/Asir-Mountain-Villages.doc_cvt.htm)

Skoda. (2018). *trolleybus-30-tr*. Retrieved from [skoda.cz](http://skoda.cz):

<https://www.skoda.cz/en/references/trolleybus-30-tr/?from=prod>

Titi, A. (2016). *Dam rainfall in the city of Abha*. Retrieved from [ar.wikipedia.org](https://ar.wikipedia.org): [https://ar.wikipedia.org/wiki/%D9%85%D9%84%D9%81:Saad\\_abha.JPG](https://ar.wikipedia.org/wiki/%D9%85%D9%84%D9%81:Saad_abha.JPG)

vacationidea. (2016). *best-time-to-visit-copenhagen-denmark*. Retrieved from [vacationidea.com](http://vacationidea.com): <https://vacationidea.com/tips/best-time-to-visit-copenhagen-denmark.html>

watersaving - Switzerland. (2014, May 6). *saudi-arabia*. Retrieved from [watersaving.com](http://watersaving.com): <https://www.watersaving.com/en/infos/saudi-arabia/>

Weather spark. (n.d.). *Average-Weather-in-Abha-Saudi-Arabia-Year-Round*. Retrieved June 2, 2018, from Weatherspark: <https://weatherspark.com/y/102305/Average-Weather-in-Abha-Saudi-Arabia-Year-Round>

wikipedia. (2008). *Trolleybus*. Retrieved from [en.wikipedia.org](https://en.wikipedia.org): <https://en.wikipedia.org/wiki/Trolleybus>

wikipedia. (2009). *Zero-emissions\_vehicle*. Retrieved from [en.wikipedia.org](https://en.wikipedia.org):

# 14<sup>th</sup> Annual Research Day

Organised by the Deanship of Scientific Research in Collaboration with the College of Engineering  
Research Centre

4<sup>th</sup> April 2019

---

## A review on bioclimatic Architecture for improving the residential building environment in hot dry regions of Saudi Arabia

Farhat Ali

Department of Architecture and Planning, College of Engineering, King Khalid University,  
PO Box 394, Abha 61411 KSA.  
E-mail address: faalali@kku.edu.sa

**Abstract:** Designing of Residential building according to principles of bioclimatic provisions became important for achieving ecologically sustainable development. Bioclimatic means a well-developed relationship between climate and the living organisms. Research conducted in bioclimatology is about the climate for human comfort within an indoor environment. In the present scenario, the problem of Saudi Arab has to face heat during hot season due to its geographical conditions. Which causes residential building indoor environment becomes hot and enhances the energy consumption because of our dependency on mechanical resources. So, sustainability is supposed to be an emerging issue in society, especially in hot-dry regions of Saudi Arabia. Therefore, it becomes mandatory to achieve a balance between the requirement of indoor inhabitants, residences and climate. This important relationship is heading towards to a need to adopt the bioclimatic design considerations in terms of indoor environment. The methodology will involve the review of the climatic study on Saudi Arabia through various articles and journals and observing their methods and finding regarding the bioclimatic strategies for the sustainable residential environment through a case study method also. As a result, it's reframing of bioclimatic design in the reference of sustainability in hot dry regions of Saudi Arabia. Therefore, bioclimatic work on the ideology of local climate features with the adoption of passive strategies reviews related to the buildings which rarely include mechanical sources of energy. So finding will be focused on involving passive strategies in an economical way to reduce the energy consumption and enhancing the building life depending upon the natural resources for the bioclimatic design of building in Saudi Arabia.

**Keywords:** *Bioclimatic design, Architecture, Sustainability, Indoor environment, Climate, Energy and buildings*

---

### 1. Introduction:

The aim of this paper is to explain and discuss the idea of bioclimatic architecture as one of the most actual and important phenomena in contemporary building.[1] Richard Hyde describe [2]about the component of design, which oriented towards the interior environment conditions as follow:-

- Types of Climate with its requirements
- Adaption of thermal comfort parameters
- Vernacular approaches & strategies
- Microclimate: sun path, wind and rain;

- Working with the elements, such as passive and active system; and
- Development of responsive form.

### 2. The Concept of Bioclimatic Architecture:

The first rule of bioclimatic architecture is to take benefit of local bioclimatic situation with the advantage of the natural and built environment. That methodology should always be depending upon multidisciplinary in-depth research of individual circumstances. As a final effect safe and comfortable building which should

# 14<sup>th</sup> Annual Research Day

Organised by the Deanship of Scientific Research in Collaboration with the College of Engineering  
Research Centre

4<sup>th</sup> April 2019

---

contributes to its health and enriched biodiversity and should not harm the environment.[3]

Bioclimatic buildings are characterized by the use of building elements including walls, windows, roofs and floors for collecting, storing and distributing the solar thermal energy and prevent over-heating. So the major strategies to implement the natural environment through the consideration of clean energy and renewable energy systems because the energy use in buildings contributes to a huge amount of destructive emissions [4]. So, a basic objective is to reduce the need for energy for winter heating, summer air conditioning and lighting [5-7]. The definition also includes natural cooling and shading. The building is cooled by rejecting unwanted heat to ambient heat sinks (air, sky, earth and water) by means of natural modes of heat transfer. But the cooling load is firstly minimized through architectural design by reducing solar gains to the building fabric or through its windows, and by reducing internal gains [8]. Thirdly, the use of radiant energy for day lighting while maintaining standards of visual comfort is also encompassed within the bioclimatic approach [2].

### 3. Methods review:

#### 3.1 Active and passive method for bioclimatic design in Saudi Arab residential building:-

Bioclimatic design emphasizes on the development of passive and active system both. It is more recommended to find out the use of passive and active system for the local Saudi climate conditions. Basically the aim of active and passive system in the building is to reduce the energy requirement (increasing energy efficiency) of building interior through various energy conservation measures; and utilizing the solar energy incident on the exterior wall surface, roof and ground surfaces surrounding the house for daylighting production and for satisfying the building interior's heating requirement [8-10].

The implementation of these actions entails the careful assessment of economic feasibility, benefits for the environment and human comfort. So, according to the Saudi climate, Bioclimatic design can be implemented in three categories; Passive cooling techniques, Passive solar heat protection and natural day lighting systems.

#### a) Passive cooling techniques (maximum heat reduction)

It's a technique of passive cooling which occurs naturally, that is without any mechanical system. In this method the coupling of spaces and building elements to ambient heat sinks (air, sky, earth and water) by means of natural modes of heat transfer leads to an appreciable cooling effect indoors [11, 12].

Fixed or adjustable shading devices, or shading provided by vegetation and special glazing may be used to reduce the amount of solar radiation reaching the building. As a heat protection, it does not mean the 'zero heat gain', a associated system is implemented which operates by dissipating heat accumulated in the building by natural methods. Passive cooling contributes in various techniques such as natural ventilation, direct and indirect radiative cooling, night flush cooling, earth coupling as well as evaporative cooling. For a better working ventilation system, there should be sufficient location of opening is to be provided in wind direction [13, 14].

#### b) Passive solar heat protection (Heat gain reduction)

These strategies can be achieved by utilizing the exact location and building orientation which will protect our building environment from the sun overheating. Shading devices can be applied in the direction of sun path i.e. horizontal and vertical louvers. The presence of surrounding trees of any landscape elements contributes in solar heat gain reduction and cut the sunrays to penetrate the building envelope. At the same situation [15], effort can be made for applying

# 14<sup>th</sup> Annual Research Day

Organised by the Deanship of Scientific Research in Collaboration with the College of Engineering  
Research Centre

4<sup>th</sup> April 2019

materials as exposed façade treatment that absorbs significant amount of incident solar heat and radiation [8].

External heat gains due to solar radiation also can be minimized by insulation, reduced window sizes, thermal inertia in the building envelope, reflective materials and compact building layout.

Internal heat gains can be reduced by the use of more efficient lighting and appliances and appropriate control strategies for their operation and by the use of natural daylight wherever possible to re-place artificial lighting [16, 17].

## c) Natural Daylighting system

Daylighting system functions by location of windows and reflective surfaces based on the sun movement. In Saudi Arabia, it is usually seen in north and south facing facades. It permits sufficient diffused natural light and access effective indoor lighting throughout the day with the avoidance of glare problem (Figure-1). This provision enhances visual effectiveness and limit energy consumption as minimum involvement of artificial light [18, 19].

So, Good Daylighting can be achieved by consideration of the following in relation to the incidence of daylight on the building (Figure-2):

- The orientation, space organization, function and geometry of the spaces to be lit.
- The location, form and dimensions of the openings through which daylight will pass.
- The location and surface properties of internal partitions which will reflect the daylight and play a part in its distribution.
- The location, form and dimensions, etc., of movable or permanent devices which provide protection from excessive light and glare.
- The optical and thermal characteristics of the glazing materials.[20]

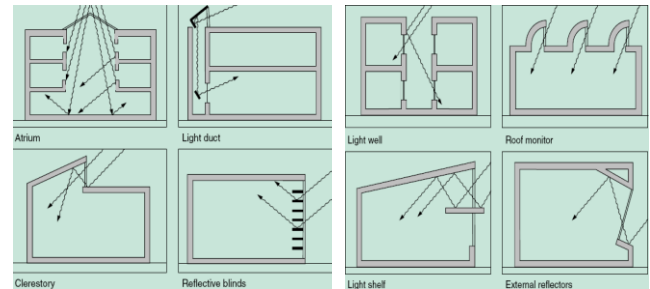


**Figure (1)** Natural daylighting provisions sketches for skylight, light well, chimney and windows opening. Drawn by authors based on research

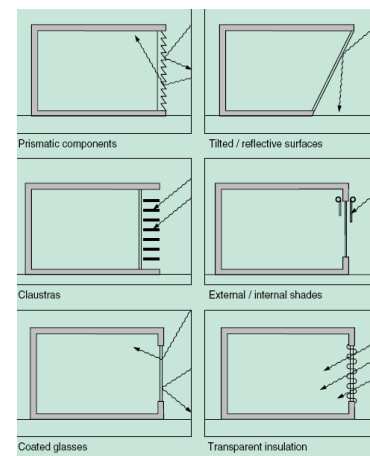


**Figure (2)** Natural daylighting provisions sketches for skylight and windows opening. Drawn by authors based on research.

*3.2 Case study method:- Sino-Italian Ecological and Energy Efficient Building (SIEEB), 2005-2006, Beijing, China, Mario Cucinella Architects*

This project was designed by Mario Cucinella Architects. Located in Tsinghua University Campus in Beijing (Figure-3). It is situated on the plot 60x60 meters, it is 40 meters high and provides 20 sqm floor area.

The Architectural concept of SIEEB is based on the local climate conditions including sun angle in winter and summer, wind directions, temperature and humidity. Computer simulations helped to review the building performance by considering its orientation, shape, structure, envelope etc.

# 14<sup>th</sup> Annual Research Day

Organised by the Deanship of Scientific Research in Collaboration with the College of Engineering Research Centre

4<sup>th</sup> April 2019

Also a variety of technological results were analyzed to maintain equilibrium between expected energy efficiency, functional demands, indoor comfort and esthetics. In fact the combination of passive and active strategies, controlled by the Building Management System (BMS), allowed for the optimization of the Bioclimatic Architecture [1, 14]. Eastern and western double skin façades are designed to optimize the amount of daylight in the internal offices. Blue curtain walls form a geometric composition of opaque and transparent modules



**Figure (3)** SIEEB, Tsinghua University, Beijing, China. View from south-east. Source: MCA Archive

Double glazed back enameled panels create the background for external silk-screen façade. Silk-screen glass panels are covered with unobtrusive linear pattern, which not only gives the building a modern and elegant appearance but also helps to prevent glare and provide advantageous penetration of light [1, 21]. So, this building has been designed according to the summer and winter environment strategies with light management, solar protection green surface, photovoltaic system, open spaces ventilation and rainwater collection ([13, 21, Figure-4].

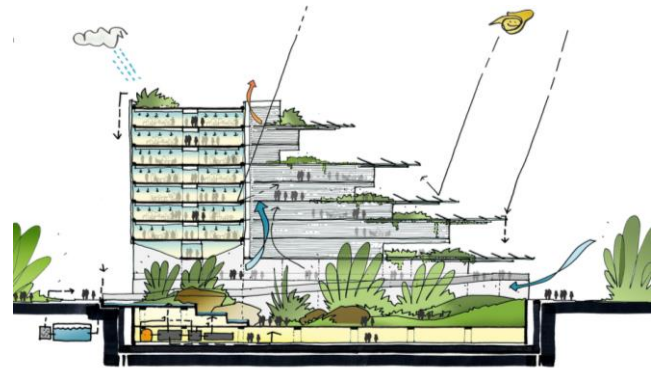


**Figure (4)** showing summer environmental strategies. Source: MCA Archive.

Other components of light management system are internal roller blinds and external light-shelves, followed by internal aluminum light shelves. These elements allow for solar radiation control as well as for sunlight filtration and distribution. Winter environment strategies includes the solar support to the building indoor, high insulation wrap, winter winds protection and rainwater collection [21, Figure-5].



**Figure (5)** showing winter environmental strategies. Source: MCA Archive.

### 3. Discussion for a sustainable bioclimatic future in Saudi residential buildings

From the above climatic responsive active-passive and case study analysis, the following are key guidelines that would help to attain bioclimatic architecture, in terms of energy efficient use, within the Saudi residential sector:

- a) Follow the principles of bioclimatic responsive design while designing residential

# 14<sup>th</sup> Annual Research Day

Organised by the Deanship of Scientific Research in Collaboration with the College of Engineering  
Research Centre

4<sup>th</sup> April 2019

---

buildings to improve energy efficiency of building.

- b) Solid walls, roofs and materials receives more heat so recovery ventilation system can be installed i.e. solar thermal panels, insulation, triple-glazed Low-E windows, supply & extract air etc.
- c) Window placing should allow the natural light and lesser the need of artificial light in a day. And opened during winter for natural ventilation and reduce the need of mechanical air conditioning sources.
- d) For avoiding excessive solar heating, implement shading devices attached to building and gardens.
- e) Only energy efficient lighting and Electrical equipment should be used.
- f) Evaporative cooling and cross ventilation for summer cooling.
- g) Maximum use of solar energy for lighting and winter heating.
- h) Abundant use of skylight and strategically placing them according to sun positions for best natural lighting.
- i) The use of natural insulation and waterproof materials for the roof.
- j) Using local resources for building materials to cut down on transportation carbon energy.
- k) Home should be close to deciduous trees (trees that shed their leaves annually) which will provide shade in the summer.
- l) Main façade face south which provides shade in the summer and sunlight during the winter time.

## 4. Conclusions:

In conclusion, as per the climatic study Saudi Arab has to face very high temperature during summer season. Due to which, Saudi Arabia has to adopt bioclimatic design parameters into considerations along with their sustainable passive design approach. By optimizing the implication of Bioclimatic design; we can create more natural preferable conditions and building comfort suited to indoor environment of

residential building. There are also many alternative passive strategies to improve building comfort and not wasting money on mechanical sources. There are others traditional and contemporary sustainable methodologies which can be use in future after associated with bioclimatic building design. Eco houses, vernacular architecture and recent energy related software to achieve the maximum thermal comfort for buildings in Saudi Arabia.

## Acknowledgement

This research is conducted by FARHAT ALI, based on my previous papers, contents based on Bioclimatic Architecture and climatic responsive design, sustainability, renewable energy, climate etc. The authors thank KKU, which created interest to conduct research on Saudi Arabia hot climate & finding out a bioclimatic approach in the field of passive architecture & energy efficient buildings.

## References

1. Widera, B., Bioclimatic Architecture. Journal of Civil Engineering and Architecture Research, 2015. 2(4): p. 12.
2. Hyde, R., BIOCLIMATIC HOUSING-INNOVATIVE DESIGNS FOR WARM CLIMATES. 2008, Earthscan in the UK and USA in 2008 Cromwell Press, Trowbridge 477.
3. Tewari, P., et al., Advancing building bioclimatic design charts for the use of evaporative cooling in the composite climate of India. Energy and Buildings, 2019. 184: p. 177-192.
4. Belkacem, N., et al., Assessment of energy and environmental performances of a bioclimatic dwelling in Algeria's North. Building Services Engineering Research & Technology, 2017. 38(1): p. 64-88.
5. Akande, O.K., Passive design strategies for residential buildings in a hot dry climate in Nigeria. Eco-Architecture Iii: Harmonisation

# 14<sup>th</sup> Annual Research Day

Organised by the Deanship of Scientific Research in Collaboration with the College of Engineering  
Research Centre

4<sup>th</sup> April 2019

---

- between Architecture and Nature, 2010. 128: p. 61-71.
6. Alalouch, C., et al., Energy saving potential for residential buildings in hot climates: The case of Oman. *Sustainable Cities and Society*, 2019. 46.
  7. Bravo, G. and E. Gonzalez, Thermal comfort in naturally ventilated spaces and under indirect evaporative passive cooling conditions in hot-humid climate. *Energy and Buildings*, 2013. 63: p. 79-86.
  8. Gomez-Munoz, V.M. and M.A. Porta-Gandara, Simplified architectural method for the solar control optimization of awnings and external walls in houses in hot and dry climates. *Renewable Energy*, 2003. 28(1): p. 111-128.
  9. Gutierrez, T., R. Romero, and C. Sotelo, Thermal energy impact of bioclimatic techniques applied to low-income housing in a hot dry climate. 2013 *Ises Solar World Congress*, 2014. 57: p. 1743-1752.
  10. Hamdani, M., et al., The Study Natural Ventilation by Using Buildings Windows: Case Study in a Hot Dry Climate, Ghardaia, Algeria. *Materials & Energy I (2015) / Materials & Energy II (2016)*, 2017. 139: p. 475-480.
  11. Alaidroos, A. and M. Krarti, Impact of Passive Cooling Strategies on Energy Consumption Reduction of Residential Buildings in the Kingdom of Saudi Arabia. *Proceedings of Asme 9th International Conference on Energy Sustainability*, 2015, Vol 2, 2016.
  12. Ben Cheikh, H., Experimental Studies of a Passive Cooling Roof in Hot Arid Areas. *Sustainable Architecture and Urban Development (Saud 2010)*, Vol Iv, 2010: p. 203-212.
  13. Del Rio, M.A., et al., Evaluation of passive cooling methods to improve microclimate for natural ventilation of a house during summer. *Building and Environment*, 2019. 149: p. 275-287.
  14. Farhat, A., Integration of the Active-Passive Architecture techniques for attaining optimum building sustainability in the hot-dry climate regions of Saudi Arabia, in 13th Annual Research Day, F. Ali, Editor. 2018, King Khalid University: Abha, Kingdom of Saudi Arabia. p. 6.
  15. Singh, M.K., S. Mahapatra, and S.K. Atreya, Solar passive features in vernacular architecture of North-East India. *Solar Energy*, 2011. 85(9): p. 2011-2022.
  16. Kumar, G. and G. Raheja, Design Determinants of Building Envelope for Sustainable Built Environment: A Review. *International Journal of Built Environment and Sustainability*, 2016. 3(2): p. 111-118.
  17. Taleb, H.M., Towards Sustainable Residential Buildings in the Kingdom of Saudi Arabia, in *Conference On Technology & Sustainability in the Built Environment 1995*, King Saud University, College of Architecture and Planning: Saudi Arab. p. 16.
  18. Altan, H., et al., An internal assessment of the thermal comfort and daylighting conditions of a naturally ventilated building with an active glazed facade in a temperate climate. *Energy and Buildings*, 2009. 41(1): p. 36-50.
  19. Nair, M.G., K. Ramamurthy, and A.R. Ganesan, Classification of indoor daylight enhancement systems. *Lighting Research & Technology*, 2014. 46(3): p. 245-267.
  20. Dabe, T.J. and V.S. Adane, The impact of building profiles on the performance of daylight and indoor temperatures in low-rise residential building for the hot and dry climatic zones. *Building and Environment*, 2018. 140: p. 173-183.
  21. Architects, M.C., SIEEB Sino Italian ecological & energy efficient building. <https://www.mcarchitects.it>.

# 14<sup>th</sup> Annual Research Day

Organised by the Deanship of Scientific Research in Collaboration with the College of Engineering  
Research Centre  
4<sup>th</sup> April 2019

## Creating a unique sustainable rating system for Saudi Arabia to achieve environmental assessment and 2030 Vision

Wael A. Aboneama

<sup>1</sup>Department of Architecture & Planning, College of Engineering, King Khalid University,  
PO Box 394, Abha 61411 KSA.

E-mail address: waboneama@kku.edu.sa – Mob: (+966) 539 193 501

**Abstract:** Saudi Arabia Vision 2030 is a planning for 15 years that announced in 2016 to make Saudi Arabia's economy more powerful and has multi income channels not only oil, and developing public services. The planning focuses for better life enhancement with creating new economic regions inside the country with huge investments with hundreds of billions of US dollars. Sustainable development in this case is a mandatory to can achieve the goals of this vision. Sustainability is the process of change, in which the exploitation of resources, the direction of investments, the orientation of technological development and institutional change are all in harmony and enhance both current and future potential to meet human needs and aspirations.

A unique sustainable rating system for Saudi Arabia environment should be created and applied under the protection of law umbrella to insure applying sustainable principals on all new developments and constructions.

This paper focuses on reviewing applied sustainable rating system in Saudi Arabia against the environmental conditions and people culture in this area of the world and redistribute the weights of each item to be more compatible with the environment, local resources, and human needs.

**Keywords:** Sustainable rating system, Saudi Arabia 2030 Vision.

### 1. Introduction:

All over the world, buildings consume 17% of potable water, 25% of forest wood, 33% of carbon dioxide emissions and 40% of energy consumption and manufactured materials (Candace Say, 2008). That was the reason for the whole world to start thinking for sustainable development and searching for green buildings, but the assessment method to measure the credibility of applying sustainable criteria on buildings was new issue. Sustainable rating systems are the only reliable method to measure green buildings fig (1).

BREEAM and LEED are the most popular green building certification programs used worldwide (wikipedia, 2015). The Building Research Establishment (BRE) publishes BREEAM in

1990 in UK; meanwhile development of LEED began in 1993 in USA. They are the world's longest established method of assessing, rating, and certifying the sustainability of buildings (BREEAM, 2014).



**Figure (1)** Sustainability rating systems (James Woodall, 2017)

# 14<sup>th</sup> Annual Research Day

Organised by the Deanship of Scientific Research in Collaboration with the College of Engineering Research Centre  
4<sup>th</sup> April 2019

On 25 April 2016, Saudi Arabia leaders announced Saudi Vision 2030, which is a plan to minimize Saudi Arabia's dependence on oil as the only source of energy in the country (Wikipedia, 2016). More than 80 giant projects are planned to be developed and constructed in Saudi Arabia before the year 2030. On 24 Oct 2017 Saudi government announced NEOM project at the Northern West of the country close to the border of Jordan and Egypt. It is a planned to have an area of 26,500 sq km and it will act as transnational city with estimated budget 500 billion US dollars (Wikipedia, 2018).

Average domestic water use in Saudi Arabia compared to other countries (liters per day per person)

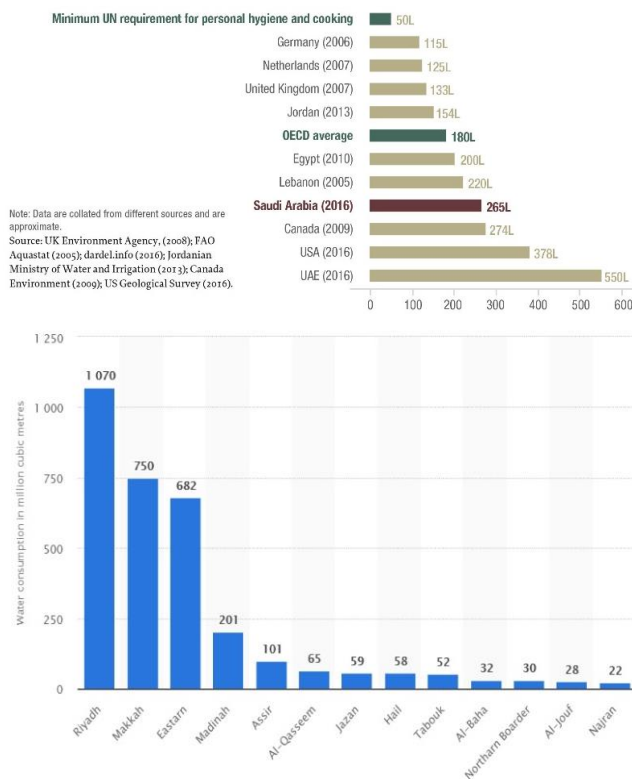


**Figure (2)** on top, describes average domestic water use in Saudi Arabia compared other countries (Ahmed Almansouri, 2017), on left water consumption per region in Saudi Arabia (statista, 2018)

It is obvious that Saudi Arabia is planning for a great economic and urban development jump.

Lack of potable water and renewable energy resources chase this future planning and vision. In the wake of a World Bank report on global water scarcity released in February 2016, various Saudi government officials and water experts warned that the kingdom could run out of water entirely by 2029 if it did not radically reform its agricultural practices and address high water consumption patterns across the country (Ahmed Almansouri, 2017). Fig (2) this statistic shows the total water consumption in Saudi Arabia by region in million cubic meters in 2017. Table (1) describes that the fossil fuels are the most important source of energy in Saudi Arabia, which means more carbon dioxide emissions, and more pollution and the renewable energy resources do not reflect the real potential in this country.

**Table 1:** Describes the energy sources in Saudi Arabia compared with Europe in 2014 (saudi-arabia/energy-consumption, n.d.)

Energy source	Total in Saudi Arabia	percentage in Saudi Arabia	percentage in Europe	per capita in Saudi Arabia	per capita in Europe
Fossil fuels	604.27 bn kWh	99,9 %	48,9 %	18,722.24 kWh	7,994.86 kWh
Nuclear power	0.00 kWh	0,0 %	7,2 %	0.00 kWh	1,185.87 kWh
Water power	0.00 kWh	0,0 %	23,4 %	0.00 kWh	3,829.91 kWh
Renewable energy	604.88 m kWh	0,1 %	16,2 %	18.74 kWh	2,655.34 kWh
Other energy sources	0.00 kWh	0,0 %	4,3 %	0.00 kWh	696.17 kWh
Total production capacity	604.88 bn kWh	100,0 %	100,0 %	18,740.98 kWh	16,362.15 kWh

Sustainability in Saudi Arabia is not an option; it is a mandatory to protect the environment for Saudis grandsons' future. Saudi Arabia should work through a strategy, which aims to satisfy development needs of energy. This strategy depends on diversifying energy resources and achieving the most benefit of it besides improving energy devices to enhance the consumption rates. In addition, the strategy should aim also at environmental conservation and improving local manufacturing of energy equipment (Aboneama, Applying the new sustainable urban development

# 14<sup>th</sup> Annual Research Day

Organised by the Deanship of Scientific Research in Collaboration with the College of Engineering Research Centre

4<sup>th</sup> April 2019

towards the location of the renewable energy resources in Egypt, Oct. 2015)

## 2. Literature review:

### 2.1 Sustainability rating system

Sustainability rating systems are created to push all architects, developers, and contractors to protect the environment through their projects by applying the most effective sustainable criteria. Rating systems should be under the protection of law umbrella (Aboneama, Local Rating Systems for Sustainability are Mandatory to Protect the Planet – LEED in the Middle East, 2013)

**Table 1:** General information of mainstream building rating systems (Mohamed Shaawat, June 2014)

	LEEDS	GS	BREEAM	CASBEE	GG	BCA-GM	GSAS	PBRS	BREEAM-G
Name of System	Leadership in Energy & Environmental Design	Green Star	Building Research Environment Assessment Method	Comprehensive Assessment System for Building Environment Efficiency	Green Globe	BCA-Green Mark	Global Sustainability Assessment System	Pearl Building Rating System	BREEAM-Gulf Version (Withdrawn)
Origin	United States of America	Australia	United Kingdom	Japan	United States of America	Singapore	Qatar	United Arab Emirates	United Kingdom
Managing Organization	United States Green Building Council	Green Building Council Australia	Building Research Establishment	Japan Green Build Council	Green Building Initiative	Building & Construction Authority	Gulf Organization for Research & Development	Estimada	Building Research Establishment
Launch Date	2000	2002	1990	2001	2002	2005	2010	2010	2008
Ratings	Certified, Silver, Gold, Platinum	1 Star, 2 Star, 3 Star, 4 Star, 5 Star, 6 Star	Pass, Good, Very Good, Excellent	C, B-, B+, A, S	1 GG, 2 GG, 3 GG, 4 GG	Platinum, Gold Plus	1 Star, 2 Star, 3 Star, 4 Star, 5 Star, 6 Star	1 Pearl, 2 Pearl, 3 Pearl, 4 Pearl, 5 Pearl	Pass, Good, Very Good, Excellent
Area of Coverage	United States of America	Australia	United Kingdom & some European Countries	Japan	United States of America	Singapore	Qatar	United Arab Emirates	Saudi Arabia, Qatar, Oman, Bahrain, Yemen etc.

Each rating system developing meets the following principles, table (2):

1. Ensure environmental quality through an accessible, holistic, and balanced measure of environmental impacts.
2. Measuring environmental quality.
3. Quantifying and calibrating a cost-effective performance standard for defining environmental quality.
4. Reflect the social and economic benefits of meeting the environmental objectives covered.

5. Provide a common framework of assessment that is tailored to meet the ‘local’ context, including regulation, climate, and sector.

### 2.2 Saudi Green Building Forum SGBF & BREEAM-G

The Saudi Green Building Forum (SGBF) has become the newest member of USGBC’s LEED International Roundtable, which means that Saudi’s government realizes the impact of negative behaviors towards the environment and its future’s vision and planning. They started to take actions towards sustainability. In addition, they realize the importance of sustainability rating system to ensure the actual practice of sustainable design and construction (Crea, 2017). The question now, if there is any changes on LEED item weights to accommodate the environment of Saudi Arabia? Unfortunately, the answer is no. The LEED certificate issues in Saudi Arabia with the same weights and items of United States however, the environment in both countries are totally different and contradictory.

In 2008, a version called BREEAM-G produced by the British Research Establishment (BRE) for the Arabian Peninsula countries. Unfortunately, this version withdrawn and there is no any data about it for evaluation. Qatar took the step in advance and produced in 2010 its rating system.

### 2.3 The Global Sustainability Assessment System GSAS

The Global Sustainability Assessment System (GSAS) originally is a rating system developed for Arabian Peninsula countries. This system was announced after QSAS (Qatar sustainability assessment system) launching. GSAS is developed after comparison between 40 rating systems all over the world. The most important feature of GSAS is that it takes into account the region’s social, economic, environmental and cultural aspects, which are

# 14<sup>th</sup> Annual Research Day

Organised by the Deanship of Scientific Research in Collaboration with the College of Engineering Research Centre

4<sup>th</sup> April 2019

different from other parts of the world. Several countries in the Middle East and North Africa countries called (MENA) region, such as Saudi Arabia, Kuwait, Jordan and Sudan, have shown keen interest in the adoption of GSAS as unified green building code for the region (Zafar, 2017). Unfortunately, for political reasons, it is not used in Saudi Arabia and before any political unrest, LEED dominated Saudi construction market.

## 2.4 Wind power in Saudi Arabia

There are 20 locations in Saudi Arabia that can generate energy from wind. Fig (3) illustrates the potential areas in Saudi Arabia to generate energy and install wind turbines. Results suggest that most of the country can be supported by wind power (Ph.Martin, 20 April 1985).

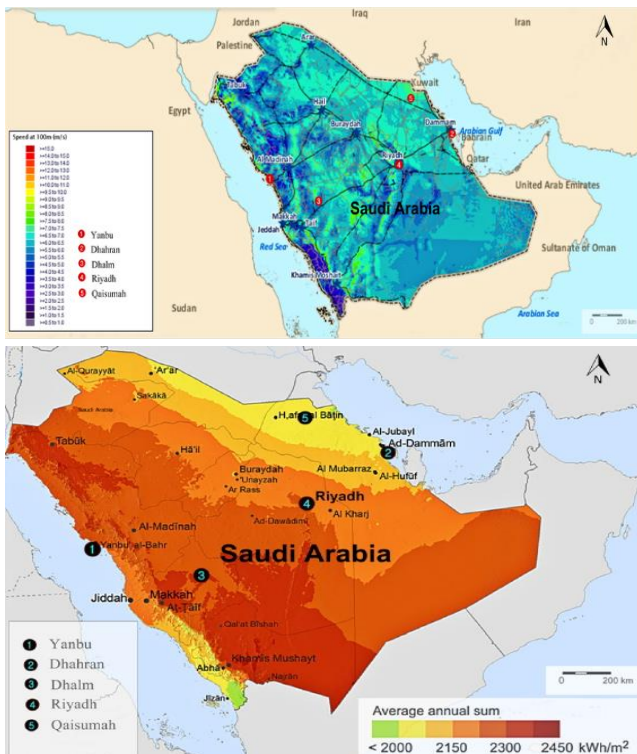


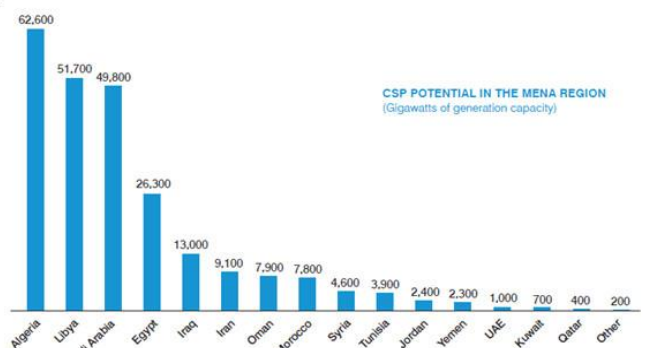
**Figure (3)** on top wind speed in Saudi Arabia (Mohamed Mohamed, August 2016), below; solar energy strength (solargis, 2011)

## 2.5 Solar energy in Saudi Arabia

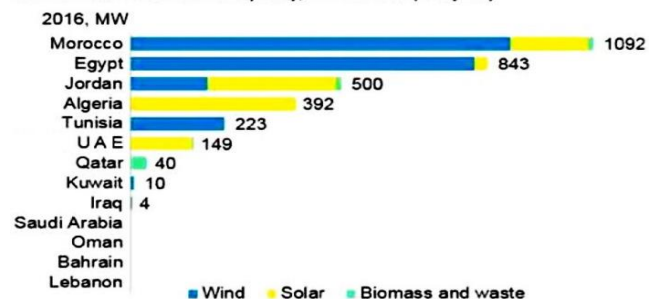
The Saudi Arabia location is one of the best countries to generate energy from solar radiation because it is located inside the Sun Belt, which has led it to become one of the largest solar energy producer's fig (3). Average solar irradiation in Saudi Arabia is about twice as high as in Germany. Average solar irradiation exceeds 1.800 kWh/m<sup>2</sup> up to 2.200 in some locations. The Tabuk area has the highest irradiation. Saudi Arabia also has vast expanses of open desert seemingly tailor-made for solar-panel arrays (Aljamaan, Dec. 2012).

## 2.6 Renewable energy resources in Saudi Arabia

Electricity demand in Saudi Arabia increases year and after, which means that energy generation should seek new resources (Saudigazette, 2016). Conventional generation that uses fossil fuels is the reason of pollution and destroying the ecology and human health. Saudi Arabia can be the largest solar energy producers. (Aljamaan, Dec. 2012). Fig (4) illustrates the potential of generating power from renewable energy in the MENA countries and the actual generated renewable energy from those countries. Saudi Arabia has the third place as available resources but unfortunately listed as last place for actual generated renewable energy.



**Title: Cumulative Installed Capacity, Renewables (Ex hydro)**



# 14<sup>th</sup> Annual Research Day

Organised by the Deanship of Scientific Research in Collaboration with the College of Engineering Research Centre

4<sup>th</sup> April 2019

**Figure (4)** on top renewable energy production (Saudigazette, 2016),

Below, renewable energy potential in MENA (Aljamaan, Dec. 2012),

## 2.7 The importance of passive design in Saudi Arabia

Saudi Arabia, has one of the warmest weather in the world, which means the air conditioner is turned on day and night. Saudi Arabia uses more than 50% of its electricity on air conditioning and cooling. Also, desalinate sea water for drinking consume around 20% of energy. Desalinating sea water is an extremely energy-intensive process, making it very expensive (Schlanger, 2018). All previous data lead to the importance of passive design in Saudi Arabia. It clarifies that the architectural history of the Middle East have abundant techniques for passive and environmental design such as courtyards, mashrabia, takhtaboosh, and orientation techniques. Passive design criteria is focusing on reduction of air-conditioning usage, and moves towards natural lighting and ventilation systems. Trying to achieve or get closer to zero-energy buildings.

## 3. Methodology steps for creating a Saudi Arabian sustainable rating system:

### 3.1 Rating systems category weights

All sustainable rating systems are based on identical categories fig (5). Each category has certain weight that reflects the actual need for this nation to protect this item according to its environmental requirements (Bsria, 2012). For

example, if we build in a place that has lack of water resources. The weight of category called “water efficiency” will be huge to encourage designers, developers, and contractors to use all methods for water saving to can achieve the minimum requirements of this category and that is exactly what we need from them to save our particular environment.

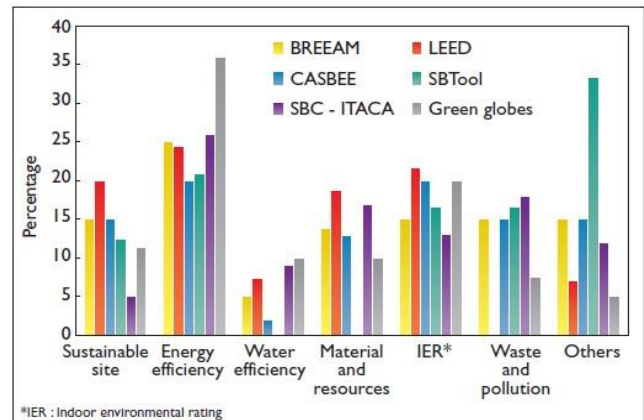


**Figure (5)** Comparison between sustainability rating systems weights (Bsria, 2012)

It is obvious that we use the expression of “particular environment”. The environmental characteristics and circumstances are totally different from place to place. We never can say that Ohio State has the same environmental conditions as Saudi Arabia. They are totally different. Ohio has a huge amount of rainfall average and forests, on the contrary, Saudi Arabia has lack of potable water resources and most of its lands are desert. Obviously, we can’t use rating system category weights from certain environment to protect another one with contradictory conditions. It is like that we feed the horse with gasoline fuel because it is a mean of transportation.

### 3.2 Rating system categories

# 14<sup>th</sup> Annual Research Day

Organised by the Deanship of Scientific Research in Collaboration with the College of Engineering Research Centre

4<sup>th</sup> April 2019

All countries share common concerns about their ecology with different weights fig (6). These concerns are the rating systems categories. The global warming, pollution, limited resources and greenhouse gas emissions are the reasons of these categories (Sundus L. Shareef, Nov. 2016). Fig (6&7) has three different rating systems which are; BREEAM, LEED, and GSAS. They are the most famous in the world. Saudi Green Building Forum SGBF made an agreements with USGBC, BRE and GSAS. May GSAS is the most closer to the Arabian Peninsula environment because Qatar is in the same Peninsula. But, obviously Saudi Arabia ecology is totally different from UK and USA. In the following we can summarize these categories and the actual need of Saudi Arabia ecology from each one which will be transformed into category weight.

Figure (6) on top BREEAM categories & weights (BREEAM, 2016), below LEED categories (USGBC, 2010)



Figure (7) GSAS categories (Services/ Green buildings /Why environmental accreditations, 2016)

### 3.2.1 Sustainable sites

The sustainable sites category focuses on the environment surrounding the building. Protecting Greenfield and restoring Brownfields are main tasks for this category (USGBC, 2017). It creates a framework that the teamwork should protect ecosystem and minimize carbon emissions and heat islands effect (Sustainable sites, 2015). This category helps to reduce water demand, filter and reduce storm water runoff, provide wildlife habitat, reduce energy consumption, improve air quality, improve human health and increase outdoor recreation opportunities. Saudi Arabian rating system can give 10% of category weights to the sustainable sites. The following items are the main divisions of sustainable sites and their importance for Saudi Arabia environment:

BREEAM Scoring			
Refurbishment process	Issue & category scoring	Category Weighting	BREEAM score
Design targets	<ul style="list-style-type: none"> <li>• Management</li> <li>• Energy</li> <li>• Water</li> <li>• Materials</li> <li>• Pollution</li> <li>• Waste</li> <li>• Health &amp; Wellbeing</li> </ul>	12%	Pass (≥30) Good (≥45) Very Good (≥55) Excellent (≥70) Outstanding (≥85)
Wider design opportunities		43%	
Procurement process		11%	
Contractor requirements		8%	
Additional measures		6%	
	• Innovation	3%	10%
		17%	

### LEED Credit Categories



# 14<sup>th</sup> Annual Research Day

Organised by the Deanship of Scientific Research in Collaboration with the College of Engineering  
Research Centre

4<sup>th</sup> April 2019

---

- Construction activity pollution prevention; the same weight for any place in the world
  - Site assessment (it differs from place to another inside the same country)
  - Site development - protect or restore habitat (it differs from place to another inside the same country)
  - Open space (it depends on each country's culture)
  - Rainwater management (it differs from place to another inside the same country)
  - Heat island reduction (it is very important for hot countries like Saudi Arabia)
- Light pollution reduction (the same weight for any place in the world).

### 3.2.2 Location and transportation

Sustainable projects users should find means of transportation with less carbon emissions and environmental friendly. It is obvious that moving Saudi Arabia to the level of sustainable development with minimizing depending on fossil fuel is restricted to minimize using private car as the main mean of transportation. There are several items should be assessed to ensure this category (USGBC, 2018). This category should have 20% of category weights.

- Neighborhood Development location
  - Sustainable means of transportation (it is a major item with high score of points)
  - High priority site
  - Surrounding density and diverse uses
  - Access to quality transit
  - Bicycle facilities (it is difficult item to be applied in very hot weather countries. The research recommend to eliminate this item)
  - Reduced parking footprint
- Green vehicles (it is a major item with high score of points).

### 3.2.3 Water efficiency

The Water Efficiency category concerns about water in everything, looking at indoor use, outdoor use, and metering. The category is based on efficiency to save water consumption (USGBC, 2018). As a result, each prerequisite looks at water efficiency and reductions in potable water use alone. Then, the points additionally recognize the use of non-potable and alternative sources of water. This category should have at least 20% of the weight of Saudi rating system as a result of lack resources for potable water. The points will be distributed on the following items;

- Outdoor water use reduction
- Indoor water use reduction
- Building-level water metering
- Cooling tower water use

### 3.2.4 Energy and atmosphere

The Energy and atmosphere category focuses on energy in two perspectives which are; reducing energy consumption and using renewable energy sources (USGBC, 2018). The sector of atmosphere is responsible about avoiding the use of harmful components for the planet atmosphere such as refrigerants. Fig (4) clarifies that Saudi Arabia does not produce energy from renewable resources meanwhile it has one of the highest potential to produce this kind of energy. It means this category should have at least 25% of the total weights.

- Optimize energy performance
- Building-level energy metering
- Renewable energy production (at least 20% of the total rating systems weights)
- Fundamental refrigerant management

### 3.2.5 Passive design

The indoor environmental quality category aims to enhance indoor air quality, thermal and visual comfort, and occupants' satisfaction

# 14<sup>th</sup> Annual Research Day

Organised by the Deanship of Scientific Research in Collaboration with the College of Engineering  
Research Centre

4<sup>th</sup> April 2019

---

(USGBC, 2018). Passive design is one of the most important categories for hot weather and desert countries. The only way to reduce air condition use is following design techniques in the history of architecture in all Middle East countries. In the past, they had the ability to produce comfortable buildings which are existing nowadays without using any kind of energy consumption. It is not an overstatement to say that, historical buildings like (Bayt Al-Suhaymi in Cairo) Fig (8) and more are the real zero-energy buildings with high indoor environmental quality.

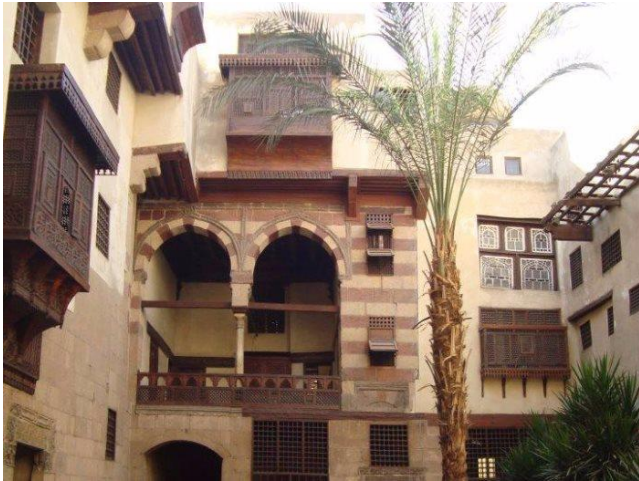


**Figure (8)** Al-Suhaymi (Al-gammal, 2017)

During last five decades a great leap in construction happened in Saudi Arabia with importing building types from cold weather countries with full of glazed façade that increased energy consumption for cooling and don't respect people culture. This category in Saudi Arabian rating system should has at least 18% of the total weights. The following items are the main items for passive design category;

- Enhanced indoor air quality strategies
- Thermal comfort
- Interior lighting
- Daylight and quality views

## 3.2.6 Material and resources

Reduce, reuse, and recycle are the main critical component of this category. Clearly, reducing consumption is critical, and reusing and recycling waste are important strategies (USGBC, 2018). The total weight of this category should not exceed 7% of the total weight.

## 4. Results and Findings

We can conclude from this research that we have an excellent opportunity to encourage architects, developers, and contractors to think work and behave in actual sustainable way with creating a unique rating system for Saudi Arabia. The number of certified buildings in Saudi Arabia clarifies the desire of sustainable buildings. In addition, Saudi vision 2030 and NEOM project elucidate the intension of the government for a grand economic and sustainable development step.

## 5. Discussion and analysis

Creating sustainable rating system for Saudi Arabia will be focused on studying the actual challenges that facing its ecology and its supplies of energy and potable water. Importing one of the rating systems of cold weather and high rainfall average countries gives ostensible results and does not match environmental needs. Calculating rating system categories weight is the most important task to produce a real rating that reflect ecology and country requirements.

## 6. Conclusion and recommendations

Most of the sustainable rating systems have similarities in categories definition more than differences. Each category has different weight from country to another based on each one environmental needs. This is due to the fact that

# 14<sup>th</sup> Annual Research Day

Organised by the Deanship of Scientific Research in Collaboration with the College of Engineering  
Research Centre

4<sup>th</sup> April 2019

all of these systems are trying to help us create a better world and leave our children a better and cleaner world (Altin, Jan. 2016). It will be a waste of efforts to use certain rating system that reflects the requirements for cold weather country and full of forests due to high rainfall average in a hot weather country which is full of desert like Saudi Arabia. If it is mandatory to use one of the rating systems all over the world, we should search for a similar environmental requirements like countries inside the Arabian Peninsula and apply their rating systems.

In conclusion, creating a unique rating system for Saudi Arabia will be the best choice. Emphasizing on the weights of generating renewable energy, saving water consumption, using passive design techniques to minimize using air-conditioner, and installing means of sustainable transportation are the actual reflection of Saudi Arabia ecology and future needs.

## Acknowledgement & Note

This paper published in European Journal of Sustainable Development – Volume 7, NO4 – September 2018, Rome, Italy (European Center of Sustainable Development)

ISSN 2239-5938 (Print)

ISSN 2239-6101 (Online)

<https://www.ecsdev.org/ojs/index.php/ejsd/article/download/695/690>

## BIBLIOGRAPHY

Abdallah, A.-H. (2017, Jan 6). *أبها عاصمة السياحة العربية 2017*. Retrieved from al-jazirah: <http://www.al-jazirah.com/2017/20170106/ew1.htm>

Abir. (2015, Sep. 28). *Abha photos*. Retrieved from 3bir: <https://v.3bir.net/345832/>

Aboneama, W. (2013). Local Rating Systems for Sustainability are Mandatory to Protect the Planet – LEED in the Middle East. *The center of*

*environment behaviour studies (cE-Bs), Faculty of architecture, planning, & surveying, Universiti teknologi, Mara, Malaysia, 83-99.*

Aboneama, W. (2015). Installing various means of sustainable transportation to achieve sustainable urban development and Cairo vision 2050. *Future north Africa transportation summit* (pp. 11-12). Cairo: IQPC.

Aboneama, W. (Oct. 2015). Applying the new sustainable urban development towards the location of the renewable energy resources in Egypt. *Wind power North Africa, Discus upcoming wind projects and how to drive growth in north African wind power market* (pp. 2-3). Cairo: IQPC.

Ahmed Almansouri, F. d. (2017, April 4). *Saudi-Arabia-water-resources*. Retrieved from revolve-water.com: <http://www.revolve-water.com/saudi-arabia-water-resources/>

Al-Almaey, I. (2018). *abotalal40041*. Retrieved from Twitter: <https://twitter.com/abotalal40041>

Al-gammal, E. (2017, May 22). *بيت السحيمي درة العمارة الإسلامية*. Retrieved from 3ain.net: <http://www.3ain.net/Article/14522/http://www.3ain.net/Article/14522/>

Aljamaan, H. (Dec. 2012). *The Importance of Solar Energy in Saudi Arabia*. Stanford University.

Altin, M. (Jan. 2016). Green Building Rating Systems in Sustainable Architecture. Chapter 43. American society of landscape architects. (2018). *sustainable urban development*. Retrieved from [www.asla.org](http://www.asla.org):

<https://www.asla.org/sustainableurbandevelopment.aspx>

BREEAM. (2014, May 8). *Why choose BREEAM?* Retrieved from [breeam.com](http://www.breeam.com): <https://www.breeam.com/discover/why-choose-breeam/>

BREEAM. (2016, Feb 29). *scoring\_and\_rating*. Retrieved from [breeam.com](http://www.breeam.com): [http://www.breeam.com/domrefurbmanual/content/03scoring/01scoring\\_and\\_rating.htm](http://www.breeam.com/domrefurbmanual/content/03scoring/01scoring_and_rating.htm)

Bsria. (2012, May). *Rating environmental assessments*. Retrieved from [bsria.co.uk](http://www.bsria.co.uk):

# 14<sup>th</sup> Annual Research Day

Organised by the Deanship of Scientific Research in Collaboration with the College of Engineering  
Research Centre

4<sup>th</sup> April 2019

- <https://www.bsria.co.uk/news/article/rating-environmental-assessments/>
- burn an energy journal. (2010). *MAP: How much energy is the world using?* Retrieved from [burnanenergyjournal.com](http://burnanenergyjournal.com): <http://burnanenergyjournal.com/how-much-energy-are-we-using/>
- Candace Say, A. W. (2008). Sustainable rating systems around the world. *CTUBUH*, Issue II.
- Carter, M. (2014, June 4). *Eight US States Form Alliance to Put 3.3 Million Zero Emission Vehicles on the Road by 2025*. Retrieved from [inhabitat.com](http://inhabitat.com): <https://inhabitat.com/eight-us-states-form-alliance-to-put-3-3-million-zero-emission-vehicles-on-the-road-by-2025/>
- Crea, J. (2017, March 20). *Saudi Green Building Forum joins LEED International Roundtable*. Retrieved from [usgbc.org](http://usgbc.org): <https://www.usgbc.org/articles/saudi-green-building-forum-joins-leed-international-roundtable>
- Douglas F. Welsh, W. C. (2001). *Xeriscape Landscape Water Conservation*. Texas: Texas agriculture extension service. [en.wikipedia.org](http://en.wikipedia.org). (2008). *Sustainable city*. Retrieved from Wikipedia: [https://en.wikipedia.org/wiki/Sustainable\\_city](https://en.wikipedia.org/wiki/Sustainable_city)
- feedyeti. (2018). *Abha*. Retrieved from [feedyeti.com](http://feedyeti.com): <https://feedyeti.com/hashtag.php?q=abha>
- FuelCellsWorks. (2018, April 14). *zero-emission-buses*. Retrieved from [fuelcellsworks.com](http://fuelcellsworks.com): <https://fuelcellsworks.com/news/zero-emission-buses-equipped-with-freudenberg-seals-set-durability-milestone>
- globalrailnews. (2018, June 2). *CRRC tests suspended monorail called the 'Sky Train'*. Retrieved from [globalrailnews.com](http://globalrailnews.com): <https://www.globalrailnews.com/2017/07/27/crrc-tests-suspended-monorail-vehicle/>
- govnews. (2015, Nov). *Victoria taps Bombardier for new \$274 mil E-Class trams*. Retrieved from [govnews.com.au](http://govnews.com.au): <http://www.govnews.com.au/victoria-taps-bombardier-for-new-274-mil-e-class-trams/>
- Green home building. (2001). *Local materials*. Retrieved from [greenhomebuilding.com](http://www.greenhomebuilding.com): <http://www.greenhomebuilding.com/localmaterials.htm>
- Hiroaki Suzuki, W. B. (2010). *Ecological cities as economic cities*. (ISBN 978-0-8213-8046-8): Synopsis.
- Hoiberg, D. H. (2010). *Encyclopædia Britannica* (Vol. 15th ed). A-ak Bayes.
- Jain, A. (2013, Nov 29). *passive techniques*. Retrieved from [slideshare.net](http://slideshare.net): <https://www.slideshare.net/anvitajain3/passive-techniques>
- James Woodall. (2017, Nov 27). *Evolution of Green Building Rating Systems: A New Frontier?* Retrieved from [james-woodall.com](http://james-woodall.com): <https://www.james-woodall.com/blog/>
- Jeon, C. M., & Amekudzi. (2005). *Sustainable transport*. Retrieved from [en.wikipedia.org](http://en.wikipedia.org): [https://en.wikipedia.org/wiki/Sustainable\\_transport](https://en.wikipedia.org/wiki/Sustainable_transport)
- Liu, H., Wennersten, R., Luo, P., Jiang, L., & Dong, a. W. (2016). Conceptual Sustainability Framework for Eco-City Development in the City Core of Xuzhou. *Journal of Urban Planning and Development*, Volume 142, Issue 4. Retrieved from [ascelibrary.org](http://ascelibrary.org): <https://ascelibrary.org/doi/10.1061/%28ASCE%29UP.1943-5444.0000319>
- Manea, M. (2010, Dec 28). *Teenagers bother Al-Mansek district with drifting*. Retrieved from [alwatan.com.sa](http://www.alwatan.com.sa): [http://www.alwatan.com.sa/Politics/News\\_Detail.aspx?ArticleID=34996](http://www.alwatan.com.sa/Politics/News_Detail.aspx?ArticleID=34996)
- Mohamed Mohamed, A. E. (August 2016). PSO-Based smart grid application for sizing and optimization of hybrid renewable energy systems. *Plos one*.
- Mohamed Shaawat, R. J. (June 2014). A guide to environmental building rating system for construction of new buildings in Saudi Arabia. *Emirates Journal for Engineering Research*, 47-56.

# 14<sup>th</sup> Annual Research Day

Organised by the Deanship of Scientific Research in Collaboration with the College of Engineering  
Research Centre

4<sup>th</sup> April 2019

- Morton, J. (2013, Jan 25). *Regional Materials: Benefits and Advantages*. Retrieved from buildings.com: <https://www.buildings.com/article-details/articleid/15165/title/regional-materials-benefits-and-advantages/viewall/true>
- Pantsios, A. (2014, Oct. 24). *top-10-greenest-cities-in-the-world*. Retrieved from ecowatch.com: <https://www.ecowatch.com/top-10-greenest-cities-in-the-world-1881963132.html>
- Ph.Martin. (20 April 1985). Wind power potential of Saudi Arabia. *Solar & Wind Technology*, 139-142.
- Ptacek, K. (2018, Jan 10). *zero-emission-all-electric-buses*. Retrieved from dartdallas.dart.org: <http://dartdallas.dart.org/2018/01/10/dart-demos-new-proterra-zero-emission-all-electric-buses/>
- Reda, A. (2018). *rijal-alma-heritage-village-located-assir-region*. Retrieved from dreamstime.com: <https://www.dreamstime.com/rijal-alma-heritage-village-located-assir-region-capital-almaa-province-was-natural-corridor-linking-image107226437>
- Rigester, R. (2008). *advantages-and-disadvantages*. Retrieved from ecocitiescatq3rene: <https://ecocitiescatq3rene.weebly.com/advantages-and-disadvantages.html>
- saudi-arabia/energy-consumption*. (n.d.). Retrieved from World Data: <https://www.worlddata.info/asia/saudi-arabia/energy-consumption.php>
- Saudigazette. (2016, Dec. 21). *Middle East renewable energy potential bright*. Retrieved from saudigazette.com.sa: <http://saudigazette.com.sa/article/522681/BUSINESS/Middle-East-renewable-energy-potential-bright>
- Schlanger, Z. (2018, May 22). *70% of Saudi Arabia's electricity is used for air conditioning*. Retrieved from qz.com: <https://qz.com/1284239/70-of-saudi-arabias-electricity-is-used-for-air-conditioning/>
- Schmitt, A. (2013, July 31). *The Rise of The North American Protected Bike Lane*. Retrieved from momentummag.com: <https://momentummag.com/the-rise-of-the-north-american-protected-bike-lane/>
- Scott, M. (2018, Jan 18). *Saudi Arabia Plans To Source 10% Of Its Power From Renewable Energy Within 5 Years*. Retrieved from forbes.com: <https://www.forbes.com/sites/mikescott/2018/01/18/saudi-arabia-plans-to-source-10-of-its-power-from-renewable-energy-within-5-years/#3fb41fd9485f>
- SCTA. (2010). *Asir-Mountain-Villages*. Retrieved from arriyadh.com: [http://www.arriyadh.com/Eng/Tourism/Left/KSA Attract/Asir/Asir-Mountain-Villages.doc\\_cvt.htm Services/ Green buildings /Why environmental accreditations. \(2016\). Retrieved from pacte-ingenierie.com: http://www.pacte-ingenierie.com/index\\_coeur.php?rub\\_name=Green-building&lien=20&id=0](http://www.arriyadh.com/Eng/Tourism/Left/KSA Attract/Asir/Asir-Mountain-Villages.doc_cvt.htm Services/ Green buildings /Why environmental accreditations. (2016). Retrieved from pacte-ingenierie.com: http://www.pacte-ingenierie.com/index_coeur.php?rub_name=Green-building&lien=20&id=0)
- Skoda. (2018). *trolleybus-30-tr*. Retrieved from skoda.cz: <https://www.skoda.cz/en/references/trolleybus-30-tr/?from=prod>
- solargis. (2011). *Africa & Middle East Solar Insolation Map*. Retrieved from hotspotenergy.com: <http://www.hotspotenergy.com/DC-air-conditioner/solar-map-africa-middle-east.php>
- statista. (2018, May). *saudi-arabia-water-consumption-by-region*. Retrieved from statista.com: <https://www.statista.com/statistics/627146/saudi-arabia-water-consumption-by-region/>
- Sundus L. Shareef, H. A. (Nov. 2016). Building sustainability rating systems in the Middle East. *Engineering Sustainability*, 1-11.
- Sustainablesites. (2015). *certification-guide*. Retrieved from sustainablesites.org: <http://www.sustainablesites.org/certification-guide>
- Titi, A. (2016). *Dam rainfall in the city of Abha*. Retrieved from ar.wikipedia.org:

# 14<sup>th</sup> Annual Research Day

Organised by the Deanship of Scientific Research in Collaboration with the College of Engineering  
Research Centre

4<sup>th</sup> April 2019

---

[https://ar.wikipedia.org/wiki/%D9%85%D9%84%D9%81:Saad\\_abha.JPG](https://ar.wikipedia.org/wiki/%D9%85%D9%84%D9%81:Saad_abha.JPG)

USGBC. (2010). *LEED-Credit-Categories*. Retrieved from igbc.ie: <https://www.igbc.ie/wp-content/uploads/2014/11/LEED-Credit-Categories.png>

USGBC. (2017). *sustainable-sites*. Retrieved from [usgbc.org](https://www.usgbc.org):

<https://www.usgbc.org/credits/new-construction/v4/sustainable-sites>

USGBC. (2018). *energy-atmosphere*. Retrieved from [usgbc.org](https://www.usgbc.org):

<https://www.usgbc.org/credits/new-construction/v4/energy-%26-atmosphere>

USGBC. (2018). *green-building-101-sustainable-materials-and-resources*. Retrieved from [usgbc.org](https://www.usgbc.org): <https://www.usgbc.org/articles/green-building-101-sustainable-materials-and-resources>

USGBC. (2018). *indoor-environmental-quality*. Retrieved from [usgbc.org](https://www.usgbc.org):

<https://www.usgbc.org/credits/existing-buildings/v4/indoor-environmental-quality>

USGBC. (2018). *location-transportation*. Retrieved from [usgbc.org](https://www.usgbc.org):

<https://www.usgbc.org/credits/new-construction/v4/location-%26-transportation>

USGBC. (2018). *water-efficiency*. Retrieved from [usgbc.org](https://www.usgbc.org):

<https://www.usgbc.org/credits/healthcare/v4/water-efficiency>

vacationidea. (2016). *best-time-to-visit-copenhagen-denmark*. Retrieved from [vacationidea.com](https://vacationidea.com):

<https://vacationidea.com/tips/best-time-to-visit-copenhagen-denmark.html>

watersaving - Switzerland. (2014, May 6). *saudi-arabia*. Retrieved from [watersaving.com](https://www.watersaving.com):

<https://www.watersaving.com/en/infos/saudi-arabia/>

Weather spark. (n.d.). *Average-Weather-in-Abha-Saudi-Arabia-Year-Round*. Retrieved June 2, 2018, from Weatherspark:

[en.wikipedia.org](https://en.wikipedia.org): [wikipedia](https://en.wikipedia.org). (2008). *Trolleybus*. Retrieved from [en.wikipedia.org](https://en.wikipedia.org):

[wikipedia](https://en.wikipedia.org). (2009). *Zero-emissions\_vehicle*. Retrieved from [en.wikipedia.org](https://en.wikipedia.org):

[wikipedia](https://en.wikipedia.org). (2015, April 15). *Leadership\_in\_Energy\_and\_Environmental\_Design*. Retrieved from [en.wikipedia.org](https://en.wikipedia.org):

Wikipedia. (2016, May 1). *Saudi\_Vision\_2030*. Retrieved from [en.wikipedia.org](https://en.wikipedia.org):

Wikipedia. (2018, June 5). *Neom*. Retrieved from [en.wikipedia.org](https://en.wikipedia.org):

Zafar, S. (2017, March 4). *Green Building Rating Systems in MENA*. Retrieved from [ecomena.org](https://ecomena.org):

# 14<sup>th</sup> Annual Research Day

Organised by the Deanship of Scientific Research in Collaboration with the College of Engineering  
Research Centre

4<sup>th</sup> April 2019

## Comparative study of Salvia Officinal essential oil from different countries geographic areas

Atef El Jery<sup>1,2,\*</sup>, Mudassir Hassan<sup>1</sup>, MD Mamoon Rashid<sup>1</sup>

<sup>1</sup> Chemical Engineering Department, College of Engineering, King Khalid University,  
PO Box 394, Abha 61411 KSA.

<sup>2</sup> Agro-alimentary Department, Higher Institute of Applied Biology of Medenine, Gabes University,  
Street El Jorf – km 22.5, Medenine 4119, Tunisia  
E-mail address: ajery@kku.edu.sa

**Abstract:** A comparative analysis of the chemical composition of the essential oils of Salvia Officinalis leaves plant, from Abha (Saudi Arabia) and others countries geographic areas, was the mean objective in the present study. The extraction was carried out by hydro-distillation, the obtained yield of the essential oil is 3.24 %. The chemical analysis of essential oils was accomplished by using CPG-MS identified 26 compounds. Among the majority identified compounds of the essential oil of sage are: camphor (20.30 %), 1,8-cineole (15.01 %),  $\alpha$ -thujone (14.89 %), viridiflorol (9.91 %), carvone (6.19 %) and  $\beta$ -thujone (5.68 %).

**Keywords:** Essential oil ; Sage ; Chemical composition.

### 1. Introduction:

The valorization of these natural resources can have considerable economic benefits. Indeed, different plants contain essential oils composed of molecules with olfactory activity and high added values. The officinal sage (*Salvia Officinalis* L.), belonging to the lamiaceae family [1-2], is composed of small shrubs with fine windy leaves, with a characteristic camphoric odor. It is an medicinal and aromatic plant quite widely used either in the natural state, or in the form of extract or essential oil. Beside a traditional use, as family food and folk medicine, this plant and especially its essential oils are used by the perfume and cosmetology industries, by the food industry and finally by the pharmaceutical industry.

The existence, in the essential oil, of three rather toxic components ( $\alpha$ , $\beta$ -thujone and camphor) is at the origin of accidents occurred during ingestion of too high doses of this products. It is therefore necessary to consume this plant in moderation. Thus the regulation in some

countries limits the possibilities of use of the officinal sage. But the existence of interesting properties makes that, despite the existence of toxic components, we attribute to the sage and its extracts many medicinal virtues [3,4]: antiseptic, antispasmodic, soothing, cephalic, digestive, febrifuge ... etc.

Several recent works have studied the chemical composition of the essential oil of sage in different regions on the world, especially on both sides of the Mediterranean basin such as, Tunisia [5-11], Greece [12-13], Algeria [14-17], Serbia [18-20], Iran [21-23], India [24-26], Turkey [27-28], Yugoslavia [29, 30], Germany [31], Italy [32-34], Egypt [35] and Morocco [36], etc. The medicinal plants are as many rich sources of pharmacologically active substances. These herbaceous plants have been used in a wide range of purposes, including nutrition, medicine, beverage, flavor, repellent, dyeing, cosmetic, perfume, smoking, charm and industrial uses. Sage is present in different areas. The leaves are well known for their antioxidant properties,

# 14<sup>th</sup> Annual Research Day

Organised by the Deanship of Scientific Research in Collaboration with the College of Engineering  
Research Centre

4<sup>th</sup> April 2019

especially in the food industry. It is appreciable on human health through biological activities, such as antibacterial, fungistatic, virostatic, astringent, eupeptic and antihydrotic effects. It is known in the pharmaceutical and medicinal fields, such as the management of Alzheimer's disease [37], by hypoglycemic and antimutagenic activities [38]. It is included as an active ingredient in combination plant preparations for the treatment of acute and chronic bronchitis [39].

In order to help exploit the plants growing in Saudi Arabia and known for their medicinal properties, we have studied the physico-chemical properties of essential oils extracted by hydrodistillation of *Salvia officinalis*, picked from Abha region. The identification of the chemical compounds of the extracted essential oil was carried out by means of gas chromatography coupled to mass spectrometry (GC/MS). This work is finalized by a comparative study of our results with those of the literature.

## 2. Materials and Methods:

### 2.1. Sampling and preparations

The *Salvia officinalis* freshly leaves were harvested from the south of Saudi Arabia (Abha city - altitude: 2400 m), in spring – winter, 2017. After collection, *Salvia officinalis* herbs samples were soon carried from field to the laboratory in an insulated bag and then submerged in tap water for few minutes and washed with distilled water, so that, to remove the foreign particle from the plants. The samples were then air dried for 15 days at ambient temperature without presented to sunlight before using. The leaves separated from the stems and then was shelled using the decorticating disc mill machine.

### 2.2. Moisture Content

Some leaves fraction dried is taken also in an isothermal oven at  $60 \pm 2$  °C for 3 hours and 30 minutes so that to measure the moisture content. Ten samples of 30 g of leaves were weighed in a crucible and dried in an oven then weighed after every 30 min. The process was

repeated until a constant weight of the sample reached. The percentage of moisture content is determined by using equation (1).

$$\text{Moisture (\%)} = \left( \frac{\omega_1 - \omega_2}{\omega_1} \right) \times 100 \quad (1)$$

$\omega_1$ : weight of sample before drying;

$\omega_2$ : weight of sample after drying.

### 2.3. Oil percentage yield

Dried aerial leaves of *Salvia officinalis* were well milled and put into hydrodistillator Clevenger-type for 4 hours (200 g + 1 l of distilled water). The collected mixed liquids results in distillates present a thin layers of oil at the surface. After standing, liquids will thereafter be separated in two fractions. The extracted essential oil, then stored at 4 °C for further investigation. Then, the preceding mixtures was separated in separating ampoules into two immiscible phases. A denser aqueous phase is sited in the lower section, and an organic phase with lower density and containing the solvent (petroleum ether) and essential oils is sited above. A rotary evaporator apparatus is used to make the separation of these phases and in which the volatile solvent was rapidly eliminated by evaporation. The obtain oil volume was measured and the yield shown as oil content (%) was calculated by the following equation:

$$\text{Yield (\%)} = \left( \frac{m_1}{m_2} \right) \times 100 \quad (2)$$

Where:

$m_1$ : extract weight (before distillation);

$m_2$ : separated oil weight.

### 2.4. Determination of pH value

A pH meter (Metrohm AG 913) was used to measure the pH value of *Salvia officinalis* leaves. The calibration of the pH meter was done before the readings by using two buffer solutions (pH = 4.00 and pH = 7.00 at 20 °C). Once the pH electrode immersed into the oils samples, the pH value will be determined and recorded.

# 14<sup>th</sup> Annual Research Day

Organised by the Deanship of Scientific Research in Collaboration with the College of Engineering  
Research Centre

4<sup>th</sup> April 2019

## 2.5. Chemical analysis of essential oils

Essential oil, extracted by hydrodistillation, was analyzed using Gas-Chromatography (with flame ionization detector) to detect the composition and to quantify by using a gas chromatogram type Hewlett Packard 5890, equipped with an FID detector, and a DB-5 column (0.25 mm film thickness silicone capillary of dimension 25 m × 0.25 mm). The temperature of the furnace was taken at 50 °C for one minute and then increased by ramping up to 280 °C (at rate 9 °C/min) and hold for 5 minutes. The injection temperature was fixed at 240 °C, while the detector temperature was kept at 250 °C. At the rate of 1.2 ml/min, carrier gas flowed into the system, and 0.2 µl volumes of feed were injected in Split mode. The injected oil concentration is 1% in hexane. The percentage by mass of the various chemical constituents of the *Salvia officinalis* oil is given on the relative surface area of the peaks (GC-FID). The essential oil components were identified and quantified by the GC/MS, HP 5890 gas chromatogram coupled to an HP 5972 mass spectrum under the same CG analysis conditions, but with one DB-5 column (0.25 mm thickness of the film, 30 m × 0.25 mm, dimension). The ionization energy is 70 eV. The mass order is 40-300 m/z. The oil composition is distinguished on the basis of their mass spectrum with those reference compounds defined in the HP Chemstation, Wiley 275 Library, and comparing retention times published in the literature [40].

## 3. Results and Discussion

### 3.1. Influence of drying on the vegetable matter mass

The experimental results of the drying operation of sage leaves in an oven have been exploited. The mass of the material of the initial sage leaves is 20 g. it was brought to a stable temperature of 60 °C along the drying time. The amount of vegetable matter decreases rapidly during drying. The drying rate was faster in the first two hours and then slowed down during the

remaining drying period. Indeed, they lose their half-weight after 2 hours and 15 minutes. It goes from 20 g at  $t = 0$  to 7.84 g after 3 hours 30 minutes. This concludes that sage leaves are rich in water that weighs more than half.

### 3.2. Essential oil extraction

From 200 g of officinal sage leaves mass in one liter of distilled water, a volume of 9 ml of essential oil was extracted with a colourless or yellowish colour and a spicy characteristic odour has a note of rosemary. This essential oil is characterized by a density of  $\rho = 719.8 \text{ kg/m}^3$ . The extraction yield was determined  $\eta = 3.24 \%$ .

### 3.3. Physicochemical analysis of sage essential oil

The pH of the sage extract is 2.9; this proves that the medium is a strong acidic. Practically this value is similar to those given by Fellah et al. (41), from Marsa and Jebel Oust regions sage oil.

### 3.4. Chemical composition oil

The essential oils extracted from dried leaves, of *Salvia officinalis* by hydrodistillation process. Sage oil is aromatic in odor and somewhat bitter in taste. The results obtained further analyzed qualitatively and quantitatively by GC/MS, to identifying the components. Chromatographic analyzes determined the average chemical composition of essential oils constituents, 99.92 % with 26 compounds greater than 0.3% on percentage.

All, the average, minimum and maximum, volatile oil compounds acquired are listed in the order of their elution in *table 1*, indicating the chemical compounds and their percentages. Small differences observed in essential oil composition between samplings for along the study period (for one year a half) are given as minimum and maximum values. The mean monoterpene fraction of the oil amounted to 76.21 %, as is summarized in Tables 2, with a richness in oxygen containing monoterpenes as the largest

# 14<sup>th</sup> Annual Research Day

Organised by the Deanship of Scientific Research in Collaboration with the College of Engineering  
Research Centre

4<sup>th</sup> April 2019

group of this fraction (67.36 %). Camphor (20.30 %), 1,8-cineole (15.01 %),  $\alpha$ -thujone (14.89 %), carvone (6.19 %) and  $\beta$ -thujone (5.68 %), were the main compounds of the monoterpene oxygenated fraction (9 compounds). Among the sesquiterpene fraction (22.85 %), sesquiterpene hydrocarbons (11.58 %) is dominated by the major component trans- $\beta$ -Caryophyllene (4.01 %) while a viridiflorol (9.91 %) was identified as the main constituent of sesquiterpene oxygenated fraction. This obtained *Salvia officinalis* essential oil showed also a low oxygenated sequiterpenoid content, humulene epoxide (0.86 %). Most of the results were in agreement with the results presented in this study, as indicated in the table 4 and its references; from Farhat M. et al. (5) to Bayrak A. et al. (28); but with varying concentrations. those essential oils obtained from *Salvia Officinalis* showed significant variability in their chemical composition depending on country, location, altitude and developmental stages, etc..

The oxygenated monoterpene percentage (table 2) such as camphor, 1,8-cineole,  $\alpha$ -thujone and  $\beta$ -thujone showed that the extracted *Salvia Officinalis* oil quality. According to the references a good quality oil of *Salvia Officinalis* should contain as  $\alpha$ -thujone and  $\beta$ -thujone more than 50 % and the camphor less than 20 % (42-43). Eleven constituents percentages are standardized according to ISO 9909 (44) ( $\alpha$ -pinene, camphene, limonene, 1,8-cineole, linalool and its esters, cis-thujone, trans-thujone, camphor, bornyl acetate and  $\alpha$ -humulene) in the essential oils of *Salvia Officinalis* for its medicinal uses. Following to the ISO specifications (18.00 – 43.00 %)  $\alpha$ -thujone and (3.00 – 8.50 %)  $\beta$ -thujone are allowed. For considering the safety of botanicals and botanical preparations used in food and drug, leaves of

common sage containing essential oil is:  $\alpha$ -thujone (12.00 – 65.00 %),  $\beta$ -thujone (1.20 – 35.60 %), total thujone content (30.00 – 60.00 %), 1,8-cineole (8.00 – 22.50 %), camphor (4.40 – 30.00 %) (64). Our composition differs from that given by other studies (table 3), mostly due to the different geographic sources areas. The essential oil contents of *Salvia Officinalis* collected from Tunisia, were 1,8-cineole (14.14 – 33.27 %),  $\beta$ -thujone (0.57 – 18.40 %),  $\alpha$ -thujone (13.45 – 34.43 %), borneol (0.51 – 7.39 %), and camphor (0.60 – 28.94 %). They found that essential oil from mountainous region in the center west of Tunisia was mainly the essential oil quality. Those studies from various countries suggested that the average percentage of monoterpenes oxygenated, for the same components found in our work, was more significant in results from Tunisian (78.21 %) and India essential oils (70.37 %) than our results (67.36 %), and then those relative to Greece, Algeria, Serbia, Iran and Turkey essential oils (respectively: 69.89 %, 66.03 %, 56.06 % and 51.59 %). From all given studies, small differences will be considered in terms of quality, because the major fraction was absolutely monoterpenes. It was observed the carvone as the constituent of *Abha* essential oil only, with a considerable percentage 6.19 %, this compound is used as a natural inhibitor of sprouting, mainly in many stored vegetables (43-45). Other works (46-47) shown the carvone as a biologically active compound, inhibiting germination of seeds. Carvone has been considered with special insecticide properties (48). Alkanes compound classes were almost the main compounds in *Salvia officinalis* leaves parts and the chains lengths were comprised only between C10 to C15 at different amounts.

# 14<sup>th</sup> Annual Research Day

Organised by the Deanship of Scientific Research in Collaboration with the College  
of Engineering  
Research Centre  
4<sup>th</sup> April 2019

**Table 1:** Chemical Analysis Results of Sage Oil Using GC-MS for Compounds  
Percentage all are greater than 0.3%.

Chemical class and components	Retention time (min)	% compounds			formulas
		Min	Mean	Max	
<b>Monoterpenes Hydrocarbons</b>					
<i>α</i> -Pinene	4.42	1.05	1.15	1.25	C <sub>10</sub> H <sub>16</sub>
Camphene	4.64	2.41	2.58	2.75	C <sub>10</sub> H <sub>16</sub>
<i>β</i> -Pinene	5.04	2.01	2.06	2.11	C <sub>10</sub> H <sub>16</sub>
Myrcene	5.18	1.15	1.26	1.37	C <sub>10</sub> H <sub>16</sub>
<i>α</i> -Terpinene	5.59	0.29	0.32	0.35	C <sub>10</sub> H <sub>16</sub>
<i>p</i> -Cymene	5.73	0.35	0.36	0.37	C <sub>10</sub> H <sub>14</sub>
<i>γ</i> -Terpinene	6.21	0.54	0.59	0.64	C <sub>10</sub> H <sub>16</sub>
<i>α</i> -Terpinolene	6.66	0.51	0.53	0.57	C <sub>10</sub> H <sub>16</sub>
<b>Monoterpenes Oxygenated</b>					
1,8-Cineole	5.86	14.50	15.01	15.52	C <sub>10</sub> H <sub>18</sub> O
<i>α</i> -Thujone	7.02	14.54	14.89	15.24	C <sub>10</sub> H <sub>16</sub> O
<i>β</i> -Thujone	7.15	5.41	5.68	5.95	C <sub>10</sub> H <sub>16</sub> O
Camphor	7.64	19.39	20.30	21.21	C <sub>10</sub> H <sub>16</sub> O
Pinocamphone	7.80	0.35	0.38	0.41	C <sub>10</sub> H <sub>16</sub> O
Borneol	7.89	2.02	2.16	2.30	C <sub>10</sub> H <sub>18</sub> O
<i>α</i> -Terpineol	8.03	1.09	1.15	1.21	C <sub>10</sub> H <sub>18</sub> O
Carvone	9.01	6.34	6.19	6.04	C <sub>10</sub> H <sub>14</sub> O
Bornyl-Acetate	9.54	1.67	1.60	1.53	C <sub>12</sub> H <sub>20</sub> O <sub>2</sub>
<b>Sesquiterpenes hydrocarbons</b>					
<i>β</i> -Bourbonene	10.93	0.86	0.89	0.92	C <sub>15</sub> H <sub>24</sub>
<i>β</i> -Elemene	10.98	0.79	0.82	0.85	C <sub>15</sub> H <sub>24</sub>
<i>Trans-β</i> -Caryophyllene	11.41	3.28	4.01	4.74	C <sub>15</sub> H <sub>24</sub>
<i>α</i> -Humulene	11.85	2.02	2.13	2.24	C <sub>15</sub> H <sub>24</sub>
Germacrene-D	12.18	1.99	2.52	3.05	C <sub>15</sub> H <sub>24</sub>
Germacrene-B	12.37	0.98	0.90	0.82	C <sub>15</sub> H <sub>24</sub>
<b>Sesquiterpenes Oxygenated</b>					
Globulol	13.48	1.51	1.67	1.83	C <sub>15</sub> H <sub>26</sub> O
Viridiflorol	13.61	9.24	9.91	10.58	C <sub>15</sub> H <sub>26</sub> O
<b>Sesquiterpenoids Oxygenated</b>					
Humulene epoxide	13.78	0.84	0.86	0.88	C <sub>15</sub> H <sub>24</sub> O

**Table 2:** Classification of the constituents of *Salvia Officinalis* .

Chemical class	% compounds
<i>Monoterpenes hydrocarbons</i>	8.85
<i>Monoterpenes oxygenated</i>	67.36
<i>Sesquiterpenes hydrocarbons</i>	11.27
<i>Sesquiterpenes oxygenated</i>	11.58
<i>Sesquiterpenoids oxygenated</i>	0.86
Total	99.92

# 14<sup>th</sup> Annual Research Day

Organised by the Deanship of Scientific Research in Collaboration with the College of Engineering  
Research Centre

4<sup>th</sup> April 2019

**Table 3:** Comparative study of extracted compounds percentages.

Chemical class and components	Retenti on time (min)	Abha (KSA) Present work	Tunisia (5-11)	Greece (12-13)	Algeria (14-17)	Serbis (18-20)	Iran (21-23)	India (24-26)	Turkey (27-28)
<i>Monoterpenes</i>									
<i>Hydrocarbons</i>									
<i>α</i> -Pinene	4.42	1.15 ± 0.10	2.89 – 0.84	3.10 – 2.60	3.72 – 0.19	8.26 – 2.93	5.50 – 2.50	7.69 – 0.70	3.50 - 3.02
Camphene	4.64	2.58 ± 0.17	4.51 – 0.77	1.04 – 0.83	3.28 – 0.17	7.27 – 0.29	5.54 – 1.95	6.11 – 1.20	4.70 - 0.60
<i>β</i> -Pinene	5.04	2.06 ± 0.05	5.11 – 0.44	--	1.40 – 0.18	2.72 – 0.52	9.11 – 1.95	<b>28.33 – 0.90</b>	<b>13.08 – 1.80</b>
Myrcene	5.18	1.26 ± 0.11	2.49 – 0.63	0.32 – 0.27	1.3 – 0.25	0.87 – 0.34	1.00 – 0.50	1.00 – 0.30	1.02 – 0.8
<i>α</i> -Terpinene	5.59	0.32 ± 0.03	0.79 – 0.09	0.15 – 0.13	--	1.89 – 0.58	0.50 – 0.20	0.26 – 0.01	0.27 – 0.10
<i>p</i> -Cymene	5.73	0.36 ± 0.02	1.71 – 0.28	0.32 – 0.18	3.6 – 0.20	0.34 – 0.24	1.50 – 1.07	1.19 – 0.10	1.10 – 0.01
<i>γ</i> -Terpinene	6.21	0.59 ± 0.05	1.24 – 0.24	0.23 – 0.20	0.70 – 0.14	0.59 – 0.30	0.50 – 0.10	0.66 – 0.10	0.40 – 0.01
<i>α</i> -Terpinolene	6.66	0.53 ± 0.04	0.52 – 0.26	0.14 – 0.11	0.50 – 0.20	0.38 – 0.27	0.50 – 0.13	0.53 – 0.01	--
<i>Monoterpenes Oxygenated</i>									
1,8-Cineole	5.86	<b>15.01 ± 0.51</b>	<b>33.27 – 14.14</b>	<b>37.60 – 33.20</b>	<b>22.97 – 8.11</b>	<b>20.13 – 6.35</b>	<b>20.00 – 6.30</b>	<b>13.80 – 0.97</b>	--
<i>α</i> -Thujone	7.02	<b>14.89 ± 0.35</b>	<b>34.43 – 13.45</b>	5.90 – 6.10	<b>36.74 – 3.62</b>	<b>37.52 – 8.47</b>	<b>37.18 – 5.67</b>	<b>41.00 – 17.20</b>	<b>31.98 – 20.60</b>
<i>β</i> -Thujone	7.15	<b>5.68 ± 0.27</b>	<b>18.40 – 0.57</b>	4.69 – 3.18	<b>16.44 – 6.50</b>	6.04 – 1.33	4.32 – 9.10	4.97 – 2.17	<b>15.10 - 4.68</b>
Camphor	7.64	<b>20.30 ± 0.91</b>	<b>28.94 – 0.60</b>	<b>23.20 – 19.90</b>	<b>20.40 – 8.99</b>	<b>24.80 – 0.15</b>	6.50 – 0.15	<b>36.97 – 0.88</b>	<b>22.90 – 0.01</b>
Pinocamphon	7.80	0.38 ± 0.03	0.55 – 0.38	--	0.20 – 0.10	0.49 – 0.14	--	0.30 – 0.20	--
Borneol	7.89	2.16 ± 0.14	7.39 – 0.51	2.42 – 1.74	3.13 – 1.89	8.50 – 0.20	<b>11.58 – 1.40</b>	<b>18.38 – 1.30</b>	7.90 – 0.01
<i>α</i> -Terpineol	8.03	1.15 ± 0.06	2.03 – 0.54	0.12 – 0.11	0.64 – 0.10	2.76 – 0.14	3.80 – 0.24	0.50 – 0.30	--
Carvone	9.01	<b>6.19 ± 0.15</b>	--	--	--	--	--	--	--
Bornyl-Acetate	9.54	1.60 ± 0.07	1.05 – 0.17	0.99 – 0.63	1.86 – 0.37	4.91 – 0.05	4.90 – 0.98	1.60 – 0.20	--
<i>Sesquiterpenes hydrocarbons</i>									
<i>β</i> -Bourbonene	10.93	0.89 ± 0.03	1.83 – 0.02	--	0.18 – 0.10	--	--	0.15 – 0.03	--
<i>β</i> -Elemene	10.98	0.82 ± 0.03	4.82 – 0.00	--	--	--	6.20 – 0.08	--	--
Trans- <i>β</i> -Caryophyllen	11.41	4.01 ± 0.73	6.48 – 0.67	2.61 – 1.37	5.85 – 1.54	9.41 – 1.04	<b>11.50 – 1.69</b>	<b>17.32 – 1.20</b>	3.08 – 0.01
<i>α</i> -Humulene	11.85	2.13 ± 0.11	6.27 – 0.06	2.30 – 1.80	4.69 – 0.67	12.49 – 3.35	5.00 – 1.72	3.60 – 1.50	<b>10.17 – 4.10</b>
Germacrene-D	12.18	2.52 ± 0.53	0.17 – 0.02	--	0.17 – 0.10	--	2.70 – 2.48	0.42 – 0.04	2.10 – 0.01
Germacrene-B	12.37	0.90 ± 0.08	0.62 – 0.00	--	--	--	0.46 – 0.01	--	--
<i>Sesquiterpenes Oxygenated</i>									
Globulol	13.48	1.67 ± 0.16	0.12 – 0.09	--	--	--	0.74 – 0.64	--	--
Viridiflorol	13.61	<b>9.91 ± 0.67</b>	<b>16.32 – 2.52</b>	2.30 – 1.59	<b>10.92 – 6.35</b>	<b>26.10 - -1.19</b>	8.00 – 5.33	5.60 – 0.79	<b>10.74 – 0.01</b>
<i>Sesquiterpenoids Oxygenated</i>									
Humulene epoxide	13.78	0.86 ± 0.02	0.85 – 0.62	0.14 – 0.11	1.82 – 0.10	1.82 – 0.60	--	0.53 – 0.11	--

# 14<sup>th</sup> Annual Research Day

Organised by the Deanship of Scientific Research in Collaboration with the College of Engineering  
Research Centre

4<sup>th</sup> April 2019

## References

- [1.] L.M.L. Mollet. Handbook of meat, poultry and seafood quality. First edition, 2007.
- [2.] M. Gantner, M. Brodowska, E. G. Horczyczak, I. W. Kalinowska, A. Najda, E. Pogorzelska, J. Godziszewska. Antioxidant Effect of Sage (*Salvia Officinalis* L.) Extract on Turkey Meatballs Packed in Cold Modified Atmosphere. Abingdon, Oxfordshire, UK : Taylor & Francis, 2018.
- [3.] P. Catione, M. Marotti, G. Toderi, P. Tetenyi, *Cultivazione della piante medicinali e Aromatiche*. Patron, Ed, Bologna, 1986, 253-263.
- [4.] R. C. Beier, *Natural pesticides and bioactive components in food*. Rev. Environm. Contam. Toxicol., 1990, 113, 61-66. Proceedings of the National Conference on Utilization of Bioresources. Allied Publishers, 2002.
- [5.] Mouna Ben Farhat, Maria J. Jordan, Rym Chaouch-Hamada, Ahmed Landoulsi, Jose A. Sotomayor. Phenophase effects on sage (*Salvia officinalis* L.) yield and composition of essential oil. Journal of Applied Research on Medicinal and Aromatic Plants 3 (2016) 87-93
- [6.] Mouna Ben Taârit, Kamel Msaada, Karim Hosni, and Brahim Marzouk. GC Analyses of *Salvia* Seeds as Valuable Essential Oil Source. Advances in Chemistry (2014), 1-6.
- [7.] Lazreg H., Cheraiee I. and Fekih A. Chemical composition of Tunisian *Salvia Officinalis* essential oil. J. Soc. Alger Chem., (2007) 1:43-50.
- [8.] Med Raâfet Ben Khedher, Saoussen Ben Khedher, Ikbâl Chaieb, Slim Tounsi, Mohamed Hammami. Chemical composition and biological activities of *Salvia Officinalis* essential oil from Tunisia. Experimental and Clinical Sciences Journal 2017;16:160-173
- [9.] El Akrem Hayouni, Imed Chraief, Manaf Abedrabba, Marielle Bouix, Jean-Yves Leveau, Hammami Mohammed, Moktar Hamdi. Tunisian *Salvia officinalis* L. and *Schinus molle* L. essential oils: Their chemical compositions and their preservative effects against *Salmonella* inoculated in minced beef meat. International Journal of Food Microbiology 125, 3, (2008): 242-251
- [10.] Mohamed Bouaziz, Thabèt Yangui, Sami Sayadi, Abdelhafidh Dhouib. Disinfectant properties of essential oils from *Salvia officinalis* L. cultivated in Tunisia. Food and Chemical Toxicology 47 (2009) 2755-2760.
- [11.] Ali Lamari, Hassen Teyeb, Hassen Ben Cheikh, Wahiba Douki & Mohamed Neffati. Chemical Composition and Insecticidal Activity of Essential Oil of *Salvia officinalis* L. Cultivated in Tunisia. Journal of Essential Oil Bearing Plants 17 (3) 2014 pp 506 – 512.
- [12.] Christos N. Hassiotis. The role of aromatic *Salvia officinalis* L. on the development of two mycorrhizal fungi. Biochemical Systematics and Ecology 77 (2018) 61-67.
- [13.] E. Skoufogianni, A. D. Solomou, F. Kamperllari and N.G.Danalatos. Ecology, Cultivation, Composition and Utilization Of *Salvia Officinalis* L. In Greece: A Review. Global Advanced Research Journal of Agricultural Science. 2017, 6 (12): 449-455.
- [14.] S. Benkherara O. Bordjiba A B. Djahra. In vitro evaluation of the antibacterial activity of essential oil of *Salvia officinalis*. Phytothérapie (2015) 13:14-18.
- [15.] Lakhâl H, Ghorab H, Chibani S, Kabouche A, Semra Z, Smati F, Abuhamdah S and Kabouche Z. Chemical composition and biological activities of the essential oil of *Salvia officinalis* from Batna (Algeria). Der Pharmacia Lettre, 2013, 5 (3):310-314.
- [16.] S. Mehalaine O. Belfadel T. Menasria A. Messaili. Chemical Composition and Antibacterial Activity of Essential Oils of Three Medicinal Plants from Algerian

# 14<sup>th</sup> Annual Research Day

Organised by the Deanship of Scientific Research in Collaboration with the College of Engineering  
Research Centre

4<sup>th</sup> April 2019

- Semi-Arid Climatic Zone. *Phytothérapie*, DOI 10.1007/s10298-017-1143-y.
- [17.] T. Dob, T. Berramdane, D. Dahmane, T. Benabdelkader and C. Chelghoum. Chemical composition of the essential oil of *Salvia officinalis* from Algeria. *Chemistry of Natural Compounds*, Vol. 43, No. 4, 2007.
- [18.] Maria Couladis, Olga Tzakou, Neda Mimica-Dukic, Radisa Jancic and Danilo Stojanovic. Essential oil of *Salvia officinalis* L. from Serbia and Montenegro. *Flavour and fragrance journal*, 2002; 17: 119–126.
- [19.] B. Vukovic-Gacic, S. Nikcevic, T. Beric-Bjedov, J. Knezevic-Vukcevic, D. Simic. Antimutagenic effect of essential oil of sage (*Salvia officinalis* L.) and its monoterpenes against UV-induced mutations in *Escherichia coli* and *Saccharomyces cerevisiae*. *Food and Chemical Toxicology* 44 (2006) 1730–1738.
- [20.] Svetolik Maksimovic, Zeljka Kesic, Ivana Lukic, Stoja Milovanovic, Mihailo Ristic, Dejan Skala. Supercritical fluid extraction of curry flowers, sage leaves, and their mixture *J. of Supercritical Fluids* 84 (2013) 1–12
- [21.] Majid Mohammad hosseini, Abolfazl Akbarzadeh, and Guido Flamini. Profiling of Compositions of Essential Oils and Volatiles of *Salvia limbata* Using Traditional and Advanced Techniques and Evaluation for Biological Activities of Their Extracts. *Chem. Biodiversity* 2017, 14.
- [22.] Mohsen Kazemi. Essential Oil of the Aerial Parts of *Salvia officinalis* (Lamiaceae) from Iran. *Journal of Essential Oil Bearing Plants*. 18 (3) 2015 pp 725 – 727.
- [23.] Ahmad Reza Golparvar, Amin Hadipanah, Mohammad Mehdi Gheisari, Davood Naderi, Shima Rahmaniyan, Mojtaba Khorrami. Chemical composition and antimicrobial activity of essential oil of *Salvia officinalis* L. and *Salvia virgata* Jacq. *Journal of Herbal Drugs*, Vol. 8, No. 2: 71-78, 2017.
- [24.] Vahid Rowshan and Sharareh Najafian. Evaluation of the essential oil composition of *Salvia officinalis* L. by different drying methods in full flowering stages. *International Journal of Farming and Allied Sciences*. Vol., 2 (12): 350-354, 2013.
- [25.] Ram S. Verma, Rajendra C. Padalia, Amit Chauhan. Harvesting season and plant part dependent variations in the essential oil composition of *Salvia officinalis* L. grown in northern India. *journal of herbal medicine* 5 ( 2 0 1 5 ) 165–171.
- [26.] Gulzar Bhat, Shahid Rasool, Shakeel-u-Rehman, Mudasar Ganaie, Parvaiz H. Qazi & Abdul S. Shawl. Seasonal Variation in Chemical Composition, Antibacterial and Antioxidant Activities of the Essential Oil of Leaves of *Salvia officinalis* (Sage) from Kashmir, India. *Journal of Essential Oil Bearing Plants* 19 (5) 2016 pp 1129 – 1140.
- [27.] Kiarash Afshar Pour Rezaeieh and Bilal Gurbuz. Volatile Oil Yield and Constituents of *Salvia officinalis*, *S. tomentosa* Mill. and *S. glutinosa* Growing in Ankara, Turkey. *Asian J. Agric. Res.*, 11 (2): 43-47, 2017.
- [28.] Ali Bayrak and Anita Akgll. Composition of essential oil from Turkish *Salvia* species. *Phytochemistry*. (1987) 26:3: 846-847.
- [29.] N. B. Perry, A. J. Baxter, N. J. Brennan, J. W. Van Klin. Dalmatian Sage. Part 1. Differing Oil Yields and Compositions from Flowering and Non-flowering Accessions *Flavour and Fragrance Journal*, 11(4),231-238 (1996).
- [30.] E. Putievsky, U. Ravid, D. Sanderovich. Morphological Observations and Essential Oils of Sage (*Salvia officinalis* L.) Under Cultivation. *Journal of Essential Oil Research* Vol. 4, 3, 291-293. 1992.
- [31.] F. S. Sharopov, P. Satyal, W. N. Setzer, M. Wink. Chemical compositions of the essential oils of three *Salvia* species

# 14<sup>th</sup> Annual Research Day

Organised by the Deanship of Scientific Research in Collaboration with the College of Engineering  
Research Centre

4<sup>th</sup> April 2019

---

- cultivated in Germany. *American Journal of Essential Oils and Natural Products* 2015; 3(2): 26-29.
- [32.] L. Pace & R. Piccaglia. Characterization of the Essential Oil of a Wild Italian Endemic Sage: *Salvia officinalis* L. var. *angustifolia* Ten. (Labiatae). *Journal of Essential Oil Research* Vol. 7, 4, 443-446. 1995.
- [33.] Bianchi, A.; Severi, A.; Albasini, A.; Pecorari, P.; Melegari, M. *Salvia officinalis* L.: indagini botaniche e chimiche su piante coltivate, *ibid. ATTI Soc. Nat. Mat. Modena*, 1987, 118, 1-21.
- [34.] R. Piccaglia, M. Marotti. Characterization of several aromatic plants grown in northern Italy. *Flavour and Fragrance Journal*, 1993, 8, 115.
- [35.] H. Said-Al Ahl, M. S. Hussein, A. S. H. Gendy, K. G. Tkachenko. Quality of Sage (*Salvia officinalis* L.) Essential Oil Grown in Egypt. *International Journal of Plant Science and Ecology*. 2015, 1, 4:119-123.
- [36.] A. Et-Touys, H. Fellah, M. Mniouil, A. Bouyahya, N. Dakka, H. Abdennebi, A. Sadak and Y. Bakri. Screening of Antioxidant, Antibacterial and Antileishmanial Activities of *Salvia officinalis* L. Extracts from Morocco. *British Microbiology Research Journal* 16(5): 1-10, 2016.
- [37.] M.C. Cuvelier. C. Berset. H. Richard (1994). Antioxidant constituents in sage (*Salvia officinalis*). *Journal of Agricultural and Food Chemistry* 42. 665–669.
- [38.] D. Baricevic a., S. Sosa b. R. Della Loggia b. A. Tubaro b. B. Simonovska c. A. Krasna c. A. Zupancic. (2001) Topical anti-inflammatory activity of *Salvia officinalis* L. leaves: the relevance of ursolic acid. *Journal of Ethnopharmacology* 75. 125–132.
- [39.] S. Akhondzadeh. M. Noroozian. M. Mohammadi. S. Ohadinia. AH. Jamshidi. M. Khani (2003) *Salvia officinalis* extract in the treatment of patients with mild to moderate Alzheimer's disease: a double blind, randomized and placebo-controlled trial. *J. Clin. Pharm. Ther.* 28. 53–59.
- [40.] Adams RP. (1995). Identification of essential oil components by gas chromatography/mass spectroscopy. Allured Publishing Corporation. Carol Stream. IL. USA pp:312–452.
- [41.] Fellah S., Romdhane M., Abderraba M. (2006). Extraction et étude des huiles essentielles de la *salvia officinalis*.l cueillie dans deux régions différentes de la Tunisie, *Journal of the Algerian Chemical Society*. 16. 2:193-202.
- [42.] Gunther, G. (1961). *The Essential Oils*. Nastrand Press, New York, USA.
- [43.] Putievsky, E., Ravid, U. and D. Sanderovich (1992). Morphological observations and essential oils of sage (*Salvia officinalis* L.) under cultivation. *J. Ess. Oil Res.*, (4): 291-293.
- [44.] ISO, 9909(1997). Oil of Dalmatian Sage (*Salvia officinalis* L.), American National Standards Institute (ANSI), New York, NY, USA.
- [45.] Raal, A., Orav, A. and E. Arak (2007). Composition of the essential oil of *Salvia officinalis* L. from various European countries. *Natural Product Research*, 21(5):406-411.
- [46.] H.J. Bouwmeester, J. Gershenzon, M.C.J.M. Konings and R. Croteau, Biosynthesis of the monoterpenes limonene and carvone in the fruit of caraway. *Plant. Physiol*, 117, 901–912 (1998).
- [47.] H. Toxopeus and H.J. Bouwmeester, Improvement of caraway essential oil and carvone production in The Netherlands. *Ind. Crop. Prod.*, 1, 295–301 (1992).

# 14<sup>th</sup> Annual Research Day

Organised by the Deanship of Scientific Research in Collaboration with the College of Engineering  
Research Centre

4<sup>th</sup> April 2019

## Effect of Structure and Chemical Activation on the Adsorption Properties of Green Clay Minerals for the Removal of Cationic Dye

Abdelfattah Amari

<sup>1</sup>Department of Chemical Engineering, College of Engineering, King Khalid University,  
PO Box 394, Abha 61411 KSA.

<sup>2</sup> R.U. Energy and Environment, National School of Engineers, Gabes University, Tunisia

\* Correspondence: aamary@kku.edu.sa

**Abstract:** In this study, natural clay minerals with green appearance were treated with sulfuric acid. Mass percentage of acid (wt%), temperature (T), contact time ( $t$ ), and liquid-to-solid mass ratio (R) are used as the prevailing factors that determine the extent of acid-activation. The values of these factors range from 15–50%, 60–90°C, 1.5–6h and 4–7, respectively. The study has focused on the structural changes as well as textural characteristics of the clay. Three activated clay samples were prepared under different treatment conditions. The samples were characterized using XRD, FTIR, SEM, chemical analysis and N<sub>2</sub> adsorption techniques. Characterization of the treated clay minerals exhibited significant structural changes to a greater extent of acid-activation, from being partially crystalline to being amorphous silica. The surface area and total pore volume of clay increased proportionally with the level of acid treatment. The average pore diameter behaved differently. During the strong acid treatment, a large increase in pore volume and the enlargement of the pore size distribution were observed. This suggests that considerable structural changes and partial destruction may have occurred in this condition. The removal of methylene blue, used as cationic dye, from aqueous solution by the batch adsorption technique on three prepared acid-activated clay samples was studied. The Langmuir model was found to agree well with the experimental data.

**Keywords:** clay minerals; acid activation; characterization; structural changes; cationic dye; adsorption

### 1. Introduction

Clays and clay minerals are of significant interest because of their interesting characteristics that make them suitable for industrial applications. They have been accepted as one of the most appropriate low-cost adsorbents and common component in different industrial applications [1–7]. Among the various types of clays, bentonite is more popular. Its physicochemical and adsorption properties depend on the montmorillonite content, the crystalline structure of the clay minerals that constitute them and the nature of the inter-layer cations [8,9]. In order to eliminate impurities and different exchangeable cations from clay minerals and to prepare a well-defined material for use as

catalyst and adsorbent, various activations have been used, most often with inorganic acids [10–13]. Indeed, the treatment with mineral acids significantly changed their textural characteristics. This can expand their applications to include environmental protection [14,15], catalytic cracking of petroleum [16], catalyst supports in many chemical processes, and detergent in paper industries and textile fabrications [17–19]. In fact, the most applications of these clays are bleaching, purification, and stabilization of vegetable oils.

Acid-activated clays have attracted much current interest as adsorbents and catalysts for a range of acid mediated processes [20–22]. Nowadays, considerable progress is achieved in the synthesis of many new inorganic mesoporous

# 14<sup>th</sup> Annual Research Day

Organised by the Deanship of Scientific Research in Collaboration with the College of Engineering  
Research Centre

4<sup>th</sup> April 2019

molecular sieves based on solid acids. However, modified clay minerals remain one of the widely and mostly used in the industry as mesoporous solid catalysts and adsorbents [23]. The acid attack on clay minerals has additional effects on the mineralogical composition of the raw material and related properties; i.e., organic matter is leached out and feldspar can be partly attacked (or dissolved). This process causes increase in surface area and surface acidity, and introduces permanent mesoporosity [18,24–27] and also removes metal ions from the crystal interlayer, that partially delaminated the clay.

The acid treatment strips octahedral ions such as Fe, Al, Mg and removes tetrahedral ions from the clay minerals due to the isomorphous substitution in the crystal lattices [28]. The extent to which these ions are removed depends on the relevant factors. Several factors may contribute when a clay undergoes an acid activation such as; the nature of acid, the mass percentage of acid, the temperature of activation reaction, contact time of solid-to-liquid, the stirring rate of mixture, the size of the solid particle and the liquid-to-solid mass ratio. Four parameters are known to strongly influence the structural properties and can affect significantly the required results: the temperature, the contact time, the solid-to-liquid ratio and mass percentage of acid. These parameters are the main factors that delimit the extent of acid-activation, and thus, the induced physicochemical and structural changes [13–15]. As a consequence of these structural changes, acid-treatment can extend the fields of application of these porous solids such as in the control of atmospheric pollution [15]. This work is a continuation of numerous studies carried out in the field of surface and colloid science and dealing with clay minerals [15,29–35]. Natural green clay mineral collected from south of Tunisia was treated with sulfuric acid in order to prepare suitable adsorbent for several organic compounds. The present work aims to prepare, characterize and investigate the effect of acid

treatment factors on some physicochemical and bleaching properties of the raw material. Removal of cationic dye, methylene blue used as textile dye in industries, by the batch adsorption technique was studied.

## 2. Materials and Methods

### 2.1. Materials

All the required chemicals used in this work were of analytical grade. Sulfuric acid  $H_2SO_4$  and Methylene blue (MB) were purchased from Sigma-Aldrich chemicals. The formula of MB is  $C_{16}H_{18}N_3SCl \cdot 2H_2O$ , the molecule is positively charged and its aromatic moiety is planar.

A MB stock solution of mass concentration 1g/L was prepared by dissolving 1g of dye in double distilled water in 1000 mL volumetric flask. Other required solutions with various dye concentrations in the range of 10mg/L to 120 mg/L, were prepared by serial dilution. The pH of solutions was adjusted using 0.1 M solution of HCl or NaOH. The structural formula of methylene blue is given in Figure 1.

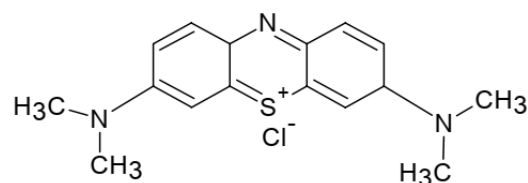


Figure 1. Structure of methylene blue.

### 2.2. Adsorption Studies

In this section, batch adsorption technique is used. Appropriate clay quantity of 200 mg was added in 250 mL conical flask to solutions of MB of different initial concentrations and stirred by magnetic hot plate stirrer with 10 positions of type Scilogex MS-H-S10 at the rate 300rpm and at temperature 20°C. The time required to attain equilibrium was predetermined previously based on some experiments of kinetic study and estimated to be 60 min. To ensure that the time chosen was enough to reach equilibrium, all

# 14<sup>th</sup> Annual Research Day

Organised by the Deanship of Scientific Research in Collaboration with the College of Engineering  
Research Centre

4<sup>th</sup> April 2019

experiments were conducted at 1.5 h. Once the dye solutions had reached equilibrium, the suspensions were separated by centrifugation within 30 min at the rate of 3000 rpm using centrifuge of type 80-2C, for further analysis of the dye concentrations. The residual concentration of the dyes was determined using a UV-visible spectrophotometer of type Shimadzu UV-1700 at 665 nm. The pH of the solutions for adsorption experiments was set to 7 and controlled using a pH-Meter of type Basic 20<sup>+</sup>. The temperature of experiments was maintained at 20°C and its control was performed using a thermostatically controlled incubator.

The amount of MB adsorbed  $q_e$  (mg/g) was calculated from the difference between the initial and equilibrium MB concentrations, and is given by:

$$q_e = \frac{(C_0 - C_e) \times V}{m}$$

$C_e$  (mg/L) is the concentration of adsorbate at equilibrium;  $C_0$  (mg/L) is the initial concentration of adsorbate;  $m$  (g) is the mass of the adsorbent; and  $V$  (L) is the volume of the solution.

### 2.3. Preparation and Purification of the Adsorbent

The starting material is clay collected from the deposit of “Djebel Aïdoudi” of “Hamma”, located in south Tunisia, at the east of Gabes town. The raw material contained, in addition to the mineral phases, impurities which can be reduced or eliminated completely by applying a purification protocol. After collection, and before use for activation, the raw material is purified by sedimentation. This is achieved by suspending the crude lumps in distilled water at mass ratio 1:10 (clay:water). The mixture was stirred very vigorously to ensure efficient mixing, and then sieving was carried out three times through a sieve of different mesh size, and particles smaller than 43 μm were collected. Then, the suspended

particles were recovered after allowing coarser mineral particles to settle. Finally, the water is siphoned off and the clay is dried in an air oven at 60 °C.

### 2.4. Preparation and Analysis of Oriented Aggregates of Clay

Oriented aggregate specimens of clay were carried out using the standard procedure of Brown and Brindley [33] according to the following steps [36]: a few gram of finely ground clay was added to a vessel containing distilled water, and then the mixture was stirred and allowed to stand. After a few minutes, the heavy and/or coarse fractions are separated by decanting. Only clay grains that remain suspended in the liquid are removed using a pipette. The liquid was extended on a horizontal glass slide to obtain a well oriented regular deposit, then left to dry in open air. Three oriented clay specimens were prepared; the first one was analyzed in normal state. The normal state of the material refers to the raw material, merely freed from its coarse fraction by sedimentation and keeping the clay fraction in its natural state (without changing the interlayer space by ion exchange). This sample was used as the reference to judge the movements caused by other treatments. The second one is subjected to ethylene glycol vapor in a desiccator for 24 h (glycolated aggregate), this treatment leads to the swelling of smectites. The last one is heated in an oven for one hour at a temperature of 500 °C. This heating can destroy kaolinite and keep chlorite. After this treatment, the minerals of smectite group are dehydrated irreversibly and interlayer space will be blocked to 10 Å.

### 2.5. Acid Activation of Raw Material

Clay mineral was treated with sulfuric acid. According to previous works [12] and preliminary tests, it was shown that the particle size of the solid had no significant effect on the kinetics of the activation or the pore properties of

# 14<sup>th</sup> Annual Research Day

Organised by the Deanship of Scientific Research in Collaboration with the College of Engineering  
Research Centre

4<sup>th</sup> April 2019

---

clay particles when the dimensions were equal to or less than 40  $\mu\text{m}$ . Moreover, it was found that the agitation does not have much effect on the kinetics of the acid attack from certain values. Hence, the stirring has been adjusted to the maximum value of a laboratory stirrer in order to ensure the homogenisation of the reaction mixture. Consequently, this study was conducted using only four major factors: the strength of acid (wt%), the reaction temperature (T), the reaction time ( $t$ ), and the liquid to solid mass ratio (R).

Based on preliminary tests and from the literature review [12], samples were prepared according to the following ranges: Temperature (60–90°C), contact time (1.5–6h), liquid/solid mass ratio (4–7) and mass percentage of acid (15–50%). It was shown that the selected ranges of these factors, are appropriate to investigate the effect of acid activation on raw material, and efficient to make difference in activation degree between the samples. Three activated clay samples were prepared: the first sample ( $S_1$ ) was prepared under low conditions (wt=15%, T=60 °C,  $t$ =1.5h, R=4), the second sample ( $S_2$ ) was activated at average conditions (wt=32.5%, T=75 °C,  $t$ =3.75h, R=5.5), while the last sample ( $S_3$ ) was prepared under strong conditions (wt=50%, T=90 °C,  $t$ =6h, R=7).

A series of treatment steps were used for the acid-treatment of clay. Experiments were carried out with sulfuric acid in a jacketed glass reactor equipped with a thermometer, a reflux condenser, and a stirrer. Each sample was prepared according to the following procedure: 100 g of raw clay, with a particle size less than 40  $\mu\text{m}$ , was mixed with an appropriate aqueous solution of  $\text{H}_2\text{SO}_4$ . The slurry was stirred at maximum speed by a laboratory agitator of type (Kirk.210.Bicasa). Then, slurry was air-cooled and filtered with a glass fibber. The filter cake was washed with distilled water several times until the wash water was neutral with no trace of sulphate. The pH of the filtrate is monitored by universal pH test strips.

Finally, the clay product was dried in an oven at 70 °C for 48 h until the weight remains constant. The freshly prepared dry sample was crushed into powder by a mortar. Then the activated clay was sieved before use according to U.S. standard sieve designations (Afnor nF-11504). All the activated clay samples ( $S_1$ ,  $S_2$  and  $S_3$ ) were prepared with the same described procedure.

## 3. Characterization

The mineralogical compositions were determined by the techniques of X-ray powder diffraction (XRD) using Philips Panalytical X'Pert PRO powder diffractometer equipped with X' Celerator detector and with cobalt  $K_\alpha$  radiation ( $\lambda = 1.789 \text{ \AA}$ ). Tension and current were set to 40 kV and 40 mA respectively. Scans were collected between 3 and 60° 2 $\theta$  angular range at steep angle of 0.017°. Orientated aggregate samples were scanned from 3° to 35° 2 $\theta$  angular range at 1°/min with a scanning step of 0.01°/step. The clay fraction was maintained at three different conditions (1 to 3); 1: untreated (natural state), 2: after treatment with ethylene glycol vapours in a desiccator for 24 h at 60 °C, 3: after heating at 500 °C for 1 h. The micromorphological features of the samples before and after activation were studied using a scanning electron microscope (SEM) of type Philips XL30 ESEM operating with up to 30 kV acceleration voltage field emission gun. Sample clays fragments were previously coated with a thin layer of gold before proceeding to morphological observations. The Fourier transform infrared spectroscopy (FT-IR) was applied using a Perkin-Elmer 983 G IR-spectrometer equipped with IR source, KBr beam splitter, and DTGS KBr detector. Prior to analysis, samples were lightly ground using a mortar and pestle and sieved again through the 45  $\mu\text{m}$  sieve. This was done to minimize the scattering, distortion and peak broadening of IR radiation due to larger-sized particles that may have resulted from agglomeration during drying.

# 14<sup>th</sup> Annual Research Day

Organised by the Deanship of Scientific Research in Collaboration with the College of Engineering Research Centre

4<sup>th</sup> April 2019

The spectra were recorded in the spectral range from 4000 to 250  $\text{cm}^{-1}$ . Quantitative chemical analysis of raw material ( $S_0$ ) and acid-activated clays were performed using atomic absorption spectrometer (AAS) of type Analytikjena AG, NOVA 400 and X-ray fluorescence (ARL<sup>®</sup> 9800 XP spectrometer). By X-ray fluorescence, the loss on ignition (LOI) content of dried and powdered clay sample was attributed to the release of water and was measured by calcinations at 975 °C. Then the dried clay samples were mixed with lithium-tetraborate and lithium iodide and the mixture was fused in a Pt crucible and mounded to a glass disk for chemical analysis.  $\text{N}_2$  adsorption/desorption isotherms were measured using Quantachrome Autosorb AS1C equipment at liquid nitrogen temperature of  $-196.15^\circ\text{C}$ . Before adsorption measurements, the samples were degassed in vacuum at 300 °C for more than 3 h to remove any adsorbed contaminants from the surface and pores of the samples. The Brunauer-Emmett-Teller (BET) method was used to determine the surface areas and pore volume of samples and the pore size distribution was calculated using the BJH method based on the nitrogen adsorption or desorption data.

## 4. Results and Discussions

After acid-activation, clays underwent chemical analysis and textural characterizations. The expected results obtained by acid-activated clays ( $S_1$ ,  $S_2$ ,  $S_3$ ) were compared to those found by raw material ( $S_0$ ). For full description of the mineralogical composition of clay materials, and to understand the structure changes, it is required first to determine the nature of the various impurities contained in each sample. The reflections of phylitic phases were then established.

### 4.1. Determination of Non-Clay Minerals

It should be noted that the quantification of non-clay minerals found in the clays by XRD

alone was difficult, since some components are hardly detectable by X-ray. These non-clay minerals in the raw material were marked by different peaks. An X-ray diffraction pattern of raw clay mineral ( $S_0$ ) is shown in Figure 2.

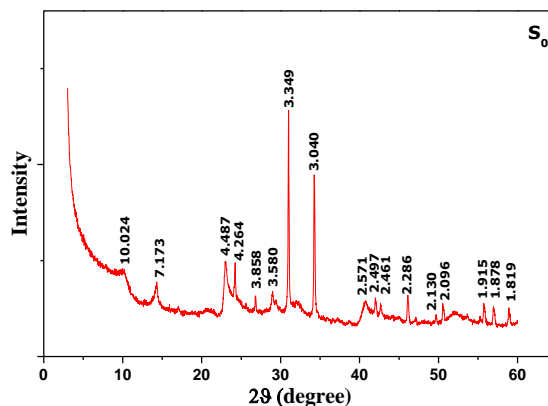
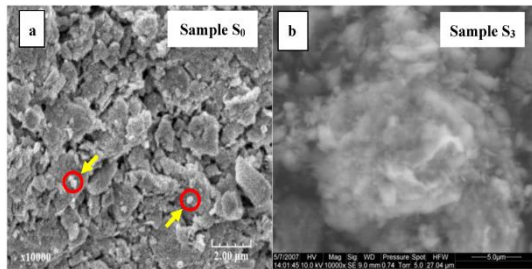


Figure 2. XRD patterns of raw material ( $S_0$ ).

Quartz appeared as major non-clay minerals by the reflection peaks observed at  $d=3.34$ ; 2.28; 2.13; 1.819 Å and  $d = 4.26$  Å. Other non-clay minerals are also detected, such as the calcite at 3.858; 3.04; 1.915, 1.878 Å and gypsum at 2.09 Å. It is remarkable that the non-clay minerals were still present even after purification. This is probably due to their fine particle size which makes their complete separation impossible during clay pre-treatment.

### 4.2. Observation by Scanning Electron Microscope (SEM)

Figure 3 presents the morphologies of raw material ( $S_0$ ) and the acid-activated clay prepared at strong condition ( $S_3$ ) observed by SEM.



**Figure 3.** Scanning electronic micrographs of raw material S<sub>0</sub> (a), and acid-activated clay sample S<sub>3</sub> (b).

In agreement with the results obtained from XRD patterns, very large aggregates appeared on SEM images of the raw material (Figure 3a) (size up to 400 nm approximately) and well observed deposited on the mineral layers (indicated by an arrow). These minerals of small size, considered as non-clay minerals, are closely associated to clay and not easily eliminated during purification. Also, SEM examination revealed natural clay morphology of very fine-grained aggregates of clay platelets, irregular curved flakes and mats of coalesced flakes. In any case, and because of particle coalescence, it is difficult to determine their exact texture. A sharp decrease in particle size caused by acid activation is visible in the modified clay (Figure 3b). It consists mainly of small aggregates of nanoparticles and exhibits a distinct porous structure.

### 4.3. Determination of the Phylitic Phases by X-Ray Diffraction

The XRD patterns of oriented specimens, natural state (air dried), saturated with ethylene glycol, and heated at 500°C of raw clay sample, S<sub>0</sub>, are illustrated in Figure 4.

A non-symmetrical peak at 15.05 Å is observed by X-ray diffraction patterns of (001) reflection for the air-dried sample. This peak is characteristic of divalent cations occupying the interlayer sites. Once the sample is saturated by ethylene glycol, the peak expands to 17.39 Å, indicating the presence of smectite. This phase of

expandable layers remain predominant. The asymmetrical form of the latter reflection is characteristic of a partly interstratified phase illite/smectite. It is frequently observed that illite is interstratified with the smectite by small particles included in the smectite[34,35]. It is not ambiguous that the reflections at 7.18 Å and 3.58 Å unaffected by the treatment with ethylene glycol and disappeared following the heat treatment, correspond to the reflection of the phylitic phase 1:1 kaolinite. As previously mentioned, the examination of oriented clay specimens by X-ray diffraction shows peaks at 3.34 Å and 3.03 Å corresponding to quartz and calcite, respectively. The infrared spectrum (IR) of natural clay (S<sub>0</sub>) is presented in Figure 5.

The results of IR spectrum (Figure 5) confirmed the data obtained by X-ray diffraction, i.e., smectite was the dominant mineral phase. The two bands between 3500 cm<sup>-1</sup> and 3700 cm<sup>-1</sup> and near 3430 cm<sup>-1</sup> indicate the presence of smectite[35]. The peak at 3620 cm<sup>-1</sup> is assigned to stretching vibrations of the OH group of water molecules. The broad band at 3430 cm<sup>-1</sup> and the band at 1640 cm<sup>-1</sup> belong to the OH stretching and bending vibration of sorbed water molecules present in the clay, respectively. Furthermore, the strong absorption band at 1040 cm<sup>-1</sup> and the band at 795 cm<sup>-1</sup> are a result of Si–O stretching vibrations, whereas the bands at 528 and 472 cm<sup>-1</sup> are assigned to the deformation vibrations of Si–O–Al and Si–O–Si, respectively.

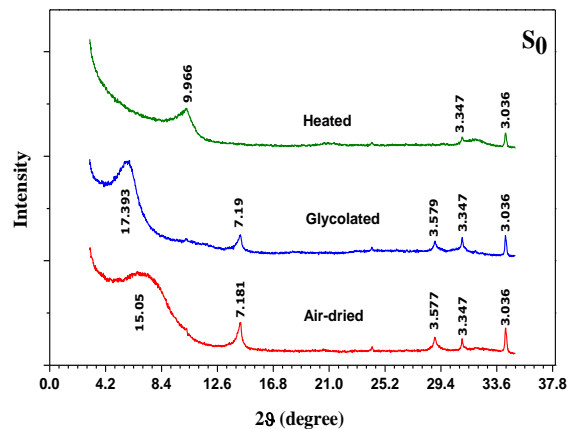


**Figure 4.** XRD patterns of oriented aggregate specimens of raw material (S<sub>0</sub>): Air dried, glycolated and heated to 500°C.

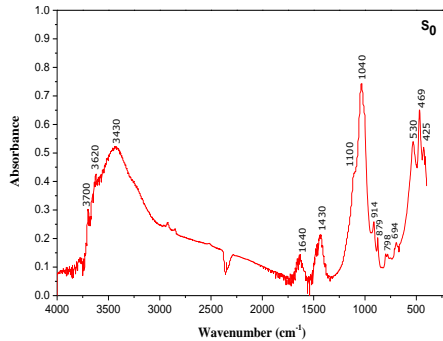


**Figure 5.** FTIR spectrum of raw material (S<sub>0</sub>).

#### 4.4. Effect of Acid-Activation

Changes in crystallinity resulting from acid activation of raw material were investigated by the X-ray powder diffraction patterns of some typical samples. Figure 6 presents the XRD patterns together of raw material S<sub>0</sub> and acid-activated clays (S<sub>1</sub>, S<sub>2</sub>, S<sub>3</sub>).

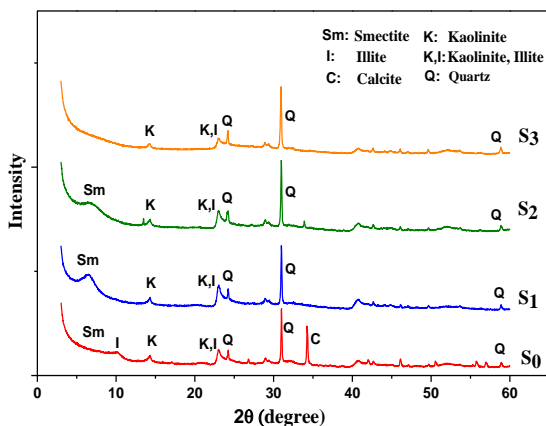


**Figure 6.** XRD patterns of raw material (S<sub>0</sub>) and acid-activated clay samples (S<sub>1</sub>, S<sub>2</sub>, S<sub>3</sub>).

The pattern of raw material is shown here for sake of comparison. It is observed that acid-

activation causes a clear decrease in the crystallinity as indicated by decreasing intensity of the smectite peaks. Some of them are gradually deteriorated and completely disappeared. As it can be seen, XRD analysis has shown that clay acid-activation leads to total dissolution of calcite (reflections at 3.858; 3.04; 1.915 and 1.878 Å) and gypsum (reflections at 2.09 Å).

Under strong conditions of H<sub>2</sub>SO<sub>4</sub>, some of the quartz peaks are still present in the activated samples indicating that quartz is more resistant to acid attack than smectite. This result was similar to that found by Komadel and Madejova [13], hence quartz which appeared as the most abundant non-clay mineral in the natural clay (see reflections at d=3.34; 2.28; 2.13; 1.819 Å and d = 4.26 Å) cannot be completely eliminated from clay by acid-activation. Temuujin et al. [36] have reported similar results for montmorillonite activated by hydrochloric acid. For a greater extent of acid treatment (sample S<sub>3</sub>), it is observed that layered structure of clay mineral is indicated by the loss of crystallinity and the appearance of amorphous silica remaining from leached smectite phase. These results are in agreement with those obtained by Shinoda et al. [37]; indicating that the acid-activated product of smectite is generally amorphous silica.

X-ray diffraction patterns of oriented activated clay specimens (Figure 7 S<sub>1</sub>–S<sub>3</sub>) prove a complete disappearance of the interstratified phase illite/smectite for the severity conditions, but no effect on the kaolinite phase was observed (reflection at d=7.18 Å and d= 3.58 Å).

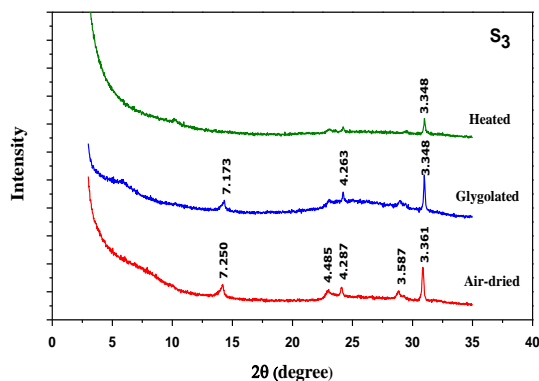
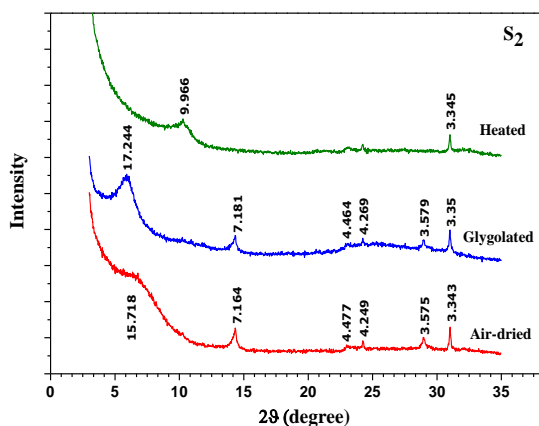
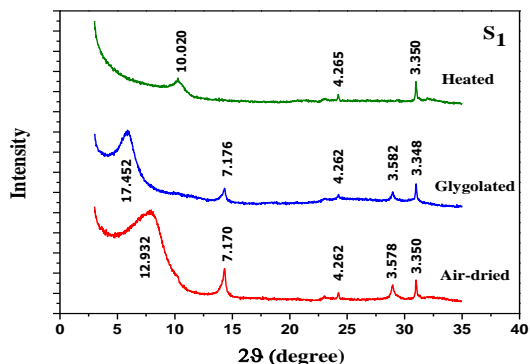


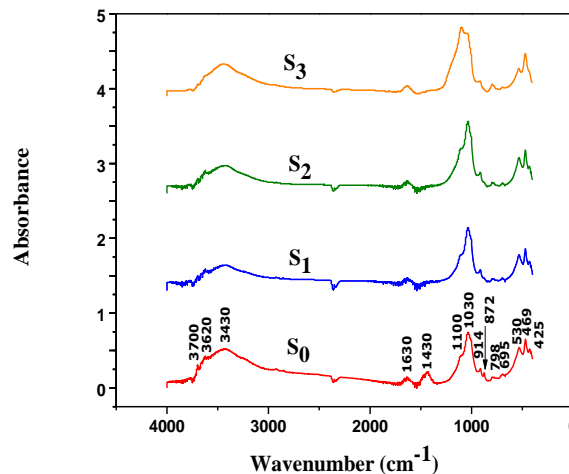
**Figure 7.** XRD patterns of oriented activated clay specimens:  $S_1$ ,  $S_2$ , and  $S_3$ .

From these results, it can be concluded that acid treatment mainly affected the smectite phase and led to a partial decrystallization of the clay structure.

The IR spectra presented in Figure 8 showed that the acid-activation led to a partial dissolution of the octahedral sheets especially with the sample  $S_3$  prepared at high conditions of acid treatment. This is confirmed by the decrease in intensity of the band at  $914\text{ cm}^{-1}$  corresponding to  $-\text{OH}$  bending vibration ( $\text{AlAlOH}$ ), bands at  $530\text{ cm}^{-1}$  assigned to  $(\text{Si}-\text{O}-\text{Al})$ ,  $1030\text{ cm}^{-1}$  attributed to  $(\text{Si}-\text{O})$ , and band at  $3430\text{ cm}^{-1}$  related to adsorbed  $\text{H}_2\text{O}$ . The broadening of the IR bands between  $1100$  and  $900\text{ cm}^{-1}$  is indicative of the formation of amorphous opal.

In addition, a significant decrease or almost disappearance of the band at  $3620\text{ cm}^{-1}$  was observed, this is due to the important leaching of cations after the acid activation. The comparison between raw material and acid-activated clay IR spectra showed that for more severe conditions ( $S_3$ ), acid-activation destroys the smectite mineral phase as proved by the disappearance of the bands located between  $3500\text{ cm}^{-1}$  and  $3700\text{ cm}^{-1}$  [35]. The complete disappearance of bands at  $1430\text{ cm}^{-1}$  and  $872\text{ cm}^{-1}$  pointed out to the dissolution of calcite  $\text{CaCO}_3$  and dolomite  $\text{CaMg}(\text{CO}_3)_2$  for the three samples ( $S_1$ ,  $S_2$ ,  $S_3$ ) as previously reported by Khalil et al. [38].

Chemical analysis was performed on both raw material ( $S_0$ ) and acidified clays ( $S_1$ ,  $S_2$ , and  $S_3$ ). The results are illustrated in Table 1.



# 14<sup>th</sup> Annual Research Day

Organised by the Deanship of Scientific Research in Collaboration with the College of Engineering Research Centre

4<sup>th</sup> April 2019

**Figure 8.** Infra-red spectra of raw material ( $S_0$ ) and acid-activated clays ( $S_1, S_2, S_3$ ).

**Table 1.** Chemical analyses of raw material ( $S_0$ ) and acid activated clay samples ( $S_1, S_2, S_3$ ).

Samples	MgO	Fe <sub>2</sub> O <sub>3</sub>	Al <sub>2</sub> O <sub>3</sub>	SiO <sub>2</sub>	SO <sub>3</sub>	CaO	K <sub>2</sub> O	Na <sub>2</sub> O	P <sub>2</sub> O <sub>5</sub>	TiO <sub>2</sub>	ZnO	L.I. at 975°C
$S_0$	1.46	6.07	14.27	49.87	0.77	7.00	1.09	0.53	0.19	1.41	0.18	17.62
$S_1$	1.23	5.56	13.58	50.82	0.76	0.86	1.03	0.23	0.06	1.62	0.37	16.54
$S_2$	0.98	4.89	12.38	52.69	0.75	0.58	0.97	0.11	0.01	1.80	0.51	15.27
$S_3$	0.43	1.89	9.40	67.63	0.68	0.14	0.61	0.13	0.01	2.26	0.24	11.24

L.I. Loss on Ignition.

The chemical analysis of raw clay ( $S_0$ ) proved the presence of silica, alumina, iron and calcium as major constituents, along with traces of sodium, potassium, phosphate and titanium oxides. The higher mass percentage of silica and alumina reveals that clay mineral is an aluminosilicate matter.

After acid-activation, the SiO<sub>2</sub> content of clay ( $S_0$ ) increased from 49.87% to 50.82%, 52.69% and 67.63% for  $S_1, S_2$  and  $S_3$ , respectively. However the content of Al<sub>2</sub>O<sub>3</sub>, Fe<sub>2</sub>O<sub>3</sub>, and MgO are decreased from 14.27%, 6.07% and 1.46% to 13.58%, 5.56%, 1.23% and to 12.38%, 4.89%, 0.98%, and to 9.4%, 1.89%, 0.43%, for  $S_1, S_2$  and  $S_3$ , respectively. This may be due to the partial destruction (dissolution) of the octahedral layer (Al,Fe,Mg–O layers) and the exposure of the tetrahedral layers (Si–O layers) in acid solution.

The N<sub>2</sub> adsorption/desorption isotherms of raw material and activated clays presented in Figure 9 showed that isotherms are reversible for lower equilibrium pressure, but at higher relative pressure, they exhibited a hysteresis loop of H<sub>3</sub> type [39]. Such hysteresis loops exist in the slit-shaped pores or in the ink-bottle pores (pores with narrow necks and wide bodies).

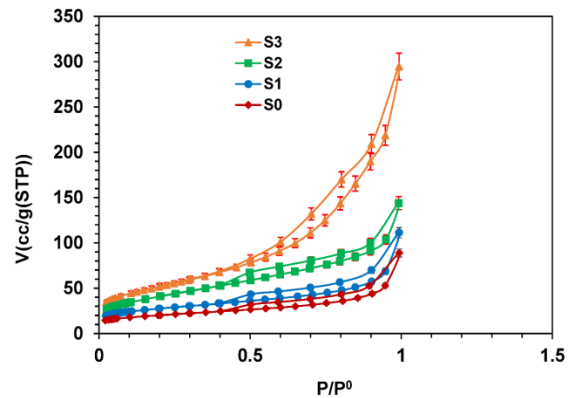


**Figure 9.** N<sub>2</sub> adsorption isotherms of the raw material ( $S_0$ ) and activated clay samples ( $S_1, S_2, S_3$ ) with  $\pm 5\%$  error bars in volume.

The textural properties of raw clay ( $S_0$ ) and acid-activated clays ( $S_1, S_2, S_3$ ) are presented in Table 2.

**Table 2.** Textural properties of raw material ( $S_0$ ) and acid-activated clay samples ( $S_1, S_2, S_3$ ).

Samples	Total Pore Volume ( $10^{-2}\text{cm}^3/\text{g}$ )	Average Pore Diameter (Å)	BET Surface Area. $S_{\text{BET}}$ ( $\text{m}^2/\text{g}$ )
$S_0$	13.74	79.56	69.00
$S_1$	17.20	72.92	94.36
$S_2$	22.26	60.76	146.50
$S_3$	45.58	98.9	184.40

It can be noted that surface area, total pore volume and average pore diameter were changed as the severity of acid treatment was increased. Data presented in Table 2 shows that surface area depends on acid attack but the relation between surface area and acid treatment is non-linear. Taylor et al. have reported that surface area

increases with acid concentration [25]. As it can be seen from Table 2, acid activation improves the volume of pores. The pore volume was only  $0.1374 \text{ cm}^3/\text{g}$  for natural clay ( $S_0$ ), but after acid treatment it becomes much higher and reaches  $0.4558 \text{ cm}^3/\text{g}$  for more severe treatment (sample  $S_3$ ). Assuming that the pores are cylindrical, the mean pore diameter was calculated from the formula  $d = 4V_p/S_p$ , where,  $V_p$  is the pore volume and  $S_p$  is the specific surface area of the pores. The average pore diameter for starting material ( $S_0$ ) is  $79.56 \text{ \AA}$ . It decreases for low acid treatment and average condition, and then increases at higher conditions for sample  $S_3$ , to reach the value of  $98.9 \text{ \AA}$ . This can be explained by the fact that acid-activated samples had a greater increase in percentage of pore volume of micro pores than meso pores. As a consequence the lower values of the average pore diameter for samples  $S_1$  and  $S_2$  were obtained compared to that of natural clay. However, the strong acid treatment that produced  $S_3$ , caused large increase of pore volume in the range of micro pore and meso pore diameter and consequently an increase in average pore diameter. This suggests a considerable structural changes and decomposition occurred in this sample. Similar result was observed by Jovanovic and Janackovic [40].

The change in mean pore diameter with the acid treatment is also confirmed by the mesopore size distribution curve calculated by BJH equation [41]. The pore size distribution for both raw material and acid-activated clays ( $S_1$ ,  $S_2$ , and  $S_3$ ) is presented in Figure 10.

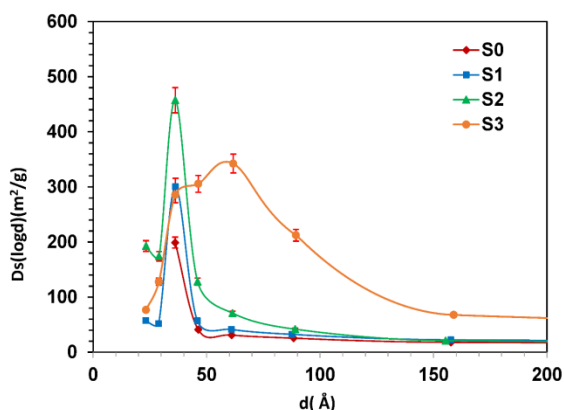


**Figure 10.** Pore size distribution curves of the raw material ( $S_0$ ) and activated clays ( $S_1$ ,  $S_2$ ,  $S_3$ ) with  $\pm 5\%$  error bars.

From pore size analysis, it was found that the most frequent pore size of the raw material ( $S_0$ ) is  $3.7 \text{ nm}$ , the same result is found for samples  $S_1$  and  $S_2$ . However, in higher conditions, the activated clay mineral ( $S_3$ ) has mesopores with the most frequent size of  $6 \text{ nm}$ . The increase of peak amplitude and width of the sample  $S_3$  confirm that the pore volume increases with acid-activation. The large increase in pore volume and the enlargement of the pore size distribution, observed during the strong acid treatment, suggest that significant structural changes and partial destruction may occur in this sample. Similar tendency was reported by Tatjana [9]. These changes in pore structure may result from the removal of exchangeable cations and impurities from the clay lattice following the  $\text{H}_2\text{SO}_4$  attack.

#### 4.5. Adsorption Equilibrium Studies of Methylene Blue (MB)

In order to evaluate the equilibrium characteristics of adsorption, three models were used to analyze the adsorption data; Langmuir; Freundlich and Frumkin models. The non-linearized forms of Langmuir, Freundlich and Frumkin models can be described by Equations (1)–(3), respectively.

$$q_e = \frac{q_{\max} K_L C_e}{1 + K_L C_e}$$

$$q_e = K_f C_e^{\frac{1}{n}}$$

$$q_e = \frac{q_{\max} K_{Fr} C_e}{\left[ e^{\left( \frac{2aq_e}{q_{\max}} \right)} + K_{Fr} C_e \right]}$$

where  $K_L$  (L/mg) is the Langmuir adsorption constant related to the energy of adsorption,  $q_{\max}$  and  $q_e$  (mg/g) are the maximum and equilibrium adsorption capacity, respectively.  $K_f$  and  $n$  are the Freundlich constants corresponding to adsorption capacity and intensity, respectively. For Frumkin model, the constant  $K_{Fr}$  is related to equilibrium adsorption and “ $a$ ” is the interaction parameter. A positive value of “ $a$ ” corresponds to repulsive interactions among adsorbed molecules, whereas a negative value means attraction between the adsorbed molecules. When  $a = 0$  the adsorbed molecules do not interact each other and the Frumkin isotherm reduces to Langmuir isotherm.

The adsorbed quantity of MB dye at the equilibrium ( $q_e$ ), versus residual concentration ( $C_e$ ) is presented in Figure 11.

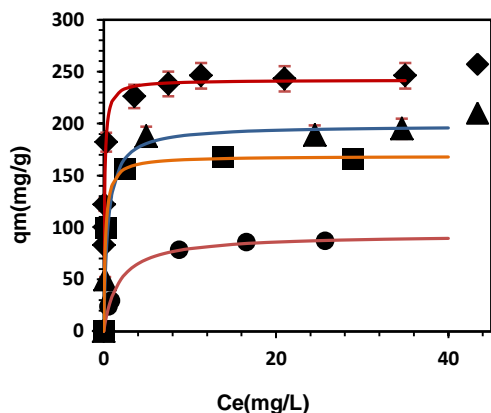


**Figure 11.** Adsorption isotherms of MB on raw material ( $S_0$ ) and activated clay samples ( $S_1, S_2, S_3$ ) with  $\pm 5\%$  error bars in uptake: The lines represent the fit of Langmuir model, ( $T=20^\circ\text{C}$ ,  $\text{pH}=7$ ,  $m_{\text{ads}}=200\text{mg}$ ).

The adsorption isotherms exhibited the classical type-I behaviors of adsorbents. The Langmuir model provided the best fit to the experimental data in all range of concentrations (Figure 11). The Freundlich and Frumkin isotherms failed to correlate the results and showed large deviation (not presented). The linearization of Freundlich model ( $\ln q_e$  vs.  $\ln C_e$ ) shows a correlation factor ( $R^2$ ) of 0.87, 0.89, 0.84 and 0.97 for sample isotherms  $S_0, S_1, S_2$  and  $S_3$ , respectively. However the plot of equation

$$\ln \left( \frac{\theta}{(1-\theta) C_e} \right) \text{ versus } \theta$$

for Frumkin isotherm shows linear relationship with correlation factor,  $R^2$  which did not reach 0.8 in all sample isotherms;  $S_0, S_1, S_2$  and  $S_3$  ( $\theta = \frac{q_e}{q_{\max}}$  represent the degree of surface coverage by the adsorbent).

The adsorption data were compared with the adsorption isotherm model of Langmuir and the parameters were estimated with regression by minimizing the sum of squared residuals. The fitting function  $\delta q$  to be minimized is established in the following equation:

The adsorption data were compared with the adsorption isotherm model of Langmuir and the parameters were estimated with regression by minimizing the sum of squared residuals. The fitting function  $\delta q$  to be minimized is established in the following equation:

$$\delta q = \sum_{i=1}^N \left( \frac{q_{\text{exp}} - q_{\text{cal}}}{q_{\text{exp}}} \right)^2$$

$q_{\text{exp}}$  and  $q_{\text{cal}}$  are the experimental and the calculated adsorbed quantities at concentration  $C_e$ , respectively.  $\delta q$  is an objective function, and has a relative value that depends on the fitting model and the experimental data. The deviations between the fitting model and the experimental

# 14<sup>th</sup> Annual Research Day

Organised by the Deanship of Scientific Research in Collaboration with the College of Engineering  
Research Centre

4<sup>th</sup> April 2019

data were determined by Equation (4), N is the number of experimental points.

$$\Delta q(\%) = \frac{100}{N} \sum_{i=1}^N \left( \frac{q_{\text{exp}} - q_{\text{cal}}}{q_{\text{exp}}} \right)$$

For Langmuir model, the overall mean deviation calculated by Equation (4) was <2%. The results of this analysis are illustrated in Table 3.

**Table 3.** Estimated parameter values of the Langmuir model for the raw material (S<sub>0</sub>) and acid-activated clay samples (S<sub>1</sub>, S<sub>2</sub>, S<sub>3</sub>).

Samples	Langmuir Constants			
	$q_m$ (mg/g)	$K_L$ (L/mg)	$\delta q$	$\Delta q$ (%)
S <sub>0</sub>	241.91	11.019	$9.77 \times 10^{-3}$	2.63
S <sub>1</sub>	198.36	2.096	$2.29 \times 10^{-3}$	1.82
S <sub>2</sub>	168.59	5.115	$0.19 \times 10^{-3}$	0.13
S <sub>3</sub>	93.42	0.577	$5.00 \times 10^{-3}$	2.42

Many works have been reported that MB adsorption on montmorillonite, phosphorous rock and palygorskite correlate well the Langmuir isotherm and provided a good fit to the experimental data than other isotherms [42–45]. As expected, the result suggests that the MB adsorption process by clay minerals was a single layer adsorption and that the maximum monolayer adsorption capacities were found to be 241.96, 198.36, 168.59, and 93.42 mg/g, for S<sub>0</sub>, S<sub>1</sub>, S<sub>2</sub> and S<sub>3</sub>, respectively. It is observed that the maximum quantity of MB adsorbed on raw material (S<sub>0</sub>) was reduced by about 60% for sample activated by strong conditions (S<sub>3</sub>).

The uptake of methylene blue by clays is strongly related to cationic exchange. As reported by Li et al. [46] a complete balance between MB adsorbed and desorbed exchanged cations is needed to account for the mechanism of cationic

exchange. Therefore the uptake of MB is accompanied by dual mechanism of ion exchange as well as adsorption. Overall, the quantities of desorbed (5) exchangeable cations are linearly proportional to those of adsorbed MB [45]. Moreover, the decrease in adsorption ability of MB for activated samples (S<sub>1</sub>, S<sub>2</sub>, and S<sub>3</sub>) could be a consequence of the collapse of the clay lattice to some extent of acid activation. Similar result was found by Zhansheng et al. [47], when more concentrated acids were used, the crystallinity of the clay minerals deteriorated. The decrease in MB uptake could also be attributed to the electrostatic repulsion between the positively charged surface of acid activated clays and the positively charged dye molecule in the acidic medium, in addition to the competitive adsorption between the H<sup>+</sup> ions and dye cations to reach the surface.

## 5. Conclusions

This paper deals with the acid activation of clay minerals. It is concluded that a deep interlayer modification occurs even at low percentage of H<sub>2</sub>SO<sub>4</sub>. Spectroscopy analysis by infra-red (IR), X-ray diffraction (XRD), and chemical analysis have shown that chemical structure of clay changes from a partially crystallized state to amorphous silica state at a great extent of acid-activation. This result was confirmed by the disappearance of the interstratified phase illite/smectite, which leads almost to a total destruction of natural clay structure. During acid-activation, a part of octahedral cations (magnesium, iron, aluminium) was dissolved creating new acid sites, and the interlayer exchangeable cations are replaced by protons. The content of three oxides Al<sub>2</sub>O<sub>3</sub>, Fe<sub>2</sub>O<sub>3</sub> and MgO of the raw material decreased from 14.27; 6.07; 1.46 to 9.4%; 1.89%; 0.43% for severe acid-treatment (S<sub>3</sub>), respectively. Acid attack process mainly affected the smectite phase of clay and caused a broad pore distribution of material, created mesopores and increased

# 14<sup>th</sup> Annual Research Day

Organised by the Deanship of Scientific Research in Collaboration with the College of Engineering  
Research Centre

4<sup>th</sup> April 2019

external surface area of clay. Acid-activation of clay minerals reduces the adsorption capacity of methylene blue used as cationic dye; this is attributed to the competition between the H<sup>+</sup> ions and dye cations to reach the surface. Also, this clear decrease could be a consequence of the partial collapse of the clay lattice to some extent of acid activation.

**Acknowledgments:** The authors extend their appreciation to the Deanship of Scientific Research at King Khalid University, Abha-KSA, for funding this work.

## References

- [1] Fonseca, C.G.; Vaiss, V.S.; Wypych, F.; Diniz, R.; Leitão, A.A. Investigation of the initial stages of the montmorillonite acid-activation process using DFT calculations. *Appl. Clay Sci.* **2018**, *165*, 170–178.
- [2] Arus, V.A.; Nousir, S.; Sennour, R.; Shiao, T.Z.; Nistor, I.D.; Roy, R.; Azzouz, A. Intrinsic affinity of acid-activated bentonite towards hydrogen and carbon dioxide. *Int. J. Hydrogen Energy.* **2018**, *43*, 7964–7972.
- [3] Vryzas, Z.; Kelessidis, V.C.; Nalbantian, L.; Zaspalis, V.; Gerogiorgis, D. I.; Wubulikasimu, Y. Effect of temperature on the rheological properties of neat aqueous Wyoming sodium bentonite dispersions. *Appl. Clay Sci.* **2017**, *136*, 26–36.
- [4] Bouazizi, A.; Saja, S.; Achiou, B.; Ouammou, M.; Calvo, J.I.; Aaddane, A.; Younssi, S. A. Elaboration and characterization of a new fl at ceramic MF membranemade from natural Moroccan bentonite. Application to treatment of industrial wastewater. *Appl. Clay Sci.* **2016**, *133*, 33–40.
- [5] Garshasbi, V.; Jahangiri, M.; Anbia, M. Equilibrium CO<sub>2</sub> adsorption on zeolite 13X prepared from natural clays. *Appl. Clay Sci.* **2017**, *393*, 225–233.
- [6] Elmoubarki, R.; Mahjoubi, F.Z.; Tounsadi, H.; Moustadrafa, J.; Abdennouri, M.; Zouhri, A.; El Albani, A.; Barka, N. Adsorption of textile dyes on raw and decanted Moroccan clays: Kinetics, equilibrium and thermodynamics. *Water Resour. Ind.* **2015**, *9*, 16–29.
- [7] Carrado, K.A.; Komadel, P. Acid Activation of Bentonites and Polymer-Clay Nanocomposites. *Elements.* **2009**, *5*, 111–116.
- [8] Zhua, J.; Zhanga, P.; Wang, Y.; Wena, K.; Sua, X.; Zhua, R.; Hea, H.; Xie, Y. Effect of acid activation of palygorskite on their toluene adsorption behaviors. *Appl. Clay Sci.* **2018**, *159*, 60–67.
- [9] Tatjana, N.; Rozi, L.; SrdanPetrovic, S.; Rosi, A. Synthesis and characterization of acid-activated Serbian smectite clays obtained by statistically designed experiments. *Chem. Eng. J.* **2008**, *37*, 436–442.
- [10] Javed, S.H.; Zahir, A.; Khan, A.; Afzal, S.; Mansha, M. Adsorption of Mordant Red 73 dye on acid activated bentonite: Kinetics and thermodynamic study. *J Mol Liq.* **2018**, *254*, 398–405.
- [11] Liu, Y.; Gates, W. P.; Bouazza, A. Acid induced degradation of the ben tonite component used in geosynthetic clay liners. *Geotext. Geomembr.* **2013**, *36*, 71–80.
- [12] Gannouni, A.; Bellagi, A.; Bagane, M. Preparation of Activated Clay for the Bleaching of Olive Oil. *Ann. Chim.-Sci. Mat.* **1999**, *24*, 407–416.
- [13] Komadel, P.; Madejova, J. Acid activation of clay minerals. In *Handbook of clay science*; Bergaya, F.; Theng, B.K.G.; Lagaly G., Eds.; Elsevier Science: Amsterdam, **2006**; pp. 263–287.

# 14<sup>th</sup> Annual Research Day

Organised by the Deanship of Scientific Research in Collaboration with the College of Engineering  
Research Centre

4<sup>th</sup> April 2019

- [14] Jedli, H.; Brahmi, J.; Hedfi, H.; Mbarek, M.; Bouzgarrou, S.; Slimi, K. Adsorption kinetics and thermodynamics properties of Supercritical CO<sub>2</sub> on activated clay. *J. Pet. Sci. Eng.* **2018**, 166, 476–481.
- [15] Amari, A.; Chlendi, M.; Gannouni, A.; Bellagi, A. Experimental and Theoretical Studies of VOC Adsorption on Acid-Activated Bentonite in a Fixed-Bed Adsorber. *Ind. Eng. Chem. Res.* **2010**, 49, 11587–11593.
- [16] Moraes, D.S.; Miranda, L.C.R.; Angélica, R.S.; Filho, G.N.R.; Zamian, J.R. Functionalization of Bentonite and Vermiculite after the Creation of Structural Defects through an Acid Leaching Process. *J. Braz. Chem. Soc.* **2018**, 29, 320–327.
- [17] Sidorenko, A.Y.; Kravtsova, A.V.; Aho, A.; Heinmaa, I.; Kuznetsov, T.F.; Murzin, D.Yu.; Agabekova, V.E. Catalytic isomerization of  $\alpha$ -pinene oxide in the presence of acid-modified clays. *J. Mol. Catal.* **2018**, 448, 18–29.
- [18] Wu, Z.; Li, C.; Sun, X.; Xu, X.; Dai, B.; LI, J.; ZHAO, H. Characterization, Acid Activation and Bleaching Performance of Bentonite from Xinjiang. *Chin. J. Chem. Eng.* **2006**, 14, 253–258.
- [19] Anirudhan, T.S.; Ramachandran, M. Adsorptive removal of basic dyes from aqueous solutions by surfactant modified bentonite clay (organoclay): Kinetic and competitive adsorption isotherm. *Process Saf Environ.* **2015**, 95, 215–225.
- [20] Yan, Z.; Fu, L.; Yang, H.; Ouyang, J. Amino-functionalized hierarchical porous SiO<sub>2</sub>-AlOOH composite nanosheets with enhanced adsorption performance. *J. Hazard. Mater.* **2018**, 344, 1090–1100.
- [21] Bergaya, F.; Lagaly, G. Surface modification of clay minerals. *Appl. Clay Sci.* **2001**, 19, 1–3.
- [22] Bergaya, F.; Theng, B.K.G.; Lagaly, G. Modified Clays and clay minerals. In *Handbook of clay science*; Bergaya, F., et al., Eds.; Elsevier Science: Amsterdam, **2006**; pp. 261–262.
- [23] Hart, M.P.; Brown, D.R. Surface acidities and catalytic activities of acid-activated clays. *J. Mol. Catal. A: Chem.* **2004**, 212, 315–321.
- [24] Mikhail, S.; Zaki, T.; Khalil, L. Desulfurization by an economically adsorption technique. *Appl. Catal., A.* **2002**, 227, 265–278.
- [25] Taylor, D.R.; Jenkins, D.B.; Ungermann, C.B. Bleaching with alternative layered minerals: A comparison with acid activated montmorillonite for bleaching soybean. *J Am Oil Chem Soc.* **1989**, 66, 334.
- [26] Rhodes, C.N.; Brown, D.R. Structural characterization and optimization of acid-treated montmorillonite and high-porosity silica supports for ZnCl<sub>2</sub> alkylation catalysts. *J. Chem. Soc., Faraday Trans.* **1992**, 88, 2269.
- [27] Komadel, P. Chemically modified smectites. *Clay Miner.* **2003**, 38, 127–138.
- [28] Mokaya, R.; Jones, W. Pillared clays and pillared acid-activated Clays: A comparative study of physical, acidic, and catalytic properties. *J. Catal.* **1995**, 53, 76–85.
- [29] Pardo, L.; Cecilia, J.A.; Moreno, C.L.; Hernández, V.; Pozo, M.; Bentabol, M.J.; Franco, F. Influence of the Structure and Experimental Surfaces Modifications of 2:1 Clay Minerals on the Adsorption Properties of Methylene Blue. *Minerals.* **2018**, 8, 359.

# 14<sup>th</sup> Annual Research Day

Organised by the Deanship of Scientific Research in Collaboration with the College of Engineering  
Research Centre

4<sup>th</sup> April 2019

- [30] Şahin, O.; Kaya, M.; Saka, C. Plasma-surface modification on bentonite clay to improve the performance of adsorption of methylene blue. *Appl. Clay Sci.* **2015**, 116–117, 46–53.
- [31] Guerra, D.J.L.; Mello, I.; Freitas, L.R.; Resende, R.; Silva R.A.R. Equilibrium, thermodynamic, and kinetic of Cr (VI) adsorption using a modified and unmodified bentonite clay. *Int. J. Min. Sci. Technol.* **2014**, 24, 525–535.
- [32] Hu, P.; Wang, J.; Huang, R. Simultaneous removal of Cr(VI) and Amido black 10B (AB10B) from aqueous solutions using quaternized chitosan coated bentonite. *Int. J. Biol. Macromol.* **2016**, 92, 694–701.
- [33] Brown, G.; Brindley G.W. X-ray diffraction procedures for clay minerals identification? in Brindley, G.W.; Brown G., Eds.; *Crystal Structures of Clay Minerals and their X-ray Identification*, Mineralogical Society, London, **1980**; pp. 305–360.
- [34] Fiore, S.; Cuadros, J.; Huertas, F.J. *Interstratified Clay Minerals: Origin, Characterization and Geochemical Significance*. Digilabs - Bari, Italy, **2013**.
- [35] Reynolds, R. C. Interstratified clay minerals. In *Handbook of Crystal structures of clay minerals and their X-ray identification*; Brindley, G.W.; Brown, G., Eds.; Mineralogical Society: London, **1980**; pp. 249–303.
- [36] Temuujin, J.; Jadambaa, Ts.; Burmaa, G.; Erdenechimeg, Sh.; Amarsanaa, J.; MacKenzie, K.J.D. Characterisation of acid activated montmorillonite clay from Tuulant (Mongolia). *Ceram. Int.* **2004**, 30, 251–255.
- [37] Shinoda, T.; Onaka, M.; Izumi, Y. Proposed models of mesopore structures in sulfuric acid-treated montmorillonites and K10. *Chem. Lett.* **1995**, 495–496.
- [38] Khalil, A. A.; Abo, O.; El-Wafa, Sh.; Sallam, A.; ElKorashy, S. A. Characterization of some Sinai clay deposits. *Mag. Verfahrenstech.* **1988**, 12, 396–400.
- [39] Sing, K.; Everet, D.; Haul, R.; Moscou, L.; Pierotti, R.; Rouquerol, J.; Siemieniowska, T. Reporting physisorption data for gas/solid systems with special reference to the determination of surface area and porosity. *Pure Appl. Chem.* **1985**, 57, 603.
- [40] Jovanovic, N.; Janackovic, J. Pore structure and adsorption properties of an acid – activated bentonite. *Appl. Clay Sci.* **1991**, 6, 59–68.
- [41] Barrett, E.P.; Joyner, L.C.; Halenda. P.P. The determination of pore volume and area distribution in porous substances. I. Computation from nitrogen isotherms. *J. Am. Chem. Soc.* **1951**, 73, 373–380.
- [42] Almeida, C.A.P.; Debacher, N.A.; Downsc, A.J.; Cotteta, L.; Mello, C.A.D. Removal of methylene blue from colored effluents by adsorption on montmorillonite. *J. Colloid Interface Sci.* **2009**, 332, 46–53.
- [43] Al-Futaisi, A.; Jamrah, A.; Al-Hanai, R. Aspects of cationic dyemolecule adsorption to palygorskite. *Desalination.* **2007**, 214, 327–342.
- [44] Malash, G.F.; El-Khaiary, M.I. Methylene blue adsorption by the waste of AbuTartour phosphate rock. *J. Colloid Interface Sci.* **2010**, 348, 537–545.
- [45] Mouzdahir, Y.E.; Elmchaouri, A.; Mahboub, R.; Gil, A.; Korili, S.A. Adsorption of methylene blue from aqueous solutions on a Moroccan clay. *J. Chem. Eng. Data.* **2007**, 52, 1621–1625.

# 14<sup>th</sup> Annual Research Day

Organised by the Deanship of Scientific Research in Collaboration with the College of Engineering  
Research Centre

4<sup>th</sup> April 2019

---

[46] Li, Z.; Chang, O.H.; Jiang, W.T.; Jean, J.S.;  
Hong, H. Mechanism of methylene blue  
removal from water by swelling clays. *Chem.  
Eng. J.* **2011**, 168, 1193–1200.

Characterization, Acid Activation and  
Bleaching Performance of Bentonite from  
Xinjiang. *Chinese J. Chem. Eng.* **2006**, 14,  
253–258.

[47] Zhansheng, W.; Chun, L.; Xifang, S.;  
Xiaolin, X.; Bin, D.; Jin'e, L.; Hongsheng Z.

# 14<sup>th</sup> Annual Research Day

Organised by the Deanship of Scientific Research in Collaboration with the College of Engineering  
Research Centre

4<sup>th</sup> April 2019

---

## Synthesis, Characterization and Application of Ferrochrome slag/polyaniline Nanocomposite as Corrosion Protection Coatings for Carbon Steel

Mohammad Ilyas Khan

Department of Chemical Engineering, College of Engineering, King Khalid University,

PO Box 394, Abha 61411 KSA.

E-mail address: mkaan@kku.edu.sa

---

**Abstract:** The corrosion protection ability of waste ferrochrome slag (FeCr-slag) material was investigated. FeCr-slag has been milled for 4 hours in order to obtain nanostructured material. As a nanomaterial, this compound was used as prepared as well as a nanocomposite with polyaniline. The nanocomposites were prepared by in-situ polymerization technique. The prepared materials were characterized by FTIR, XRD and SEM. The anticorrosion performance of FeCr-slag material, polyaniline (PANI) and a nanocomposite of FeCr-slag material with polyaniline was evaluated by incorporating these pigments in a commercial epoxy paint system. The prepared coatings were investigated for their anticorrosion ability by exposure to corrosive media in salt spray chamber as well as the electrochemical potentiodynamic polarization (PDP) and electrochemical impedance spectroscopy (EIS) methods. The results show that the nanocomposite pigments performed better, followed by FeCr-slag material and followed by PANI respectively. Modification of the FeCr-slag material with PANI has significantly improved the anticorrosion properties of the paint system used.

**Keywords:** carbon steel, corrosion inhibition, FeCr-slag, polyaniline, nanocomposites

---

### 1. Introduction:

Corrosion is a natural phenomenon and has a significant impact on the socio-economic aspects of life. Carbon steel is commonly used as a construction material in various applications such as in construction, transportation, pipeline etc. However, the life span of carbon steel like many other materials is limited primarily due to corrosion. To overcome this issue, the use of various types of commercially available anticorrosion paints and inhibitors are being introduced into the market. However, researchers and scientists are always on the outlook for more efficient, cheaper and environmental friendly coatings and inhibitors. Among the conductive polymers, polyaniline is probably the one of the

oldest synthetic conductive polymer [1]. It is the green protonated emeraldine base that exhibits the conductive form of polyaniline [2]. The exact mechanism of protection offered by conductive polymers is still not clear but one of the most commonly accepted mechanism is the surface ennobling and anodic passivation of the steel surface induced by the inherent redox capability of conductive polymers. Another recently proposed mechanism of protection is the so-called self-healing mechanism in which doping the conductive polymers with suitable anionic inhibitors can act as a reservoir of corrosion inhibitors [3].

Protective coatings are commonly used to protect steel structures against corrosion. The use

# 14<sup>th</sup> Annual Research Day

Organised by the Deanship of Scientific Research in Collaboration with the College of Engineering  
Research Centre

4<sup>th</sup> April 2019

---

of organic-inorganic composites or hybrid materials have proven to be effective because it combines the various attractive properties such as flexibility, ductility and dielectric of organic as well as the desirable properties such as thermal stability, strength and hardness etc. of the inorganic constituent [4]. The use of conductive polymers modified inorganic nanoparticles are also known to improve the physical properties of materials [5]. These types of modified pigments are capable of providing the highest level of protection against corrosion. The use of polyaniline modified anticorrosive pigments include; polyaniline-SiO<sub>2</sub> composite [6-7], polyaniline-Fe<sub>2</sub>O<sub>3</sub> composite coatings [8], polyaniline-ZnO-epoxy composite coatings [9], polyaniline-TiO<sub>2</sub> composite containing coatings [10], polyaniline glass flake composite coatings [11] and various other inorganic pigments as corrosion inhibitors [12]. The current research is focusing on investigating the use of waste slag material (FeCr-slag) from ferrochrome industry as corrosion inhibitor for carbon steel. The surface of these pigments will be modified by treatment with polyaniline. The anti-corrosion efficiency will be evaluated both for the untreated pigments and for the pigments modified with polyaniline. The use of this material as a corrosion inhibitor is scarce in literature and therefore is the focus of the current research.

## 2. Materials and Methods:

### 2.1 Materials

The ferrochrome slag waste material was taken from a steel manufacturing facility in Oman. The solid waste slag material was ball milled for 4 hours to convert it into a nanostructured material. Hydrochloride and ammonium peroxy disulphate (APS) were purchased from Sigma Aldrich and used without any modifications. Carbon steel coupons and the paint (epoxy zinc rich primer) were provided by Aljazeera Paint Company.

### 2.2 Preparation of PANI-FeCr-slag Nanocomposite

Aniline hydrochloride (2.59g) was dissolved in distilled water in a 50 ml volumetric flask. Also, ammonium peroxy disulphate (5.71g) was dissolved in a 50 ml volumetric flask. Both solutions were kept in an ice-cold bath for 1 hour. Pre-cooled APS solution was added dropwise to the aniline hydrochloride solution while constantly stirred using a magnetic stirrer. The nanocomposite material with PANI was prepared in similar manner except that the FeCr-slag was added during the mixing and polymerization process. After the complete addition of APS solution, stirring was allowed to continue for another two hours in order to achieve complete polymerization. The mixture was then filtered, washed several times with distilled water to neutralize the pH. The solid filtrate was dried in the oven at 60°C for 24 hours followed by grinding in a mortar and sieved to size of less than 126 µm.

### 2.3 Preparation of the coating formulations

Epoxy zinc rich phosphate primer was used. The prepared pigments as nanomaterials incorporated into the primer were 1% by weight. Three nanomaterials namely PANI (sample A), FeCr-slag material (sample B), nanocomposite (C) were tested. These materials were blended into the primer using commercial blender in a paint manufacturing facility. Salt spray coating technique was employed to apply the blended coatings on carbon steel coupons. The finished coated samples were allowed to cure for 7 days prior to salt spray testing.

### 2.4 Characterization of the prepared nano pigments

The structure of the synthesized polymer and composites was characterized by means of an IR spectrometry (TA instrument with universal

# 14<sup>th</sup> Annual Research Day

Organised by the Deanship of Scientific Research in Collaboration with the College of Engineering  
Research Centre

4<sup>th</sup> April 2019

ATR attachment, range 400–4000  $\text{cm}^{-1}$ ). As for the X-ray Diffractometer (Rigaku, Japan) using Cu K $\alpha$  radiation ( $\lambda = 0.15406 \text{ \AA}$ ) with operating voltage of 40 kV and current of 30 mA was employed to examine the phase and crystal structure identification in a  $2\theta$  range from 10 to 80°. Surface morphologies of synthesized polymer and composite samples were analyzed using Scanning electron microscopy (JSM-6360, JEOL) at an acceleration voltage of 20 kV and irradiation current of 10  $\mu\text{A}$ .

## 2.5 Characterization of the coated steel panels

### 2.5.1 Dry film thickness measurements

Dry film thickness measurements were carried out according to ISO 19840 using commercial coating thickness meter (from Paint Test Equipment). Thickness measurements were conducted at five different points and the average values are used in the final evaluation. The results are presented in Table 1. As can be seen, the coated thickness on the three samples is relatively uniform and in close agreement with each other.

**Table 1.** Dry film thickness measurements of the coated samples ( $\mu\text{m}$ )

	A (PANI)	B (FeCr-slag)	C (Nanocomposite)
1	38	39	48
2	44	43	55
3	28	37	39
4	31	41	48
5	41	35	34
Average	36	39	45

### 2.5.2 Exposure in Salt Spray Chamber

The coated steel coupons were subjected to salt spray testing conditions in accordance with ASTM B117. Salt spray testing method provides a controlled corrosive environment that has been utilized to produce relative corrosion resistance information for the test samples exposed in the test chamber.

### 2.5.3 Electrochemical Testing

Electrochemical corrosion tests were conducted using the Gamry Potentiostat Reference 600 together with Echem analyst software to analyze the experimental data. Conventional three electrode assembly was used to perform the electrochemical experiments in which carbon steel specimen with exposure area of  $1\text{cm}^2$  acts as working electrode, silver/silver chloride (Ag/AgCl) electrode and graphite rod act as reference and counter electrode respectively. Carbon steel specimens were immersed for about 1 h to check the steady-state prior to each measurement. Potentiodynamic polarization tests were performed at the potential of  $\pm 250 \text{ mV}$  from open circuit potential (OCP) at a scan rate of  $1 \text{ mVs}^{-1}$ . Electrochemical impedance spectroscopic tests were monitored over the frequency range of  $10^4$  to  $10 \text{ mHz}$ , with acquirement of 10 points per decade and a signal amplitude of 10 mV at OCP. All measurements were repeated at least three times and good reproducibility of the results was observed.

## 3. Results and Discussion

### 3.1 FTIR Analysis

Fig. 1 presents the IR spectra of synthesized PANI, FeCr-slag and its nanocomposite. The obtained peaks at 1462 and  $1555 \text{ cm}^{-1}$  of PANI are ascribed to the stretching mode of C=C and C=N of benzenoid and quinoid rings, respectively. The peaks at 1287 and  $1229 \text{ cm}^{-1}$  are accredited to C-N stretching mode of benzenoid ring and peak at  $1039 \text{ cm}^{-1}$  related to a plane bending vibration of C-H. In the case of IR spectra of ferrochrome nanoparticles, the appeared peaks around  $600\text{--}400 \text{ cm}^{-1}$  are allocated to Fe-O and Cr-O stretching respectively. The IR spectra of nanocomposite is similar to that of pure PANI when the peaks for C=N, C=C and C-N altogether moved to lower wave numbers (red shift), i.e. 1552, 1455, 1282 and  $1224 \text{ cm}^{-1}$  due to strong interaction of

ferrochrome, which is in good agreement with the previous reports [13-15].

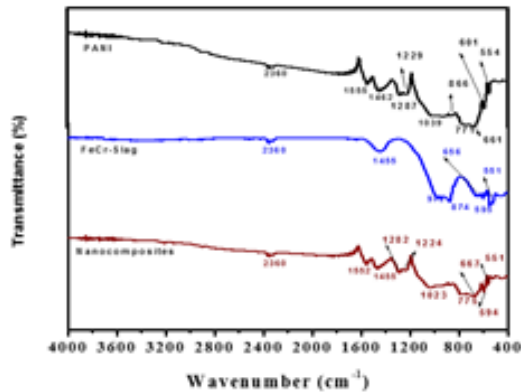


**Figure 1.** IR spectra of synthesized PANI, FeCr-slag and its nanocomposites

### 3.2 XRD Analysis

The XRD data for all the three samples is presented in Figure 2. The XRD pattern obtained for PANI is similar to the one reported by [8] and [9]. The two main Bragg diffraction peaks of PANI appeared at angles of  $2\theta = 19.3$  and  $2\theta = 25.7$  in the spectrum as reported by [9].

The presence of the rigid aromatic backbone of PANI makes it a semi-crystalline polymer [16]. Peaks of the FeCr-slag has become smaller by the addition of PANI as shown by the spectra of the nanocomposite that confirms the formation of the organic-inorganic nanocomposite.

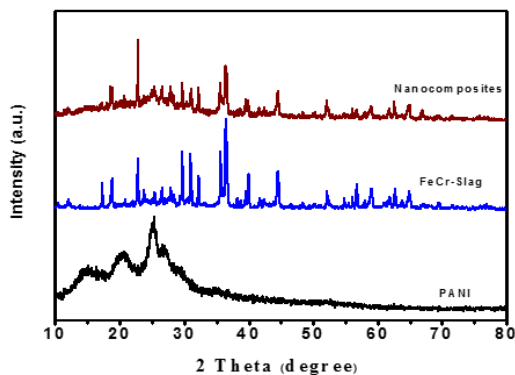


**Figure 2.** XRD pattern of synthesized PANI, FeCr-slag and its nanocomposites

### 3.3 SEM Analysis

The SEM micrographs of the prepared PANI, FeCr-slag and FeCr-slag modified PANI nanocomposite are introduced in Figure 3. As it is clear, the PANI showed non-uniform morphology which satisfies its poor crystalline characteristics as confirmed by XRD. Morphology examinations of FeCr-slag indicated that the nanoparticles are homogeneously dispersed with minor agglomeration and have the diameter of about 80–100 nm with spherical morphology. In contrast, the microstructural observation of nanocomposite obviously implies that FeCr-slag nanoparticles are well embedded and strongly held to the PANI matrix, signifying the presence of some interaction between the FeCr-slag nanoparticles and the PANI matrix. Nano-scale particles can be identified in the nanocomposite; these nano particles can effectively distribute through the coating matrix and help in enhancing the corrosion protection efficiency.

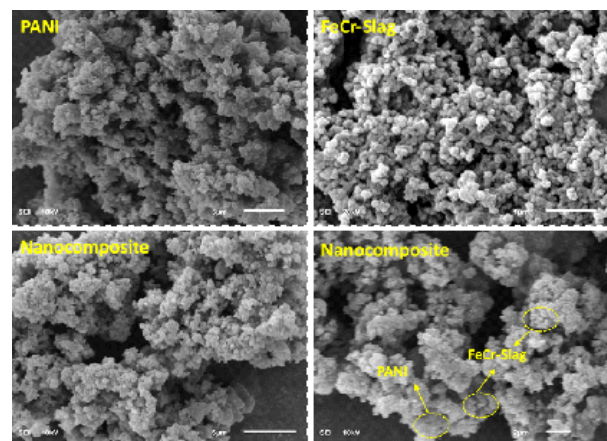


**Figure 3.** SEM images of synthesized PANI, FeCr-slag and its nanocomposite

### 3.4 Salt Spray Exposure Test

As shown in Figure 4, visual observations of the specimens after salt spray exposure reveal

that the carbon steel (CS) sample coated with the paint containing PANI (sample A) has experienced the most corrosion. The paint system containing the FeCr-slag nanoparticles (sample B) exhibits less corrosion than the PANI system followed by the coating system containing the nanocomposite (sample C). In other words, the coating system containing the nanocomposite pigment exhibited the least corrosion as anticipated.



**Figure 4.** Picture of the coated CS specimens after 8000 hours of exposure in salt spray

### 3.5 Electrochemical Corrosion Studies

As for the electrochemical results, the typical potentiodynamic polarization results for PANI, FeCr-slag and nanocomposite coated CS specimens in 3.5% NaCl solution at 25 °C after 24 h immersion are presented in Figure 5. The electrochemical parameters extracted from the Tafel plot analysis are presented in Table 2. The steel specimens with coatings exhibited more positive  $E_{\text{corr}}$  values compared to that of the bare specimen, indicating that the polymer coatings become a physical barrier for diffusion of aggressive species from solution and improve the corrosion resistance of the steel specimens [17]. In particular, a larger shift of  $E_{\text{corr}}$  towards nobler direction was observed with an inclusion of nanocomposites into the coatings. Moreover, a significant shift towards lower current densities ( $i_{\text{corr}}$ ) was observed, and particularly,  $i_{\text{corr}}$  was

reduced by about two orders of magnitude. The corrosion rate (CR) was calculated using the  $i_{\text{corr}}$  values and Eq. (1).

$$\text{CR} = 3268 \times i_{\text{corr}} \times \text{EW}/D \quad (1)$$

where  $i_{\text{corr}}$  denotes the corrosion current density ( $\text{mA cm}^{-2}$ ), EW and D is the equivalent weight and density ( $\text{g cm}^{-3}$ ) of the specimen, respectively.

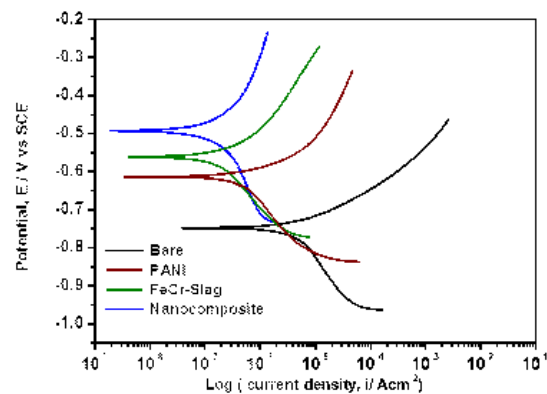


**Figure 5.** Polarization curves of bare and coated CS specimens after 24 h of immersion in 3.5 % NaCl solution at room temperature with a scan rate of  $1 \text{ mVs}^{-1}$

Generally, the high corrosion potential along with the low corrosion current density of the coatings specifies a lower corrosion rate with a higher corrosion protection performance [18]. The protection efficiency (PE) of the polymer coatings were calculated using the following expression:

$$\text{PE}(\%) = R_p(\text{coated}) - R_p(\text{bare}) / R_p(\text{coated}) \times 100 \quad (2)$$

From equation 2, the PEs obtained are 81.75, 82.95 and 95.79% for PANI, FeCr-slag and nanocomposite samples, respectively. From the obtained results, it is revealed that the addition of PANI into the coatings act as a barrier which restrict the permeation of the electrolyte and also reducing the corrosion rate by participating in the electrochemical reactions. Furthermore, the inclusion of the nanocomposite

into the coating matrix could hinder the corrosion process of the CS specimens due to the existence of FeCr-slag nanoparticles within the PANI matrix which might function as a reinforcement network and make a coating which is more compact and corrosion resistant [19].

**Table 2.** Polarization parameters for bare and coated CS samples in 3.5% NaCl at 25 °C after 24 h immersion

Samples	$E_{cor}$ (mV Vs Ag/AgCl)	$I_{cor}$ $\mu$ A/cm <sup>2</sup>	$\beta_a$ (mV/dec.)	$\beta_c$ (mV/dec.)	CR (mm/yr)	PE (%)
Bare	-748	3.510	158	62	40.69	-----
PANI	-614	0.668	127	73	7.74	81.75
FeCr-slag	-561	0.865	187	98	10.14	82.95
Nanocomposites	-493	0.171	165	75	1.98	95.79

In order to gain further insight into the corrosion protection behavior of PANI and its nanocomposite coated CS specimens, EIS tests were conducted and the results obtained are presented in Figure 6 and 7 in Nyquist and Bode formats respectively. Nyquist diagram of the coated CS specimens exhibited two-time constants at low and high frequency regions (Fig. 6), whereas the former is attributed to the responses of electrolyte/coating interface, the latter is associated with the corrosion processes occurring at the electrolyte/metal interface [20].

Generally, the length of the semicircle arc is related with the polarization resistance ( $R_p$ ) and therefore the corrosion rate; the lengthier the semicircle arc, the lesser the corrosion rate [21]. Comparing the Nyquist plots of the bare and coated specimens, the coated specimens exhibited the highest  $R_p$ . The diameter of the capacitive arc for the nanocomposite coatings is observed to be larger in comparison to others, signifying that the nanocomposite coatings conferred the highest corrosion protection performance on the CS specimens in 3.5% NaCl solution.

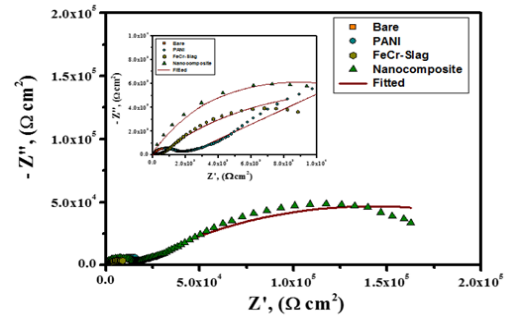


**Figure 6.** Nyquist plots of bare and coated CS specimens after 24 h of immersion in 3.5 % NaCl solution at room temperature

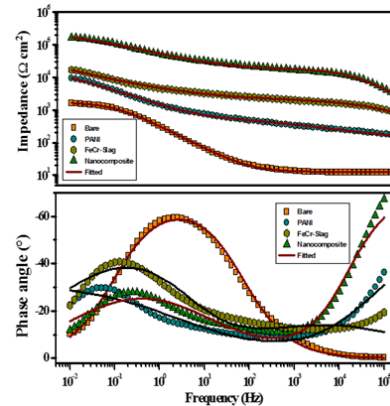


**Figure 7.** Bode plots of bare and coated CS specimens after 24 h of immersion in 3.5 % NaCl solution at room temperature

Bode plots of the bare and coated CS specimens are presented in Figure 7. The impedance parameters of interest was generated by fitting the experimental data into equivalent circuit models, and the achieved fitting values displayed proper reliability with the experimental results.

The equivalent circuit models are represented as (Fig. 8a)  $R_s(R_{ct}Q_{dl})$  for the bare and (Fig. 8b)  $R_s(R_fQ_f)(R_{ct}Q_{dl})$  for the coated specimens, where  $R_s$ ,  $R_{ct}$ ,  $R_f$  means the solution, charge transfer, and film resistances, respectively, and  $Q_{dl}$  and  $Q_f$  are the double layer and coating capacitances, respectively [22].

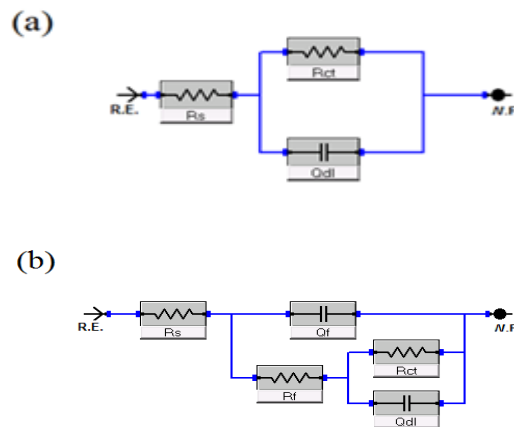


**Figure 8.** EIS circuit models for (a) bare and (b) coated CS specimens

Constant phase elements (CPE/Q) were used to get the accurate fitting by replacing the capacitive elements in the circuits. The impedance of a CPE can be represented as:

$$Z_{CPE} = [Y_0 (j \omega)^n]^{-1}, \quad (3)$$

where  $Y_0$  and  $n$  are frequency independent parameters and  $\omega$  is the angular frequency [21]. The obtained experimental results were well fitted to the theoretical data and the estimated impedance values are listed in Table 3.

Generally, the impedance values at the lower frequency region (10 mHz) hold an important part in relating the electrochemical behavior and integral features of the coating at the interface [23]. All of the coatings exhibited a higher impedance value at a lower frequency region compared to that of the bare CS specimen. From the Table 3, the  $R_{ct}$  value of the coated CS specimens increased from 1.76  $k\Omega \text{ cm}^2$  for bare to 9.45, 16.54 and 166.8  $k\Omega \text{ cm}^2$  for the PANI, FeCr-slag and nanocomposite coated specimens, respectively, representing improved corrosion protection behavior for the coatings.

Generally,  $R_f$  values could be influenced by the number of pores/passageway networks in the

metallic surface, through which the permeation of corrosive species occurs [24]. The highest  $R_f$  value was observed for the specimens coated with nanocomposite, demonstrating that the micro cracks and pores are closed by the reinforcement of nanocomposites. Hence, the inclusion of the nanocomposites seems to significantly decrease the porosity of the coatings by filling the probable micro cracks/cavities inside the coating [25].

Moreover, this performance proficiently hinders and extends the diffuse pathway of aggressive elements, such as  $\text{Cl}^-$  and  $\text{H}_2\text{O}$  [26]. From the obtained results, it can be concluded that the steel specimens coated with coating formulation containing the nanocomposite display enhanced corrosion protection behavior in 3.5% NaCl solution.

**Table 3.** EIS parameters for bare and coated CS samples in 3.5% NaCl at 25 °C after 24 h immersion

Samples	$R_s$ ( $\Omega$ $\text{cm}^2$ )	$R_{ct}$ ( $k\Omega$ $\text{cm}^2$ )	$R_f$ ( $k\Omega$ $\text{cm}^2$ )	$CPE_{dl}$ ( $\mu\text{F cm}^2$ )	$n_{dl}$	$CPE_f$ ( $\mu\text{F cm}^2$ )	$n_f$	PE (%)	$\chi^2 \times 10^3$
Bare	28.2	1.76	-----	838.60	0.80	-----	-----	-----	2.25
PANI	173.3	9.45	2.23	231.65	0.96	99.00	0.94	81.37	3.30
FeCr-slag	152.0	16.54	2.15	180.00	0.94	3.84	0.92	89.35	2.47
Nanocomposite	121.0	166.80	46.96	10.54	0.97	0.74	0.96	98.94	3.21

## 4. Conclusions

In this paper, the anticorrosion performance of three different pigments namely; FeCr-slag nanomaterial, PANI and a nanocomposite of these two materials was evaluated by incorporating these pigments in a commercial epoxy zinc rich phosphate primer. As highlighted in the salt spray exposure and electrochemical tests, the coating formulation that contain the nanocomposite demonstrate superior corrosion protection properties. The results show that the nanocomposite pigments performed better, followed by the FeCr-slag nanomaterial followed by PANI respectively. As expected, modification of the FeCr-slag nanomaterial (raw

# 14<sup>th</sup> Annual Research Day

Organised by the Deanship of Scientific Research in Collaboration with the College of Engineering  
Research Centre

4<sup>th</sup> April 2019

material) with conductive polymer PANI has significantly improved the anticorrosion properties of the paint system used.

## Acknowledgement

The author gratefully acknowledges the research funding for this project No.455, provided by Deanship of Scientific Research, King Khalid University, ABHA, KSA. Also, the author would like to acknowledge the technical support of Engineer Mohamed Al-Zaher from Aljazeera Paints Company in Saudi Arabia.

## References

1. J. Prokeš, J. Stejskal and M. Omastová, *Chem. listy*, 95 (2001) 484.
2. J. Stejskal, P. Kratochvíl and A. D. Jenkins, *Polymer*, 37 (1996) 367.
3. T. Niratiwongkorn, G. E. Luckachan and V. Mittal, *RSC Adv.*, (2016) 43237.
4. R. Suleiman, H. Dafalla and B.El Ali, *RSC Adv.*, (2015) 39155.
5. A. Kalendova, E. Halecka, K. Nechvilova and M. Kohl, *Koroze a ochrana materiálu*, 61 (2017) 39.
6. A. A. Al-Dulaimi, S. Hashim and M.I. Khan, *Sains Malays.*, 40 (2011) 757.
7. G. Ruhi, H. Bhandari and S. K. Dhawan, *Prog. Org. Coat.*, 77 (2014) 1484.
8. S. Sathiyarayanan, S. S. Azim and G. Venkatachari, *Synth. Met.*, 157 (2007) 751.
9. A. Mostafaei, and F. Nasirpouri, *Prog. Org. Coat.*, 77 (2014) 146.
10. S. Sathiyarayanan, S. S. Azim and G. Venkatachari, *Prog. Org. Coat.*, 59 (2007) 291.
11. S. Sathiyarayanan, S. S. Azim and G. Venkatachari, *Electrochim. Acta*, 53 (2008) 2087.
12. A. Kalendova, D. Vesely and J. Stejskal, *Prog. Org. Coat.*, 62 (2008) 105.
13. M. Kryszawski and J.K. Jezka, *Synth. Met.*, 94 (1998) 99.
14. X. Li, G. Wang, X. Li and D. Lu, *Appl. Surf. Sci.*, 229 (2004) 395.
15. C. Wang, Z. Tan, Y. Li, L. Sun and T. Zhan, *Thermochim. Acta*, 441 (2006) 191.
16. L. Shi, X. Wang, L. Lu, X. Yang and X. Wu, *Synth. Met.* 159 (2009) 2525.
17. A. M. Kumar, B. Suresh, S. Ramakrishna and Kye-Seong Kim, *RSC Adv.*, 5 (2015) 99866.
18. N. Attarzadeh, K. Raeissi and M.A. Golozar, *Prog. Org. Coat.*, 63 (2008) 167.
19. A. M. Kumar and N. Rajendran, *Ceram. Int.*, 39 (2013) 5639.
20. N. Imaz, M. Ostra, M. Vidal, J.A. Díez, M. Sarret and E. García-Lecin, *Corros. Sci.*, 78 (2014) 251.
21. Y. Maocheng, A. C. Vetter and J. V. Gelling, *Corros. Sci.*, 70 (2013) 37.
22. A. M. Kumar, Z and M. Gasem, *Surf. Coat. Technol.*, 276 (2015) 416.
23. M. Hattori, A. Nishikata and T. Tsuru, *Corros. Sci.*, 52 (2010) 2080.
24. P. G. Pawar, R. Xing, R. C. Kambale, A. M. Kumar, S. Liu and S. S. Latthe, *Prog. Org. Coat.*, 105 (2017) 235.
25. A. M. Kumar, S. Nagarajan, N. Rajendran and T. Nishimura, *J. Solid State Electrochem*, 16 (2012) 2085.
26. Y. Jafari, S.M. Ghoreishi and M. S. Nooshabadi, *Synth. Met.*, 217 (2016) 220.

# 14<sup>th</sup> Annual Research Day

Organised by the Deanship of Scientific Research in Collaboration with the College of Engineering  
Research Centre

4<sup>th</sup> April 2019

## The Graphene/Gold @ Polyaniline nanocomposite for the Removal of Methylene Blue and Its Thermal Electrical Stability Studies

Mudassir Hassan<sup>\*1</sup>, Atef El Jery<sup>1</sup>

<sup>1</sup>Department of Chemical Engineering, College of Engineering, King Khalid University,  
PO Box 394, Abha 61411 KSA.

\*E-mail address: m-hasan@kku.edu.sa

**Abstract:** In this work, composite of polyaniline with graphene and gold was prepared and applied for the removal of methylene blue organic dye from the aqueous solution at room temperature. Thermal electrical stability of the fabricated composite material was also studied. The composite material showed excellent performance towards the removal of the MB dye. Also the electrical stability even after several heating cycles was remarkably high. The fabricated material can be used an excellent dye removal material. The high performance towards dye removal can be associated with good surface properties of the composite due to the presence of the GNP and GN in the matrix of PANI.

**Keywords:** Polyaniline, Gold Nanoparticle, Graphene, Methylene blue, Dye, Electrical Stability.

### 1. Introduction:

Polyaniline (PANI) has been researched globally owing to its several unique properties. Amongst those are its inexpensive synthesis, excellent acid base flexibility, and good adsorptive capability towards dye removal [1-4]. Graphene (GN) too has been studied by several researchers across the globe. As GN is known to have high aspect ratio and excellent barrier and electromechanical properties [5-6]. The application of GN is achieved in several fields owing to its extraordinary unique properties. Such as in adsorption, photo catalysis, electrodes, photovoltaics, sensors and capacitors etc. [7-10]. Gold nanoparticle (GNP) has been studied widely due to its excellent surface, optical and catalytic properties [11]. Therefore it is expected that the composite of GNP, GN and PANI will show better performance towards dye removal and enhanced electrical stability due to its synergism between GN, GNP and PANI.

Also it can be understood that a homogeneous interaction between GNP and PANI might reflect in enhanced surface properties of the composite material. However, the contact between GNP and PANI is generally not easy to accomplish.

Therefore in this work GN is used to bind both PANI and GNP in its composite structure. We think that further research is needed to study the details about the interaction between the GNP and PANI in order to harness its surface related application such as adsorptive dye removal and etc.

In the past several workers has studied about the synthesis of PANI with different metal oxide nanoparticles [12-15].

However, few research is available on synthesis and of composite of polyaniline with graphene and gold. Therefore, the aim of this work is to report the fabrication of the above composite material. Thermal electrical stability, dye removal study were presented.

### 2. Materials and Methods:

#### 2.1 Materials

GNP, aniline and camphorsulfonic acid (CSA) were purchased from Sigma Aldrich. Ammonium persulphate (APS), cetyl tri methyl ammonium bromide (CTAB), HCl, and methanol were purchased from Duksan Chemicals Korea. All the chemicals were used as received without any further pretreatment.

#### 2.2 Experimental Procedure

PANI was synthesized using *In situ* chemical oxidative polymerization technique. CTAB as surfactant and ammonium persulfate (APS) as an oxidizing agent was used towards fabrication of composite material. To achieve homogeneity in the composite structure the GNP was dissolved with a 1 M HCl solution and ultra sonicated. GN was also ultra sonicated similarly. Then, CTAB was added to this ultra sonicated solution. Further Aniline was mixed slowly to thus prepared solution. The solution was stirred thoroughly for homogeneous mixing of GN and GNP. Then it was polymerized using an oxidant (APS). The resulting mixture was observed to be changing into thick greenish material. which was filtered and washed with distilled water and methanol until the filtrate was found to be colorless. The synthesized HCl doped composite was neutralized using ammonia solution. Then it was re doped using CSA.

### 3. Results and Discussion

#### 3.1. Electrical conductivity study of the composite.

Fig. 1 shows the DC electrical conductivity data of neat and composite material. Composite material compared with neat showed increased electrical conductivity. The enhancement in conductivity can be ascribed to the homogeneous incorporation of GNP and GN in the matrix of PANI. The conductivity of the composite material was found to be almost 60% more than that of PANI at room temperature. It was also observed that the conductivity of neat material increased until 106 °C. Further increase in temperature didn't improve conductivity. However, electrical conductivity of composite material showed an increase of 41 (S/cm) at 91 °C. After this temperature a decrease in conductivity was recorded. The reduction in electrical conductivity can be associated with drying of composite material after heating. It is well known that the presence of water molecule in the composite enhances the charge uniformly throughout the material.

#### 3.2. Thermal Electrical stability study of the composite.

Table. 1 shows the data for thermal electrical stability and DC electrical conductivity of the PANI and composite material. Thermal electrical stability was performed using the four probe method. The conductivity was measured with increasing the temperature and this phenomena was repeated with several heating cycles. Thermal electrical stability of neat and composite material was calculated as 88% and 93% respectively. thermal electrical stability was calculated using the following formula.

$$\text{Thermal Electrical Stability} = \frac{\text{conductivity at cycle 1} - \text{conductivity at end cycle}}{\text{conductivity at cycle 1}} \times 100$$

(1)

**Table 1:** Thermal Electrical stability DC electrical conductivity of the neat and composite material

Materials	Thermal Electrical stability (%)	DC Electrical conductivity (S/cm)
PANI	88	4.5
Graphene/Gold @Polyaniline	93	7

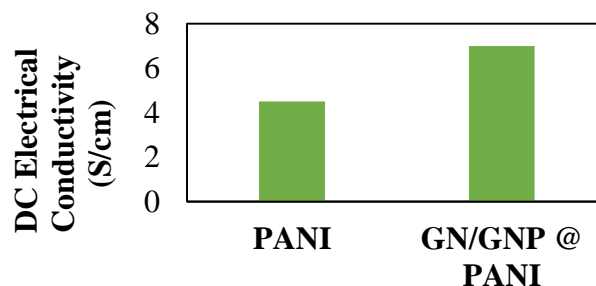


**Figure (1)** DC Electrical conductivity of PANI and the composite at room temperature.

#### 3.2. Methylene blue dye removal study of the composite material.

Fig. 2 shows the dye degradation of MB with composite material. The figure clearly shows that the MB was degraded in 3 hour using composite material as an adsorbent. After 2 hour of

# 14<sup>th</sup> Annual Research Day

Organised by the Deanship of Scientific Research in Collaboration with the College of Engineering Research Centre

4<sup>th</sup> April 2019

experiment the degradation efficiency was recorded to be 93%. Fig. 3 shows the  $\ln C$  vs. time plot for the degradation of MB. MB was observed to be degrading with first order kinetics with K value as  $0.436 \text{ (h}^{-1}\text{)}$ . The degrading activity of the composite material for MB was excellent, which might be due to enhanced surface area of the composite structure. Degradation efficiency of MB was measured using the following relation.

$$\text{Degradation (\%)} = \frac{C_0 - C}{C_0} \cdot 100 \quad (2)$$

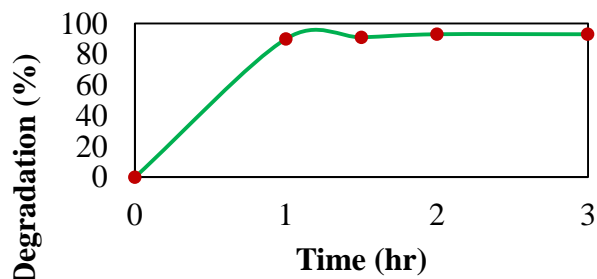


Figure (2) Removal percentage of MB by composite material

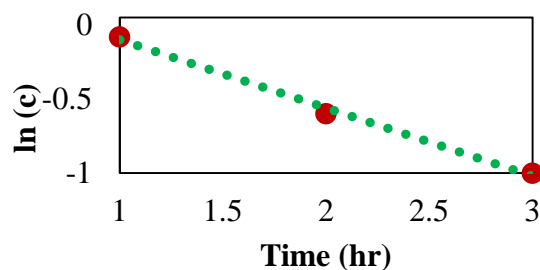


Figure (3) Plot of  $\ln(c)$  versus time for the Kinetic study of MB by the composite material.

## 4. Conclusions:

Polyaniline with graphene and gold was fabricated using in-situ oxidative chemical polymerization technique. The composite material was tested for the removal of methylene blue organic dye from the aqueous solution. Thermal electrical stability of the synthesized composite material was also investigated. The composite material showed remarkably high

capacity for the removal of MB dye. Also the electrical stability even after several heating cycles was remarkably high. Thus it can be stated that the fabricated material can be used as an excellent dye removal material. The high performance towards dye removal can be associated with good surface properties of the composite due to the presence of the GNP and GN in the matrix of PANI.

## Acknowledgement

No support was received for this work.

## References

- [1] M. M. Hossain, O.-K. Park, J. R. Hahn and B.-C. Ku, *Mater.Lett.*, 2014, 123, 90–92.
- [2] M. Hossain, H. Shima, M. A. Islam, M. Hasan and M. Lee, *RSC Adv.* 2016, 6, 4683–4694.
- [3] M. Hasan, M.O. Ansari, M. Cho, M. Lee, *Electron. Mater. Lett.* 11 (1) (2015) 1.
- [4] M. Hasan, A.N. Banerjee, M. Lee, *JIEC* 21 (2015) 828
- [5] M. Hasan, M. Lee, *Prog. Nat. Sci. Mater. Int.* 24 (2015) 579.
- [6] M. Hasan, M.O. Ansari, M. Cho, M. Lee, *JIEC* 22 (2015) 147.
- [7] P. Simon, Y. Gogotsi, *Nat. Mater.* 7, 845–854 (2008).
- [8] M. Hasan, M. M. Hossain, M. Lee, *J. Ind. Eng. Chem.* 32 (2015) 123.
- [9] A.G. Pandolfo, A.F. Hollenkamp, *J. Power Sour.* 157 (2006) 11–27.
- [10] A.R. McKellar, *J. Chem. Phys.* 136 (2012) 094305.
- [11] N. Mohanty, V. Berry, *Nano Lett.* 8 (2008) 4469–4476.
- [12] V.K. Gupta, M.L. Yola, T. Eren, N. Atar, *Sens. Actuators B Chem.* 218 (2015) 215–221. [13] Y. Yang, J. Luan, *Molecules.* 17 (2012) 2752.
- [14] F. Wang, S. X. Min, *Chinese Chemical Letters* 18 (2007) 1273.

## Application of Saudi Building Code Recommendations to Design Shear Critical Concrete Members

Mohd. Ahmed<sup>1</sup>, Nabil Ben Kahla<sup>1</sup>

<sup>1</sup>Department of Civil Engg., College of Engineering, King Khalid University,  
PO Box 394, Abha 61421 KSA.  
E-mail address: mall@kku.edu.sa

**Abstract:** The present study apply Saudi Building Code (SBC: 304) recommendations to some of the shear critical or deep concrete members design where the beam theory is not applicable. The study compares the shear critical concrete member design using beam theory based section method and using Strut-and-Tie method. Strut-and-Tie Models technique is a unified approach that considers all load effects (bending, axial, shear, and torsion) simultaneously, not just applicable to shear loading only. The model developed provides a rational basis for representing a concrete structural element with an appropriate simplified truss model. The paper uses the Saudi design codes provision on the effective stress of concrete, tie end anchorage, and transverse reinforcement demand under different load transfer mechanism in context of Strut-and-Tie Modeling technique. It concludes that the strut-and-tie method for RCC member is a conservative design method.

**Keywords:** Shear critical Member, Strut-Tie Method, Deep Concrete Members, National Codes, Disturbed regions

### 1. Introduction:

Strut-and-Tie models (STM) are the distinct depiction of statically equivalent distributed stress field by resultant straight lines and concentrate the curvature of the stress field in nodes. Truss members that are in compression, termed as struts, are made up of concrete, while truss members that are in tension consist of steel reinforcement. Transverse reinforcement may be necessary to prevent splitting caused by transverse tension due to high compressive stress in the strut. The building structural elements, i.e., beam, column, etc may be divided into portions called B-regions in which beam theory applies and other portions called discontinuity region, or D-regions adjacent to discontinuities or disturbances, where the beam theory does not apply. In D-regions, in-plane forces carry a significant portion of the load. The Strut-and-Tie Models may be used to design the D-regions of the concrete members. Prior to the cracking of the

concrete structural element, an elastic stress field can be determined using an elastic analysis. Cracking disrupts this stress field causing a major reorientation of the internal forces. After cracking the internal forces can be modeled using a strut-and-tie method consisting of concrete struts, steel tension ties, and joints referred to as nodes. Examples of D-regions are regions near concentrated loads and reactions, corbels, deep beams, joints, dapped ends, abrupt changes in cross-section, holes and other discontinuities.

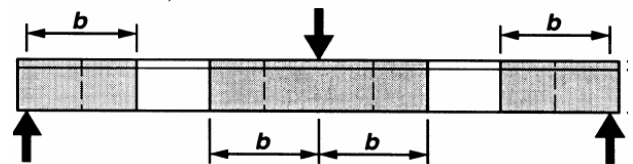


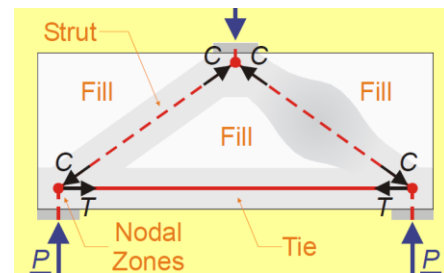
**Figure (1)** B and D-regions of Concrete Members

The several empirical approaches are proposed to aid in generating STM. Schlaich et al. [1] suggested that one possible approach for the development of suitable strut and tie models is to

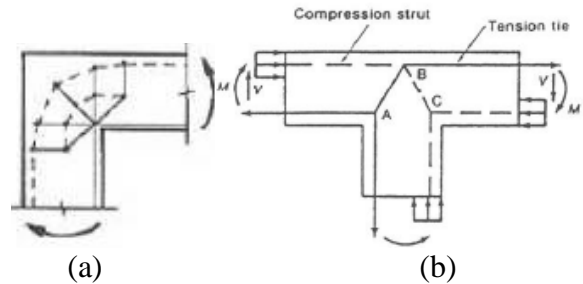
orient the struts and ties members within  $15^\circ$  from the principal stress path obtained from elastic uncracked stress field and the most valid model tends to be the one that minimize the amount of reinforcement. SBC: 304- 2007 [2] and SP-308 [3] and has given detailed guidelines and examples related to the design of structural members using the strut-and-tie method. Ahmed et al. [4] have proposed the load transfer mechanism based strut-and-tie model for the design of concrete members. Shuraim [5] studied the behavior and shear design provisions of D-regions in reinforced concrete (RC) normal-size beams by experimental and numerical observations (conventional sectional method, strut-and-tie method and nonlinear finite element method). Strut-and-tie model technique is applied by Ahmed et al. [6] to design the T-cantilever deep beam. The double corbel has been designed by Singh, et al. [7] using the strut-and-tie method. The strut-and-tie method has been applied to analyses of the lateral structural system of a high-rise building by Su, et al [8]. Park et al. [9] have predicted strength of deep beam using STM. They consider cracked concrete constitutive law for wide range of provided horizontal and vertical web reinforcement ratios, concrete compressive strengths, and shear span-to-depth ratios ( $a/d$ ). Based on transfer mechanism of shear loads, an analytical method has been proposed by Kuo et al. [10] to define the boundaries of Bernoulli (B) regions and disturbed (D) regions. Based on published literature [11], Ahmed et al. [4] has suggest load transfer mechanism based namely Arch action, Truss action or combined Arch - Truss action as for the modeling of STM elements. Zhi et al. [12] derive the relationship for fraction of load transfer between direct strut and truss mechanism in combined force transfer action, separately for corbel and deep beams.

## 2. Typical Strut-And-Tie Models for Deep Concrete Members:

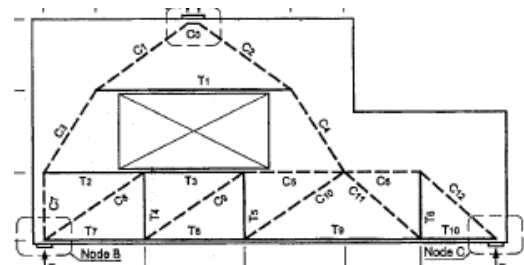
### 2.1 Deep Beam with Single Point Load



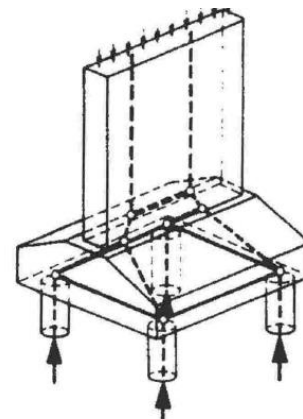
2.2 Beam Column Joints



2.3 Deep Beam with Opening



2.4 Pier on Pile Cap



## 3. STRUT- AND -TIE MODELLING AND DESIGN STEPS

The Strut- and -Tie design process involves the steps described below.

1. Define the boundaries of the D-Region and determine the imposed local and sectional forces.
2. Sketch the internal supporting truss, determine equivalent loadings, and solve for truss member forces
3. Select reinforcing steel to provide the necessary tie capacity and ensure that this reinforcement is properly anchored in the nodal zone Evaluate the dimensions of the struts and nodes, such that the capacity of these components (struts and nodes) is sufficient to carry the design forces values.

### 4. DEEP BEAM DESIGN EXAMPLE

A 2 m deep beam is required to resist dead load of 800kN and live loads of 400 kN. The beam is 500mm wide and made from 25MPa concrete and 420MPa steel reinforcement. Supports/loadings have bearing plates with dimension of 450x500x10mm and assumed to be safe in bending. The grade of Steel is Fe420 and grade of concrete is 25MPa.

Strut-and-Tie Method procedure is applied to the examples of deep beams using three trial models and model namely arch, truss and combined arch-truss type load transfer are considered for the deep beam structure. The design guidelines are based on Saudi Building Code SBC: 304 -2007. The three assumed Strut-and-Tie models for deep concrete beam with two point loads correspond to arch, truss and combined arch and truss load transfer mechanism are shown in Figure 2, 5 and 7 respectively.

#### 4.1 Deep Beam with Point Load (Trial Model 1)

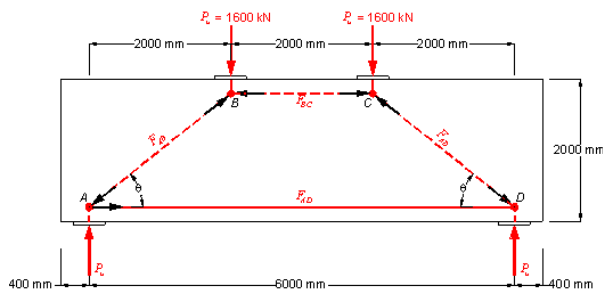


**Figure (2):** Strut-and-Tie Model 1 (Arch)

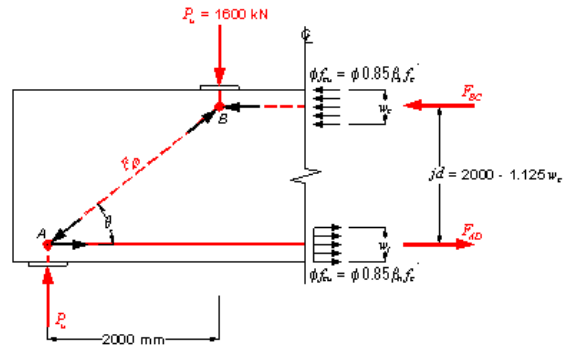


**Figure (3):** Strut-and-Tie Member Forces

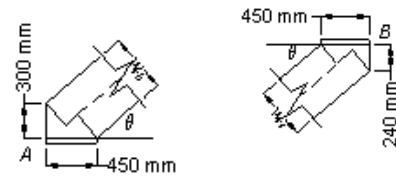


**Figure (4):** Node A and Node B

#### 4.2 Deep Beam with Point Load (Trial Model 2)

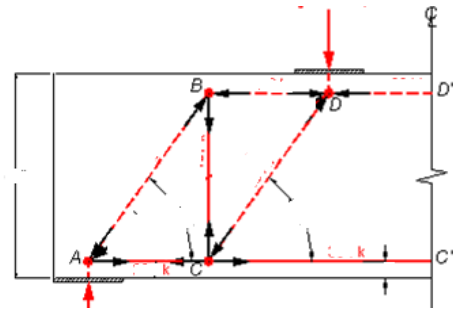


**Figure (5):** Strut-and-Tie Model 2 (Truss)

**Table 1:** Forces in Truss members and angles

Member	Force (kN)	Slope (Deg.)
AB	-1847.5	60
AC	923.8	0
CC'	1850	0
CD	-1847.5	60
BC	1600	90
BD	-923.8	0
DD'	-1850	0

**Table 2:** Forces and Node Width ( $w_n$ )

Memb.	Force (kN)	$w_n$ (mm)	Provided $w_n$ (mm)
A- AB	1847.5	290	539
A- AC	923.8	145	240
A-Rea	1600	251	450
B- BA	1847.5	290	509
B- BC	1600	351	450
B- BD	923.8	145	300
C- CA	923.8	193	240

# 14<sup>th</sup> Annual Research Day

Organised by the Deanship of Scientific Research in Collaboration with the College of Engineering Research Centre

4<sup>th</sup> April 2019

C- CB	1600	335	450
C-CC'	1850	388	240
C- CD	1847.5	387	509
D- DB	923.8	116	300
D- DC	1847.5	232	509
D-DD'	1850	233	300
D- P	1600	201	450

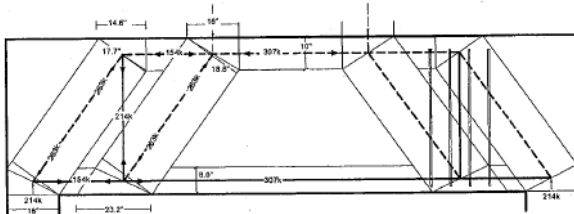


Figure (6): Strut-and-Tie Model with dimensions

## 4.3 Deep Beam with Point Load (Trial Model 3)

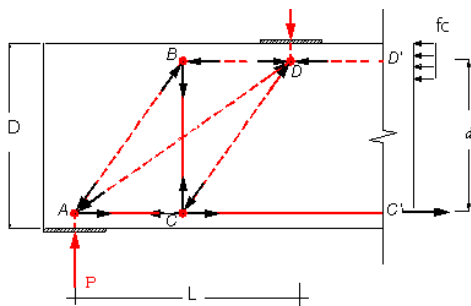


Figure (7): Strut-and-Tie Model 3 (Arch-Truss)

Table 3: Forces in Truss members and angles

Member	Force (kN)	Slope (Deg.)
AB	-923.8	60
AC	1460.4	0
AD	-1221.9	40.9
CC'	1850	0
CD	-923.8	60
BC	800	90
BD	-461.9	0
DD'	-1850	0

### 4.4 3.4 Flexure Design of Deep Beam Example

Beam Maximum Bending Moment (at 1/3rd)

$$= 2 \times 1600 = 3200 \text{ kNm.}$$

Required Flexural Tensile reinforcement

$$= M_n = \phi A_s f_y (d - a/2)$$

$$= \phi A_s f_y [d - (A_s f_y / 2.0.85.f_c b)]$$

$$A_s = 4703 \text{ mm}^2$$

## 5. Results and Discussion

The Strut-and-Tie modeling is applied to the analysis and design of deep concrete beam problem. For deep beam, three Strut-and-Tie models are assumed and design results are obtained based on the Strut-and-Tie based design recommendations of Saudi Building Code (SBC: 304). The deep beam is also designed according to the section based flexural theory.

The concrete deep beam vertical, horizontal and longitudinal reinforcement demand for the assumed strut-and-tie models and designed using Saudi Building Code (SBC: 304) recommendations are compared in Table 4. It is clear from the Table 4 that the strut-and-tie method for RCC member is a conservative design method as compared to the section design method. The longitudinal reinforcement demand in STM is 5873 mm<sup>2</sup> while longitudinal reinforcement demand is 4707 mm<sup>2</sup>. The reinforcement requirement in STM is about 25% more than the section design method. It is also evident from the Table that different lay out of the strut-and-tie models require different reinforcement at the support and at the middle of the beam. This means that the anchorage requirement at the support varies with the assumed strut-and-tie model. The maximum anchorage requirement is for the STM model 1 (arch type load transfer to support) while the least anchorage requirement is for the STM model 2 (truss type load transfer to support).

Table 4: Comparison of deep beam STM models reinforcement demand

Design method	Type of Reinforcement	
	Longitudinal Reinforcement (mm <sup>2</sup> )	
	At mid span	At support
STM Model 1	5873	5873
STM Model 2	5873	2923
STM Model 3	5873	4636
Section Method	4703	1568

# 14<sup>th</sup> Annual Research Day

Organised by the Deanship of Scientific Research in Collaboration with the College of Engineering  
Research Centre

4<sup>th</sup> April 2019

## 6. Conclusions

Significant conclusions of the present study are summarized below.

(1) The strut-and-tie method could be used as an alternative to section based flexure design method for the design of deep concrete member (shear critical member).

(2) The strut-and-tie method is a unified approach that considers all load effects simultaneously and the strut-and-tie approach carry out analysis and design of concrete structure together.

(3) As the strut-and-tie model (STM) approach is a load path approach, the behavior of structure can be controlled by developing a load path by providing the reinforcement according to chosen layout of strut-and-tie model.

(4) The concrete design results that the strut-and-tie method for RCC member is a conservative design method.

(5) The reinforcement demand for longitudinal reinforcement in central portion of beam for various strut-and-tie models based on load path are same but the reinforcement demand is different at the support or for reinforcement anchorage.

(6) The minimum reinforcement recommendations for ties of strut-and-tie model are on lower side than section design method.

## References

- [1] Schlaich, J., Schäfer, K., Jennewein, M. Towards a consistent design of structural concrete. PCI Journal 1987; 32(3):74-150.
- [2] SBC: 304 - 2007, Structural-Concrete Structures, Saudi Building Code, Structural Technical Committee (SBC-STC), Appendix-A, 2007.
- [3] SP-208. 'Examples for the Design of Structural Concrete with Strut-and-Tie Models'. American Concrete Institute, Michigan, USA, 2003, pp. 242.
- [4] Ahmed, M., Yasser A., Mahmoud H., Ahmed, A., Abdulla M. S., Nazar, S., (2013) Load Transfer Mechanism Based Unified Strut-and-Tie Modeling for Design of Concrete Beams, International J. of Civil Science and Engineering Vol:7 No:3, pp. 836-843.
- [5] Shuraim, A. B., 2013, Behavior and shear design provisions of reinforced concrete D-region beams, Journal of King Saud University – Engineering Sciences, 25, 65–74.
- [6] Ahmed, M., Khan, M.K.D., Wamiq, M., Application of Strut-and-tie Model to Analyze Complex Structural Members, IE (India) journal, 89, 2008, pp. 3-6.
- [7] B Singh, Y Mohammadi and S K Kaushik. 'Design of Double Corbel using the Strut-and-Tie Method'. Asian Journal of Civil Engineering, vol. 6, nos 1-2, 2005, pp. 21-33.
- [8] R. K. L. Su, P C W Wong and A M Chandler. 'Application of Strut-and-Tie Method on Outrigger Braced Core Wall Buildings'. Tall Buildings, 2002.
- [9] Park, W.J., Yindeesuk, S., Tjhin, T., Kuchma, D., Automated Finite-Element-Based Validation of Structures Designed by the Strut-and-Tie Method, J. Struct. Engrg. Vol. 136, 2, 2010, pp. 203-210.
- [10] Kuo, W.W., Cheng, T.J., Hwang, S.J., Force transfer mechanism and shear strength of reinforced concrete beams, Engineering Structures, 32, 2010, pp. 1537-1546.
- [11] Foster, S.J., Gilbert, R.I., 1999, "The Design of Non-flexure member with normal and high Density Concrete", ACI Structural Journal, V. 93, No. 1, pp. 3-10.
- [12] Zhi, Q. H., Zhao, L., Zhongguo, J. M., Investigation of Load-Transfer Mechanisms in Deep Beams and Corbels, ACI Structural Journal, V. 109, No. 4, July-August 2012.

# 14<sup>th</sup> Annual Research Day

Organised by the Deanship of Scientific Research in Collaboration with the College of Engineering  
Research Centre

4<sup>th</sup> April 2019

## A smart tower crane to improve safety in Masjid Al-Haram of Mecca

Mohamed Hechmi El Ouni<sup>1</sup>, Nabil Ben Kahla<sup>1</sup>, Rahmath Ulla Baig<sup>2</sup>, Saiful Islam Fakhru<sup>1</sup>, Amir Kessentini<sup>3</sup>, Mongi Zaidi<sup>4</sup>

<sup>1</sup>Department of Civil Engineering, College of Engineering, King Khalid University, PO Box 394, Abha 61421, KSA.

<sup>2</sup>Department of Industrial Engineering, College of Engineering, King Khalid University, PO Box 394, Abha 61421, KSA.

<sup>3</sup>Department of Mechanical Engineering, College of Engineering, King Khalid University, PO Box 394, Abha 61421, KSA.

<sup>4</sup>Department of Electrical Engineering, College of Engineering, King Khalid University, PO Box 394, Abha 61421, KSA.

E-mail address: melouni@kku.edu.sa

**Abstract:** Crane accidents under natural hazards are occurring with increasing frequencies in many sites around the world. In 2015, a crane collapse killing 111 and injuring more than 394 people in Mecca Grand Mosque was blamed on violent storms. In this paper, a smart tower crane is proposed to mitigate turbulent wind and prevent collapse. A dynamic analysis of the crane is investigated under turbulent wind excitation. The main contribution consists in implementing active tendons using pairs of force actuator-displacement sensor and using a robust control strategy based on decentralized Direct Velocity Feedback. Active damping is successfully provided and amplitudes of vibrations of the tower crane are attractively damped in all directions. It is concluded that the proposed smart tower crane model is adequate for turbulent wind mitigation and prevents its global stability which will increase the safety in crowded zones such as Grand Mosque of Mecca.

**Keywords:** Smart tower crane; Wind turbulence; Vibration; Active Tendon Control.

### 1. Introduction:

Tower cranes are widely used to cover the working area in different civil construction projects such as high-rise buildings, bridges, nuclear reactors, dams, stadiums, airports, etc... They are flexible spatial lattice structures and thus they are sensitive to vibrations induced by natural hazards (wind or earthquakes) which may cause their failure or overturning. Crane accidents under natural hazards are occurring with increasing frequencies in many sites around the world to reach more than 1125 documented accidents between 2000 and 2010 [1]. Recently in Saudi Arabia, a crane collapse killed 111 and injured more than 394 people in Mecca Grand Mosque blamed on violent storms [2].



**Figure (1)** Crane collapse in Grand mosque of Mecca, KSA.

Tower cranes have in general low structural damping, leading to challenges with respect to vibrations induced by natural hazards which affect the serviceability and cause structural damage and even failure. In general, vibrations of structures may be reduced by passive [3,4], semi-active [5] and active methods [6]. For more details about control strategies the papers reported by Korkmaz [7] and Ghaedi et al. [8] provided a

# 14<sup>th</sup> Annual Research Day

Organised by the Deanship of Scientific Research in Collaboration with the College of Engineering  
Research Centre

4<sup>th</sup> April 2019

detailed review of earlier and recent studies on vibration control of structures. Active control has the best performances compared to other strategies. It uses a set of actuators and sensors connected by a feedback or feed-forward loops [6]. Active tendon control [9-12] has high performances on the target mode and also acts indirectly on other modes. The stability is only guaranteed if the sensors are collocated with the actuators. Semi-active control performs significantly better than passive control, thus allowing an effective response reduction for different dynamic loading conditions but it is not better than the active control in term of performances. The cost of active control is very high when it is implemented on large heavy structures because they need large control efforts. But for very flexible steel structures such as tower cranes, the control forces will not be very high as in the case of Reinforced Concrete buildings or bridges. If the safety of pedestrians and workers is also taken as a priority, the active control strategy can be selected to reduce the vibrations of tower cranes even if it is more expensive than the semi-active control.

To the best of authors' knowledge, although control is widely applied on civil and mechanical domains, the active vibration control of the tower cranes under natural hazards has not been studied yet. The researchers have focused more on the control of the pay load which is reviewed by Ramli et al [13], but not on the control of the tower crane structure.

The present work is an initiative to investigate the vibration control of the tower crane from the structural point of view. The main objective is to prevent the collapse of the crane which will increase the safety in crowded zones such as Grand Mosque of Mecca. The design of a smart tower crane to mitigate natural hazards is presented. A Finite Element model of the smart crane is created. Then, dynamic analysis of the crane will be investigated under turbulent wind loads. The main contribution consists in

implementing active tendons using pairs of force actuator-displacement sensor and using robust a control strategy based on decentralized Direct Velocity Feedback.

## 2. Modeling of the smart tower crane equipped with an Active Mass Damping:

Assuming that the deformations of structural members are linear elastic, the governing equations of motion of the smart tower crane equipped with pairs of collocated force actuator and displacement sensor can be expressed as follows:

$$[M]\{\ddot{x}\} + [C]\{\dot{x}\} + [K]\{x\} = [B]\{^n F_{control}\} + \{W_{excit}\} \quad (1)$$

Where  $\{\ddot{x}\}$ ,  $\{\dot{x}\}$  and  $\{x\}$  are respectively the acceleration, velocity and displacement vectors.  $[M]$ ,  $[C]$  and  $[K]$  are the mass, the damping and the stiffness matrices of the smart tower crane expressed in a global coordinate system. These matrices are determined using the space truss formulation in Matlab/Structural Dynamic Toolbox.  $\{W_{excit}\}$  is the wind excitation force; it will be derived later in section 3.

$[B]$  is the influence matrix indicating the location of the active elements.

The vector representing the control forces of the decentralized DVF [14] are:

$$^n F_{cont} = -^n g (^n \dot{x}_i - ^n \dot{x}_j) = -^n g .s .(^n x_i - ^n x_j) \quad (2)$$

where  $^n g$  are the controller gains and  $(^n \dot{x}_i - ^n \dot{x}_j)$  and  $(^n x_i - ^n x_j)$  are respectively the relative velocities and displacements of extremities ( $i$  and  $j$ ) of the  $n$  active elements projected on their local axes;  $s$  is Laplace variable.

The state space representation is given by:

$$\dot{X} = \begin{Bmatrix} \dot{x} \\ \ddot{x} \end{Bmatrix} = \begin{bmatrix} 0 & I \\ -M^{-1}K & -M^{-1}C \end{bmatrix} \begin{Bmatrix} x \\ \dot{x} \end{Bmatrix} + \begin{bmatrix} 0 & 0 \\ M^{-1} & M^{-1}B \end{bmatrix} \begin{Bmatrix} W_{excit} \\ ^n F_{control} \end{Bmatrix} \quad (3)$$

$$Y = \begin{Bmatrix} x \\ \dot{x} \end{Bmatrix} = \begin{bmatrix} I & 0 \\ B^T & 0 \end{bmatrix} \begin{Bmatrix} x \\ \dot{x} \end{Bmatrix} + \begin{bmatrix} 0 & 0 \\ 0 & 0 \end{bmatrix} \begin{Bmatrix} W_{excit} \\ n_{F_{control}} \end{Bmatrix} \quad (4)$$

### 3. Wind model:

The dynamic wind velocity can be calculated as the sum of the laminar mean wind speed  $\bar{V}(z)$  and the fluctuating wind speed  $V_f(z,t)$  varying with height  $z$  and time  $t$  as shown in Figure 2. The fluctuating wind is a random dynamic load which follows a stochastic process [15]. The dynamic wind velocity is given by:

$$V(z,t) = \bar{V}(z) + V_f(z,t) \quad (5)$$

According to the Eurocode 1 (EN 1991-1-4:2005), the mean wind velocity  $\bar{V}(z)$  depends on the terrain roughness  $C_r(z)$  and orography  $C_0(z)$  (recommended value is 1) and on the basic wind velocity  $V_b$  defined at 10m above ground. The mean wind velocity can be expressed as follows:

$$\bar{V}(z) = C_r(z) \cdot C_0(z) \cdot V_b \quad (6)$$

$$V_b = C_{dir} \cdot C_{season} \cdot \ln\left(\frac{z}{z_0}\right) \quad (7)$$

Where:  $C_{dir}$  is the directional factor;  $C_{season}$  is the season factor;  $z_0$  is the roughness length.

$$C_r = 0.19 \left(\frac{z_0}{0.05}\right)^{0.07} \quad (8)$$

A commonly used model proposed by Kaimal et al [16] is adopted for the turbulent wind simulation. The power spectral density function of the longitudinal wind velocity fluctuations at different heights is expressed as follows:

$$S(\omega, z) = \frac{200}{2\pi} u_*^2 \frac{z}{\bar{V}(z)} \cdot \frac{\omega}{\left[1 + 50 \frac{\omega \cdot z}{2\pi \bar{V}(z)}\right]^{5/3}} \quad (9)$$

Where:  $u_*$  is the shear velocity that depends on the characteristics of the soil, it is given by  $u_* = k_r k_a \bar{V}(10)$ ;  $k_r$  is the terrain factor and  $k_a$  is

the Von Karman constant equal to 0.4;  $\omega$  is the wind frequency,  $z$  is the height.

According to the theory of Shinozuka (1972), the velocity time series of fluctuating wind  $V_f(z,t)$  can be determined by:

$$V_f(z,t) = 2 \sum_{m=1}^h \sum_{l=1}^N |H_{jm}(\omega_{ml})| \sqrt{\Delta\omega_{ml}} \times \cos\left[\omega_{ml} \cdot t - \theta_{jm}(\omega_{ml}) + \phi_{ml}^i\right] \quad (10)$$

where :  $\omega_{ml} = l\Delta\omega_{ml} - \frac{N-1}{N}\Delta\omega_{ml}$  is the wind frequency.  $\Delta\omega_{ml}$  is the wind frequency increment,  $N$  is the total number of division of wind frequency ( $m=1,2, \dots,h$ ),  $h$  is the number of different levels of wind application on the tower crane ( $l=1,2, \dots,N$ ),  $H_{jm}$  is the transform matrix calculated based on the Cholesky decomposition of the wind cross spectral density matrix [17].  $\theta_{jm}$  is the phase angle between two different points of wind load application.  $\phi_{ml}^i$  is the uniform random number in  $[0, 2\pi]$ .

The mean wind speeds at 10 m height is 152km/h (in Mecca, KSA). Figure 2 shows a simulated field of fluctuating wind speed at different points.

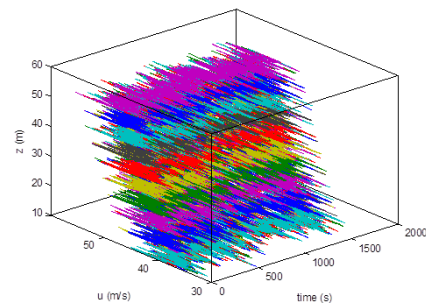


**Figure (2)** The wind velocity as a function of time for different levels

The along-wind loads are applied on all nodes of the tower according to the height. They are given by

$$W_{excit} = F(z, t) = \frac{C_x \cdot A \cdot V(z, t)^2}{1.6} \quad (11)$$

Where  $C_x$  is the drag coefficient which is equal to 2.5 for tower cranes (latticed structure).  $A$  the effective wind exposed area reported to the corresponding node.

## 4. Numerical Example

### 4.1 Description of the smart tower crane

The mast of the smart tower crane has a total height equal to 55 m and a square cross-section of 1.948m x 1.948m. The length of the jib is 45.87 m and the length of the counter jib is 16.03m. Both they have a triangular cross-section 1.174m x 1.404m (base x height). Angle sections are used for the mast of the crane and hollow tubes are used for the jib. Solid round bars of diameter 40 mm are used for the three supporting tensile tendons. Four brackets with hollow tubes are added at the bottom of crane (TRON 300x30). The material Steel E42 is used. The young's modulus is equal to 210 GPa. The density is 7850 kg/m<sup>3</sup>. The dimensions and sections of the mast and jib elements are detailed in Figure 4. The counter balance is equal to 10 tons. The natural damping of the tower crane is supposed to be 1%.

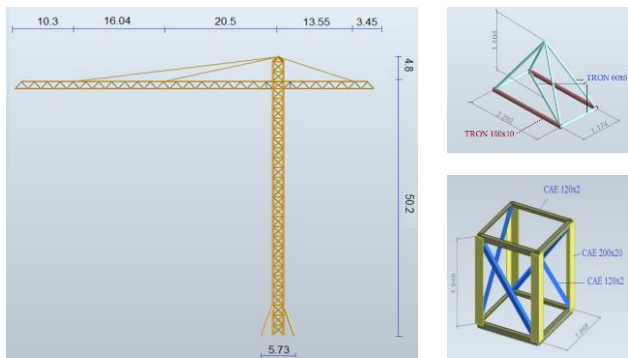


**Figure (3)** Dimensions (in [m]) and sections (in [mm<sup>2</sup>]) of the tower crane.

### 4.2 Active elements

The concept of the active element is presented in Figure 4. It contains a force actuator and 2 displacement sensors on the extremities of the

selected element with a Direct Velocity Feedback control law. The relative displacement between the extremities  $i$  and  $j$  projected on its axial line are sensed and feedback to the force actuator implemented at its lower end. In fact, the sensed displacement is differentiated and multiplied by a controller gain  $g$  to determine the control force to be feedback into the actuator. The controller gain is optimized using the root locus technique. Figure 4 shows the location of the selected active elements.

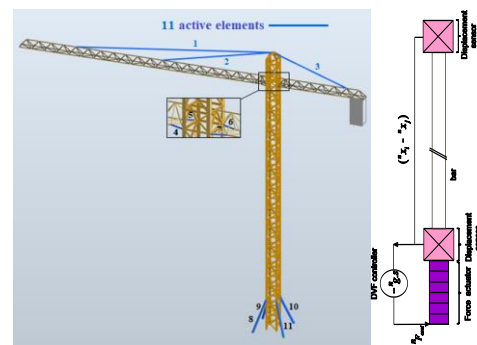


**Figure (4)** Location of the active elements and concept of active element

The active damping is added to the tower crane through 11 elements as follows:

- Three tension tendons connecting the jib to the top of the crane which are responsible for the control of the vertical vibrations of the jib.
- Four horizontal struts of the jib to control the lateral vibrations of the jib.
- Four brackets to control directly the in-plane and out-of-plane mast vibrations and indirectly the vertical vibrations of the jib.

## 5. Results and discussion

Two different wind directions shown in Figure 5 are considered: Y direction (horizontal to the crane) and X direction (lateral to the crane). The X direction produces large lateral displacements of the mast and the jib. The displacements of the top node (119) in X direction with and without control are plotted in Figure 6. The four active brackets implemented in the bottom of the tower crane are responsible for

the vibration control of the crane mast. Critical damping is obtained for the lateral displacement of the crane mast. The large displacement of the jib shown in Figure 6 is due to the torsion of mast combined with the lateral displacement of the jib. The four active brackets reduced the torsion of the mast around Z axis and the four active bars (n<sup>o</sup>: 4, 5, 6 and 7) reduced the lateral displacement of the jib. Figs.19. b and c show the lateral displacements of node 204 and 120 of the jib and counter jib respectively with and without control. Attractive control results of the lateral displacements of the tower crane are obtained.

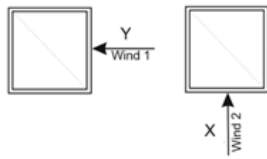


**Figure (5)** Wind directions with respect to the tower's cross section.

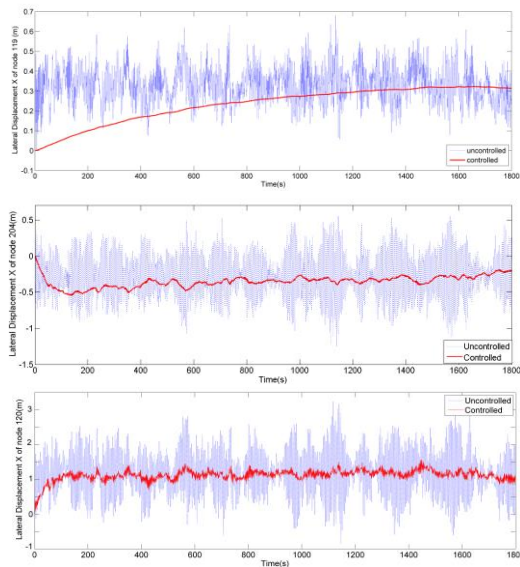


**Figure (6)** Lateral response of the tower crane under wind excitation in X direction.

The tower crane is also horizontally excited in Y direction. The horizontal and vertical displacements of the crane at the critical nodes 119, 120 and 204 are recorded for both cases of the structure with and without control as shown in

Figure 7. Again the active brackets play an important role in controlling the mast. The three active tendons (n<sup>o</sup>: 1, 2 and 3) reduce the vibrations of the jib and counter jib. The horizontal displacement of node 119 and the vertical displacements of nodes 120 and 204 are well controlled. In general, the proposed model of the smart tower crane showed incredible capabilities in controlling the tower crane vibrations in all directions. In many big cities, tower cranes are required for the rehabilitation of old monuments and constructions of modern buildings in the center of the town where the number pedestrians is high during the rush hours. So, the collapse of a tower crane will be catastrophic. The proposed smart crane may solve forever the problems of crane collapse due to turbulent wind and by the way improves the safety in crowded zones such as the grand mosque of Mecca, KSA.

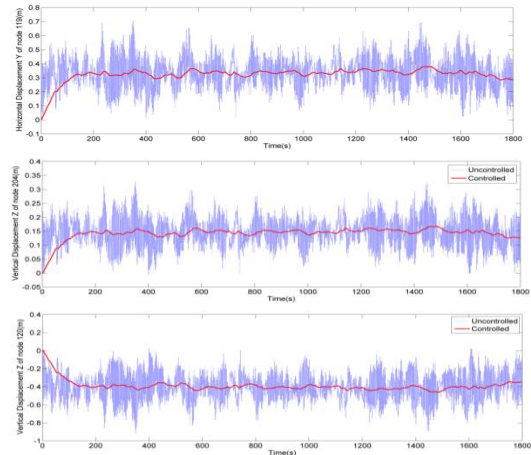


**Figure (7)** Response of the tower crane under wind excitation in Y direction.

## 6. Conclusions

A smart tower crane equipped with pairs of sensors and actuators is proposed to prevent its collapse due to turbulent wind. A 3D Finite Element model of the crane is proposed. A decentralized active vibration control method is presented to reduce the vibrations of the crane. Active damping is added to the system by using

# 14<sup>th</sup> Annual Research Day

Organised by the Deanship of Scientific Research in Collaboration with the College of Engineering  
Research Centre

4<sup>th</sup> April 2019

pairs of force actuator- displacement sensor located on selected elements and a robust control strategy based on decentralized Direct Velocity Feedback. The proposed model of the smart tower crane showed incredible capabilities in controlling the tower crane vibrations in all directions. The proposed smart tower crane will indeed increase the safety in crowded ones such as the grand mosque of Mecca. As a future work, Semi-Active control using Magneto-Rheological dampers will be applied to reduce the cost of active control.

## Acknowledgments

The authors gratefully acknowledge the project support (G.R.P-82-39) provided by Deanship of Scientific Research, King Khalid University, Abha, Kingdom of Saudi Arabia and also being thankful for providing the facilities required for the successful completion of the project.

## References

- [1] [http://www.towercranesupport.com/tower\\_crane\\_accidents.php](http://www.towercranesupport.com/tower_crane_accidents.php)
- [2] Gul F.A., Ali C.M. 2016, Saudi Crane Collapse Masjid al-Haram (Lack of Safety). *J. Social Sci. Hum. Res.* vol1 (8): 129-140.
- [3] Ormondroyd J. and Den Hartog J.P., .The theory of the damped vibration absorber., *Trans. ASME, J. App. Mech.*, 50:7, 1928.
- [4] Soong TT, Dargush GF. *Passive Energy Dissipation Systems in Structural Engineering*. Chichester: Wiley and Sons Ltd; 1997.
- [5] Karnopp D., Crosby M.J and Harwood R.A., .Vibration control using semi-active force generators. *J. Eng. Industry*, 1974; 96 (2): 619-626.
- [6] Preumont A, Seto K. *Active control of structures*. Wiley & Sons, , U.K., 2008.
- [7] Ghaedi K, Ibrahim Z, Adeli H, Javanmardi A. Invited Review: Recent developments in vibration control of building and bridge structures. *J. Vibroengin.* 2017, 19, 3564-80. Doi : 10.21595/jve.2017.18900
- [8] Korkmaz S. A review of active structural control: challenges for engineering informatics. *Computers & Structures.* 2011, 89, 2113-32. Doi: 10.1016/j.compstruc.2011.07.010
- [9] Preumont A, Voltan M, Sangiovanni A, Mokrani B, Alaluf D. Active Tendon Control of Suspension Bridges. *Smart Struct Syst.* 2016;18:31-52.
- [10] El Ouni M. H., Ben Kahla N., Preumont A., (2012) "Numerical and experimental dynamic analysis and control of a cable stayed bridge under parametric excitation". *J. eng. struct.* vol 45:244-256.
- [11] El Ouni M. H., Ben Kahla N., (2014) "Active tendon control of a Geiger dome". *J. vib. cont.* Vol. 20(2) 241–255.
- [12] El Ouni M. H., Ben Kahla N., (2014), "A numerical study of the active tendon control of a cable stayed bridge in a construction phase". *Sp. Issue of J. shock vib*, dx.doi.org/10.1155/2014/937541
- [13] Ramli L, Mohamed Z, Abdullahi AM, Jaafar HI, Lazim IM. Control strategies for crane systems: A comprehensive review. *Mech Syst Sign Process.* 2017;95:1-23.
- [14] Balas M., Direct velocity feedback control of large space structures, *J. Guid. Cont. Dyn.*, 2(1979), 252-253.
- [15] Suksuwan A, Spencer SMJ. Optimization of uncertain structures subject to stochastic wind loads under system-level first excursion constraints: A data-driven approach. *Comput Struct.* 2018;210: 58-68.
- [16] Kaimal, J., Wyngaard, J., Izumi, Y. and Coté, O. (1972). Spectral characteristics of surface-layer turbulence. *Q.J Royal Met. Soc.*, 98(417), pp.563-589.
- [17] Shinozuka M. Monte Carlo solution of structural dynamics. *Comput Struct.* 1972;2: 855-874.

# 14<sup>th</sup> Annual Research Day

Organised by the Deanship of Scientific Research in Collaboration with the College of Engineering  
Research Centre

4<sup>th</sup> April 2019

## Investigation of Geology and Hydro-geophysical Features Using Electromagnetic and Vertical Sounding Methods for Abu Zabad Area, Western Kordofan State, Sudan

Elhag A. B<sup>1</sup>

<sup>1</sup>Department of Civil, College of Engineering, King Khalid University,  
PO Box 394, Abha 61411 KSA.

E-mail address: abalhaj@kku.edu.sa

**Abstract:** The geology and hydro-geophysical features can aid in identifying borehole location. The study aims to investigate groundwater aquifers and best location of boreholes in the crystalline basement area of Abu Zabad near El Obeid Southwest, Sudan. The study area is underlain by two aquifers formations from Precambrian age. The oldest units of basement complex of area under investigation consists of metamorphic rocks including gneiss, schist, and quartzite.

The geophysical methods electromagnetic (EM) and vertical electrical sounding (VES) showed that best aquifers for construction of boreholes are in weathering and fractures formation. The EM results revealed that structural features are significant for groundwater potential and interpretation of the VES data also revealed four geo-electric layers, but generally two distinct lithologic layers, which include Superficial deposit and bedrock-basement respectively. The curves generated from the data revealed H curve and HK curve, and thickness of these layers varies from 15 m to 50 m in the area. The aquifer thickness range from 20 m to 30 m. The Electro-magnetic (EM) profiling and Vertical Electrical Soundings VES (Schlumberger sounding) data from the area were interpreted to delineate subsurface lithology, groundwater potential and identify borehole location at low resistivity of the weathered/fractured aquifer layers. The study concludes that these techniques are suitable for identifying borehole location in the basement rock in Abu Zabad Area Sudan.

**Keywords:** Borehole, aquifer, electromagnetic profiling, geo-electric, groundwater potential.

### 1. Introduction:

This paper focus on the geology and groundwater resources of western Sudan in terms of aquifers properties, investigated area includes Abu Zabad area which lies within Western Kordofan State. The target area is characterized by undulating topographical surfaces mostly covered by sand dunes and gentle slopes to the east of Torda (watercourse). It covers an area of about 25 Km<sup>2</sup> and lies between Latitudes 12° 20'–12° 38' N and Longitudes 29° 28' – 29° 45' E (Figure 1). The rainfall generally occurs in summer season, with maximum in the month of August. The prevailing winds blow from the south during summer, and blow north during winter. The average of temperatures ranges between 30°C in January and 48°C in June.

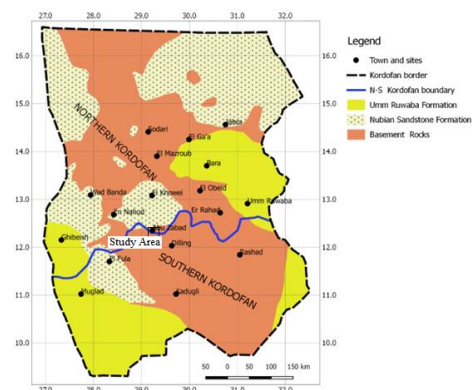


**Figure (1)** Distribution of pre-Quaternary geological units in the Kordofan Region (from Lineaments provide the pathways for groundwater movement in hard rock areas (Biswas et al., 2012, Biswas et al., 2013). Furthermore, in order to locate favorable sites for groundwater exploration a lineament density map

was prepared as suggested by (Sree Devi et al., 2001). The movement and occurrence of groundwater depends mainly on the secondary porosity and permeability resulting from faulting and fracturing etc. (Elhag, 2016). In October 1966 and 1973, Kordofan State was shaken by strong earthquakes that have great attention to hydrology due to a few of groundwater wells in the aquifer are dry (Elhag and Elzien, 2013). In study area geological formation is exposed in the eastern part of Torda (Precambrian age). They are predominantly massive and compact of schist and gneiss metamorphic rocks (Figure 4).

Surface geophysical survey is a veritable tool in groundwater exploration, owing to its economy in borehole construction by identifying borehole location prior to drilling (Obiora and Ownuka, 2005). Hydrogeophysical study is very important in basement rocks areas and considered a priority in many groundwater prospections. Many geophysical methods used in basement areas, but the electrical resistivity (ER) method is essential tools (Gautam, and Biswas, 2016).

The electromagnetic (EM) and vertical electrical sounding (VES) survey used in this work for locating the aquifers extension (Sharma, and Baranwal, 2005). The two most common arrays used for VES are Wenner array and Schlumberger array (Steve, 2017). This method is regularly used to solve a wide variety of groundwater problems such as determination of depth, thickness and boundary of aquifer, determination of zones with high yield potential in an aquifer, determination of the boundary between saline and fresh water zones and estimation of aquifer transmissivity and in environmental problems as well (Acharya, et al., 2018, Biswas, and Sharma, 2017, Parial et al., 2015, Sharma, and Biswas, 2013, Hadi, 2009).

The objective of the study is to recognize water-bearing formations in study area, and to examine suitable and available resources of groundwater. The main rocks characterization and recognition of aquifers, lateral and vertical extensions useful for drilling boreholes, as well as the main

objectives of the geophysical survey in the study area are as follows:-

- Determine anomalous (conductive) zones.
- Determine fractures, faulting and similar rock deformations which play an important role in sub-surface hydrology of the area (water movement and recharge).

## 2. Materials and Methods:

### 2.1 Materials

The study employed two direct current (DC) methods: Vertical Electric Sounding (VES) and electromagnetic (EM). In both electric potentials produced by (DC) current injected by two electrodes is measured by another pair of electrodes. VES technique employed Schlumberger array, which is particularly efficient when main resistivity gradient is in vertical direction. The electromagnetic (EM) array is more suitable to study grounds with lateral resistivity variation.

The vertical electrical sounding and electrical profiling methods are based on four-electrode principle as shown in (Figure 2). The electrical current ( $I$ ) is applied to A and B electrodes and the potential ( $\Delta U$ ) is measured between M and N electrodes. The bulk soil electrical resistivity ( $ER$ ) is calculated with:

$$ER = K \frac{\Delta U}{I} \dots \dots \dots (1)$$

Where:  $K$  = is the geometric factor.

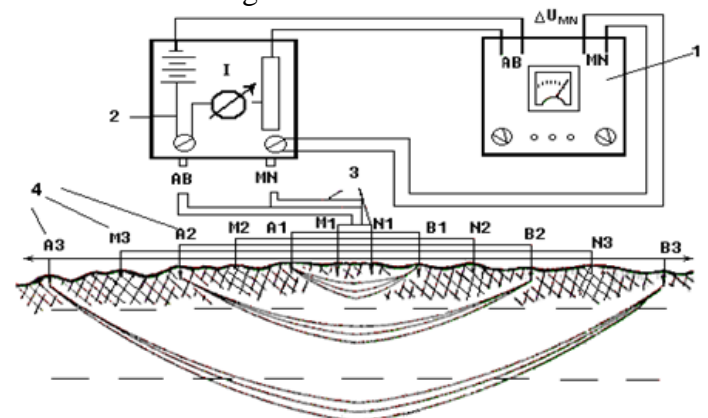


**Figure (2)** Two current and two potential electrodes on the surface of ground of resistivity.

## 2.2 Experimental Procedure

The study area lies South of Central African Shear Zone (CASZ). The Torda basin Complex is main basin in study area and in general trending North to South. The Torda basin, located in Eastern extension of Abu Zabad town (Figure 3). The basement complex is divided into three groups which include weathering, fracture and tide crystalline rocks. Hydrogeological and lithological log have been studied and evaluated to characterize aquifer potentials, and suitable sites for several wells were selected in Torda basin to define aquifers extensions (Figure 3). Geologically, Torda basin Complex is composed of two major basins, named weathering and fractures basement regolith. The groundwater occurs in drilled wells in weathering and fractures basement regolith.

The target area is generally an undulating plain of low relief with altitude ranging range from 610 to 616 m above mean sea level, and major drainage system in study area Khor El Ganam, Khor Sheween and Wadis and ground surface slopes gently to east towards Torda.

The regional geologic map of the study area is composed of igneous and metamorphic rocks surrounded by Paleozoic and Cretaceous sedimentary rocks. The Precambrian rocks are extending southward from the valley of Abu Zabad through subdued topographic basin drained by Torda.

In Eastern Abu Zabad city (Fig. 3), groundwater extraction from hand dug wells (shallow boreholes) and deep boreholes around the water pool (Torda) is used for drinking and irrigation. The geological logs from the surface down to 53 m depth revealed that the structural features consist of Superficial deposits, and bedrock-basement. The individual thickness of these layers varies from 5 m to 10 m in the area (Figure 4). The main aquifer appears at depths below 20 m, composed of fragment of metamorphic and igneous rocks.

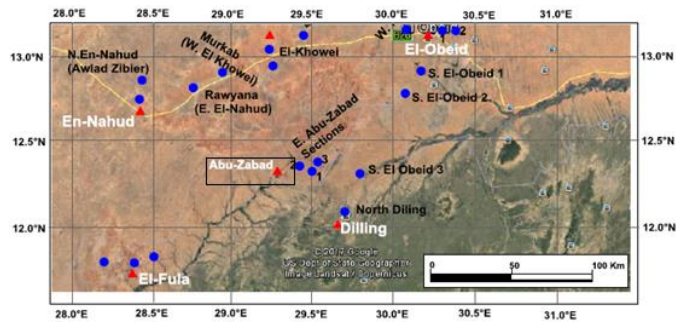


**Figure (3)** Geomorphological map of the study area. (from Dawelbeit, 2018).

## 3. Results and Discussion

The geological setting of the study area consists of superficial deposits and Precambrian basement rocks. The sediments exposed in Northern part are mostly Cretaceous in age belong to the Wadi of Ger Ellassal formation. They are dominated by fine to coarse grained cross-bedded fluvatile sandstones forming. The Precambrian basement rocks consist of gneisses, schists and quartzites (Figure 4). The weathered and fractured basement rocks constitute major aquifers or aquitards.

The degree of weathering is one of the most significant factors controlling the type and abundance of clay minerals (Duzgoren-Aydin et al., 2002). In basement rock of study area percentage of clay minerals is proportional with intensity and time interval of weathering (Figure 4). Whereas, weathered and fractured basement rocks constitute the major aquifers or aquitards.



**Figure (4)** Weathering and fractured profile on genesis of Abu Zabad (Torda). Photograph with the author (May, 2018).

### 2.1. Resistivity method:

The resistivity method data indicates variation in groundwater potential because rock formation is

# 14<sup>th</sup> Annual Research Day

Organised by the Deanship of Scientific Research in Collaboration with the College of Engineering Research Centre

4<sup>th</sup> April 2019

not isotropic. The resistivity and thicknesses of geo-electric/lithology layers within the subsurface are presented in figure (7). The profiles and curves generated for apparent resistivity data using surfer-8 and IPI2win softwares are presented in figure (6 and 7), and the geo-electric section for the study area is presented in figure (8). The most of the VES curves coverage to the basement complex represented by the types H and KH, these types are very important from the qualitative interpretation point of view, which increases at right branches of sounding curves often rises at an angle of 45° owing to influence from tight basement rock, that usually indicates igneous or metamorphic rocks (granite, schists and gneisses rocks) of very high resistivity which called typical basement complex, that observed in the geo-electrical curves (Figure 7).

The VES curve revealed five resistivity layers for traverse at the crack or point (7) from EM Profile figures (5 and 6). The first layer mixed with superficial deposits composed of sand with clay lenses. The resistivity of this layer range from 50 to 63 ohm.m and the thick reach about 2-10 m. The weathered and fractured basement complex forms the second layer. The resistivity range between 25 to 150 ohm-m and thickness reach about 42 m, ended by hard basement complex which are shows increase in the resistivity value attains 1400 Ωm (Figure 8).

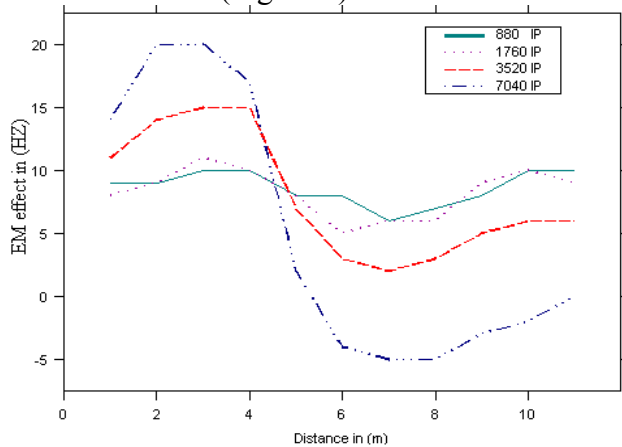


**Figure (5)** EM survey conducted in basement complex in the study area.

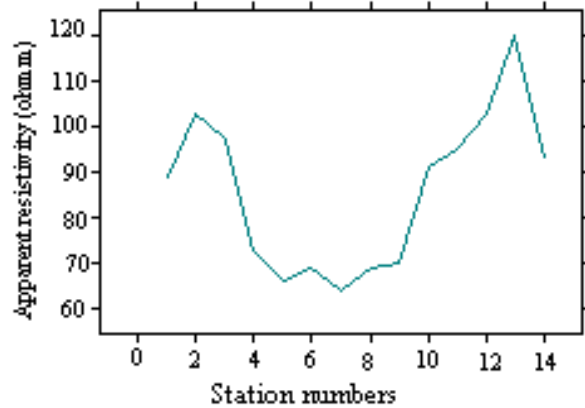


**Figure (6)** Horizontal electrical profiles showing variation in the basement complex.

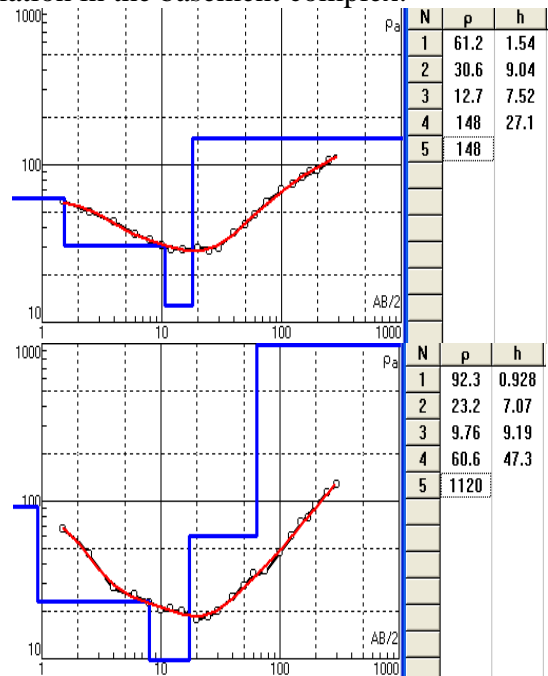


**Figure (7)** Vertical electrical sounding curves for detection of water-bearing formations.

# 14<sup>th</sup> Annual Research Day

Organised by the Deanship of Scientific Research in Collaboration with the College of Engineering Research Centre

4<sup>th</sup> April 2019

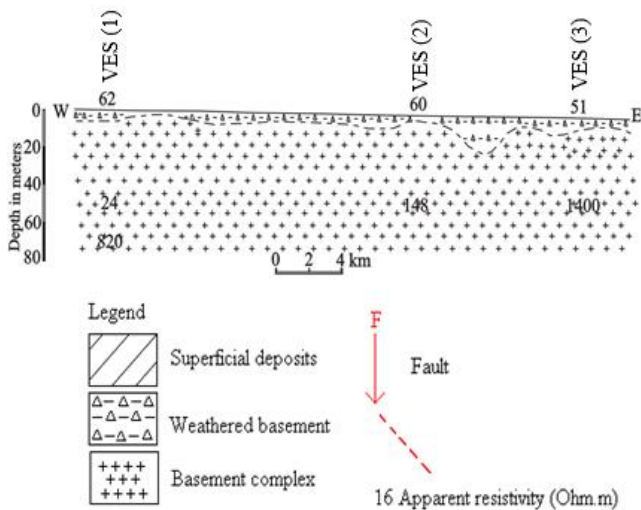


**Figure (8)** Shows that traverse of EM and three points of VES.

To recognize the two aquifers at different depths, the lithological analysis of well logs is useful for obtaining variations of weathering and fractured basement rocks (Figure 4). The water table marks of aquifer are underlain by an unsaturated zone which composed of superficial deposits, and thickness of unsaturated zone above aquifer is about 20 m to groundwater table. In Torda towards east, water table is the shallowest (about 15 m) and therefore unsaturated zone is a thin layer. The total thickness of the aquifer varies from 30 m in the eastern part to 10 m in the west with an average thickness of about 20 m.

Annual groundwater level fluctuations related to groundwater recharge and discharge in the aquifer system. Direct reflected in variations of groundwater level when recharge exceeds discharge, water table levels will rise and when discharge exceeds recharge, they will fall. Whereas, two types of fluctuations are recorded, which include either seasonal or diurnal ones. The water level in study area fluctuates in response to variation in recharge periods, rise due to the seasonal rainfalls and decline in the summer and during droughts in response to a decrease in groundwater recharge from precipitation. The influence of the recharge extends to certain distances and then becomes negligible. Seasonal groundwater level fluctuations have been studied with the help of monthly water level data of

twelve hydrograph stations for more than 30 months of observation wells, the measuring and monitoring records has been started in June 1964 (27.50 m), July (25.72 m) up to November 1964 (14.13 m) respectively and according to the U.N report (DOX-SUD-A 39, 1965). Groundwater quality is saline in the western area where is low recharge, but in eastern area (Torda basin) is good quality occurs; the total dissolved solids (TDS) range between 300 to 600 mg/l, and groundwater is suitable for drinking and irrigation purposes.

Several pumping tests that were conducted at different wells in the study area to determine the hydraulic properties of the aquifer. The base of the aquifer is at the depth of range from 20 m to 30 m, and the yield about borehole about 2500 g/h.

## 4. Conclusions:

The study area composed of two aquifers weathered and fractured basement rocks, both aquifers are found at relatively in the Torda Basin in the East direction. Groundwater recharge by the flood of many Khors; Khor El Ganam, Khor Sheween and Wadis respectively. Groundwater salinity progressively increases with the low recharge.

This study investigated the groundwater potential and aquifer extension, western Kordofan state, Abu Zabad, Sudan. Electromagnetic and vertical electrical sounding using the Schlumberger array configuration were carried out. Analysis and interpretation of EM and VES data obtained from the study area showed profile 1 and 2, and VES 3 and VES 5 to be locating the successful for borehole drilling due to low resistivity of the weathered and fractured aquifer layers coupled with the relatively high thicknesses of the weathered layers. It is therefore recommended that for future groundwater exploration in the study area, geophysical prospecting should be taken to locate the best site for groundwater drilling.

## Acknowledgement

# 14<sup>th</sup> Annual Research Day

Organised by the Deanship of Scientific Research in Collaboration with the College of Engineering  
Research Centre

4<sup>th</sup> April 2019

This study was sponsored by King Khalid University, the authors would like to express their gratitude to King Khalid University, Saudi Arabia for providing administrative and technical support.

## References

- [1] T. Acharya, A. Biswas, A. Bhattacharyya, A. Chakraborty, M. Chakraborty, and M. Sarkar, Vulnerability mapping of saline water intrusion in coastal aquifers of West-Bengal, India using flow-net approach. *Indian Groundwater* 10, (2018) P. 46-56.
- [2] A. Biswas, and S.P. Sharma, Geophysical surveys for identifying source and pathways of subsurface water inflow at the Bangur chromite mine, Odisha, India. *Natural Hazards* 88 (2), (2017) P. 947-964.
- [3] A. Biswas, A. Jana, A. and A. Mandal, Application of Remote Sensing, GIS and MIF technique for Elucidation of Groundwater Potential Zones from a part of Orissa coastal tract, Eastern India. *Research Journal of Recent Sciences* 2 (11), (2013) P. 42-49.
- [4] A. Biswas, A. Jana, and S.P. Sharma, Delineation of groundwater potential zones using satellite remote sensing and geographic information system techniques: a case study from Ganjam district, Orissa, India. *Research Journal of Recent Sciences* 1 (9), (2012) 59-66, Available online at: [www.isca.in](http://www.isca.in).
- [5] A. Dawelbeit, Late Quaternary Sedimentary and Paleoclimatic Evolution of Kordofan, Sudan, Ph.D. Dissertation for the doctorate degree of the Université Grenoble Alpes, France. (2018) 78.
- [6] N.S. Duzgoren-Aydin, A. Aydin, and J. Malpas, Distribution of clay minerals along a weathered pyroclastic profile, Hong Kong. *Catena*, 50, (2002) P. 17-41.
- [7] A.B. Elhag, Application of Remote Sensing and Geo-Electrical Method for Groundwater Exploration in Khor Al Alabyad, North Kordofan State, Sudan. *American Journal of Earth Sciences*.<http://www.openscienceonline.com/journal/archive2?journalId=715&paperId=2914>. (2016)
- [8] A.B. Elhag, and S.M. Elzien, Structures Controls on Groundwater Occurrence and Flow in Crystalline Bedrocks: a case study of the El Obeid area, Western Sudan. *Global Advanced Research Journal of Environmental Science and Toxicology* (ISSN: 2315-5140) Vol. 2(2) p. 037-046. Available online <http://garj.org/garjest/index.htm>. (2013), 77.
- [9] P. Gautam, and A. Biswas, 2D Geo-electrical imaging for shallow depth investigation in Doon Valley Sub-Himalaya, Uttarakhand, India. *Modeling Earth Systems and Environment* 2 (4), (2016) p.175.
- [10] T.N. Hadi Geoelectrical Investigation of the Aquifer Characteristics and Groundwater Potential in Bahbadan Azad University Farm, Khuzestan province, Iran. *Journal of Applied Sciences*. ISSN: 1812 – 5654. 9(20); (2009) P. 3691-3698.
- [11] D.N. Obiora, and O.S. Ownuka, Groundwater Exploration in Ikorodu, Lagos-Nigeria: A Surface Geophysical Survey Contribution, University of Nigeria, Nsukka. *The Pacific Journal of Science and Technology*, Volume 6. Number 1, (2005) p. 86 – 93, <http://www.akamaiuniversity.us/PJST.htm>
- [12] K. Parial, A. Biswas, S. Agrahari, S.P. Sharma, and D. Sengupta, Identification of contaminated zones using direct current resistivity surveys in and around ash ponds near Kolaghat Thermal power plant, West Bengal, India. *International Journal of Geology and Earth Sciences* 1 (2), (2015) P. 55-64.
- [13] H.G. Rodis, A. Hassan, L. Wahadan, Groundwater Geology of Kordofan Province-Sudan, Contribution to the hydrology of Africa and Mediterranean Region. United State government printing office. Washington. (1968) p. 45.
- [14] S.P. Sharma, and A. Biswas, A practical solution in delineating thin conducting

# 14<sup>th</sup> Annual Research Day

Organised by the Deanship of Scientific Research in Collaboration with the College of Engineering  
Research Centre

4<sup>th</sup> April 2019

---

- structures and suppression problem in direct current resistivity sounding. *Journal of earth system science* 122 (4), (2013) P. 1065-1080.
- [15] S.P. Sharma, and V.C. Baranwal, Delineation of groundwater-bearing fracture zones in a hard rock area integrating very low frequency electromagnetic and resistivity data. *Journal of Applied geophysics* 57 (2), (2005) P. 155-166.
- [16] P.D. Sree Devi, S. Srinivasulu, and K.K. Ragu, Hydro-geomorphological and groundwater prospects of the Pageru river basin by using remote sensing data. *Environmental Geology*, 40, (2001) p. 1088-1094.
- [17] C. Steve, Electrical Resistivity technique for Subsurface Investigation. (2017) p. 12.
- [18] U.N.S Special 92 Fund (DOX - SUD - A 39), United Nations Special Fund, F.A.O Land and Water Use Survey in Kordofan Province, Sudan. Reports of the following notations:- DOX - sun – A 39. (1965).
- [19] K. Van Daele, Characterization of geological materials, their weathering products and their relationship with soils in the Gilgel Gibe catchment, SW Ethiopia. Ghent University, Belgium. (published M.Sc. in geology), (2011) p. 14.

# 14<sup>th</sup> Annual Research Day

Organised by the Deanship of Scientific Research in Collaboration with the College of Engineering  
Research Centre

4<sup>th</sup> April 2019

---

## Linear Crack Simulation in Concrete Beam Using Finite Element Modelling

Sivakumar Anandan

Faculty of Civil Engineering, College of Engineering, KKU  
E-mail address: ksiva@kku.edu.sa

---

**Abstract:** The present study deals with the generation of finite element model of plain & reinforced concrete beam in 2D and 3D models with different boundary conditions and the simulation of crack propagation under monotonic loading simulated using FEM-ANSYS software and validation was carried out using theoretical analysis up to 2D plane element using MATLAB. Since cracking decreases the durability of RCC members, it is necessary to develop cracking model to predict the load deformation behavior of RCC member to reduce the number of time consuming and expensive experimental tests. In the analysis, the behavior of member is described with plane stress condition. In the generation of 2D beam, concrete & steel is considered with single plane element with different material property and in generation of 3D RCC beam, the concrete & steel is modeled as separate element & material models which are combined together with a model of the interaction between reinforcing steel and concrete through bond-slip to describe the behavior of the composite reinforced concrete material. In this concrete is assumed as linear elastic material in which the linear crack starts to propagate within the initial yield surface and the stress strain behavior of concrete is considered during the generation of 3D beam in ANSYS. The study of crack propagation is described by a system of linear cracks, followed by the principal strain direction. A finite element model of crack propagated in a plain & RCC beam is derived based on the analysis of principal stress. The beam is discretized into various finite elements, after the application of incremental loading the crack trajectory is mapped at the points where the maximum principal stress exceeds the permissible tensile stress of concrete. In the study, the accuracy of discretization, stress contours and nodal displacement are discussed. Finally the simulation of crack under monotonic loading in different boundary condition is analyzed and is validated theoretically using mathematical application software..

**Keywords:** *main keywords are added not exceeding 6 words.*

---

### 1. Introduction:

The finite element method is the way of getting numerical solution for the specific problems, it involves cutting the structure into several pieces & describing the behavior of each element in a simple way and reconnecting the entire element to analyze the whole structural behavior. In simple FE method regards as piecewise polynomial interpolation; it involves major part as mathematical calculations, as integration, equation solving & higher order matrix problems [1-3]. Because of its simplicity & diversity it

attains its more attention in major engineering problems. The finite element method a powerful computational tool, which allows complex analyses of the linear & nonlinear response of RC structures, is carried out in a usual numerical analysis method [4-7]. With this method the importance and interaction of different nonlinear effects on the response of RC structures has studied analytically [8-10]. These analytical study endeavors the use of finite element based software. Now a days large number of finite element softwares like SAP 2000, LUCAS, ABAQUS, ANSYS, etc., are available. In the

present study, an attempt has been made with ANSYS software to bring into focus the versatility and powerful analytical capabilities of finite elements technique by objectively modelling the complete response of concrete beam elements with different loading & boundary conditions. Prediction of Crack in concrete is investigated by application of finite element method coupled with Linear Elastic Fracture Mechanics (LEFM) and the Boundary Element Method (BEM). A Numerical model of 3D RCC beam element is analyzed for smeared crack based on non linear elastic behavior using FEM concepts.

## 2. Modelling of Discrete cracks

### 2.1 Crack envelope

The need for a crack model that offers automatic generation of cracks and complete generality in crack orientation, without the need of redefining the finite element topology, has led the majority of investigators to adopt the smeared crack model. Rather than representing a single crack, the smeared crack model represents many finely spaced cracks perpendicular to the principal stress direction. This approximation of cracking behaviour of concrete is quite realistic, since the fracture behaviour of concrete is very different from that of metals. In concrete fracture is preceded by micro cracking of material in the fracture process zone, which manifests itself as strain softening. In the present study the discrete crack modelling was carried by stress analysis, the basis of fracture mechanics is not considered which can be carried in the future study while crack modelling carried under cyclic loading.

### 2.2 Theoretical crack analysis

The general procedure involved in FEM for 2D stress analysis is described as follows:

- i. Select suitable field variables and the elements.
- ii. Discretization.

- iii. Selection of interpolation functions.
- iv. Determining the element properties.
- v. Assembling element properties to get global properties.
- vi. Applying boundary conditions.
- vii. Solving the system equations to get the nodal unknowns.
- viii. Additional calculations to determine the nodal & element stresses.

### 2.3 Geometric property

In the generation of 2D modeling the size of concrete beam considered (as given in **Figure 1**) is 100mm x 100mm x 500mm, this size has been selected for the study because, the flexural response of reinforced concrete beams depends upon several factors such as concrete strength, location and quantity of the reinforcement, and the section geometry. In addition, the stress-strain response of concrete in compression (particularly the post-peak) has a strong influence on the behaviour of reinforced concrete elements. To accurately predict the response of reinforced concrete beams, sufficient knowledge on the stress-strain curve of the concrete, including the post-peak behaviour (i.e., descending branch of the stress-strain curve) is required.

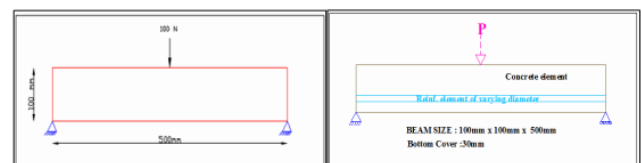


**Figure 1.** Geometry of 2D simply supported beam (plain concrete & single reinforced.)

### 2.4 Loading And Boundary Conditions

The objective of this study is to simulate the linear crack in concrete beam; in 2D plane stress analysis, the study has been carried with incremental varying point load as tabulated in table 3.1. Since the analysis process is carried in ANSYS, it is possible to study the stress variation under different loading conditions like uniformly

distributed & uniformly varying load etc., with different boundary conditions.

## 2.5 Definition of the problem

The objective of the study is to simulate the crack pattern under monotonic loading in concrete beam with & without reinforcement. To reach the objective, the various problems, nothing but the simulation of crack under various boundary conditions as described in previous topic is studied as follows:

1. The linear crack pattern in 2D plain concrete beam (100mm x 100mm x 500mm) with simply supported condition under monotonic loading (mid point loading) and the accuracy of discretization when FE concept of stress analysis is used.

2. The crack pattern in 2D reinforced concrete beam (100mm x 100mm x 500mm) with simply supported condition under monotonic loading (mid point loading) and the effect of different percentage of reinforcement (study is carried with single reinforcement element of 10mm, 16mm, 20mm & 25mm).

3. The crack pattern in 3D reinforced concrete beam (100mm x 100mm x 500mm with single 10mm dia reinforcement at centre), with simply supported condition and cantilever support under incremental loading.

4. A 3D simply supported reinforced concrete beam is designed with longitudinal & stirrup reinforcement & the cracks are simulated when it is subjected to incremental uniformly distributed loading.

## 3. Results and Discussion

The simplified analysis procedure is described in in the numerical analysis of plane stress problems using FEM. The analysis procedure involves the following procedure

1. Element selection, in this numerical analysis the basic 4 noded quadrilateral element is selected to determine the plane stress analysis.

2. Element discretization is nothing but breaking the structure into pieces. The study initiated with 2 elements discretization with 6 nodes, the

variable factor is displacement  $u_x$  &  $u_y$  at each nodes

3. The displacement at any point inside the element is approximated by using nodal displacement & shape function. The shape function used in this study is based Lagrange interpolation.

The above process of FEM plane stress analysis was carried in MATLAB. MATLAB functions have created to determine the global stiffness, nodal displacement & elemental stress. Some special MATLAB codes used to determine the above parameters are syms, int, double, matrix command & loop functions, etc. The beam element discretized as shown in **Figures 2 to 8**.

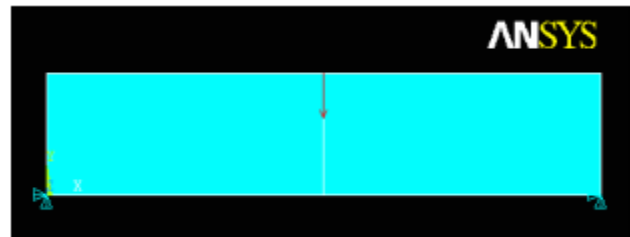


**Figure 2.** 2D simply supported concrete beam (ANSYS model)

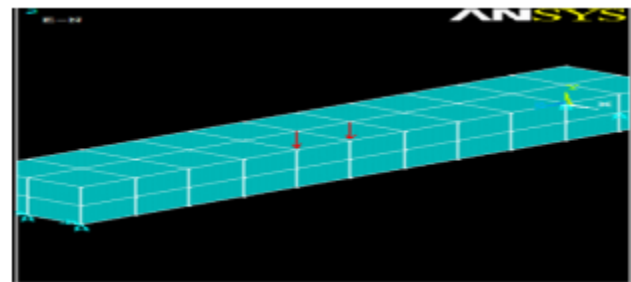


**Figure 3.** 3D simply supported concrete beam (ANSYS model)

# 14<sup>th</sup> Annual Research Day

Organised by the Deanship of Scientific Research in Collaboration with the College of Engineering Research Centre

4<sup>th</sup> April 2019

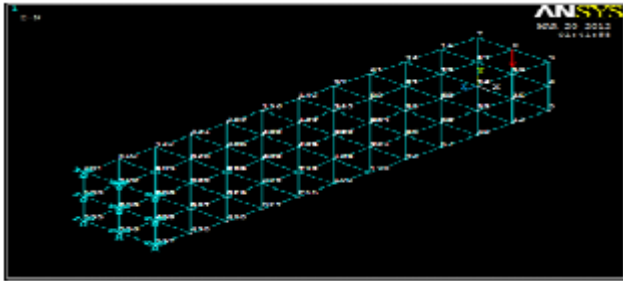


**Figure 4.** 3D cantilever concrete beam (ANSYS model)

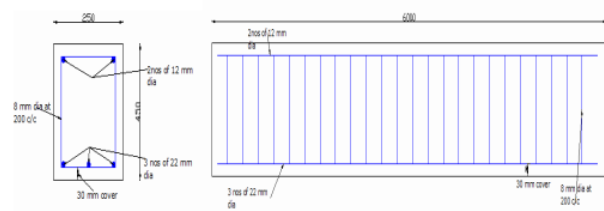


**Figure 5.** Reinforcement detailing of 6m designed beam

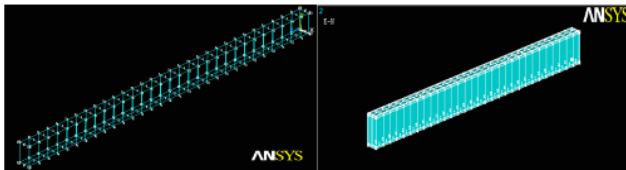


**Figure 6.** Reinforcement & concrete element of designed RCC beam (ANSYS model)

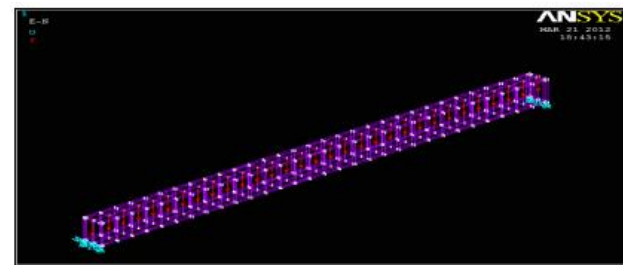


**Figure 7.** Designed RCC beam ANSYS (wire frame) model with boundary condition

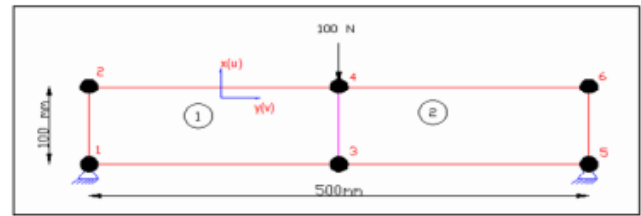


**Figure 8.** Geometry of numerical model

By using the above values of [K] & equilibration equation as mentioned in previous topic, the nodal displacements and element stress calculated using MATLAB functions are tabulated in **Table 1**.

**Table 1.** Displacement & Element Stress -2 Finite Element

Nodes	Displmnt. (mm)	Element	Stresses (N/mm <sup>2</sup> )	
u1	0.000	1	$\sigma_x$	-1.202
v1	0.000		$\sigma_y$	-0.521
u2	-0.025		$\tau_{xy}$	-1.022
v2	-0.023	2	$\sigma_x$	-1.302
u3	0.000		$\sigma_y$	-0.653
v3	-0.044		$\tau_{xy}$	1.055
u4	-0.007		$\sigma_x$	-1.302
v4	-0.092		$\sigma_y$	-0.653
u5	0.000		$\tau_{xy}$	1.055
v5	0.003			
u6	-0.029			
v6	-0.024			

In general it is well known that the number of elements increases with the increase in the accuracy as shown. Thus for this study, it is limited to proceed the analysis process under varying load with the element discretization of 80 & 320 finite elements in 2D models, because of lesser accuracy variation. In 3D analysis, the RCC beam of 100 x 100 x 500mm is meshed into 108 nodes & 44 elements. The designed RCC beam model is generated with 384 meshed elements based on the location of reinforcement element. The meshed 2D & 3D models considered. It is found that the analytical crack simulation has been carried either at integration points or at centroid of elements and from the

graph (Figure 9) it has been clear that nodal stress gives more points of exceeding stress than element stress. Thus, the linear crack trajectory under incremental loading is plotted at nodes where the maximum principle stress exceeds the limiting tensile stress of concrete i.e.,  $f_t = 0.7\sqrt{f_{ck}} = 3.5 \text{ N/mm}^2$ . Under different loads with meshing 320 finite elements (1049 nodes), analysis is carried and the maximum principal stress values are calculated.

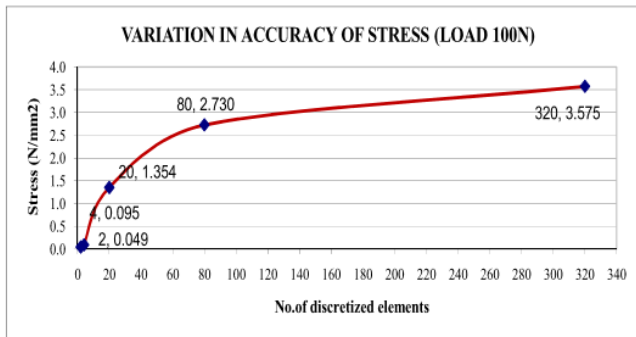


Figure 9. Variation in Accuracy of stress

The analytical results can be easily checked with the experimental results to get the accuracy of analytical study. The deflection under monotonic loading of considered models are determined just to correlate with the occurrences of maximum stress. Thus for considered 2D & 3D, plain concrete and reinforced cement concrete beams the maximum deflection under monotonic loading is plotted and shown in Figure 10.

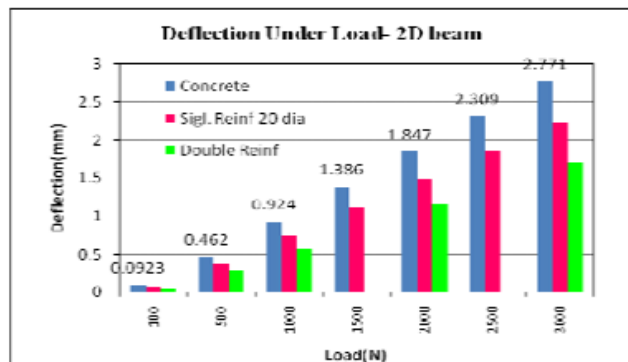


Figure 10. Deflection under load

The deformed shape of considered 3D RCC beam of considered with different boundary condition

under the ultimate load as mentioned in load specification are show in Figures 11 and 12

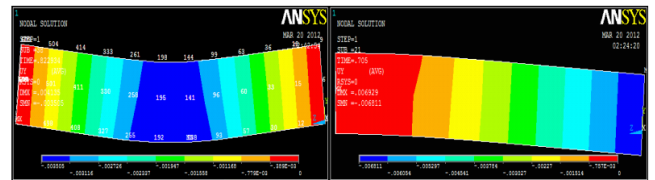


Figure 11. Deformed shape – 3D RC beam (S.S & cantilever)

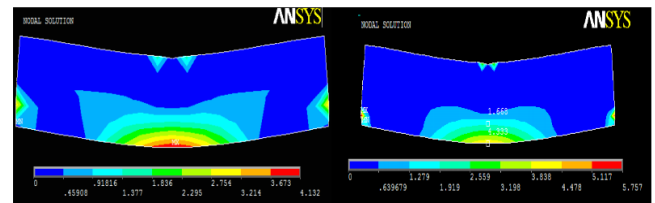


Figure 12. Stress distribution under 100N load a.80 & b.320 finite elements

### 3.1 Crack mapping

From the stress distribution contour & the nodes identified from graphs, the linear crack trajectory is mapped in plain concrete beam with 320 element of discretization. The initial crack at an integration points where the stress exceeds the permissible tensile stress of concrete under incremental loading was identified and the linear crack trajectory is mapped in hand as shown in Figure 13.

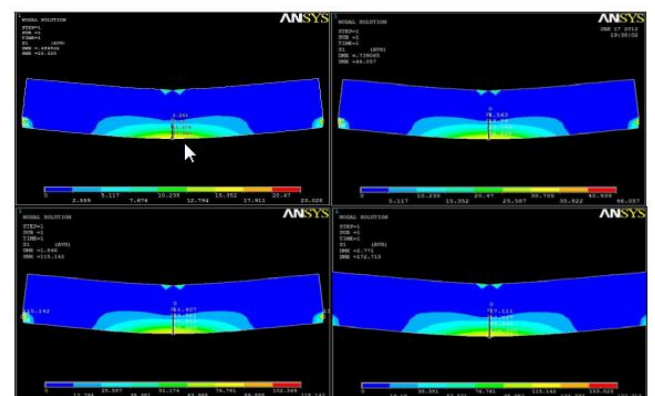


Figure 13. Linear crack simulation under 400N, 1000N, 2000N & 3000N (320 element)

## 4. Conclusions:

# 14<sup>th</sup> Annual Research Day

Organised by the Deanship of Scientific Research in Collaboration with the College of Engineering  
Research Centre

4<sup>th</sup> April 2019

From the analytical studies it can be concluded that the increase in the number of the elements in the discretized model, the convergence of the solution becomes rapid as well as increases the accuracy of the solution.

*f*

- i) In the case of 2D plain concrete beam subjected to 100N load, the variation of maximum principal stress at node (4.132 N/mm) was found to be more than 50 % of element stress (2.73 N/mm<sup>2</sup>), which shows the crack prediction at nodes will give more accurate results than compared with mapping at the centroid of elements.
- ii) In 2D plain concrete beam, the maximum principal stress under maximum considered load of 3000N is 172.71 N/mm<sup>2</sup> which is 73% more than the stress in concrete element of beam consisting of a single bar (25 mm diameter) is 99.278 N/mm<sup>2</sup>, this shows the effect of reinforcement in concrete beam.

## References

- [1] David V Hutton., Fundamentals of Finite element analysis, International edition..
- [2] Robert D Cook., Finite element modelling for stress analysis, John Wiley & Sons Incl.,
- [3] S.S.Bhavikatti., Finite element analysis, New age international publishers.
- [4] Young.W.Kwon,Hyochoong bang., Finite element method using MATLAB.,CRC Press .New york.
- [5] M. OHTSU,' Crack propagation in concrete: linear elastic fracture mechanics and boundary element method',- Theoretical and Applied Fracture Mechanics 9 (1988), 55-60.
- [6] A.F. Ashour and C.T. Morley,' Three-dimensional nonlinear finite element modeling of reinforced concrete structures', Finite Elements in Analysis and Design 15 (1993), 43-55
- [7] M.V.K.V. Prasada, C.S. Krishnamoorthy, ' Computational model for discrete crack growth in plain and reinforced concrete',- Comput. Methods Appl. Mech. Engrg. 191, (2002) 2699–2725.
- [8] Z.J. Yang , Jianfei Chen,' Finite element modelling of multiple cohesive discrete crack propagation in reinforced concrete beams',- Engineering Fracture Mechanics 72, (2005) 2280–2297.
- [9] Potisuk, T., "Finite Element Modeling of Reinforced Concrete Beams Externally Strengthened by FRP Composites." Masters Thesis, Oregon State University, Corvallis, Oregon, 2000.
- [10] Ngo, D. and Scordelis, A. C., "Finite Element Analysis of Reinforced Concrete Beams," Journal of the American Concrete Institute, 64(3), pp. 152-163, 1967.

# 14<sup>th</sup> Annual Research Day

Organised by the Deanship of Scientific Research in Collaboration with the College of Engineering  
Research Centre

4<sup>th</sup> April 2019

---

## Non-Linear Analysis of Floating Structures

Mohammed Jameel<sup>1</sup>

<sup>1</sup>Department of Civil Engineering, College of Engineering, King Khalid University,  
PO Box 394, Abha 61411 KSA.  
E-mail address: jamoali@kku.edu.sa

---

**Abstract:** Spar platform is a compliant floating structure used for deep water applications of drilling, production, processing, storage and off-loading of ocean deposits. The analysis of Spar-mooring system poses serious computational problems, primarily because of the uncertainties associated with the environmental loads, structural configuration and resulting nonlinearities. Coupled analysis, presently adopted, employs a fully integrated spar mooring system. It incorporates the major contribution of drag, inertia and damping due the longer lengths, larger sizes and heavier weights of moorings. A finite element model consisting of a rigid cylinder linked and supported by tensioned mooring lines at fairleads has been analysed. Hybrid beam elements are used to model the mooring lines. Their linkage with spar cylinder is suitably modeled to ensure integrated coupling and structural continuity. The Studies cover surge, heave, pitch and mooring line tension responses, highlighting the coupling effect. High degree of non-linearities involved cause complex irregular responses under regular sea states. Operational water depth influences the mooring line dynamics and non-linearities involved. The integrated coupled model clearly shows its significance in terms of hydrodynamic damping on mooring lines. There is a major difference in responses obtained with and without drag and inertia forces on mooring lines.

**Keywords:** Spar platform; Deepwater structures; Floating structures; Deepwater mooring lines.

---

### 1. Introduction:

Spar platforms (Fig. 19) are increasingly used for exploration of oil and natural gas from deep sea. Its popularity is attributed to its economical performance and distinguished sea keeping characteristics besides various other merits. The need for coupled analysis of moored structure has long been recognized (Paulling and Webster 1986). They used the 6-DOF non-linear motion equation for coupled dynamic analysis of a TLP. The studies on coupled analysis between a moored structure and its mooring system had been carried out by various investigators (Ran and Kim 1997, Ormberg and Larsen 1998, Ran et al. 1999, Kim et al. 2001a, Kim et al. 2001b, Kim et al. 2005, Chen et al. 2006,). Tahar and Kim (2008) developed numerical tool for coupled analysis of deepwater floating platform with polyester mooring lines. All the above authors, in

general, followed a similar approach, which was developed by (Paulling and Webster 1986).

Low and Langley (2008) presented a hybrid time/frequency domain approach for coupled analysis of vessel/mooring/riser. The vessel was modeled as a rigid body with six degrees-of-freedom, and the lines were discretized as lumped masses connected by linear extensional and rotational springs. The method was found to be in good agreement with fully coupled time domain analysis, when used for relatively shallow water depths. Low (2008) used the same hybrid method to predict the extreme responses of coupled floating structure. Yang and Kim (2010) carried out coupled analysis of hull-tendon-riser for a TLP. The mooring line/riser/tendon system was modeled as elastic rod. It was connected to the hull by linear and rotational springs. The equilibrium equations of hull and mooring line/risers/ tendon system were solved

# 14<sup>th</sup> Annual Research Day

Organised by the Deanship of Scientific Research in Collaboration with the College of Engineering  
Research Centre

4<sup>th</sup> April 2019

---

simultaneously. Zhang et al. (2008) studied the effect of coupling for cell-truss Spar platform. The Spar mooring/riser was modeled by three methods namely quasi-static coupled, semi-coupled and coupled. The results from frequency-domain and time domain analyses were compared with experimental data.

In most of these conventional procedures of analysis, the force and displacement of mooring heads and vessel fairleads are iteratively matched at every instant of time marching scheme while solving the equilibrium equations. However, the velocity and acceleration do not reportedly match. Further, the continuity of vessel and mooring is missing. In this process the major contribution of moorings in terms of drag, inertia and damping due to their longer lengths, larger sizes and heavier weights are not fully incorporated. This effect is more pronounced in deep water conditions. Hence, the main objective of present study is to idealize the Spar mooring integrated system as a fully/strongly coupled system and also to study the moorings drag and inertia effect on Spar platform.

The fully coupled integrated Spar-mooring line system used in the present study essentially means that the large spar cylinder is physically linked with mooring lines at fairleads provided by six nonlinear springs. The mooring lines as an integral part of the system, support the spar at fairlead and pinned at the far end on the seabed. They partly hang and partly lying on the sea bed. Sea bed is modeled as a large flat surface with a provision to simulate mooring contact behavior. The mooring line dynamics takes into account the instantaneous tension fluctuation and damping forces with time-wise variation of other properties. Drag, inertia and damping forces due to waves and current on mooring lines act simultaneously on Spar cylinder. Hence, there is no need of iteratively matching the force, displacement, velocity and acceleration at the fairlead position.

## 2. Mathematical Formulation:

### 2.1 Finite Element Model

The analysis of Spar platform considering actual physical coupling between the rigid vertical floating hull and mooring lines is possible using the finite element method. In actual field problems hydrodynamic loads due to wave and currents act simultaneously on Spar platform and mooring lines. In finite element model, the entire structure acts as a continuum. This model can handle all non-linearities, loading and boundary conditions. The commercial finite element code ABAQUS/ AQUA is found to be suitable for the present study. The other reason to use ABAQUS is that its module AQUA appropriately models an off-shore environment. It is capable of simulating the hydrodynamic loading due to wave and current.

The equation of motion has been solved using the above finite element code. It has the capability of modeling slender and rigid bodies with realistic boundary conditions, including fluid inertia and viscous drag. The mooring lines are modelled as three dimensional tensioned beam elements. It includes the non-linearities due to low strain large deformation and fluctuating pretension. Hybrid beam element is used to model the mooring lines. It is hybrid because it employs the mixed formulation involving six displacements and axial tension as nodal degrees of freedom. The axial tension maintains the catenary shape of the mooring line. The hybrid beam element is selected for easy convergence, linear or non linear truss elements can also be considered with associated limitations. The beam element under consideration experiences the wave forces due to Morison's equation. The self weight and axial tension are duly incorporated. The  $12 \times 12$  consistent elemental mass matrix consists of the structural mass and the added mass and respective mass moments of inertia. The force vector consists of the concentrated forces  $f_x$ ,  $f_y$  &  $f_z$  and the corresponding moments  $m_x$ ,  $m_y$  &  $m_z$  at each node. The three dimensional stiffness matrix in ABAQUS is capable of including geometric stiffness matrix with elastic stiffness matrix. [KG]

# 14<sup>th</sup> Annual Research Day

Organised by the Deanship of Scientific Research in Collaboration with the College of Engineering  
Research Centre

4<sup>th</sup> April 2019

---

models the large deformation associated with mooring configuration. Instantaneous stiffness matrix with varying axial tension in the modified geometry takes into account the associated non-linearity. The structural damping is simulated by Rayleigh model. Hydrodynamic damping is dominant in case of oscillating slender member surrounded by water. As mentioned above ABAQUS with module AQUA is fully capable to model the above mentioned forces in the integrated finite element model.

The Spar hull is modeled as an assemblage of rigid beam elements connecting its center of gravity, riser reaction points and mooring line fair leads. The radii of gyration and the cylinder mass are defined at C.G. The rigid Spar platform has been connected to the elastic mooring lines by means of six springs (Three for translation and three for rotation). The stiffnesses of translation springs are very high, where as the stiffnesses of rotational springs are very low simulating a hinge connection.

## 2.2 Numerical Studies

The behavior of Spar platform under regular waves, with typical set of numerical data and realistic geometric configuration model are studied. The geometric characteristics and other related data for the present study are given in Table 1. The Spar platform is analyzed, assuming it to behave like a rigid body. The response is studied in terms of soft (surge, sway, yaw) and stiff (roll, pitch and heave) degrees of freedom together with mooring line tension. The response time histories of Spar are obtained and reported at the node situated on the deck top.

The wave forces are estimated with stretching modifications for accounting the influence of variable submergence. In order to avoid the violation of limitation of Morison's equation, wave lengths are restrained as greater than or equal to five times the diameter of cylinder. The regular wave of 6.0 m and 14.0 sec is used as reported by Ran et al. (1996) for predicting the response of classic Spar platform. The response

of fully coupled Spar and its moorings has been obtained for shallow and deep sea conditions. The above mentioned shallow water depth does not necessarily mean that the  $d/L \leq 0.5$  as reported in the literature. However, the shallow water depth (318 m) denotes the moderate water depth in comparisons to deeper water depth of 1018 m. The response time histories are obtained for sufficient length of time after attaining a steady state. The time interval ( $\Delta t$ ) is chosen to ensure stability and accuracy of the solution. In all the studies, stiffness matrices are updated at every time step incorporating the changes in stiffness due to large deformation, instantaneous mooring tension etc.

## 3. Results and Discussion

### 3.1 Static Equilibrium of Coupled System

The static analysis is carried out in four major steps. The basic aim is to obtain the proper catenary shape of mooring line achieving specified pre-tension, stresses and stiffnesses associated with the mean curvature. To achieve catenary shape, mooring line is suspended between two points under the self-weight. However, in the case of Spar, a pretension value is specified in the mooring line at the fairlead end. The bottom point is then iteratively fixed to achieve the catenary shape and the required tension at the top. This process is completed for all the four mooring lines simultaneously by systematically following the four steps.

In the first step the Spar hull is kept fixed and the mooring lines are horizontally stretched out in their respective orientations in the horizontal plane at the fairlead level. In the second step, anchor ends of the mooring lines are lowered to seabed. In the third step, mooring lines are iteratively moved and adjusted horizontally at the sea bed in their respective orientations so that the required tension is achieved at the fair lead level. The bottom points are then temporarily hinged at the seabed. In the fourth step, the Spar is released and the entire structure consisting of Spar hull

# 14<sup>th</sup> Annual Research Day

Organised by the Deanship of Scientific Research in Collaboration with the College of Engineering  
Research Centre

4<sup>th</sup> April 2019

---

and mooring system slowly attains an equilibrium position. The equilibrium is attained under self-weight, buoyancy forces and pretension at the fairleads. In this process the pretension and the position of the CG of hull may be altered and differ from the required value. In order to achieve the requisite pretension and the draft of the hull the hinged location at the seabed are further moved iteratively. After a few trials, all the design requirements are achieved with the equilibrium position.

In this state of equilibrium of integrated coupled system all the boundary conditions are explicitly defined in ABAQUS/AQUA environment. The mooring lines are modeled using hybrid beam elements maintaining the continuity with the Spar hull at fairlead. This modeling of mooring line is more realistic as it also incorporates the changed stiffnesses due to curvature of catenary shaped mooring line. The resulting stiffness matrix consists of two parts namely KE, elastic stiffness matrix and KG, geometric stiffness matrix. The inclusion of large deformation makes the model more accurate and realistic. This realistic model is not widely used in the literature.

### 3.2 Validation of Static Behavior

Static profile of mooring lines and their resultant tensions for different cases are reported in the literature. Mathematical models differ in different approaches. However, these models do not significantly influence the reported static results.

Chen et al. (2001) reported the variation of net tension in four mooring lines at the fair lead position, varying against various static off-sets in surge direction. Fig 1 shows the same variation of tension versus the Spar off-set for 318 m water depth. Using the present approach the surge off-sets are incremented by 5 m ranging from 0 to 25 m. The corresponding net tension ranges from 0 to 5.7E6 N at fairlead level. The values obtained by the present study closely match with the study carried out by Chen et al. (2001). It shows the validity of the coupled mathematical model using

finite element in ABAQUS/AQUA environment. The boundary conditions are appropriately implemented for the required state of equilibrium.

Similar validation has been carried out for the deep water condition (water depth = 1018 m) as well. However, the results do not match with Chen et. al (2001) as closely as for shallow water depth (318 m). Fig. 2 shows difference of 6.5% almost equally for all the off-sets ranging from 10 m to 25m. However, the trend of the results is quite matching. The variation in the numerical values of net tension is mainly due to the basic difference in mathematical model. The present study takes into account, the actual integrated coupling of entire structure by finite element assembly considering all major non-linearities, while Chen et al. (2001) did it differently.

### 3.3 Free Vibration Analysis

As described earlier Spar and mooring line system are modeled like a space frame maintaining the continuity together with all structural characteristics and relevant boundary conditions. The free vibration analysis of Spar-mooring system is carried out by Lanczos method to obtain the natural frequencies and corresponding mode shapes. These frequencies are used to analyse the non linear dynamic response of Spar platform. Table 2 shows the comparison of natural time periods between Chen et al. (2001) and the present study for 318 m water. The natural periods obtained by Chen et al. (2001) are 322.5, 26.2 and 54.6 seconds in surge, heave and pitch respectively. The natural periods obtained by the present simulation are close to the experimentally measured values for 318 m water depth. Table 2 also shows the time periods obtained by present study for 1018 m water depth.

### 3.4 Response of Spar platform in shallow and deep water conditions

In the present study the behavior of Spar platform has been studied under shallow and deep

# 14<sup>th</sup> Annual Research Day

Organised by the Deanship of Scientific Research in Collaboration with the College of Engineering  
Research Centre

4<sup>th</sup> April 2019

---

sea conditions. The Spar hull is same (diameter = 40.54 m) for shallow as well as deep water case. But the mooring lines are much longer to operate in greater water depths. Wave forces are simulated by considering a single wave of 6 m, 14 sec. The main focus is on the dynamic behavior of Spar in terms of its six degrees of freedom viz surge, sway, heave, pitch, roll and yaw strongly influenced by the system non-linearities as discussed earlier. Steady state responses are obtained discarding the transient state. In general, off-shore structures do not show the participation of more than one frequency under regular sea state. However, the strong non-linearities involved in the Spar structure lead to the participation of other frequencies too. In some cases it is explicitly visible, while in other cases it is not. This is mainly because of the degree of non-linearity activated.

The following studies highlight the salient features of Spar platform in shallow and deep sea conditions.

### 3.4.1 Surge response

The surge response of Spar platform in shallow water conditions under 6 m, 14 sec wave is shown in Fig. 3. The response is mainly governed by the forcing frequency due to single wave. Maximum surge ranges from  $\pm 3.6$  m from the mean position. However, the regular response at a frequency of 0.448 rad/sec oscillates mildly at lower frequency of 0.115 rad/sec which is close to six times the natural frequency of surge. The low frequency (0.115 rad/sec) is close to pitch while wave frequency matches with 0.448 rad/sec. The power spectral density as shown in Fig. 4 shows the participation of two frequencies. Fig. 4 also shows the small oscillation of the harmonic response at a low frequency of 0.115 rad/sec. There is no evidence of any significant participation of other frequencies. Effect of non-linearity is not very strong on surge response.

Fig. 7 shows the surge response of Spar platform in deep sea conditions (water depth = 1018 m). The surge response time history shows the

participation of two frequencies. The major oscillations occur at low frequency of 0.13 rad/sec as confirmed by PSD in Fig. 8. This frequency happens to be the natural frequency of pitch. The time history also shows an over riding fluctuations at the peaks of the response, showing a typical non-linear behavior. The peak at the wave frequency of forcing function is very small. However, the major peak corresponds to pitch motion which is coupled with surge.

On comparison of this response with the same for shallow water shows a major difference in PSD. Fig. 4 and Fig. 6 shows the occurrence of peak at 0.448 rad/sec which is nothing but the frequency of wave. Hence, a major shift in the response is observed from shallow to deep water condition under the same wave force. The major difference in the two systems is due to the length and profiles of mooring lines of the coupled system. The mooring line dynamics and its participation in the response have been taken care of by finite element modeling of the entire system in integrated fashion. The responses also show a strong coupling between surge and pitch degrees of freedom. It is therefore, recommended to keep this coupling effect in mind while designing the Spar platform.

The surge response observed at the centre of gravity is shown in Fig. 9 for 1018 m water depth. It shows a marked difference in surge behavior in comparison to the same at top of the platform level (Fig. 7). At CG level it oscillates at time period 341 seconds which is close to the surge natural period. About this oscillation there are continuous fluctuations of wave frequency, showing the pronounced non-linear behavior. Fig. 10 clearly shows the peaks at low frequency and wave frequency. However, there is a relatively smaller peak occurring at 0.14 radians, which is close to the pitch frequency. The participation of low and wave frequency responses feature differently in comparison to the deck response. This surge response at centre of gravity significantly enhanced and shows a substantial

# 14<sup>th</sup> Annual Research Day

Organised by the Deanship of Scientific Research in Collaboration with the College of Engineering  
Research Centre

4<sup>th</sup> April 2019

---

pitch response too. Likewise, in shallow water also the surge response is significant at surge frequency (low) with significant value at wave frequency (Fig. 5 and Fig. 6).

### 3.4.2 Heave response

Time wise response of heave for 318 m water depth is shown in Fig. 11. The response is periodic in nature with superimposed ripples. The maximum value ranges from  $\pm 0.12$  m due to resonance of the force component with the natural frequency of heave. It is clearly shown in the PSD plot of Fig. 12. The local fluctuations near the peaks in the time history have small participation in the response. Fluctuations about the mean position also show unequal peak distributions. However, participation at frequency other than heave is comparatively insignificant.

Fig. 13 shows the heave response of Spar platform for deep sea conditions. The heave response fluctuates about the mean position oscillating from smaller to larger amplitudes and repeating the same trend onwards all through the time history as shown in the Fig. 13. The fluctuations gradually increase from narrow to broad by 30 %. Reaching the peak, it gradually reduces by 30 %. The maximum response of heave ranges from  $\pm 1.1$  m. The PSD in Fig. 14 shows a major frequency content near heave natural frequency of 0.27 rad/sec, other peaks show minor contributions.

In shallow water conditions also, the same trend is followed only with the difference in magnitude which is almost one tenth of the deep water conditions. Unlike surge and pitch response, excitation frequency always occurs near natural frequency of the heave. No peak occurs at the wave frequency. Response is, therefore, governed by the structural characteristics attracting only a component of forcing function. Heave motion is coupled with all major degrees of freedom (i.e surge, sway, pitch etc.) Hence excitation of any major mode contributes to heave response.

### 3.4.3 Pitch response

Fig. 15 and 16 show the pitch time history and corresponding PSD in shallow water depth. The extreme value of pitch ranges from  $\pm 0.024$  rad/sec. Like surge response, pitch time history also shows the similar behavior. The periodic response oscillates at frequency of 0.448 rad/sec about the mean position. It is the wave frequency response as the pitch derives its force from the wave. The frequency of 0.115 rad/sec. is quite close to the natural frequency of pitch response. However, the participation at low frequency is very small.

The pitch response in deep sea conditions is shown in Fig.17. It shows a matching behavior with the surge response (Fig. 7). The maximum pitch response in deep sea conditions is 0.087 rad/sec, which is 3.5 times more than the response in shallow water depth. The PSD of pitch, as shown in Fig. 18, also appears to be the replica of the same behavior of surge response. It implies that the pitch and surge responses are strongly coupled. The time history of pitch shows the non-linear behavior due to coupled system. The super imposed fluctuations on regular pitch response are clearly visible. There is a clear resonance of pitch at frequency 0.144 rad/sec. This resonance enhances the pitch response to  $\pm 0.087$  rad/sec. The major difference in deep and shallow conditions is visible on comparing corresponding PSD plots (Fig. 16 and 18). Major peak in deep sea occurs at low frequency near pitch, while in case of shallow water it occurs at wave frequency.

The pitch response in shallow water is mainly dominated by the forcing function as shown in Fig. 16. The major frequency content occurs at 0.448 rad/sec or time period 14 sec. which is nothing but the wave frequency response. The difference in the response of shallow and deep sea conditions draw our attention to thoroughly investigate the possibility of resonance for the wide range of water depths. It is mainly because in shallow water 6 m, 14 sec wave causes larger force in comparison to deep water condition.

# 14<sup>th</sup> Annual Research Day

Organised by the Deanship of Scientific Research in Collaboration with the College of Engineering Research Centre

4<sup>th</sup> April 2019

Table 1: Geometrical and Hydrodynamic Properties of Spar and Moorings

Spar (Classic JIP Spar)	
Length	213.044 m
Diameter	40.54 m
Draft	198.12 m
Mass	2.515276E8 kg
Mooring Point	106.62 m
No. of Nodes	17
No. of Elements	16
Type of Element	Rigid beam element
Sea-bed	5000 × 5000 m <sup>2</sup>
Drag	0.6
Drag (vertical)	3.0
Inertia	2.0
Added mass	1.0

Table 2: Natural Time Periods

	Time Periods (sec)		
	Experimental study, Water Depth 318 m	Present Study Water Depth 318 m	Present Study Water Depth 1018 m
Surge	331.86	322.5	341.97
Heave	29.03	26.2	22.60
Pitch	66.77	59.6	43.48

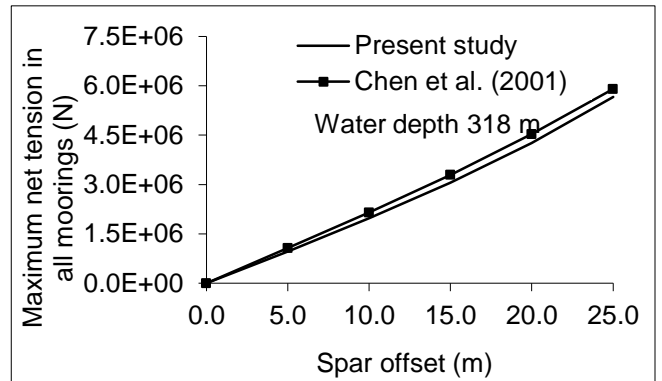


Fig. 1 Tension comparison for 318 m water depth

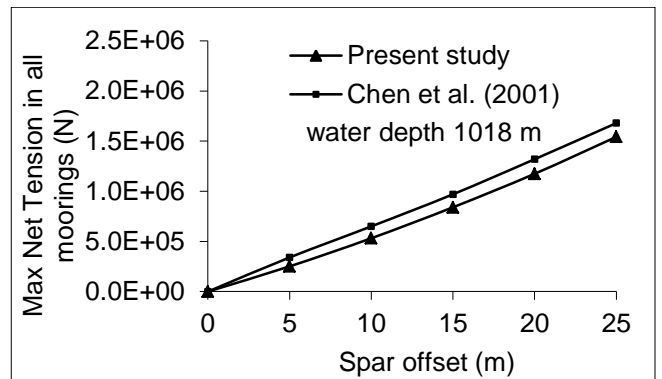


Fig. 2 Tension comparison for 1018 m water depth

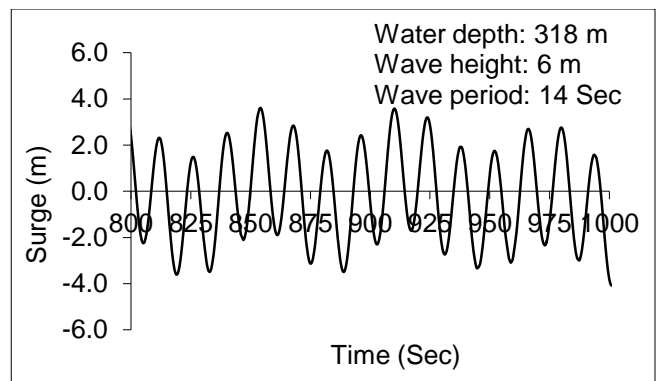


Fig. 3 Surge time history for 318 m water depth

# 14<sup>th</sup> Annual Research Day

Organised by the Deanship of Scientific Research in Collaboration with the College of Engineering

Research Centre

4<sup>th</sup> April 2019

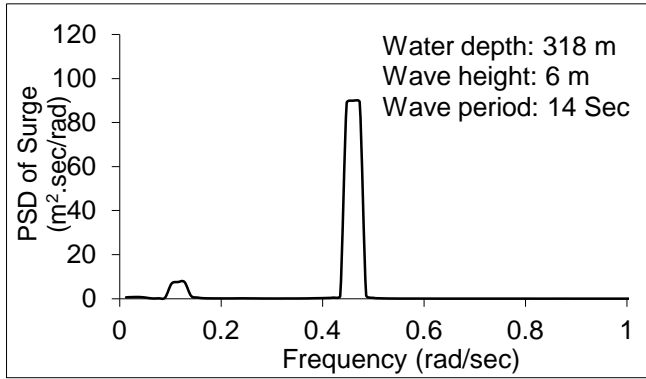


Fig. 4 PSD of Surge response for 318 m water depth

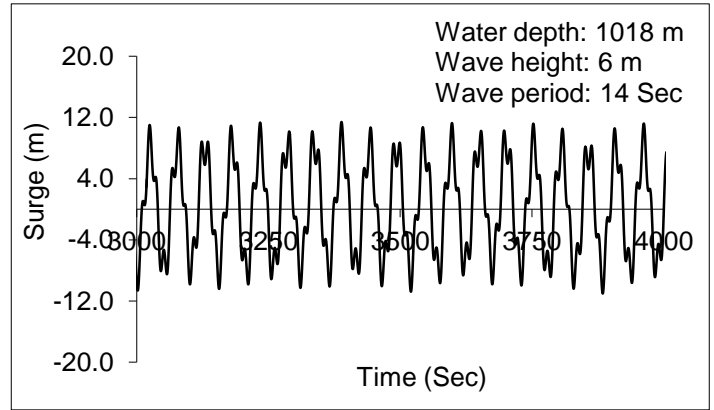


Fig. 7 Surge time history for 1018 m water depth

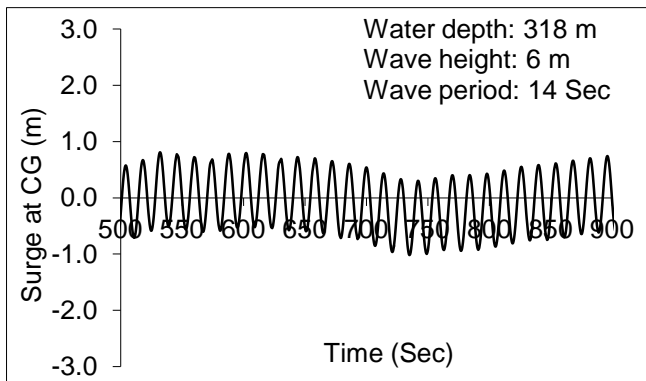


Fig. 5 Surge time history at C.G

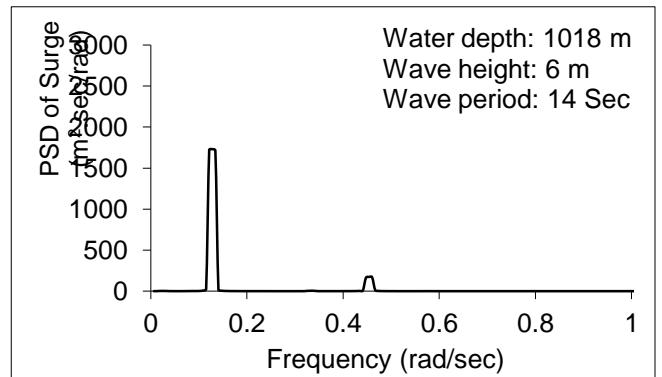


Fig. 8 PSD of Surge response for 1018 m water depth

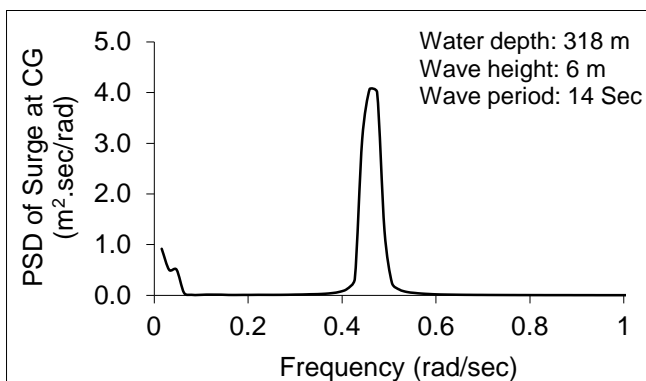


Fig. 6 PSD of Surge response at C.G for 318 m water depth

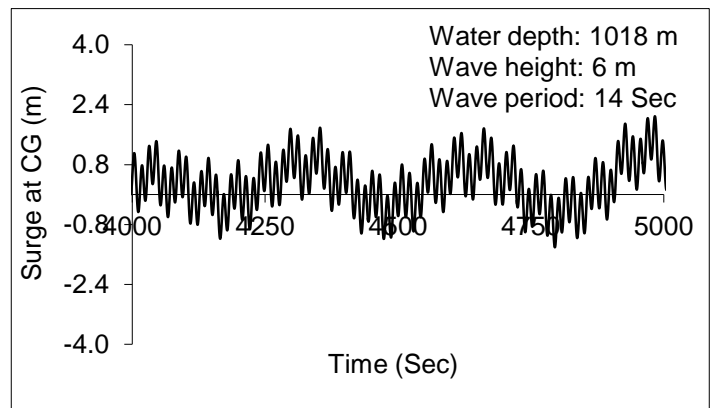


Fig. 9 Surge time history at C.G for 1018 m water depth

# 14<sup>th</sup> Annual Research Day

Organised by the Deanship of Scientific Research in Collaboration with the College of Engineering  
Research Centre

4<sup>th</sup> April 2019

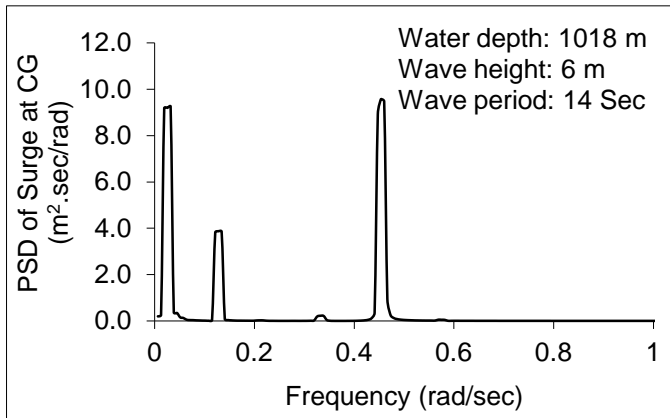


Fig. 10 PSD of Surge response at C.G for 1018 m water depth

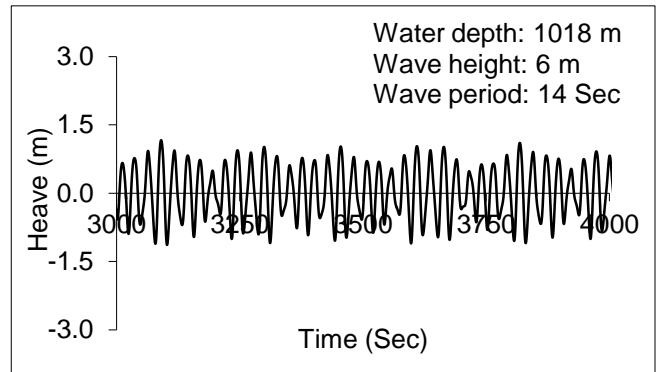


Fig. 13 Heave time history for 1018 m water depth

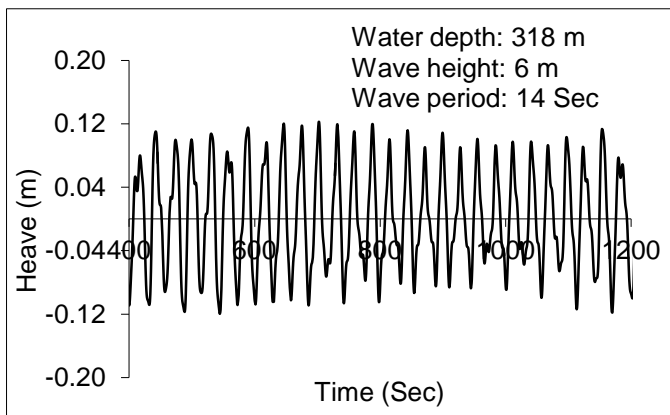


Fig. 11 Heave time history for 318 m water depth

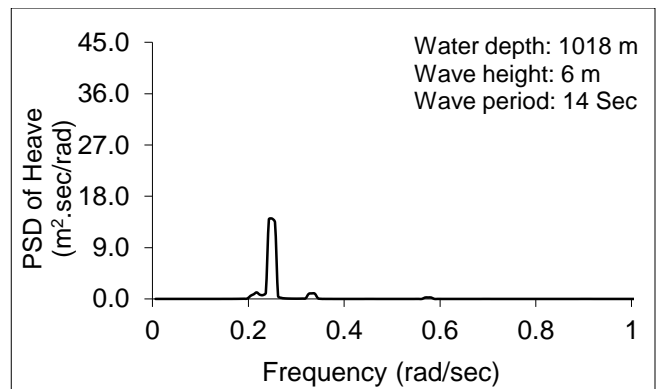


Fig. 14 PSD of Heave response for 1018 m water depth

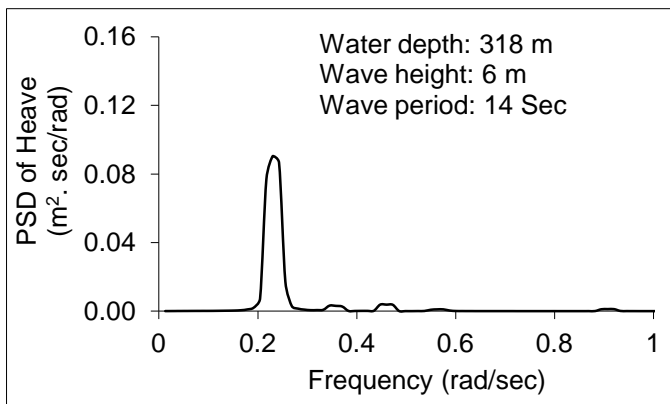


Fig. 12 PSD of Heave response for 318 m water depth

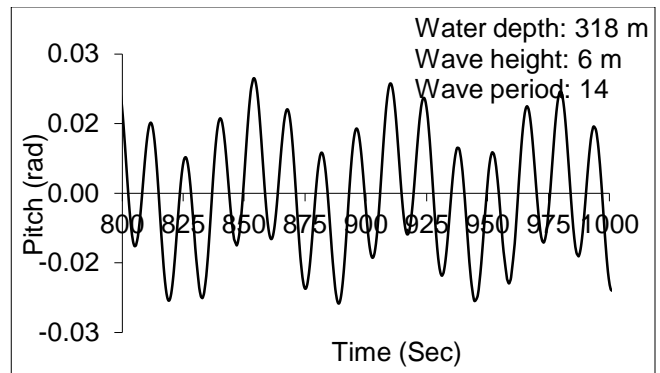


Fig. 15 Pitch time history for 318 m water depth

# 14<sup>th</sup> Annual Research Day

Organised by the Deanship of Scientific Research in Collaboration with the College of Engineering Research Centre

4<sup>th</sup> April 2019

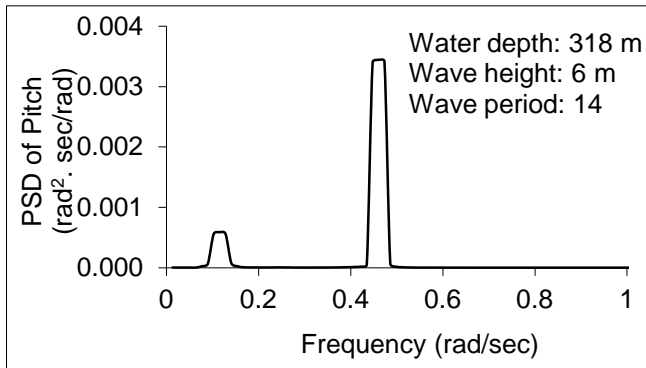


Fig. 16 PSD of Pitch response for 318 m water depth

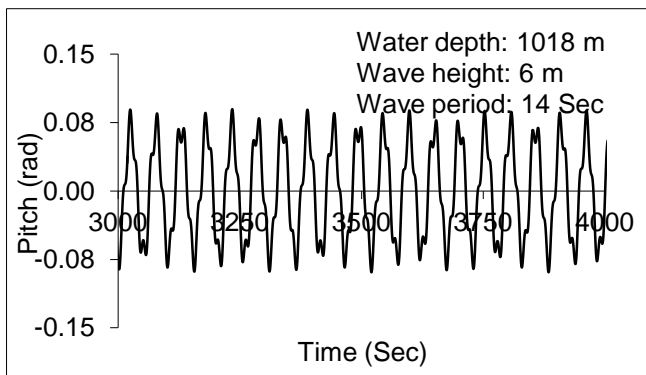


Fig. 17 Pitch time history for 1018 m water depth

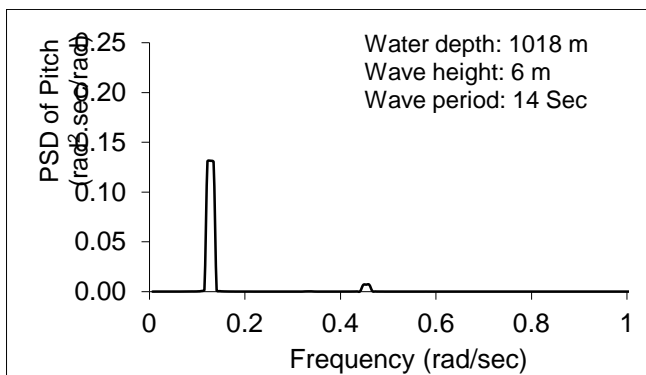


Fig. 18 PSD of Pitch response for 1018 m water depth



Fig. 19 Genesis Spar Platform

## 4. Conclusions:

Non-linear dynamic analysis of Spar platform is carried out under regular wave. The wave considered models the extreme loading condition. The results obtained from present study are partly validated with the published results. The major non-linearities are incorporated and their effects on responses are studied. The following conclusions are drawn on the basis of detailed non-linear dynamic analysis of Spar platform, using integrated coupled model.

1. The coupled Spar platform model employed in the present study is more realistic because it maintains the continuity of the structure, incorporates the instantaneous stiffness due to time-wise response, curvature of catenary, tension fluctuations, damping, geometric and other non-linearities.

2. Touch-down point of the mooring line is a time wise phenomenon that directly influences the boundary conditions. This parameter significantly influences the convergence of solution of governing equations.

3. High degree of non-linearities involved cause complex irregular responses under regular sea states. Spectral density distributions are more informative to highlight the important features like low and wave frequency responses.

4. Response due to surge at centre of gravity is found to be significantly different than that obtained at the platform level. Both of these responses are important for various functional requirements of Spar platform.

5. Operational water depth influences the mooring line dynamics and non-linearities involved. It significantly features in case of surge at CG where low frequency and pitch frequency responses also occur apart from wave frequency response in deep water. In case of shallow water depth, wave frequency response is only significant.

## References

# 14<sup>th</sup> Annual Research Day

Organised by the Deanship of Scientific Research in Collaboration with the College of Engineering  
Research Centre

4<sup>th</sup> April 2019

---

- [1] Chen, X., Ding, Y., Zhang, J., Liagre, P., Niedzwecki, J., Teigen, P., 2006. Coupled dynamic analysis of a mini TLP: Comparison with measurements. *Ocean Engineering* 33, 93-117.
- [2] Chen, X., Zhang, J., Ma, W., 2001. On dynamic coupling effects between a spar and its mooring lines. *Ocean Engineering* 28, 863-887.
- [3] Fan, Z., Jian-min, Y., Run-pei, L.,Gang, C., 2008. Coupling effects for cell-truss spar platform: Comparison of frequency- and time-domain analyses with model tests. *Journal of Hydrodynamics* 20 (4), 424-432.
- [4] Jameel, M., 2008. Non-linear dynamic analysis and reliability assessment of deepwater floating structure. PhD thesis. Department of Applied Mechanics, Indian Institute of Technology, Delhi (IIT Delhi).
- [5] Kim, M. H., Koo, B. J., Mercier, R. M., Ward, E. G., 2005. Vessel/mooring/riser couple dynamic analysis of a turret-moored FPSO compared with OTRC experiment. *Ocean Engineering* 32, 1780-1802.
- [6] Kim, M. H., Ran, Z., Zheng, W., 2001. Hull/mooring coupled dynamic analysis of a truss spar in time domain”, *International Journal of Offshore and Polar Engineering* 11, No. 1, 42- 54.
- [7] Kim., M. H., Ward, E. G., Harnig, R., 2001. Comparison of numerical models for the capability of hull/mooring/ riser coupled dynamic analysis for spars and TLPS in deep and ultra deep water, *Proceedings of the Eleventh International Offshore and Polar Engineering Conference*, pp 474-479.
- [8] Low, Y.M., 2008. Prediction of extreme responses of floating structures using a hybrid time/frequency domain coupled approach. *Ocean Engineering* 35, 1416–1428.
- [9] Low, Y.M., Langley, R.S., 2008. A hybrid time/frequency domain approach for efficient coupled analysis of vessel/mooring/riser dynamics. *Ocean Engineering* 35 (5-6), 433–446.
- [10] Ormberg, H., Larsen, K., 1998. Coupled analysis of floater motion and mooring dynamics for a turret-moored ship, *Applied Ocean Research*, Vol. 20, pp 55-67.
- [11] Paulling, J.R., Webster, W.C., 1986. A consistent large-amplitude analysis of the coupled response of a TLP and tendon system, *Proceedings of Offshore Mechanics and Arctic Engineering (OMAE)*, Tokyo, Japan, Vol. 3, pp. 126-133.
- [12] Ran, Z., Kim, M. H., 1997. Nonlinear coupled responses of a tethered spar platform in waves. *International Journal of Offshore and Polar Engineering*, Vol. 7, No. 2, pp 111-118.
- [13] Ran, Z., Kim, M. H., Niedzwecki, J. M., Johnson, R. P., 1996. Response of a Spar platform in Random Waves and Currents (Experiment vs. Theory). *International Journal of Offshore and Polar Engineering*, Vol. 6, No. 1, pp. 27-34.
- [14] Ran, Z., Kim, M. H., Zheng, W., 1999. Coupled dynamic analysis of a moored spar in random waves and currents (time-domain versus frequency- domain analysis), *Journal of Offshore Mechanics and Arctic Engineering*, Vol. 121, pp 194-200.
- [15] Tahar, A., Kim, M. H., 2008. Coupled-dynamic analysis of floating structures with polyester mooring lines. *Ocean Engineering* 35, 1676–1685.
- [16] Yang, C. K., Kim, M. H., 2010. Transient effect of tendon disconnection of a TLP by hull-tendon-riser coupled dynamic analysis. *Ocean Engineering* 37, 667–677.

# 14<sup>th</sup> Annual Research Day

Organised by the Deanship of Scientific Research in Collaboration with the College of Engineering  
Research Centre

4<sup>th</sup> April 2019

## Rock slope stability analysis by empirical and numerical methods: case study

Abdelkader HOUAM<sup>1</sup>, Riadh BOUKARM<sup>2</sup>

<sup>1</sup>Department of Civil Engineering, College of Engineering, King Khalid University,  
PO Box 394, Abha 61411 KSA.

E-mail address: ahouam@kku.edu.sa

<sup>2</sup>Civil Engineering Department, University of Bejaia – Algeria

**Abstract:** The Kef Essenoun phosphate deposit located south of the Djebel El Onk massif (Algeria), has undergone in September 2007 a major shift (rock mass of about 7.7 million m<sup>3</sup>) in its northeast flank. As a result of this accident, exploitation has turned towards the western side. However, significant cracks were observed upstream of the platform, announcing a new potential slippage, despite the overall stability observed. The aim of this paper is to study the stability of the north-western flank of the massif. The stability verification was based on an empirical method the Slope Mass Rating, *SMR* and a numerical method the finite element method, *FEM*, by using the Hoek and Brown nonlinear model, which takes, considers the distribution influence of discontinuities in a rock mass. Finally, results shows that the rock slope is unstable due the marl layer

**Keywords:** Rock mass classification - Slope Mass Rating, *SMR* - Geological Strength Index, *GSI* - Generalized Hoek-Brown criterion, *GHB* – *FEM*.

### 1. Introduction:

Slope stability is a major problem in the field of geotechnical engineering, especially that of rock masses, which, unlike soils, exhibit anisotropy of their mechanical parameters and the presence of discontinuities, which give, points of weakness to the rock mass. There are different approaches to deal with this problem and those that are most used in the field of engineering are the empirical, Limit Equilibrium and numerical methods. The empirical methods are based on the classification of the rock mass: the slope mass rating or *RMR* of Bieniawski (1989) [1] and the Slope Mass Rating or Romana *SMR* (1985) [2]. The principle of these methods consists in assignation of a score that takes into account the mechanical behaviour and distribution of the various components of a rock mass, namely intact rock or rock matrix, discontinuities and the presence of water. The stability of rock masses can also be verified by numerical methods that can be classified into three types [3]:

1. Continuous medium: Finite Difference Method (*FDM*) Finite Element Method (*FEM*), Boundary Element Method (*BEM*);
2. Discontinuous medium: Discrete Element Method (*DEM*); Discrete Fracture Network (*DFN*) Method and the hybrid methods: Hybrid *FEM/BEM*, Hybrid *DEM/DEM*, Hybrid *FEM/DEM*; and
3. Other hybrid models.

Hammah et al (2004, 2008) [4, 5] have shown that by using the Shear Strength Reduction (*SSR*) technique, numerical methods have an undeniable advantages over limit equilibrium methods in the slope stability analysis. It can be noticed through the existence of a unique failure surface, possibility of including the non-linear failure criterion Hoek and Brown. They concluded that the problem of fractured rock mass instability can also be effectively solved.

## 2. Case study

In September 2007, a landslide occurred in the Northeast flank of the Kef Essenoun phosphate deposit (Fig. 1) during which a mass of rocks estimated at 7.7 million m<sup>3</sup> detached and filled the pit (Fig. 2). Expertise and several investigations were carried out; Gadri et al. (2015) [6] concluded that the failure mode is a planar sliding occurred along the layer of altered marls.

Furthermore, the main cause was the method of exploiting the quarry from the downstream to the upstream and which consequently weakened the stabilizing base. The company (SOMIPHOS FERPHOS Group) decided to stop the exploitation and to establish a protection station (Fig. 2). Exploitation has turned towards the western side direction of flank.

Kef Essenoun quarry suffered a huge landslide in September 2007, which led to the loss of 7.7 million cubic meters of phosphate and the immediate cessation of the exploitation of the ore. The expert reports that followed this accident concluded that the slip is of the planar type along the layer of the marl and whose main cause is the no respect of the direction of exploitation from top to bottom.

The company FERPHOS then decided to install a protective station and turn the exploitation towards the North-West di The observations made since 2013 showed the appearance of cracks and fractures all around the north-west flank of the quarry and whose spread that continues to grow prompted the company began new geotechnical investigations to ensure stability of the rock mass.

The objective of this work is the verification of the stability of our case study by the two approaches namely the empirical method *SMR* slope mass rating and *FEM* thus giving more precision and reliability in the decision-making on the continued operation or permanent cessation of that part of the mine.

## *Geological Perspective*

The Djebel El Onk deposit is in the south of Tébessa province (northeast of Algeria) (Fig. 1) about 21 km to the Algerian- Tunisian frontiers. The phosphate deposits of the Djebel El Onk region are divided into five mining districts [8]: Djemi-Djema, Djebel El Onk North, Bled El Hadba, Oued Betita and Kef Essenoun. It represents more than half of the Algerian phosphate reserves. Kef Essenoun is located in the extension of the southern Cretaceous anticline of Djebel El Onk. The Kef Essenoun deposit is one of the largest, with a power of 35 to 40 m of phosphate without intercalation of waste rock. The Kef Essenoun deposit is made up from the bottom up by the following lithological successions (Fig. 3).

- Formations of the lower Thanetian (the wall of the phosphate beam) are represented by laminated marls;
- The phosphate bundle belonging to the upper Thanetian is constituted by a single layer of phosphate without sterile intercalation;
- At the roof of the phosphate beam, the calcareous-dolomitic silex series of the Ypresian appears, above which the Lutetian limestone is deposited locally, then the Miocene sands and lastly the recent Quaternary deposits consisting essentially of alluvial deposits. The total thickness of the sterile covering varies from 40 m in the north to 198 m in the south

The pit is excavated as benches with slope angles of 75° to 85°, 30 m in height, and 10 m in width. The depth of the base of mine is 70 m.

### **2.1 Empirical method**

The slope mass rating (SMR) proposed by Romana (1985) [2] is an empirical method that derives from the Bieniawski RMR method while including adjustment factors that take into account the orientations of the families of discontinuities, slope geometry, the type of failure and the mode of excavation. Romana defined the SMR by the following expression:

$$SMR = RMR_{basic} + (F_1 \times F_2 \times F_3) + F_4 \quad (1)$$

Where  $RMR_{basic}$  : Rock Mass Rating basic [5], based on the summation of 05 parameters in order to produce a final rating and whose parameters are:

- The unconfined compressive strength of intact rock ( $A_1$ )

- $RQD$  ( $A_2$ )
- The spacing of discontinuities ( $A_3$ )
- The condition of discontinuities ( $A_4$ )
- Groundwater conditions ( $A_5$ )

$F_1, F_2,$  and  $F_3$ : adjustment factors.

$F_1$  depends on the parallelism between discontinuity dip direction and the slope face dip.

$$F_1 = (1 - \sin A)^2 \quad (2)$$

Where  $A$  reflects the parallelism between discontinuity and slope strikes.

$F_2$  depends on the dip of the joints for the plane rupture mode:

$$F_2 = \tan^2 \beta_j \quad (3)$$

Where  $\beta_j$  is the dip of the joints.

$F_3$  is related to the relationship between the slope of the embankment and the dip of the joints.

$F_4$  takes into account the excavation method.

## 2.2 Numerical method

The Shear Strength Reduction ( $SSR$ ) technique is a simple approach that involves a systematic search for a stress reduction factor ( $SRF$ ) or factor of safety value that brings a slope to failure. FEM offers a number of advantages over traditional method-of-slices analysis [7] including:

1. Elimination of a priori assumptions on the shape and location of failure surfaces
2. Elimination of assumptions regarding the inclinations and locations of interslice forces
3. Capability to model progressive failure
4. Calculation of deformations at slope stress levels, and
5. Robustness – ability to perform successfully under a wide range of conditions.

In our case, the software *Phase2* performed modeling and stability verification.

## 2. Slope stability verification by empirical method

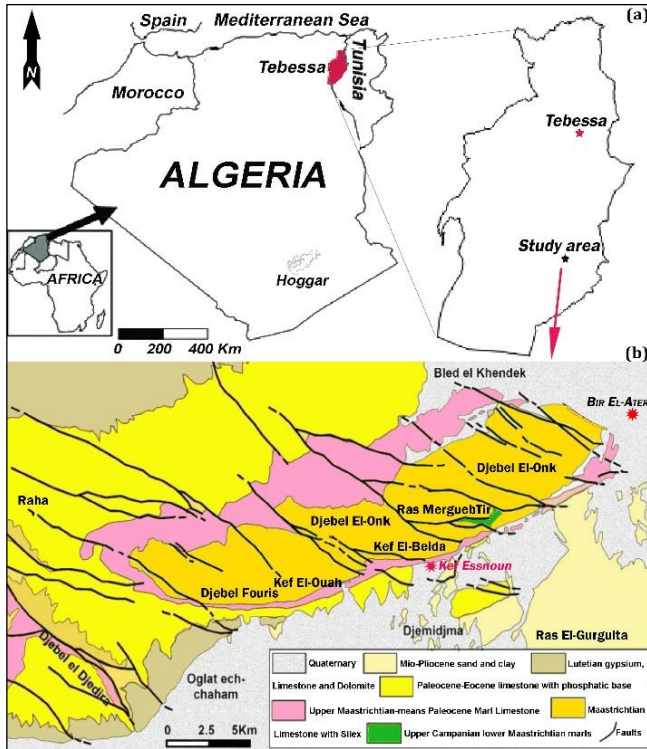


**Figure (1)** Kef Essenoun open pit position (Adapted from Google Earth)

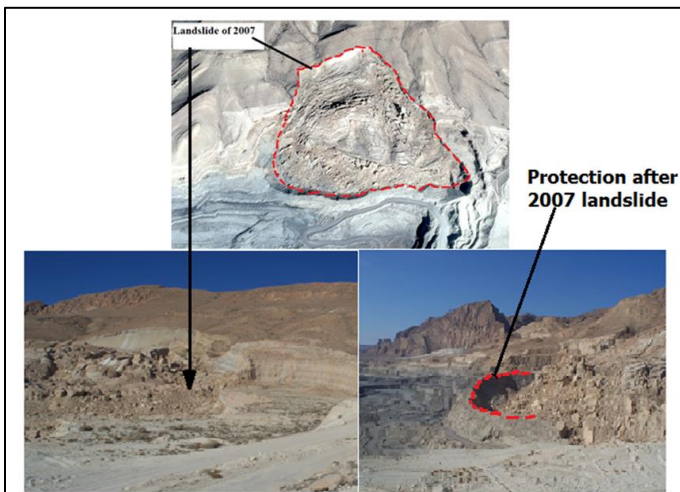


**Figure (2)** Landslide of 2007 and installation of protection

Classification of rock mass are shown in the table below

**Figure (3)** Structural Map of Northwest of Kef Essenoun

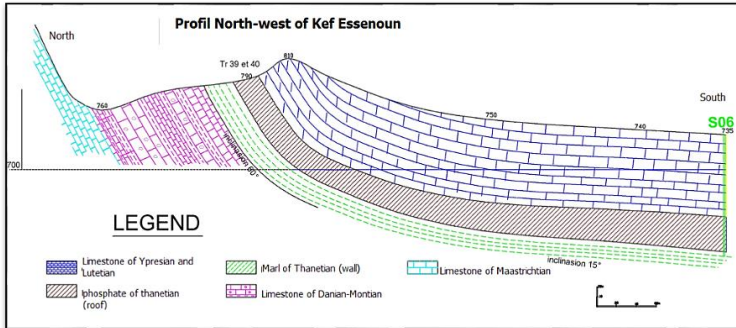


**Table 1: Classification of rock mass**

Rock type	A1	A2	A3	A4	A5	RMR basic
Limestone	4	13	15	25	15	72
Phosphate	2	17	15	20	15	69
Marl	2	08	8	10	15	43

Table 2 summarizes SMR values.

**Table 2: SMR values**

Rock type	RMR	F <sub>1</sub>	F <sub>2</sub>	F <sub>3</sub>	F <sub>4</sub>	SMR
Limestone	72	0.15	1	-6	0	71
Phosphate	69	0.15	1	-25	0	65
Marl	43	0.15	1	-60	0	1

The results in Table 2 show that the layers of limestone and phosphate are stable with respect to the orientation of the slope whereas that of marl is completely unstable. According to SMR classification, the probability of a planar failure is 90%.

### 3. Rock slope stability verification by FEM

The modeling and the study of stability by FEM was carried out through the software Phase2. A triangular element (06 nodes) was used. Uniform and dense mesh has been made (Fig.4). The failure obeys to GHB criterion

(2002) [9], which has the following advantages [10]:

- It is non- linear in form, which agrees with experimental data over a range of confining stresses.
- It was developed through an extensive evaluation of laboratory test data covering a wide range of intact rock types.
- It provides a straightforward empirical means to estimate rock mass properties.
- There is almost three decades' worth of experience with its use by practitioners on a variety of rock engineering projects.

The expression of this criterion is:

$$\sigma_1 = \sigma_3 + \sigma_{ci} \left[ m_b \frac{\sigma_3}{\sigma_{ci}} + s \right]^\alpha \quad (4)$$

Where  $\sigma_1$  and  $\sigma_3$  are respectively the effective major and minor principal stresses of the rock mass at failure.  $\sigma_{ci}$  is the uniaxial compressive strength of the intact rock and  $m_b$ ,  $s$ , and  $\alpha$  are the GHB input parameters depending on the fracturing degree of the rock mass and can be estimated from the Geological Strength Index, GSI. The disturbance factor  $D$ , and the material constant of intact rock  $m_i$ , given by

$$m_b = m_i \exp\left(\frac{GSI-100}{28-14D}\right) \quad (5)$$

$$s = \exp\left(\frac{GSI-100}{9-3D}\right) \quad (6)$$

$$\alpha = \frac{1}{2} + 1/6 \left[ \exp\left(-\frac{GSI}{15}\right) - \exp\left(-\frac{20}{3}\right) \right] \quad (7)$$

**Table 3: Hoek & Brown parameters**

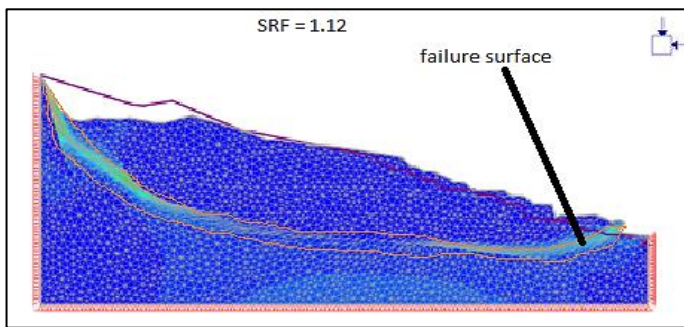
Parameters	Layers		
	Limestone	Phosphate	Marl
Hoek Brown Classification			
$\sigma_{ci}$	50 MPa	13 MPa	10,2 MPa
$GSI$	72	68	35
$m_i$	9	8	7
$D$	1	1	1
GHB Criterion			
$m_b$	1,21802	0,813611	0,067411
$s$	0,00940356	0,00482795	1,97E-05
$a$	0,50116	0,501579	0,51595

# 14<sup>th</sup> Annual Research Day

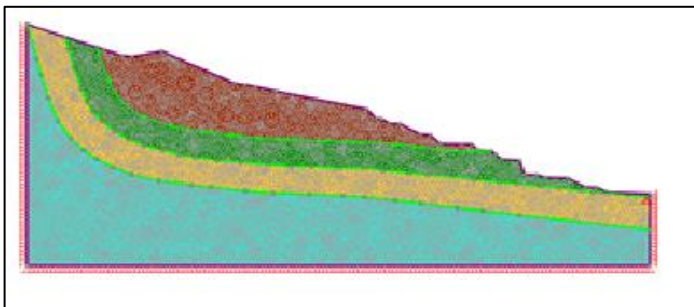
Organised by the Deanship of Scientific Research in Collaboration with the College of Engineering Research Centre

4<sup>th</sup> April 2019

The calculation results (Fig. 5) gave a critical value of  $SRF = 1.12$  and the sliding surface along



the layer of marl; which confirms the result



established through empirical methods as well, we can confirm that the slope of Kef Essenoun is unstable.

**Figure (4)** FEM model with dense and uniform mesh

**Figure (5)** FEM stability results output with failure surface

## 4. Conclusions

This study attempts to assess the geotechnical risk associated with Kef Essenoun open pit. In conclusion, the empirical and numerical methods can give similar results in rock mass stability studies, but numerical method using SSR analysis and incorporating Generalized HoekBrown criterion allow a better appreciation of the phenomenon by computing a safety factor.

## References

[1]. Bieniawski Z. T (1989). Engineering Rock Mass Classifications a Complete Manual for Engineers and Geologists in Mining, Civil, and Petroleum Engineering New York, John. Wiley & Sons

[2]. Romana M (1985). New adjustment ratings for application of Bieniawski classification to slopes. Proceedings of the international symposium on the role of rock mechanics in excavations for mining and civil works, International Society of Rock Mechanics, Zacatecas

[3]. Jing, L. (2003). "A review of techniques advances and outstanding issues in numerical modeling for rock mechanics and rock engineering." International Journal of Rock Mechanics and Mining Sciences **40**(3): 253-383.

[4]. Hammah, R., Curran, J., Yacoub, T. and Corkum, B., (2004). Stability Analysis of Rock Slopes using the Finite Element Method. *EUROCK 2004 & 53rd Geomechanics Colloquium. Schubert (ed.)*

[5]. Hammah, R., Curran, J., Yacoub, T. and Corkum, B., (2008). The Practical Modelling of Discontinuous Rock Masses with Finite Element Analysis. 42nd US Rock Mechanics Symposium and 2nd U.S.-Canada Rock Mechanics Symposium, held in San Francisco, June 29-July 2, 2008. ARMA, American Rock Mechanics Association

[6]. Gadri, L., Hadji, R., Zahri F., Benghazi Z., Boumezbeur A., Boukelloul M. L., Raïs K., (2015). "The quarries edges stability in opencast mines: a case study of the Jebel Onk phosphate mine, NE Algeria." Arab J Geoscience

[7]. Griffiths, D.V., Lane, P.A., Slope stability analysis by finite elements, *Geotechnique*, vol. 49, no. 3, pp.387-403. 1999.

[8]. Consultant BRGM – SOFREMINES (1992). "Phosphate of Djebel Onk (Algeria) Report BRGM R 36064 DEX – DMM 92." internal report.

[9]. Hoek, E., Carranza-Torres, C. and Corkum, B., (2002). Hoek–Brown failure criterion. Proceedings of the North American Rock Mechanics Society, Meeting in Toronto, TAC Conference.

# 14<sup>th</sup> Annual Research Day

Organised by the Deanship of Scientific Research in Collaboration with the College of Engineering  
Research Centre

4<sup>th</sup> April 2019

---

## Analysis of Airborne Dust Effects on Terrestrial Microwave Propagation in Arid Area

Elfaih A. A. Elsheikh<sup>1</sup>, F. M. Suliman<sup>2</sup> and Bushara S. Elnoor<sup>3</sup>

<sup>1</sup>Department of Electrical Engineering, College of Engineering, King Khalid University,  
PO Box 394, Abha 61411 KSA.  
E-mail address: eelsheikh@kku.edu.sa

---

**Abstract:** Sand and dust storms are environmental phenomena, during these storms optical visibility might be decreased, consequently, atmospheric attenuation is clearly noticed. Micro-wave (MW) and Millimeter-wave (mm) propagation is severely affected by dust and sand storms in considerable areas around the world. Suspended dust particles may directly cause attenuation and cross polarization to the Electromagnetic waves propagating through the storm. In this paper, a thorough investigation of dust storm characteristics based on measured optical visibility and relative humidity is presented. In addition, the dust storms effects of on Micro-wave and Millimeter-wave propagation have been studied based on data measured Received Signal levels (RSL) and dust storm characteristics synchronously. Analytical dust attenuation models predictions are matched to the measured attenuation data at 14 GHz and 21 GHz. It has been found that the measured attenuation is approximately ten times higher than the predicted attenuation for both frequencies.

**Keywords:** *Dust storm, Attenuation, Visibility and Microwave propagation*

### 1. Introduction:

The dust storm is a complex natural phenomenon characterized by strong winds and dust filled the air in an extensive area. Dust storm affects different parts of the world, including parts of China, India, United States of America and northeast Africa and the Middle East for a significant percentage of time annually [1]. Direct effects on wave propagation have been attributed to the complexity of the transmission medium especially at higher frequencies [2-5]. The transmission media in a dust storm is very complex compared to other transmission media.

Suspended dust particles effects on Microwave propagation has emerged as a field that attracted scholars interests recently [1-5]. Motivation to study dust storm effects stemmed from high data rates demand, quality improvement and availability of communication links. In addition, challenges to implement the

emerging 5th generation make dust storm effects on microwave propagation an inevitable problem to be addressed.

When a microwave signal encounters precipitating particles (rain, snow, and dust) the signal gets attenuated due to two physical phenomenon, (A) scattering and (B) absorption of the energy of these particles. It has been realized that the scattering effect is more severe at frequencies higher than 10 GHz [4]. Calculation of the signal attenuation induced from dust particles has been done in two ways. Either by long-term direct.

observations and statistical analysis of the measured data to articulate co-relations between the different variables [6-8] or by analysis of electrical properties of dust particles to come up with mathematical models.

All conventional methods for attenuation prediction have been based on solving Maxwell's

# 14<sup>th</sup> Annual Research Day

Organised by the Deanship of Scientific Research in Collaboration with the College of Engineering  
Research Centre

4<sup>th</sup> April 2019

equations either analytically or numerically. Numerical methods compute the scattering amplitude either by differentiation or integration using time/frequency domain, or volumetric integration of Maxwell's equations respectively [9]. On the other hand, analytical methods use certain approximations to ease such complicated calculations. Consequently, Rayleigh approximation and Mie scattering are the cornerstones of all recent analytical models [4]. Models based on numerical methods have emerged Recently, to calculate suspended dust particles effects on signal propagation[10]. Furthermore, a model has been developed as a result of a formulation of wave propagation constant based on equivalent complex permittivity [11]. Effective permittivity of dust storms has been calculated using Maxwell-Garnett formula.

Models based on numerical methods have emerged Recently, to calculate suspended dust particles effects on signal propagation[10]. Furthermore, a model has been developed as a result of a formulation of wave propagation constant based on equivalent complex permittivity [11]. Effective permittivity of dust storms has been calculated using Maxwell-Garnett formula.

Although analytical models have been developed theoretically, their depends on empirical inputs is clearly realized. Therefore, measured dust particles properties such as particle shape, size, dielectric constant, frequency, and visibility constitute main inputs of these models [12]. Consequently, variations in dust particle shape, size and dielectric constant from one place to another is a real challenge facing interested scholars[13,14].

However, different approaches are used to estimate attenuation due to dust storms based on theoretical assumption, very limited efforts are devoted to measuring attenuation incurred from a real dust storm. Long- term measurements of dust storm parameters such as visibility, humidity,

wind speed and the cross pending attenuation are very limited in the literature [9].

Therefore, this paper investigates dust storm characteristics from the presented results of measured optical visibility and relative humidity. Moreover, a comprehensive review of the available dust storm attenuation prediction models is included. In addition, the paper compares recent models predictions with the measured attenuation of two Microwave links of 2.6 km and 2.8 km operating at Ku and Ka bands (14GHz and 21GHz) respectively. This paper is organized as follows: the following section reviews the recent prediction models from the available resources. Section 3 presents measurement set up data collection and processing. Section 4 Compares between measured results and dust storms models predictions. Finally, the paper is concluded in Section 6.

## 2. Attenuation Prediction Models:

In this section, the previous works regarding the dust storm attenuation prediction models are presented. Recent mathematical models can be classified into four main categories based on their background as follows: Rayleigh approximation models, Mie scattering models, numerical models, and effective material property technique model. The coming subsections will provide a detailed review of these models.

### 2.1. Rayleigh approximation models

Rayleigh is a simple scattering approximation method which is valid when the particle is very small relative to the wave length[15]. Therefore, based on the above method a model has been proposed to estimate the suspended dust particles effects as follows [16].

$$\alpha = 566.97 \left( \frac{1}{V_0} \right) \left( \frac{r_e}{\lambda} \right) (G) \quad (1)$$

$$G = \frac{\epsilon''}{[(\epsilon'+2)^2 + \epsilon'']} \quad (2)$$

# 14<sup>th</sup> Annual Research Day

Organised by the Deanship of Scientific Research in Collaboration with the College of Engineering Research Centre

4<sup>th</sup> April 2019

Where  $\alpha$  is the attenuation,  $\lambda$  is the wavelength in meters.  $\epsilon'$ ,  $\epsilon''$ : the real and imaginary part of the dielectric constant of the dust particles.  $V_0$  is optical visibility in kilometers.  $r_e$  is equivalent particle radius in meter.

In addition, Goldhirsh derived a mathematical model based on Rayleigh approximation for dust storm attenuation expressed by[17]:

$$A = \frac{2.317 \cdot 10^{-3} \cdot \epsilon''}{[(\epsilon'+2)^2 + \epsilon''^2] \cdot \lambda} \cdot \frac{1}{V^\gamma} \text{ [dB/km]} \quad (3)$$

$V$  visibility in kilometers,  $\gamma$  consistent value equals to 1.07  $\lambda$  is the wavelength in meters.

## 2.2 Mie scattering Models

Mie scattering is suitable at a higher frequency when the particle radius is comparable to the wave length[4]. Consequently, a model has been derived to calculate attenuation as follows[18]:

$$A = \frac{r_e f}{V} (x + y r_e^2 f^2 + z r_e^3 f^3) \text{ [dB/km]} \quad (4)$$

where  $f$  is the frequency in GHz.  $r_e$  is the equivalent particle radius in meters, equal to 30  $\mu\text{m}$ .  $x, y, z$  are constants depending on the particle dielectric constant ( $\epsilon = \epsilon' + j\epsilon''$ ).

In addition, a model based on Mie scattering has been proposed considering the variation of the dust particles dimensions as follows[4]:

$$A_p = \frac{1}{V^{1.07}} [c_1'' f + c_2'' f^3 + c_3'' f^4] \text{ [dB/km]} \quad (5)$$

where  $A_p$  is the attenuation at a reference point.  $c_1'', c_2'', c_3''$  are constants.

## 2.3 Numerical Models

The numerical methods have been used to ease Maxwell equations complications especially for

the boundary conditions[9]. A combination of two methods produced the following model [10].

$$A = 8.686 \times 10^3 \sum_{k=1}^K \sigma_{ext}(k\Delta r) N(k\Delta r) \Delta r \text{ [dB/km]} \quad (6)$$

where  $K$  is an integer number of  $r_{\max}/\Delta r$ ,  $r_{\max}$  and  $\Delta r$  are the maximum particle radius in the storm and the incremental radius, respectively.

$\sigma_{ext}$  is the extinction cross section.

## 2.4 Effective material property technique

Xiao-Ying developed a model by formulating the wave propagation constant based on the equivalent complex permittivity using the Maxwell-Garnett formula. follows[11]:

$$\alpha = 8.686 \cdot \frac{2\pi}{\lambda} \left[ \frac{\epsilon_{eq}'}{2} \cdot \left( \sqrt{1 + \tan^2 \delta} - 1 \right) \right]^{\frac{1}{2}} \text{ [dB/km]} \quad (7)$$

$$\tan \delta = \frac{\epsilon_{eq}''}{\epsilon_{eq}'} \quad (8)$$

where  $\epsilon'$  and  $\epsilon''$  are the real and imaginary parts of  $\epsilon_{eq}^*$ , and  $\epsilon_{eq}^*$  is the complex relative permittivity of sand and dust.

## 3.Measurement Set Up And Data Collection :

The main objective of this paper is to compare the measured data with the recent dust storm prediction models based on different theories and techniques. Therefore, the experiment has been designed to consider all aspects such as Microwave link length, frequency, polarization, and meteorological parameters.

Measurement system constituted from two Microwave links, metrological station, and data acquisition and processing hardware. The microwave links under monitoring were operating at 14.4 GHz and 21.3 GHz with 2.6 km and 2.8 km lengths respectively. These links were located

# 14<sup>th</sup> Annual Research Day

Organised by the Deanship of Scientific Research in Collaboration with the College of Engineering Research Centre

4<sup>th</sup> April 2019

in North East Khartoum about 6 Km from Khartoum airport. Both links are not far from the Blue Nile; however, the radio links do not transverse the Blue Nile at any point. The links were installed in flat terrain.

Meteorological data was collected from an Automatic Weather Station (AWS), operating in Khartoum International Airport as an integrated weather observation system. Visibility was measured using Vaisala Transmissometer LT31, which can provide accurate and reliable measurements of the Meteorological Optical Range (MOR) from 10 to 10,000 meters with 1 min integration time and accuracy of  $\pm 3\%$ . Rainfall rate is measured with 1 min integration time and accuracy of  $\pm 1\%$  [19-20]. In addition, the automatic weather station was equipped with sensors of temperature (T), relative humidity (RH), wind speed and direction (WS, WD). Locations of the microwave links and the weather station are shown in Figure 1.

During the experiment period from 1st June 2014 to 31 May 2015, more than 22 dust storms were experienced in the city of Khartoum. Metrological parameters, as well as transmitted and received signal levels were recorded during the storm events. The receive signal levels for the microwave links 14.4 GHz with 2.6 Km and 21.3GHz with 2.8 Km were collected at Khartoum, Sudan from 1st June 2014 to 31st May.

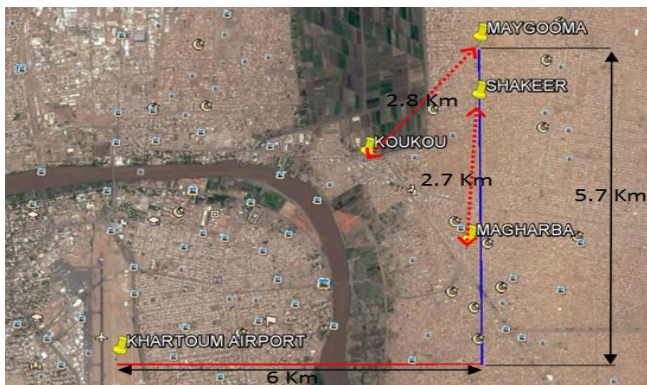


**Figure (1)** locations of the microwave links and Weather Station in Khartoum

2015 with 92 % availability. Visibility data was collected for 21 dust storm events, only one event was missed during the monitoring period

## 4. Analysis Of Dust Storm And It's Effects

Dust storms can generally be characterized by visibility and humidity parameters. The concurrently measured data on visibility and it's impacts on Shakeer- Magharba and MAYGOOMA -KOKOU microwave links are analyzed in the following subsections.

### 4.1 Optical visibility

Optical visibility has traditionally been used to measure the severity of the dust storm. It is considered such a realistic parameter that metrological observations of dust storms are based upon. Figure 2 shows the cumulative distribution function of the optical visibility based on the collected data using Vaisala Transmissometer LT31. The records include all events during which optical visibility was reduced below 10 km as a result of dust storms in Khartoum.

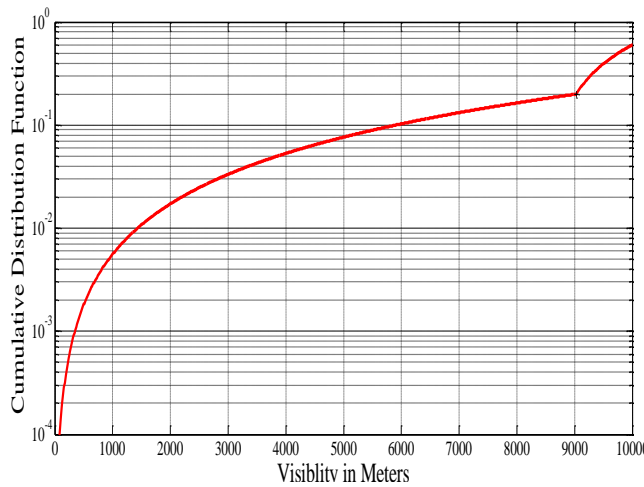
### 4.2 Relative humidity

Figure 3 shows variation in relative humidity during a recorded dust storm on 6th June 2014. It can be noticed clearly that the relative humidity increased drastically from very low to 70% during the dust storm. Measurement has shown that dust can absorb 5.1% of moisture by weight in the air with 82% relative humidity [20]. Therefore, this rapid increase in the relative humidity can continuously affect the dielectric constant of the dust and consequently degrade the signal significantly, because of the changes in the dielectric characteristics of the dust particles.

# 14<sup>th</sup> Annual Research Day

Organised by the Deanship of Scientific Research in Collaboration with the College of Engineering Research Centre

4<sup>th</sup> April 2019



**Figure (2)** Cumulative distribution of measured visibility from June 1, 2014, to May 31, 2015, in Khartoum.

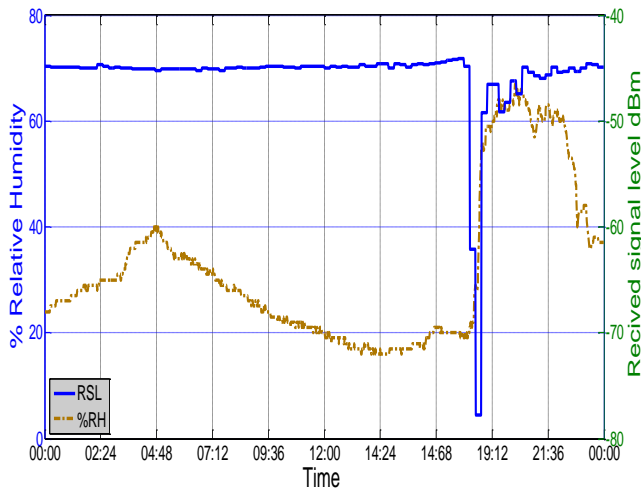


**Figure (3)** Received signal level and relative humidity on 6th June 2014.

## 4.3 Attenuation Due to Dust Storm

Figure 4 and Figure 5 present the cumulative distribution functions for the measured attenuation due to dust storm from 1st June 2014 to 31st May 2015, for the two microwave links with 2.6 km and 2.8 km path lengths operating at 14.4 GHz and 21.3 GHz, respectively. Measured total attenuation has been converted to dB/Km by assuming the intensity of dust storm is uniform over the entire link as follows

$$\frac{dB}{km} = \frac{\text{Total Measured Attenuation at 14GHz \& 21.2GHz}}{\text{Length(2.6or2.8)}}$$

However the two link lengths are almost the same, Fig. 4 shows that the measured attenuation is approaching 12 dB at 0.0001 of measurement time for 21.3 GHz link, while in Fig 5 the second link attenuation for the same percentage of time is about 6.5 dB. Therefore, for same dust storm conditions clear effect of the frequency on attenuation can be noticed.

## 5. Dust Attenuation Prediction Versus Measurement

Measured attenuation is compared at the same condition to the predicted attenuation obtained by Goldhirsh, A.S. Ahmed, Zain Elabdin, Xiao-Ying Dong Hsing-Yi Chen, and S. M. Sharif at 14 GHz and 21 GHz and is plotted in Figure 6 and 7, respectively. Equations (1), (3),(4),(5),(6), and (8) are used to predict attenuation at 14 and 21 GHz.

It has been shown that measured attenuation is greater than 6 dB/km at the lowest measured visibility 0.08 km , respectively, while for the same visibility highest analytical model the predicted attenuation is approximately 0.6 dB/km which is just one-tenth of the measured attenuation. On the other hand, Figure 7 shows that the values of the measured attenuation were approaching 11.5 dB/km , 2.7 dB/km and 1 dB/km at visibility 0.083 km , 0.279 km and 0.936 km respectively. On the contrary, analytical models predictions are close to 0.9 dB/km, 0.28 dB/km, and 0.08 dB/km at the corresponding visibility levels 0.083 km, 0.279 km, and 0.936 km respectively. It can be clearly noticed that predicted attenuation is at it's best is less than one-tenth

# 14<sup>th</sup> Annual Research Day

Organised by the Deanship of Scientific Research in Collaboration with the College of Engineering Research Centre  
4<sup>th</sup> April 2019

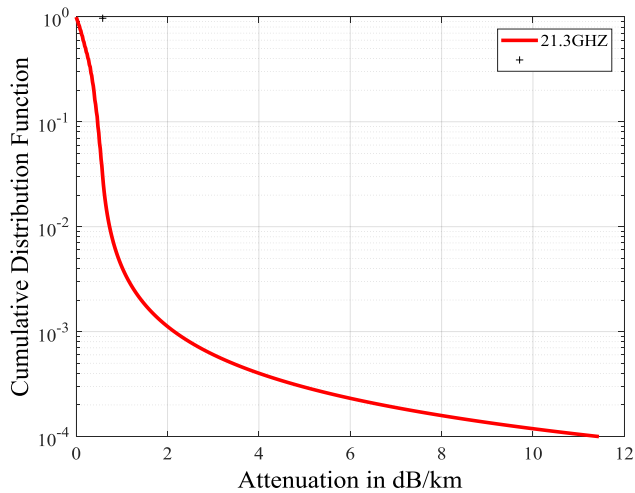


**Figure (4)** Cumulative distribution function of measured attenuation in dB/km at 21.3 GHz microwave link

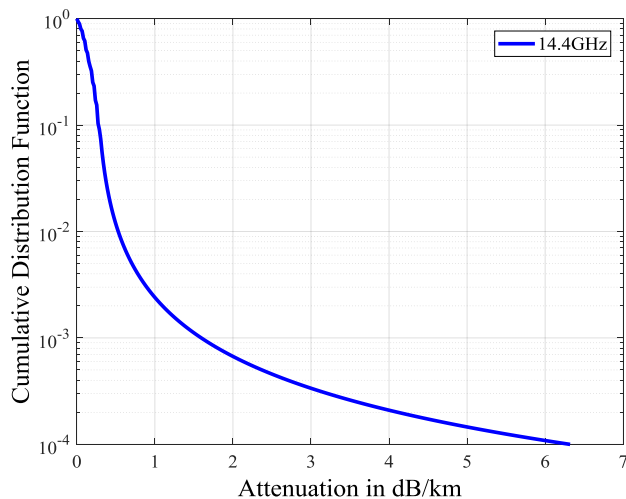


**Figure (5)** Cumulative distribution function of measured attenuation in dB/km at 14.4 GHz Microwave link.

of the measured attenuation at the same dust storm circumstances.

## 6. Conclusions:

Metrological parameters such as visibility and humidity and their effects on 14 and 21 GHz microwave propagation were measured concurrently for a one-year period in Khartoum, Sudan. Prediction models proposed by Ahmed, Goldhirsh, Elabdin, Sharif, Dong, and Hsing

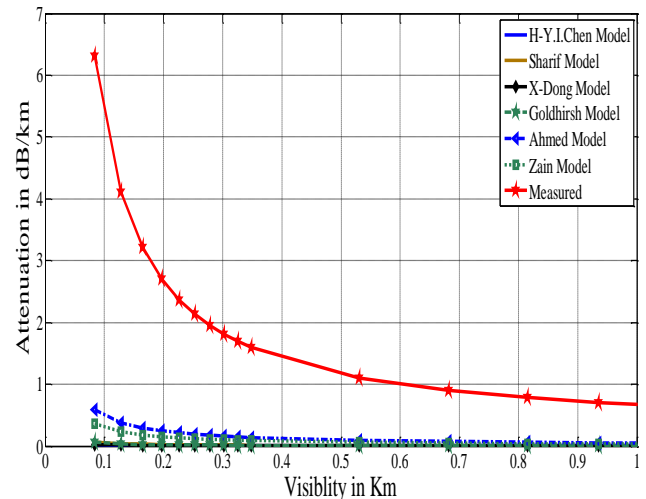


**Figure (6)** Measured and predicted attenuation at 14 GHz.

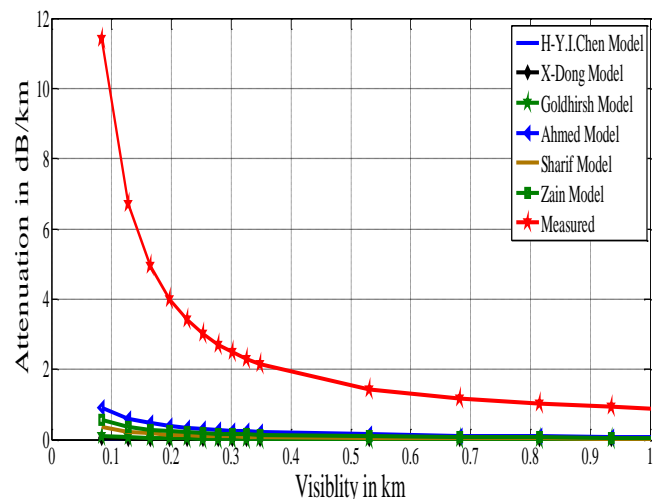


**Figure (7).** Measured and predicted attenuation at 21 GHz

to predict dust storms attenuation on Microwaves and Millimeter waves are available in the literature. Measured attenuation has been matched with analytical models predictions. It can be concluded that predicted attenuation is at its best is less than one-tenth of the measured attenuation at same dust storm circumstances for both studied frequencies. Therefore, analytical models fall away from measured attenuation for frequencies under study especially at low visibilities with the high particle concentrations. From thoroughly

# 14<sup>th</sup> Annual Research Day

Organised by the Deanship of Scientific Research in Collaboration with the College of Engineering  
Research Centre

4<sup>th</sup> April 2019

study it can be observed that the dust particle characteristics (i.e particle shape, size, and moisture content) are the main source of errors.

Hence, improving the analytical models' accuracy is one of the challenges facing researchers in this field, innovative ideas to encompass all dust particles properties, dust storm characteristics, and external environment dynamic changes are required to provide reliable predictions.

## Acknowledgement

The authors are very grateful to MTN Sudan for giving permission to monitor their links and to the Sudan Meteorological Authority for providing metrological information on a regular basis.

## References

- [1] N'tchayi Mbourou, G., J. J. Bertrand, and S. E. Nicholson, "The diurnal and seasonal cycles of wind-borne dust over Africa north of the equator," *Journal of Applied Meteorology*, Vol. 36, PP.868–882, 1997.
- [2] E. A. A. Elsheikh, et al., "A proposed vertical path adjustment factor for dust storm attenuation prediction," in *Proc. (ICOM)*, 2011, pp. 1-3.
- [3] E. A. A. Elsheikh, et al., "Proposing a horizontal path adjustment factor for microwave link's attenuation prediction based on the analysis of dust storm behavior," in *Proc (MICC)*, 2011, pp. 44-48.
- [4] Z. E. O. Elshaikh and M. Islam, "Mathematical model for the prediction of microwave signal attenuation due to dust storm", *Progress In Electromagnetics Research M*. vol.6,pp.139-153,2009.
- [5] M. R. Islam, E. A. A. Elsheikh, A. F. Ismail, S. O. Bashir, and J. Chebil, "Development of an Empirical Dust Storm Attenuation Prediction Model for Microwave Links in Arid Area - A Proposed Framework," in *proceeding of International Conference on Computer and Communication Engineering (ICCCE)*, pp. 224-227. 2014
- [6] Elsheikh, E. A. A., Rafiqul, I. M., Ismail, A. F., Habaebi, M. H., & Chebil "Dust storms attenuation measurements at 14GHz and 21 GHz in Sudan". In *Proc. International Conference on Computing, Control, Networking, Electronics and Embedded Systems*
- [7] Elfatih A. A. Elsheikh, Islam Md. Rafiqul et.al. "Dust Storm Attenuation Modeling Based on Measurements in Sudan" *IEEE Transactions on Antennas and Propagation*, DOI 10.1109/TAP.2017.2715369, Vol: 65, Issue: 8, Pages 4200-4208. June 2017,
- [8] Abdulwaheed Musa , et al., "Review and Assessment of Electromagnetic Wave Propagation in Sand and Dust Storms at Microwave and Millimeter Wave Bands — Part II" *Progress In Electromagnetics Research M*, Vol. 40, pp.101–110, 2014.
- [9] H. Y. Chen and C. C. Ku. "Calculation of Wave Attenuation in Sand and Dust Storms by the FDTD and Turning Bands Methods at 10-100 GHz." *IEEE Transactions on Antennas and Propagation* vol. 60, pp. 2951-2960,2012.
- [10] D. Xiao-Ying, et al " Microwave and Millimeter-Wave Attenuation in Sand and Dust Storms". *IEEE Antennas and Wireless Propagation Letters*. vol. 10, pp. 469-471, 2011.
- [11] S.Ghobrial and S. Sharief "Microwave attenuation and cross polarization in dust storms". *IEEE Transactions on Antennas and Propagation*. vol. 35, pp. 418-425,1987.
- [12] E. A. A. Elsheikh, M. R. Islam, et.al "The effect of particle size distributions on dust storm attenuation prediction for microwave propagation," in *proceedings of International Conference on Computer and Communication Engineering (ICCCE 2010)*, pp. 1-5. 2010.
- [13] Ansari, A. J., and Evans, B. "Microwave propagation in sand and dust storms". *IEE*

# 14<sup>th</sup> Annual Research Day

Organised by the Deanship of Scientific Research in Collaboration with the College of Engineering  
Research Centre

4<sup>th</sup> April 2019

---

- Proceedings F -Communications, Radar and Signal Processing, , Vol.129 Issue 5, PP. 315-322. ,October1982.
- [14] Vishvakarma, B. R., & Rai, C. S. Limitations of Rayleigh scattering in the prediction of millimeter wave attenuation in sand and dust storms. in Proc. (IGARSS )1993, vol.1, pp. 267-269.
- [15] Vishvakarma, B. R., and Rai, C. S. "Limitations of Rayleigh scattering in the prediction of millimeter wave attenuation in sand and dust storms." in Proc. Of IEEE International Geoscience and Remote Sensing Symposium1993, vol.1, pp. 267-269. 1993.
- [16] A. S. Ahmed, Adel A. Ali ; Mohammed A. Alhaider "Airborne Dust Size Analysis for Tropospheric Propagation of Millimetric Waves into Dust Storms." IEEE Transactions on Geoscience and Remote Sensing . vol. GE-25, pp. 593-599, 1987.
- [17] J. Goldhirsh, Attenuation and backscatter from a derived two-dimensional duststorm model. Antennas and Propagation, IEEE Transactions. vol. 49, pp. 1703-1711, 2001.
- [18] S. M. Sharif. "Attenuation properties of dusty media using Mie scattering solution." Progress In Electromagnetics Research M.Vol. 43, pp. 9-18. June 2015,.
- [19] Vaisala "Vaisala Transmissometer LT31 RVR with New Eyes," Vaisala., Helsinki, FINLAND, Tech. Rep. Ref. B210416en-C ,Vaisala 2010.
- [20] E. A. A. Elsheikh, et al., "Air Born Dust Particles Effects On Microwave Propagation In Arid-Area" in proc. of 7th International Conference on Computer and Communication Engineering (ICCCE 2018).PP.412-415, 2108.
- [21] Sharief, S.M.. "Backscatter properties of dustymedium at X band." in Proc. of Sixth International Conference on Antennas and Propagation, ICAP 89, vol.422. pp. 424-427, 1989 .

## A Novel Parallel Hardware Architecture for filter module in HEVC

Hassan Loukil<sup>1</sup>, Mohamed Abbas<sup>1</sup>

<sup>1</sup>Department of Electrical Engineering, College of Engineering, King Khalid University,  
PO Box 394, Abha 61411 KSA.  
E-mail address: hloukil@kku.edu.sa

---

**Abstract:** The de-blocking filter (DBF) constitutes an important part of the High Efficiency Video Coding (HEVC) standard. In this paper, a novel hardware architecture of the HEVC DBF is proposed for all block boundaries within a luma 32x32 coding block (CB) to reduce visual artifacts. The proposed hardware architecture employs a high degree of parallelism and includes pipeline structure in order to improve the throughput. Experimental results demonstrate that the proposed DBF architecture can reach a high operating clock frequency of 250 MHz and can support 3840x2160@50fps real-time applications on the Zynq system-on-chip (SoC).

**Keywords:** HEVC, Deblocking filter, hardware, Zynq SoC.

---

### 1. Introduction:

The High Efficiency Video Coding (HEVC) standard can be seen as an extraordinary achievement through quality and coding efficiency improvements relative to the previous video coding standards [1]. Compared to the prior major standard H.264/MPEG-4 Advanced Video Coding (AVC), the corresponding coding efficiency gain can reach 50% of bit rate reduction at the same quality. The primary goal of HEVC standard is not only to improve compression, but also to provide higher quality video in terms of higher resolutions, higher frame rates and higher dynamic range.

The power behind this video coding standard stems from the introduction of several new features, at cost of higher computational complexity. In particular, we can cite the use of the quadtree structure based on a coding tree unit (CTU) for improved prediction and transform coding. The CTU contains a luma coding tree block (CTB) and the corresponding chroma CTBs. The CTBs can be further splitted into coding blocks (CBs) along the coding tree structure including prediction blocks (PBs) and transform blocks (TBs). The size of inter-predicted PBs varies from 8x4 and 4x8, to 64x64

pixels, while the size of TBs and intra-predicted PBs varies from 4x4 to 32x32 pixels. These blocks (PBs and TBs) are coded independently from the neighboring blocks that led to create discontinuous block boundaries known as blocking artifacts. For this purpose, the HEVC standard introduces two in-loop filters, a deblocking filter (DBF) and a sample adaptive offset (SAO) which are responsible for reducing the blocking artifacts and improving quality of the decoded picture [2]. The DBF is applied first to the reconstructed samples in order to attenuate discontinuities at the PB and TB boundaries. Then, the SAO is applied to the output of the DBF to reduce the changes in the sample intensity and ringing artifacts. The DBF is quite similar to the previous one introduced in the H.264/ AVC standard, whereas SAO is recently proposed in HEVC. The HEVC DBF can achieve up to 6% bit rate decrease for certain classes of video test sequences depending on the coding configuration [2-3]. Profiling results of HEVC decoder on ARM Cortex-A9 processor illustrate that the DBF and the SAO are responsible for 17% and 4% of the decoding time [4]. Thus, reducing the complexity of DBF via a hardware

implementation represents an important research topic for real time applications.

In this paper, we focus on an efficient implementation of HEVC DBF on FPGA using a high degree of parallelism and including a pipeline structure to increase the throughput. Besides, we propose the use of an adaptive scheduling which supports all the partition types within a luma 32x32 CB.

The rest of this paper is organized as follows. In Section II, we first present background and related work. Then Section III outlines the proposed hardware architecture. The implementation results and discussion are given in section IV. Finally, Section V concludes this paper.

## 2. Background and related work:

### 2.1 Overview of Deblocking Filter in HEVC

In HEVC, the DBF attenuates discontinuities at PB and TB boundaries which may significantly affect the video quality. In order to improve both subjective and objective visual quality, the DBF is introduced to reduce the artifact by smoothing the values of reconstructed samples on the sides of the block boundary, as shown in Figure (1).

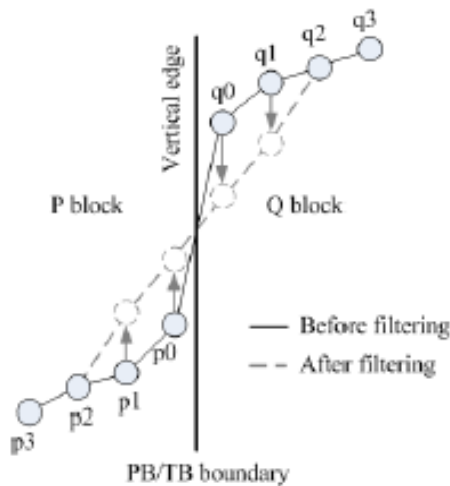


**Figure (1)** Block artifact before/after filtering Unlike H.264/AVC, HEVC applies the DBF only to the PB or TB boundaries which are aligned on an 8x8 block boundary edge instead of 4x4 block

edges. This allows more parallel processing without data dependency. When it comes to the filtering order, the vertical block boundaries are filtered first, followed by the horizontal ones. Thus, with no dependencies, all the vertical (or horizontal) block boundaries can be processed in parallel.

The boundary strength (BS) has to make a decision whether to filter a block boundary and how strong the filter is needed. The value of BS is defined between 0 and 2, and it is determined according to the bitstream information such as prediction mode, motion vector (MV), transform parameter and reference picture. The DBF is only applied when the BS is greater than zero. More details about the derivation of BS value can be found in [5].

In order to decide which filtering mode (strong or weak) to be applied, additional conditions have to be checked. Each condition is verified for the first and the fourth lines of two adjacent 4x4 blocks across the block boundary where the pixels are labeled as grey circles, as shown in Figure (2).

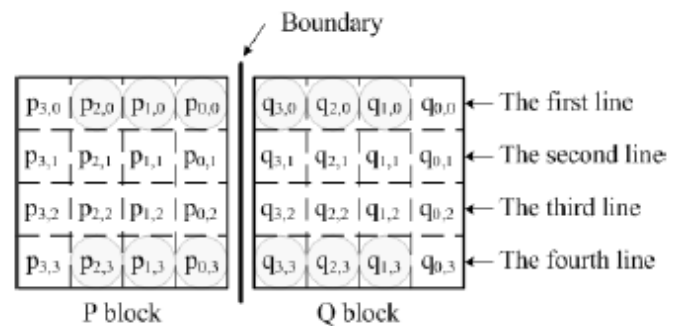


**Figure (2)** A block boundary between two adjacent 4x4 blocks (P and Q)

The filtering mode is selected according to the threshold parameters,  $\beta$  and  $t_c$ , which are derived based on the QP of P block and Q block. When a strong filtering mode is used, up to three pixels on either side of the edge can be modified in every line. However, for weak filtering mode, only two pixels can be filtered at each side of the block boundary in every line. The equations to get the filtered sample values are detailed in [6].

## 2.2 Related Work

Many research works on hardware designs for the HEVC DBF have been recently proposed in the literature [7-15]. The design in [7] proposed a multi-parallel architecture which enables to achieve a high throughput taking 280 clock cycles per 64x64 largest coding unit (LCU). Besides, it can reach 278 MHz as an operating clock frequency using a TSMC 90 nm CMOS technology. Parallel VLSI architecture was presented in [8] with a new parallel-zigzag processing order to improve the throughput by parallel vertical/ horizontal edges filtering. The proposed design by Hsu in [9] introduced novel data structures in order to enhance the timing efficiency for data accesses. Hsu's design supports identical throughput and comparable resolution as [10] with slightly less area complexity. Moreover, design illustrated in [11] reduced the intermediate data storage. The work in [11] improves the processing throughput targeting on the resolution of 7682x4320 at a frame rate of 30 fps. The design in [12] is a hardware implementation on an FPGA board using two parallel data paths that enables to code 30 fps of full HD video frames. In [13], both FPGA and ASIC implementations achieve high throughput and low area to process 4096x2048@60 fps. Finally, the works in [14] and [15] showed efficient hardware implementations on the combined DBF and SAO.

## 3. Proposed Deblocking Filter Architecture

In this section, we propose a hardware-efficient parallel architecture for the real time implementation of the DBF processing specified by the HEVC standard [16]. Actually, we propose an innovative idea to perform the filtering operations for all block boundaries supporting all the possible partition types within a luma 32x32 CB. Our architecture is the only design that realizes all edges filtering with less processing

cycles in comparison with other architectures known so far.

According to the HEVC DBF requirements, the filtering of one LCU requires the data access from upper and left neighboring LCUs. This means that the cost of memory accesses and data storage will be increased. Furthermore, the control complexity of the filtering will be very large. Therefore, it will be necessary to address this issue in order to improve the timing efficiency of memory access. The basic idea of this work is to revise the data structure as well as the filtering order. To be specific, we propose to use a modified processing unit (MPU) as the fundamental processing unit of the DBF operations. The MPU presented in Fig. 3 is defined as shifting a 32x32 CU upper left by 4x4 pixels. One MPU contains 16 single processing units (SPU) having a size of 8x8 pixels. As shown in Figure (3), each SPU consists of two vertical edges (between Bk1||Bk2 and Bk3||Bk4) and two horizontal edges (between Bk1||Bk3 and Bk2||Bk4). Each edge consists of 4 consecutive lines (or micro-edges) where each one of these includes 8 pixels along the edge.

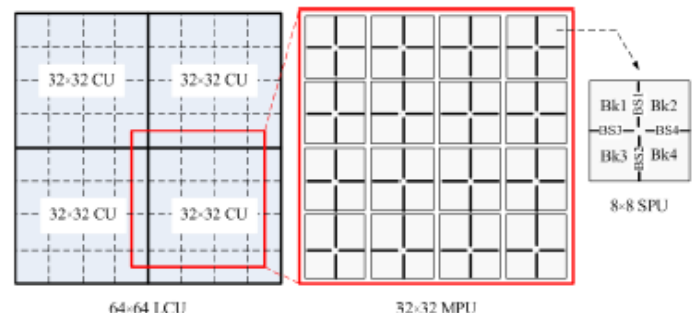


**Figure (3)** Illustration of MPU and SPU

In the proposed architecture, we perform the luma filtering of all vertical (or horizontal) edges in parallel. In other words, up to 32 edges within 16 SPUs can be operated simultaneously in order to improve the timing efficiency.

The proposed hardware architecture is presented in Figure (4).

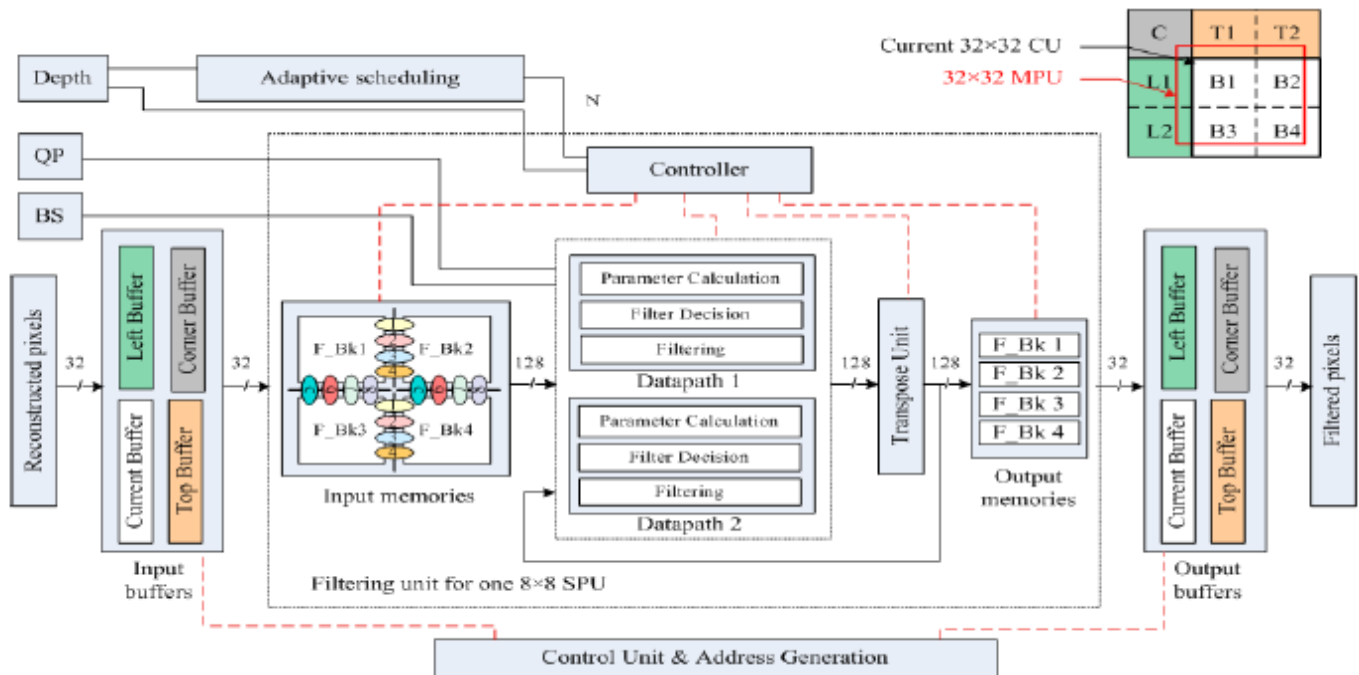


**Figure (1)** Proposed hardware architecture of HEVC DBF

This architecture includes input buffers to store reconstructed pixels, filtering unit for one 8x8 SPU, control unit for address generation, adaptive scheduling to determine the degree of parallelism and output buffers to store filtered pixels. In the current buffer, we store only the required pixels of the current CU according to the CU partition. In fact, if the size of the current CU is 32x32, we need to fetch only the 4x4 blocks adjacent to the vertical and horizontal boundaries. Furthermore, the left most 28x4 neighboring pixels of the current CU are stored in the left buffer, while the uppermost 4x28 are stored in the top buffer. The corner buffer is designed to store the upper left 4x4 pixels.

The role of the adaptive scheduling is to identify the size of the current CU according to the depth in order to determine the boundaries to be filtered. The CU partitions give us an idea about the number of filtering units to be used in parallel, so as to enable high throughput. Therefore, in order to support all possible partition sizes, the adaptive scheduling delivers six strategies of

parallelism in terms of different number of filtering units for each 8x8 SPU ( $n_{SPU}$ ) based on the CU size. Actually, our architecture can operate up to  $n_{SPU}=16$  in parallel. The scheduling of the filtering units for each SPU block is depicted in Figure (5). In the best case, we need to filter up to 8 vertical edges located on the left boundary of a CU of size 32x32 when depth=1, and 8 horizontal edges located on the top boundary. Therefore, we propose to use  $n_{SPU}=7$  where all vertical edges are processed in parallel followed by horizontal edges. Similarly, when depth=2, the current CU is divided into four 16x16 blocks and  $n_{SPU}=12$  should be selected. As a result, our multi-parallel DBF architecture can greatly improve the throughput due to reducing the processing cycles.

Each filtering unit for 8x8 SPU contains local memories to store four 4x4 blocks in different FIFOs (F\_Bk1 to F\_Bk4). It also contains two parallel data paths, where each one of these involves the filtering of four micro-edges in pipeline structure, a transpose unit and a control

module including data controller. The role of the transpose unit is to transpose a 4x4 block before starting the vertical edges filtering.

The primary function of each filtering unit is to fetch BS/QP values to perform the parameter calculation in one clock cycle. Then, it fetches the pixels from the input memories in order to determine the filter decision in 3 cycles. Finally, the strong/weak filtering operations are

performed in four-stage pipelined structure. Actually, each micro-edge is filtered in 5 cycles.

The timing schedule of the proposed architecture is illustrated in Figure (6). Thus, 32 cycles are consumed for filtering one SPU without taking account the data transfer and data storage. In addition, the data transfers, using a bus with of 32 bits, take  $16 \times n_{SPU}$  clock cycles. Therefore, a total of  $32 + 19 + (2 \times 16 \times n_{SPU})$  cycles are occupied for filtering one MPU.

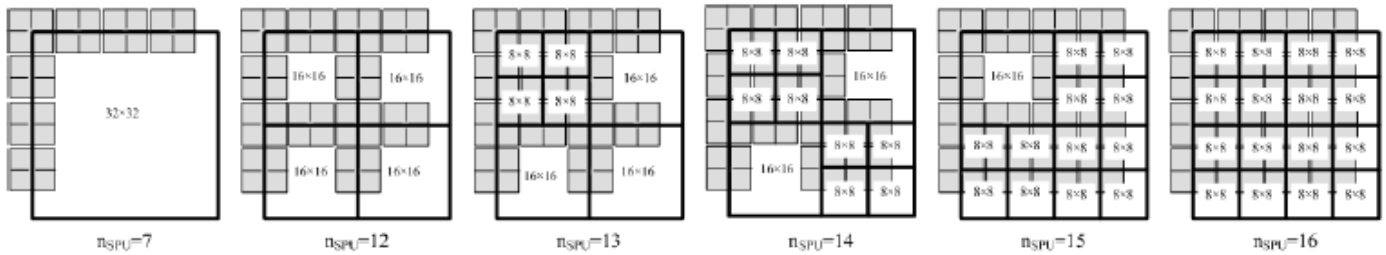


Figure (5) CU-adaptive scheduling with six strategies of parallelism

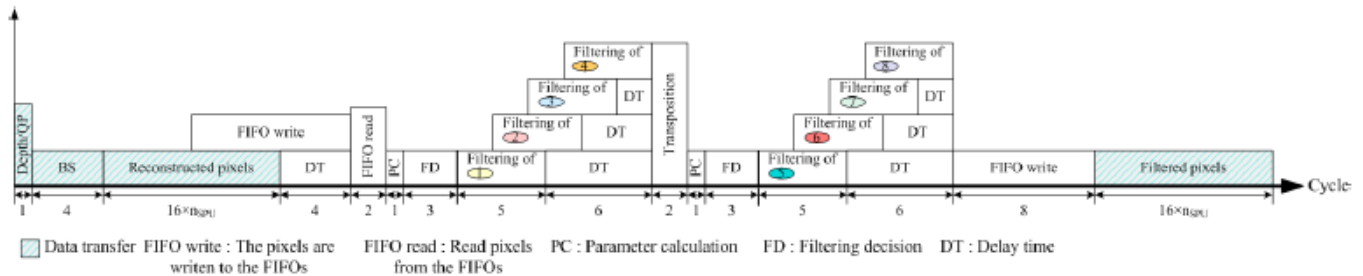


Figure (6) Timing schedule of the proposed architecture

## 4. Results and Discussion

The proposed DBF architecture was designed in VHDL and synthesized using Vivado Design Suite. The design was implemented on a Xilinx Zynq SoC based on the Z-7045. The architecture of the Zynq device combines an FPGA fabric with an ARM processor. Our architecture was implemented on the logic fabric of the XC7Z045ffg900 FPGA device with speed grade 2. The operating frequency is set to 250 MHz. The parallel architecture was tested and verified using RTL simulations where the simulation results fully conformed to the results of the

software code. The implementation results are illustrated in Table 1 in terms of resource utilization.

Table 1: FPGA UTILIZATION SUMMARY

Resources	Utilized units	Available	Utilization
Slice LUT	57456	218600	26%
Slice registers	83070	437200	19%
BRAMs	9	545	2%

# 14<sup>th</sup> Annual Research Day

Organised by the Deanship of Scientific Research in Collaboration with the College of Engineering  
Research Centre

4<sup>th</sup> April 2019

---

## 5. Conclusions:

This paper presents a hardware-efficient parallel architecture for implementing the HEVC DBF. Based on six strategies of parallelism, different number of filtering units for each 8x8 SPU has been design in order to support all the partition types within a luma 32x32 CB. Experimental results of the FPGA implementation demonstrate that the proposed architecture can achieve 50 fps for the video with a resolution of 3840x2160 pixels under an operating frequency of 250 MHz. For future work, we intend to integrate the DBF component as a coprocessor into the embedded video system in order to improve the HEVC encoder/decoder performances.

## References

- [1] G. J. Sullivan, J. Ohm, W.-J. Han, and T. Wiegand, "Overview of the high efficiency video coding (hevc) standard," *IEEE Transactions on circuits and systems for video technology*, vol. 22, no. 12, pp. 1649–1668, 2012.
- [2] A. Norkin, C.-M. Fu, Y.-W. Huang, and S. Lei, "In-loop filters in hevc," in *High Efficiency Video Coding (HEVC)*, pp. 171–208, Springer, 2014.
- [3] F. Bossen, "Common test conditions and software reference configurations," in *Joint Collaborative Team on Video Coding (JCT-VC) of ITU-T SG16 WP3 and ISO/IEC JTC1/SC29/WG11, 5th meeting*, Jan. 2011, 2011.
- [4] F. Bossen, B. Bross, K. Suhring, and D. Flynn, "Hevc complexity and implementation analysis," *IEEE Transactions on Circuits and Systems for Video Technology*, vol. 22, no. 12, pp. 1685–1696, 2012.
- [5] A. Norkin, G. Bjontegaard, A. Fuldseth, M. Narroschke, M. Ikeda, K. Andersson, M. Zhou, and G. Van der Auwera, "Hevc deblocking filter," *IEEE Transactions on Circuits and Systems for Video Technology*, vol. 22, no. 12, pp. 1746–1754, 2012.
- [6] B. Bross, W.-J. Han, G. J. Sullivan, J.-R. Ohm, and T. Wiegand, "High efficiency video coding (hevc) text spec. draft 10 (for fdis&consent)," in *JCT-VC Doc. JCTVC-L1003, 12th Meeting: Geneva, Switzerland*, vol. 1, 2013.
- [7] W. Zhou, J. Zhang, X. Zhou, Z. Liu, and X. Liu, "A high-throughput and multi-parallel vlsi architecture for hevc deblocking filter," *IEEE Transactions on Multimedia*, vol. 18, no. 6, pp. 1034–1047, 2016.
- [8] H.-H. N. Le and J. Bae, "High-throughput parallel architecture for h.265/hevc deblocking filter.," *J. Inf. Sci. Eng.*, vol. 30, no. 2, pp. 281–294, 2014.
- [9] P.-K. Hsu and C.-A. Shen, "The vlsi architecture of a highly efficient deblocking filter for hevc systems.," *IEEE Trans. Circuits Syst. Video Techn.*, vol. 27, no. 5, pp. 1091–1103, 2017.
- [10] M. Li, J. Zhou, D. Zhou, X. Peng, and S. Goto, "De-blocking filter design for hevc and h. 264/avc," in *Pacific-Rim Conference on Multimedia*, pp. 273–284, Springer, 2012.
- [11] C.-C. Fang, I.-W. Chen, and T.-S. Chang, "A hardware-efficient deblocking filter design for hevc," in *Circuits and Systems (ISCAS), 2015 IEEE International Symposium on*, pp. 1786–1789, IEEE, 2015.
- [12] E. Ozcan, Y. Adibelli, and I. Hamzaoglu, "A high performance deblocking filter hardware for high efficiency video coding," *IEEE*

# 14<sup>th</sup> Annual Research Day

Organised by the Deanship of Scientific Research in Collaboration with the College of Engineering  
Research Centre

4<sup>th</sup> April 2019

---

- Transactions on Consumer Electronics, vol. 59, no. 3, pp. 714–720, 2013.
- [13] C. M. Diniz, M. Shafique, F. V. Dalcin, S. Bampi, and J. Henkel, “A deblocking filter hardware architecture for the high efficiency video coding standard,” in Proceedings of the 2015 Design, Automation & Test in Europe Conference & Exhibition, pp. 1509–1514, EDA Consortium, 2015.
- [14] W. Shen, Y. Fan, Y. Bai, L. Huang, Q. Shang, C. Liu, and X. Zeng, “A combined deblocking filter and sao hardware architecture for hevc,” IEEE Transactions on Multimedia, vol. 18, no. 6, pp. 1022–1033, 2016.
- [15] J. Zhu, D. Zhou, G. He, and S. Goto, “A combined sao and de-blocking filter architecture for hevc video decoder,” in Image Processing (ICIP), 2013 20th IEEE International Conference on, pp. 1967–1971, IEEE, 2013.
- [16] “Hevc test model (hm) 10.0.” <https://hevc.hhi.fraunhofer.de/svn/svnHEVCSoftware/tags/HM-10.0/>.

## Design of 8b Multiplying Digital to Analog Converter in Current mode using Glitch Reduction Technique

Mohammed Abdul Muqet<sup>1</sup> Zeeshan Ahmad<sup>1</sup> Mohammed Sayeeduddin Habeeb<sup>1</sup>

<sup>1</sup>Department of Electrical Engineering, College of Engineering, King Khalid University,  
PO Box 394, Abha 61411 KSA.

E-mail address: mabdulmuqet@kku.edu.sa

---

**Abstract:** A dominant design issue of D/A converters is the accuracy, which relies on the matching capabilities of active or passive elements. A circuit that is well suited for this purpose is a R-2R ladder structure using MOS transistors instead of resistors. This paper aims to design an 8-bit Multiplying Digital to analog converter (MDAC) implemented using 90nm CMOS technology standard in current mode. The design approach involves the use of three n-type metal oxide semiconductor transistors (NMOS) for 1-bit conversion. Many applications urge for the elimination of glitch (a type of dynamic error), hence the need for glitch reduction circuitry. To enhance the performance, the proposed design incorporates the use of glitch reduction circuitry which works on the principle of sample and hold circuit (S&H) using a pulse input with peak time,  $t_p = 20\mu s$ , rise time and fall time  $t_r = t_f = 10\mu s$  applied to the gate of the NMOS transistor with width to length (W/L) ratio of 10:1 to fulfill the SAMPLE operation along with an output capacitor of about 1PF to accomplish HOLD operation. This combination optimizes the net glitch area to about 77.39%. This paper describes the use of glitch reduction technique to minimize dynamic error, thereby improving the overall performance of MDAC.

**Keywords:** Voltage & Current mode DAC, R-2R Ladder, Current Steering, Glitch reduction, sample & hold.

---

### 1. Introduction:

Telecommunication has a strong need for Analog-to-Digital and Digital-to-Analog converters with a linearity of 12 bit to 14 bits for both wireless and traditional wire-bound communication systems. In practical all of today's modern audio equipment are digital. Before one can listen to the audio signal it must be converted from the digital to the analog domain. This is achieved by digital to analog converter (DAC), whose basic function is to keep the analog output signal constant and equal to the digital input during one sample period  $T = 1/f_s$ , where  $f_s$  represents the sampling frequency.

Among variety of DAC architectures that are available, the multiplying DAC (MDAC) finds its

place as a widely used DAC in fixed reference applications. In this paper, an 8-bit MDAC was discussed and designed using NMOS transistors. An appropriate intended design can be obtained by scaling of MOS transistors to meet both speed and complexity. On the other hand, appropriate speed and minimized die area can also be achieved by using floating gate transistors. In [1], using 600nm CMOS technology, the floating gate transistors are visualized as a voltage-gated current source. Transistor matching is difficult in this type of DAC, and this can be accurately matched by using a compensation circuit and Monte-Carlo simulation [2, 3].

Practical implementation of DAC is mainly affected by its non-ideal transfer characteristics. The ideal behavior is mainly characterized by

static and dynamic performance [5]. Static errors mainly affect the accuracy of a converter when it converts the static signals. On the other hand, dynamic errors are the ones that affect the speed and are mainly caused by switching fluctuations. In this paper, the most common dynamic error 'glitch' is studied. Many glitch reduction methods are available, some of which reduces the glitch area but indeed affects the performance of the system. The main source of a glitch is during 'major carry switching activity'.

In [6], the gray code method was incorporated for reducing glitch because it switches only 1-input in a sequence of inputs. Another method is to use first-order low pass filter [7, 8] to calibrate glitch error. Another commonly used method is to use a capacitance compensation filter for segmented architecture [4] using retimed latches [9]. Using carbon nanotube FET (CNFET) in pseudo-segmented structure also reduces glitch and power consumption [10]. In [11], variable delay buffers were used for glitch reduction using current steering DAC. In [12] hybrid wideband R2RLSB segmentation with impedance attenuator was used for glitch reduction. All the methods mentioned above with compensating glitch error also affect the performance of the device in case of gray code technique, whereas some methods compensate the unwanted area in cases of designing an ideal filter.

In this paper, a sample and hold (S&H) circuitry was used [13] to reduce the glitch error that suffice the need for reducing glitch without affecting the performance of the circuit.

## 2. Proposed Design:

In this paper, the design of MDAC architectures for an 8-bit input sequence is accomplished with and without the glitch reduction technique, and the simulation results are compared to justify the efficiency of the design. With the basic R-2R design it is always possible to generate either a voltage output or current output. Generation of

voltage output requires an additional output buffer whereas for output current no output buffer is required. In this paper, the proposed circuit is designed to generate an output current.

### 2.1 8b MDAC architecture

MDAC architecture is the most flexible building block providing efficient design specifications. In this design, for each bit conversion, 3-NMOS transistor pairs under 90nm technology are used. In consistence with the traditional design of an MDAC in R-2R configuration, the implemented design for each bit operation consists of two rungs. The NMOS transistors in both the rungs were designed to operate in the triode region, whereas the third NMOS transistor operates in either weak-inversion region or active region based on the digital (LOW/HIGH) input provided for conversion expressed by the equation (1).

$$\begin{aligned} \text{For the cutoff region, } & V_{gs} > V_t \\ \text{For the linear region, } & V_{ds} < V_{gs} - V_t \\ \text{For saturation region, } & V_{ds} > V_{gs} - V_t \end{aligned} \quad (1)$$

The transistors in the circuit are designed under 8:1 and 4:1 equivalency for the parameter W/L ratio to achieve appropriate matching considerations which are shown in Table-1 along with the design considerations. The implemented circuit for MDAC is shown in Figure (1). MDAC is a low noise DAC which uses various reference voltages at every bit conversion.

### 2.2 Glitch reduction circuitry

The most common dynamic errors that affect the performance of a DAC are the glitch and settling time. In this paper, Sample and Hold (S&H) circuit was used to reduce the glitch area. The obtained analog signal was sampled using an NMOS transistor  $Q_1$  under  $2\mu\text{m}$  technology with 10:1 W/L ratio. A gate voltage was applied using a step input source with pulse time,  $T_p = 20\text{ms}$  and rise and fall time of  $T_r = T_f = 10\mu\text{s}$ . A 1pF output

capacitor was used to hold the output current as shown in Figure (2).

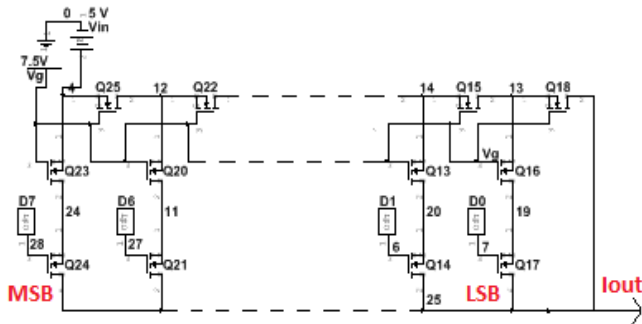


Figure (1) 8b MDAC

Table-1: Design Considerations

Parameter	MDAC	S&H
$V_{in}$	5V	-
$V_g$	7.5V	-
NMOS in linear Region	$T_1 T_3 T_4 T_6 T_7 T_9$ $T_{10} T_{12} T_{13} T_{15} T_{16} T_{18}$	-
NMOS in Cutoff /Saturation Region	$T_2 T_5 T_8 T_{11} T_{14} T_{17}$ $T_{21} T_{24}$	$T_{NMOS}$
W/L ratio	8:1(Linear) 4:1(Cutoff/Saturation)	10:1
$T_p$		20ms
$T_r$	-	10 $\mu$ s
$T_f$		10 $\mu$ s
$V_m$	-	10V
$C_{out}$	-	1pF

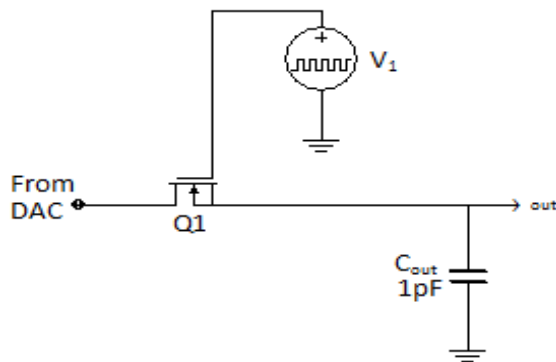


Figure (2) Sample and Hold Circuitry

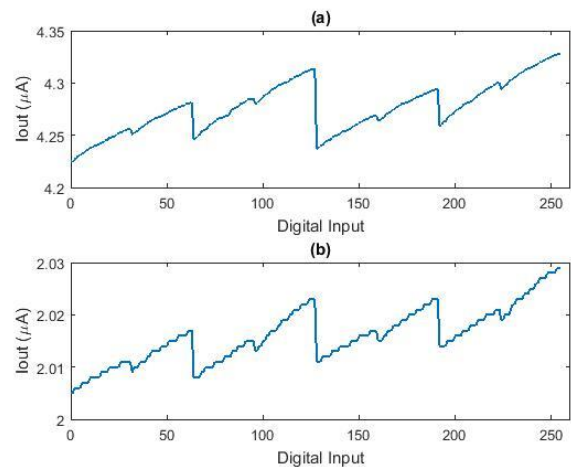
Glitch area is a measure of the area under transition of the output of DAC. In this paper, the glitch area ( $A$ ) is computed by partitioning the glitch duration, i.e., the time interval determining the start and end occurrences of a glitch into sub-intervals  $N$  as expressed in equation (2) for the specified glitch amplitude  $h_i$  at a specified interval  $w_i$ .

$$A = \sum_{i=1}^N h_i w_i \quad (2)$$

The net glitch area refers to the summation of individual glitch area.

### 3. Results and Discussion

The proposed circuit is implemented and simulated in National Instruments (NI) Multisim 13.0. The output current  $I_{out}$  was measured for the proposed design without glitch reduction circuitry as shown in Figure (3-a). The output current  $I_{out}$  is also measured for the proposed design with glitch reduction circuitry as shown in Figure (3-b). Both the results obtained are found to be proportional with the digital input code ( $D_0$ - $D_7$ ). The net glitch is calculated without and with glitch reduction technique (GRT) using equation (2) as illustrated in Table-2.



# 14<sup>th</sup> Annual Research Day

Organised by the Deanship of Scientific Research in Collaboration with the College of Engineering Research Centre

4<sup>th</sup> April 2019

**Figure (3):** (a) Proposed design without GRT, (b) Proposed circuit with GRT

**Table-2:** Net Glitch Area

Glitch occurrence	Net Glitch Area	
	Without S&H ( $\mu\text{A}$ )	With S&H ( $\mu\text{A}$ )
00011111→00100000	2.5	1
00111111→01000000	17.5	4.5
01011111→01100000	2.5	1
01111111→10000000	38.5	6
10011111→10100000	2.5	1
10111111→11000000	17.5	4.5
11011111→11100000	3	1
<b>Total</b>	<b>84<math>\mu\text{A}</math></b>	<b>19<math>\mu\text{A}</math></b>

## 4. Conclusions:

A novel deglitching method for R-2R DAC architecture is proposed and implemented under 90nm CMOS technology for 8b MDAC. Experimental results validate the glitch reduction method of sample and hold circuit. Significant glitch reduction is observed in the proposed designed. It is observed experimentally that the net glitch area is reduced by 77.39%.

## Acknowledgement

We are thankful to King Khalid University for encouraging in presenting our contribution.

## References

[1] G.Serrano, et al., "A Gloating-Gate DAC Array" in IEEE ISCAS 2004, Volume I (IEEE Cat. No.04CH37512).

[2] David Fitrio et al., "Ultra Low Power Weak Inversion Current Steered Digital to Analog Converter" in IEEE Transactions, APCCAS 4-7 Dec. 2006, ISBN: 10.1109/APCCAS.2006.342537.

[3] Jose Bastos et al., "A High Yield 12-bit 250MS/s CMOS D/A Converter" in IEEE Custom Integrated Circuits conference 06 August 2002. ISBN: 0-7803-3117-6.

[4] Feng Ye et al., "A 14-bit 2GS/s DAC with a Programmable Interpolation Filter" in IEEE 11th International Conference on ASIC (ASICON) July 2015, Electronic ISSN: 2162-755X.

[5] J De Maeyer et al., "Addressing Static and Dynamic Errors in Band pass unit Element Multibit DACs" in IEEE International Symposium on Circuits and Systems (IEEE Cat. No.04CH37512) 03 September 2004. Print ISBN: 0-7803-8251-X.

[6] Gopal Adhikari et al., "Study of Gray Code Input DAC using MOSFETs for Glitch Reduction" in IEEE (ICSICT) 03 August 2017.

[7] B.Catteau et al., "A Digital Calibration Technique for the Correction of Glitches in High-Speed DACs" in IEEE International Symposium on Circuits and Systems 25 June 2006. ISBN: 1-4244-0920-9.

[8] K.OlaAndersson et al., "Modeling of Glitches due to Rise/Fall Asymmetry in Current-Steering Digital-to-Analog Converters" in IEEE Transactions on Circuits and Systems, Vol.52, NO.11, NOVEMBER 2005.

[9] Fang-Ting Chou et al., "Glitch Energy Reduction and SFDR Enhancement Techniques for Low-Power Binary Weighted Current-Steering DAC" in IEEE Transactions on Very Large Scale Integration (VLSI) Systems, VOL.24, NO.6, 2016.

[10] P.Moslehi et al., "A 10-bit 1GS/s current-steering DAC with Carbon Nanotube Field Effect Transistor (CNFET)" in IEEE(ICDCS), April 2012.

[11] Fang-Ting Chou et al., "A Novel Glitch Reduction Circuitry for Binary-Weighted DAC" in IEEE (APCCAS) February 2015.

[12] Sang Min Lee et.al, "A 14b 750MS/s DAC in 20nm CMOS with 168dbm/Hz noise floor beyond Nyquist and 79dbc SFDR utilizing a low glitch-noise hybrid R-2R architecture" in Symposium on VLSI Circuits Digest of Technical Papers, 2015.

# 14<sup>th</sup> Annual Research Day

Organised by the Deanship of Scientific Research in Collaboration with the College of Engineering  
Research Centre

4<sup>th</sup> April 2019

---

[13] K.Khanoyan et al., "A 10b, 400MS/s Glitch-Free CMOS D/A Converter" in Symposium

on VLSI Circuits Digest of Technical Papers, 1999.

# 14<sup>th</sup> Annual Research Day

Organised by the Deanship of Scientific Research in Collaboration with the College of Engineering  
Research Centre

4<sup>th</sup> April 2019

---

## DMA communications and Photonic in chip multiprocessors: a Review

F. M. Suliman, Elfatih A. A. Elsheikh, Bushara S Elnoor

Department of Electrical Engineering, College of Engineering, King Khalid University

PO Box 394, Abha 61411 KSA.

Correspondent E-mail: fmsuliman@kku.edu.sa

---

**Abstract:** As the multi-core architectures prevail in the contemporary high-performance processor chip, design, the bottlenecks of the communication has instigated to infiltrate on-chip interconnects. With number of growing on-chip and cores computation, low- latency, a high-band width, and most, significantly infrastructure of low-power communiqué is needed critically for the upcoming generation chip multiprocessors. The latest significant advancements within the photonic elements integration and silicon photonics with standard CMOS procedure propose the utilization of the photonic networks-on-chip. The research will incorporate the fabrication of the non-blocking photonic switch. In addition, the strategic performance challenge i.e. the latency linked to the setting-up photonic paths. It can be estimated by the calculations that technique proposed can considerably decrease latency. Also, it can escalate the effective bandwidth.

**Keywords:** Photoic integration, chip multi-processors, CMOS, photonic interconnection networks

---

### 1. INTRODUCTION

Recent development of CMPs (chip multiprocessors) aimed at driving performance through increasing the amount of analogous computational cores is primarily shifted protagonist of infrastructure of worldwide communications and system interconnects [1]. Future trend is obviously on the path en route for auxiliary on-chip processing cores multiplication with one of distinctive evidence in recent presentation of 80-core multiprocessor of Intel capable of delivering the computational performance exceeding 1 TeraFLOP [2]. In the recent years, assimilated photonic technology is witnessed exceptional developments in the competences of fabrication of nano-scale devices which direct their optical properties [3]. Significantly, it escorted to development of silicon photonic device assimilation with electronics within manufacturing platforms of commercial CMOS. Photonic elements are now offered in the form of library cells within procedure of standard CMOS.

Photonic interconnection networks provide disrupting technological elucidation with primarily minimal access latencies, ultra-high communication bandwidths, and low power dissipation. In the context of CMPs, photonic NOCs give considerable diminution in power used by the intrachip comprehensive communications [4]. Photonic NoCs fundamentally alters rubrics of power scaling; because of low-loss in optical waveguides, as soon as the photonic path is developed, transmission of information from end-t-o-end starts without requirement of buffering, reiterating or regenerating.

In contrast, message is buffered in electronic NoCs, which is than rejuvenated, and then broadcasted on inner-router links number of times in transit to its destination [5]. Moreover, regenerating and switching components in CMOS ingest dynamic power that expends within the rate of data. The power ingestion of optical switching components, on the contrary, is autonomous of bit rate, so high bandwidth message are unable to devour supplementary dynamic power.

## 2. ARCHITECTURE OVERVIEW

Photonic technology gives unique benefits with regards to bandwidth and energy, however deficits two essential tasks for packet switching; processing and buffering that are challenging to implement [1, 4]. Conversely, electronic NoCs possess number of advantages in sufficient buffering space, abundant functionality, and flexibility. But, the transmission bandwidth of the NoCs is limited per line [6]. The architecture of the photonic NoC incorporates hybrid scheme, in which optical interconnection network has been deployed aimed at the transmission of prodigious bandwidth message, along with the electronic network, with similar topology as for the controlling of the optical network [7]. Both the networks have the 2-D torus topology, a topology that works well with the design of the CMP planar.

Every core of CMP is well-appointed with the gateway, the network interface, whose aim is to carry out the essential optical/electronics and electronics/optical; O/E, E/O conversions, execute number of tasks such as; synchronization, and communicate with control network. Each photonic message transmitted is heralded through a packet of electronic control i.e. a path-setup packet that can be transmitted on electronic network, setting-up plus attaining photonic pathway for message [8]. Messages buffering that is not supported by photonic network, only occurs for electronic packets throughout phase of path setup [9]. Once the path is achieved, the photonic messages can be transferred without buffering. This methodology possess number of similarities with that of optical circuit switching, a method deployed to develop an enduring connections amid the nodes within the core of optical internet. The respective section will provide the description of the primary concerns in the design and the architecture of hybrid photonic NoC [1]. Moreover, it will also include the exploration of area consumption and optical losses retrieved

from the photonic elements within a particular implementation of the network.

## 3. Building Block

Elements of modulators and photonic switching based on microring resonators are applied in silicon, along with the switching time of 30ps is also demonstrated experimentally in the figure mentioned below [10]. Their physical dimensions are small i.e. 5 $\mu$ m radius of ring, as well the power consumption, which is very small i.e. > 0.5mW when the switch is ON and approximately 1pJ to switch [11]. In case, if the switch is off, than these devices used as the passive and devour almost no power. Correspondingly, appropriate crosstalk properties are exhibit i.e. > 20dB, along with low insertion loss, about 1.5dB [12]. Typically, these switches are reported as narrow band, however, efforts of cutting-edge research are currently ongoing that are endeavouring to assemble wideband structures proficient to switch number of wavelengths concurrently, each moderated at tens of Gb/s.

Moreover, the below mention figure displays the strictly non-blocking switch with the increased interval paths in the switch [7, 13]. Numerous microrings, however, remains unchanged, which is significant for arguments of power ingestion.

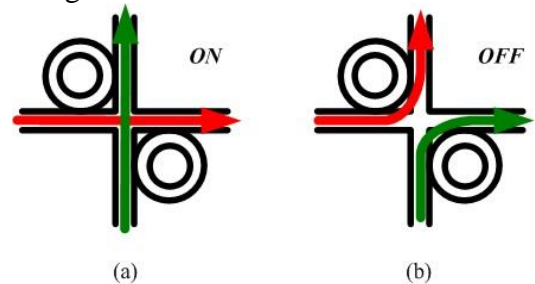


Figure 1: Photonic switching component: a) ON-state i.e. passive waveguide cusp  
b) OFF state i.e. light is tied in rings and has been forced to turn

The designed switch pledges an inner path, moves from any input towards any output

[14]. However, it only happens when no binary packets contend for similar output, in addition, in the case when the packets are not permissible to egress and ingress from similar port i.e. any U-turn is not allowed.

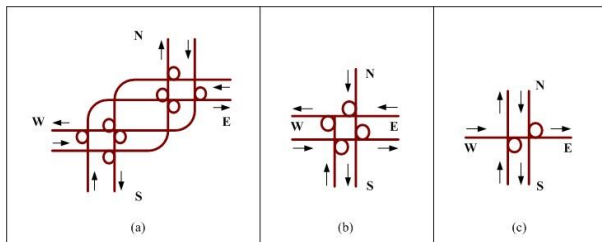


Figure 2: Outline of photonic components for (a) Routing, (b) Injection, and (c) Ejection switches

## 4. Topology

2D planar topologies i.e. tori and meshes are selected as the topologies for NoC for CMPs. Reason being, the respective topologies are particularly appropriate since, small radix of 4x4 switch [2]. Whereas, recent work proposes constructing fat-tree, interconnection networks deploying high-radix routers. However, the respective high-radix routers are extremely challenging when implemented with the photonics [3]. On the other hand, Tori provides a lower network diameter upon comparison to meshes at outlay of possessing elongated links, are hence selection, as transmission power on photonic links is considered autonomous of length, when compared with copper lines [1]. Consequently, folded torus topology has been deployed. Thus, the torus is increased with (GAPs) gateway access points linked to network borders within cores.

The GAPs are fabricated with the aim to simplify ejection and injection without intrusion of through traffic upon torus, as well to evade the blocking beaten ejected and inoculated traffic [4, 5]. These goals can be achieved with the deployment of three categories of switches within every GAP. The categories incorporate a gateway switch that is linked straight to gateway located in

processor core, along with injection switches that are situated on torus rows, along with the ejection switches that are positioned on columns of the torus [5]. Every injected message moves from gateway switch towards an ejection switch. Afterwards, it moves on network towards ejection switch linked to its terminus core from where, it be distributed to gateway switch as well as outside the network.

This has been incorporated in an explicit way with that of the loss budget that has been provided by the contemporary optical transceivers deployed within interconnects of high density [4]. It specifically utilizes those that consume sources of off-chip laser, as the DFB (distributed-feedback) lasers that have a tendency to provide output powers higher than the power of 20 dB i.e. above the sensitivities of the existing silicon optical receivers [1, 3]. Hence, it implies the practicability of hybrid methodology. Also, it has presumed loss value redirect advancements within the existing reported devices, for which the value of insertion losses are limited profoundly [1].

## 5. Flow Control and Routing

The technique of the flow control within the network is different from that of the common methods of NoC flow control [6]. The distinction stems from major variances amid the photonic and electronic technologies and primarily from concept that memory components for example; SRAM, registers etc. are prohibited for the buffering of messages or for delay during the processing [7]. Thus, electronic control packets are exchanged in order to obtain photonic paths, as well, information is transmitted in the condition when the bandwidth is very high, and one of the paths is assimilated. In addition, control packets are also deployed for the tearing down of the photonic paths once the transmission of the message is completed [8]. They are also employed for exchange of short messages.

## 6. PATH-SETUP TECHNIQUE

The procedure of the path acquirement needs path-setup package in order to travel numerous electronic routers as well experience some processing I every hop [10]. Contention may result in the blocking of the packets, leading to the latency of path-setup on order to  $10 \times 10^{-9}$ . As soon as the path is achieved, transmission latency of optical data is infinitesimal, relying upon the light group velocity in silicon wave guide; about 300 ps or  $6.6 \times 10^7$  m/s for a path of 2cm crossing a chip [9]. This mismatch of the latency is important to the communications of optical intrachip, i.e. the arbitration latency and network control, determined by the processing speed and electronic propagation velocity, can hinder the complete manipulations of latency benefits of optical transmission.

This is autonomous to if, control is carried out in distributed or centralized manner [6, 11]. Therefore, the procedure for path setup is primary concern in influencing performance of photonic NoC [1]. Reductions within the latency of the path-setup will directly interpret with the intention of enhanced network interfaces efficiency, to that of the higher average bandwidth, also for the improved manipulation of optical medium.

For the given pair of source-destination, setup latency is articulated in the form of

$$D = (H-1) \cdot t_p + t_q$$

Where,

H= hops in path of packet

$t_p$  = each router's processing latency (36=Shabani and Roohi, 2016).

$t_q$  = total additional latency because of contentions

Disputations within phase of path-setup are controlled thru arranging in line the packet of path setup till message blocking its path in turndown, clearing the path. It is evident from the simulations that  $t_q$  is regarded as the primary contributor to the latency of entire setup, specifically when network is loaded heavily [13].

In order to decrease contention-based arrangement latency, ( $t_q$ ), another technique is recommended for the handling of the congestion [2]. The new procedure depends upon statement that definite processing latency within path-setup phase i.e. H-1,  $t_p$  is lesser when compared with that of the contention based latency. In recommended modus operandi, depth of buffering within electronic router has been condensed to zero [3]. This implies that when the packet of the path; setup is blocked, it is decreased instantly. In this way, the 'packet-dropped' packet is transferred, to control network, in opposite direction with the aim to inform correspondent [1, 4].

In this way, sender can proximately endeavour to arrangement a substitute path, manipulating multiplicity of path of the network [5]. With a sufficient path multiplicity level, it is rational to undertake that it is easy to found an alternative path quicker in comparison to message blocking original path to be dismantled.

By deploying the OMNET++ based (POINTS) simulator, a 36-core system with factor of path-multiplicity factor and photonic NoC of x2 is simulated [6]. The latency components within the POINTS are based upon the projected individual latencies of photonic-silicon and electronic components within the future 22nm procedure, as well the optical size of the message are almost 16KB [7]. The results of the simulation are illustrated in the figure below.

The result display that by setting the scale of the depth of buffer to 0, that is, dropping each blocked packet and instantaneously informing sender [8]. Whereas, latency of the setup path could be reduced to about 30 percent on comparison to the packets that are not dropped on strife i.e. depth of buffer set at 2.

## 7. DMA BLOCK SIZING

The communication model of DMA (Direct Memory Access) has been deployed in number of interconnections network designs requiring

# 14<sup>th</sup> Annual Research Day

Organised by the Deanship of Scientific Research in Collaboration with the College of Engineering Research Centre

4<sup>th</sup> April 2019

rigorous bandwidth driven interactions amid the processors [9].

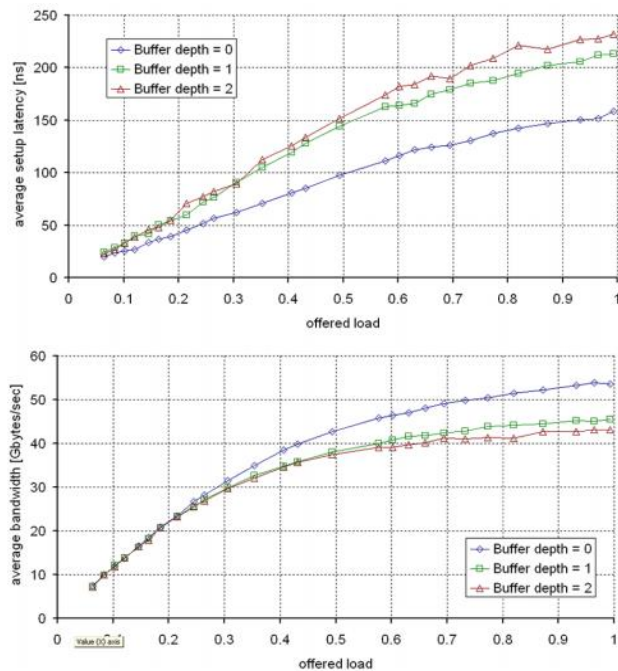


Figure 3: Bandwidth; bottom and regular path-setup latency; The top image represents the purpose of buffer depth in a 6×6 photonic NoC.

The IBM Cell EIB (Element Interconnect Bus) and QsNet II can be adopted as the illustrations. DMA is however, apposite for the respective application, reason being, it has the potential to be configured according to the transactions of even fixed, large size [11]. Such large transaction communication model, bandwidth intensive is particularly appropriate for the photonic NoC design [10]. Reason being, it possesses the potential to utilize the large network bandwidth through the reduction in the fractional over-head of the process of the path setup.

The precise modelling of DMA transaction needs acquaintance of particular implementation regarding DMA hardware. The effect of block size, however, on the average bandwidth as well as on latency within network are enthused for 6 X 6 network, for unloaded network along with network that are loaded heavily ; i.e. offered load  $\approx 0.85$  [4]. The acme

transmission bandwidth remains unchanged i.e. 960 Gb/s. Consequences are elaborated in the below mentioned figure.

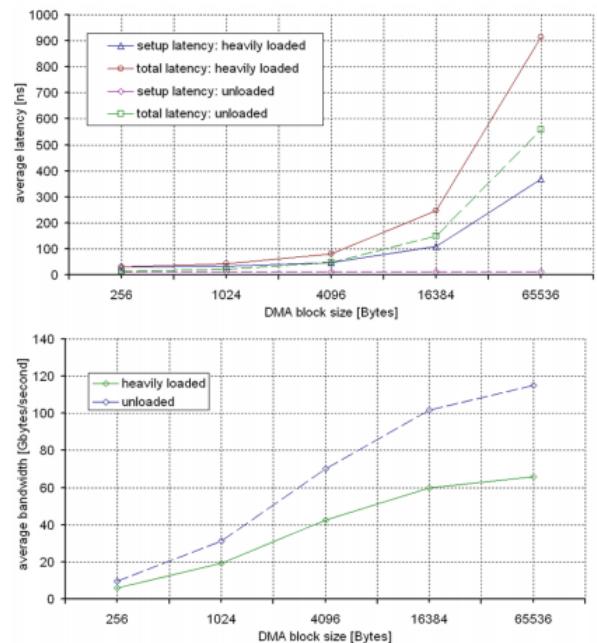


Figure 4: Average latency and bandwidth for transaction of network of number of dimensions in a 6×6 photonic NoC

## 8. CONCLUSION

As multicore processors emerged in the epoch, where bandwidth communications is regarded as the core for computing presentation, photonic NoCs provide auspicious low power elucidation, whereas providing stimulating design delinquent. The hybrid structure that has been discussed in the research of the photonic transmission NoC incorporated in electronic control NoC included design problems by deploying every technology in accordance with the advantages i.e. photonics for transmission and electronics for processing.

The latency for the path setup, has been reported as the primary key to high performance within the photonic NoS

Photonic NoC, has also been included in the research. Also, the method that decreases the problem by approximately 30 percent has been

# 14<sup>th</sup> Annual Research Day

Organised by the Deanship of Scientific Research in Collaboration with the College of Engineering  
Research Centre

4<sup>th</sup> April 2019

presented along with its evaluation in simulation. In various further high-performance network, DMA has been espoused as apt communication model due to its large block size along with possible overlap amid DMA overhead and network overhead. In addition, 4KB and 16 KB has been recognised as optimal for the network simulated within the research.

## Acknowledgements

The author would like to express his gratitude to King Khalid University, Saudi Arabia for providing administrative and technical support.

## References

1. Calhoun, D. M., Li, Q., Nikolova, D., Chen, C. P., Wen, K., Rumley, S., & Bergman, K. (2016). Hardware–Software Integrated Silicon Photonics for Computing Systems. In *Silicon Photonics III* (pp. 157-189). Springer Berlin Heidelberg.
2. Painkras, E., Plana, L. A., Garside, J., Temple, S., Galluppi, F., Patterson, C., ... & Furber, S. B. (2013). SpiNNaker: A 1-W 18-core system-on-chip for massively-parallel neural network simulation. *IEEE Journal of Solid-State Circuits*, 48(8), 1943-1953.
3. Cilaro, A., & Fusella, E. (2016). Design automation for application-specific on-chip interconnects: A survey. *Integration, the VLSI Journal*, 52, 102-121.
4. Tan, W., Zhang, B., Gu, H., & Chen, Z. (2015, July). An optimized path-setup method for mesh based Optical Network on Chip. In *Optical Communications and Networks (ICOON), 2015 14th International Conference on* (pp. 1-3). IEEE.
5. Wang, Y., Chen, Z., Chen, K., Wang, K., & Gu, H. (2015, July). An optimized optical router for mesh based Optical Networks-on-Chip. In *Optical Communications and Networks (ICOON), 2015 14th International Conference on* (pp. 1-3). IEEE.
6. Li, X., Gu, H., Chen, K., Song, L., & Hao, Q. (2016). STorus: A new topology for optical network-on-chip. *Optical Switching and Networking*, 22, 77-85.
7. Bertozzi, D., Dimitrakopoulos, G., Flich, J., & Sonntag, S. (2015). The fast evolving landscape of on-chip communication. *Design Automation for Embedded Systems, 19(1-2)*, 59-76.
8. Wen, K., Calhoun, D., Rumley, S., Zhu, X., Liu, Y., Luo, L. W., ... & Bergman, K. (2014, August). Reuse distance based circuit replacement in silicon photonic interconnection networks for HPC. In *High-Performance Interconnects (HOTI), 2014 IEEE 22nd Annual Symposium on* (pp. 49-56). IEEE.
9. Dang, D., Patra, B., Mahapatra, R., & Fiers, M. (2015, January). Mode-division-multiplexed photonic router for high performance network-on-chip. In *VLSI Design (VLSID), 2015 28th International Conference on* (pp. 111-116). IEEE.
10. Li, C., Browning, M., Gratz, P. V., & Palermo, S. (2014). LumiNOC: A power-efficient, high-performance, photonic network-on-chip. *IEEE Transactions on Computer-Aided Design*
11. Asadi, B., Reshadi, M., & Khademzadeh, A. (2016). A routing algorithm for reducing optical loss in photonic Networks-on-Chip. *Photonic Network Communications*, 1-11.
12. Shabani, H., Roohi, A., Reza, A., Reshadi, M., Bagherzadeh, N., & DeMara, R. F. (2016). Loss-Aware Switch Design and Non-Blocking Detection Algorithm for Intra-Chip Scale Photonic Interconnection Networks. *IEEE Transactions on Computers*, 65(6), 1789-1801.
13. Li, C., Gratz, P. V., & Palermo, S. (2015). Nano-Photonic Networks-on-Chip for Future Chip Multiprocessors. In *More than Moore Technologies for Next Generation Computer Design* (pp. 155-186). Springer New York.
14. Bergman, K., Carloni, L. P., Biberman, A., Chan, J., & Hendry, G. (2014). Silicon

# 14<sup>th</sup> Annual Research Day

Organised by the Deanship of Scientific Research in Collaboration with the College of Engineering  
Research Centre

4<sup>th</sup> April 2019

---

photonics. In *Photonic Network-on-Chip  
Design* (pp. 27-78). Springer New York.

# 14<sup>th</sup> Annual Research Day

Organised by the Deanship of Scientific Research in Collaboration with the College of Engineering  
Research Centre

4<sup>th</sup> April 2019

---

## Energy and Throughput of Data collection in Wireless Sensor Networks

Shamimul Qamar<sup>1</sup>, Ashraf A El Rahman<sup>2</sup>, Salman Arafath Mohammed<sup>3</sup>, Ishtiyag Ahmed<sup>4</sup>

<sup>1,2,4</sup>Department of Computer, College Computer Science, King Khalid University

<sup>3</sup>Department of Electrical, College of Engineering, King Khalid University,  
PO Box 394, Abha 61411 KSA.

E-mail address: sqamar@kku.edu.sa<sup>1</sup>, salman@kku.edu.sa<sup>3</sup>

---

**Abstract:** Wireless sensor networks (WSNs) have emerged as an effective solution for a data collection in wide range of applications. Most of the traditional WSN architectures consist of static sensor nodes which are densely deployed over a sensing area. Recently, several WSN architectures based on mobile elements (MEs) have been emerged. Wireless Sensor Networks (WSNs) are possibly one of the most important technologies of this century and have the potential to make human life more comfortable. WSNs have emerged as an effective solution applied to a wide array of problems. The increasing popularity of WSN has motivated Electrical and computer engg. For sensing and collecting data as sensors are consists of transducers and huge data. The mobile node exploit mobility and to sense the parameter to address the problem of data collection in WSNs. In this research we first define WSNs with MEs and provide a comprehensive taxonomy of their architectures, based on the role of the MEs and mobility functions. Subsequently, we present an overview of the data collection procedure in such situation, and identify the corresponding problem and challenges while node mobility. On the basis of sensing issue, A proposal of a wide-ranging survey of the related literature of sensing by node when in mobility. Finally, we propose approaches of data sensing and collection and solutions in terms of energy and throughput and sensor life in terms of sensor life, with hints and solution to open problems and future research directions.

**Keywords:** Data collection, mobility, power management, , data communication, data forwarding, sensor node.

---

### 1. Introduction:

Wireless Sensor Networks (WSN) consists of several sensor enable nodes which are distributed in an environment and use batteries as energy resource. These tiny sensor nodes, which consist of sensing, data processing, and communicating components, result in the idea of sensor networks based on collaborative effort of a large number of nodes. Such sensor nodes could be deployed in home, military, science, and industry applications such as transportation, health care, disaster recovery, warfare, security, industrial and building automation, and even space exploration.

Among a large variety of applications, phenomena monitoring is one of the key areas in wireless sensor networks and in such networks, you can query the physical quantities of the environment [1-3]. As the sensor nodes are small and battery enable devices, they have limited energy which should be used precisely. Thus, the scarce sensor resources (in particular, the battery power) are easily over consumed. Thus, the key challenge in such phenomena monitoring is conserving the sensor energy, so as to maximize their lifetime. Most of the approaches tried to response to this challenge and this will be continue to gain a better solution. In this paper,

# 14<sup>th</sup> Annual Research Day

Organised by the Deanship of Scientific Research in Collaboration with the College of Engineering  
Research Centre

4<sup>th</sup> April 2019

---

we analyze an energy-efficient and throughput in Network data aggregation approach in WSN.

There are several approaches which use tree structure for collecting and aggregating data. The presented analytical approach in [7], with combining Clustering and Directed Diffusion Protocol [8], could process, collect, and aggregate data of sensor nodes without any dependency to the related environment. This paper, with presenting a dynamic clustering structure, could enable the nodes to join to the nearest head cluster while sending data to the gateway node

## 2. Model and experimental Procedure

### 2.1 WSN Network Model

We assume that the whole network is divided in to several clusters; each cluster has a cluster-head (CH). The clustering and the selection of cluster-head (CH) can be done by using any existing protocol like LEACH, or the optimized versions of LEACH such as [9] and [12]. The proposed algorithm works in each cluster independently and performs in two phases.

### 2.2 Experimental Procedure

In this phase, the cluster head collect the information from the node transmit the information packet to its neighbors. The information packets include the information below:

- Node's location: Each node should now it location in prior
- Current Energy: Remaining energy of a node
- Hop count: Number of hops from cluster head
- Data Label: Data value which is sensed by a node When a node receives the information packet, it considers the sender as one of its possible parents and stores its information.

Then, it updates the node location, current energy and data label fields of the packets with its own, increments the hop count and transmit the packet to its neighbors. This process will be done until all the nodes in the cluster receive the information packet.

### 2.3 Energy Model for WSN

Energy Model Our energy model is like the energy model in [11]. In this model energy consumption for transmitting K bit is equal to directly proportional to distance square : And the energy for receiving K bit is depend on number of bits In these equations, a constant value which relates to the distance between two nodes and the parameters below are the constant values which are defined previously and they are equal to: 200 pJ bit m 50 nJ bit amp Eelec.

## 3. Results and Discussion

The is simulated and evaluated with MATLAB Based simulator. This is simulation software selected to implement the model. It was chosen because it is component-based, a feature that enables users to modify or improve it. The MATLAB uses the concept of components called node instead of the concept of having an object for each individual node and uses three top level components: the target node which produces stimuli, the sensor node that reacts to the stimuli, and the sink node which is the ultimate destination. For stimuli reporting, each component is broken into parts and modeled differently within the simulator; this eases the use of different protocols in different simulation runs. In our simulation analysis, sensor nodes are randomly distributed in a 150 m × 150 m area. The radio range of each node is 50 m and the default parameters for radio communication model of above are used. The cluster-head is formed by the sink. Source node randomly sends packages with constant bit rate (CBR) to the sink. Packet size is 64 bytes and package rate is 8 pkt/s.

# 14<sup>th</sup> Annual Research Day

Organised by the Deanship of Scientific Research in Collaboration with the College of Engineering  
Research Centre

4<sup>th</sup> April 2019

**Table 1: Residual Energy Vs Time**

Time	Leach(J)	V Leach (J)
5	14	14
15	14	14
25	14	13
35	13	12
45	13	11

**Table 2: Throughput Vs Time**

Time	Leach(Mbps)	V Leach(Mbps)
5	350	400
15	350	400
25	350	400
35	350	400
45	350	400

According to Table 1, the total residual energy of the nodes is decreasing as time, gradually. But comparing to other approaches, the proposed approach, because of using the mentioned technique, can remain more energy. Table 2 illustrates the throughputs of the mentioned approaches. Throughput of a node is defined as the average rate of successful message delivery over a communication channel. Thus, we can observe that V Leach has the highest throughput among LEACH and VLEACH.

## 4. Conclusions:

In this analytical work, we analyzed an energy-efficient data and throughput in data collection approach in wireless sensor networks which uses an efficient strategy to forward data toward the best route based on minimum energy. In our algorithm V Leach, there are three factors which enable the nodes to choose an appropriate parent in terms of energy. These factors are distance, residual energy and data correlation. With the suggested mechanism, the remaining energy of the nodes will be increased and the life time of the whole network will be increased, as all nodes need minimum energy.

## Acknowledgement

The authors would like to express their gratitude to Deanship of Scientific Research King Khalid University, Abha, Saudi Arabia for providing administrative, financial and technical support under grant number G.R.P 261/2018.

## References

- [1] Akkaya, K. and Younis, M. 2004. Energy-aware routing to a mobile gateway in wireless sensor networks. In Proceedings of the 47th IEEE Global Telecommunications Conference Workshops (GlobeCom 2004).16–21.
- [2] El-Moukaddem, F., Torng, E., Xing, G., and Kulkarni, S. 2009. Mobile relay configuration in data-intensive wireless sensor networks. In Proceedings of the 6th IEEE International Conference on Mobile Ad Hoc and Sensor Systems (MASS 2009). 80–89.
- [3] Anastasi, G., Conti, M., and Di Francesco, M. 2008. Data collection in sensor networks with Data Mules: an integrated simulation analysis. In Proceedings of the 13th IEEE Symposium on Computers and Communications (ISCC 2008). 1096–1102.
- [4] Haas, Z. J. and Small, T. 2006. A new networking model for biological applications of ad hoc sensor networks. IEEE/ACM Transactions on Networking (TON) 14, 1 (February), 27–40. IEEE 802.15.4 2006. IEEE 802.15.4, Part 15.4: Wireless Medium Access Control (MAC) and Physical Layer (PHY) Specifications for Low-Rate Wireless Personal Area Networks (LR-WPANs). Revision of IEEE Std 802.15.4-2003.
- [5] Juang, P., Oki, H., Wang, Y., Martonosi, M., Peh, L., and Rubenstein, D. 2002. Energy-efficient computing for wildlife tracking: Design tradeoffs and early experiences with ZebraNet. In Proceedings of the 10th International Conference on Architectural Support for Programming

# 14<sup>th</sup> Annual Research Day

Organised by the Deanship of Scientific Research in Collaboration with the College of Engineering  
Research Centre

4<sup>th</sup> April 2019

---

Languages and Operating Systems (ASPLOS 2002). 96–107.

[6] Schwager, M., Rus, D., and Slotine, J.-J. 2009. Decentralized, adaptive coverage control for networked robots. *International Journal of Robotics Research* 28, 3, 357–375.

[7] Luo, J., Panchard, J., Piorowski, M., Grossglauser, M., and Hubaux, J.-P. 2006. MobiRoute: Routing towards a mobile sink for improving lifetime in sensor networks. In *Proceedings of the 2nd IEEE International Conference on Distributed Computing in Sensor Systems (DCOSS 2006)*. 480–497

[8] Wang W, Srinivasan V, Chua KC. Extending the lifetime of wireless sensor networks through mobile relays. *IEEE/ ACM Transactions on Networking*. 2008; 16(5):1108-20. Crossref

[9] D. Turgut and L. Bölöni, "Heuristic approaches for transmission scheduling in sensor networks with multiple mobile sinks," *The Computer Journal*, vol. 54, pp. 332-344, 2011.

[10] A. Bounceur, "CupCarbon: a new platform for designing and simulating smart-city and IoT wireless sensor networks (SCI-WSN)," in *Proceedings of the International Conference on Internet of things and Cloud Computing*, 2016, p. 1.

[11] W. R. Heinzelman, A. Chandrakasan and H. Balakrishnan, "Energy-Efficient Communication Protocol for Wireless Microsensor Networks," *Proceedings of the 33rd Annual Hawaii International Conference on System Sciences*, Cambridge, 4-7 January 2000, p. 10. doi:10.1109/HICSS.2000.926982

[12] S. Hwang, G. J. Jin, C. Shin and B. Kim, "Energy-Aware Data Gathering in Wireless Sensor Networks," 6th IEEE conference on Consumer Communications and Networking, CCNC, Las Vegas, 10-13 January 2009, pp. 1-4.

[13] C. K. Liang, J. D. Lin and C. S. Li, "Steiner Points Routing Protocol for Wireless Sensor Networks," 5th International Conference on Future Information Technology (Future Tech), Busan, 21-23 May 2010, pp. 1-5.

[14] Z. G. Sun, Z. W. Zheng, S. H. Chen and S. J. Xu, "An Energy-Effective Clustering algorithm for Multilevel Energy Heterogeneous Wireless Sensor Networks," 2nd International Conference on Advanced Computer Control (ICACC), Shenyang, March 2010, Vol. 3, pp. 168-172.

[15] A. M. Brisha, "Classifying Sensors Depending on their IDs to Reduce Power Consumption in Wireless Sensor Networks," *International Journal of Online Engineering*, Vol. 6, No. 2, 2010, pp. 41-45.

[16] C. Intanagonwiwat, R. Govindan and D. Estrin, "Directed Diffusion: A Scalable and Robust Communication Paradigm for Sensor Networks," *Proceedings of Sixth Annual International Conference on Mobile Computing and Networking (MobiCom 2000)*, Boston, August 2000, pp. 56-67.

[17] J. Heidemann and F. Silva, C. Intanagonwiwat, R. Govindan, D. Estrin and D. Ganesan, "Building Efficient Wireless Sensor Networks with Low-Level Naming," *Proceedings of the Eighteenth ACM Symposium on Operating Systems Principles*, Vol. 35, No. 5, 2001, pp. 146-159. doi:10.1145/502034.502049

# 14<sup>th</sup> Annual Research Day

Organised by the Deanship of Scientific Research in Collaboration with the College of Engineering  
Research Centre

4<sup>th</sup> April 2019

---

## Energy Efficiency mechanism for Wireless Sensor Networks

Monji Zaidi<sup>1</sup>, Imen Bouazzi<sup>2</sup>, Mohammed Usman<sup>1</sup>, M.Z Shamim<sup>1</sup>, M.H Ouni<sup>3</sup>

<sup>1</sup>Department of Electrical Engineering, College of Engineering, King Khalid University

<sup>2</sup>Department of Industrial Engineering, College of Engineering, King Khalid University

<sup>3</sup>Department of Civil Engineering, College of Engineering, King Khalid University

PO Box 394, Abha 61411 KSA.

E-mail address: izaidy@kku.edu.sa

---

**Abstract:** Over the last few years, energy optimization in Wireless Sensor Networks (WSNs) has drawn the attention of both the research community and actual users. Sensor nodes are powered by attached batteries that are considered as a critical aspect of sensor nodes design. In addition, the constraint of the limited battery capacity is associated with the concern on how to reduce the energy consumption of nodes in order to extend the network lifetime. In this context, the purpose of this study is to implement an adaptive Medium Access Control (MAC) for energy saves and traffic condition enhancement using the IEEE-802.15.4 technology. This finding implements a new hybrid protocol that combines both the Carrier Sense Multiple Access with Collision Avoidance (CSMA/CA) and the Time Division Multiple Access (TDMA) methods to schedule the medium access control. This program was designed to arrange nodes into two priority groups according to their traffic rate and data transmission packet delay. Nodes that have high traffic rate and random data transmission packet delay should transmit their data immediately during the Contention Access Period (CAP) using a fuzzy logic algorithm. This fuzzy algorithm depends on their queue length where it is implemented into the CSMA/CA algorithm. However, other types of nodes should send their data during the Contention Free Period (CFP) with a GTS reallocation scheme. Those nodes are classified as low priority access to the medium and their data transmission is scheduled using time division multiple access methods. Moreover, this proposed scheme dynamically adjusts the CAP length to ensure that nodes can complete their data transmission during the same super-frame. Simulation results are done using the Network Simulator tool (NS-2) and it has improved efficiency regarding the IEEE-802.15.4 standard.

**Keywords:** Data transmission, Energy consumption, Priority, Queue, Traffic.

---

### 1. Introduction:

There has been significant research on traffic management system using WSNs in order to optimize the energy consumption and to ensure the priority for emergency condition. Several research aims to discuss MAC protocols that involve energy optimization and priority based allocation. During the last few years, a high number of researches have been concentrated on improving energy consumption and reducing delay for WSNs [1-4]. Furthermore, data transmission management was also being a

challenging task for the IEEE-802.15.4 to improve the QoS [5-7] by a new slot allocation scheme. The most research optimize the CSMA/CA method of the IEEE-802.15.4 to improve the quality of service, this method is widely used and recently gained renewed attention. Moreover, there are new techniques applied to schedule the communication and access the medium by using priority schemes. Those protocols optimize energy consumption and improved the Quality of Service (QoS), but certainly there are some expenses of something else.

# 14<sup>th</sup> Annual Research Day

Organised by the Deanship of Scientific Research in Collaboration with the College of Engineering  
Research Centre

4<sup>th</sup> April 2019

---

Various MAC protocols have been developed and studied to improve power saving [8, 9]. Multi-mode Sensor MAC protocol (MMSMAC) classified nodes into different cluster according to the application demands and traffic load. In this work, a two-tiered communication between nodes and the PAN coordinator in the network is discussed. Two groups of priority are defined in order to give priority for nodes to access the channel before other nodes. The first group of nodes is characterized by an emergency data in which devices are prioritized to send their data during the CAP period. Each transmission is managed by the PAN coordinator that provides information about the situation of the network, while the second group contains periodic traffic rate and periodic transmission during CFP. The main purpose of this work is to improve the energy consumption in WSNs under the MAC sub-layer. Sensors have a small size in which their batteries cannot be recharged or replaced, for this reason improving their energy consumption can optimize their network life time. The motivation behind this work is to propose a dynamic mechanism to adapt nodes for different traffic condition. This contribution uses a hybrid mechanism to schedule communication in the network depending on the traffic rate and data packet transmission delay of each node. The dynamic classification is used in order to perform communication in WSN and optimize the energy consumption.

The WSN is an interesting area for modern day research groups. Also, the QoS is an important factor used to improve the performance of WSN, such as increasing the throughput and reducing the delay. Furthermore, varying the inter arrival frame and allocate different level of priority for nodes can really minimized the energy consumption [10], where, a priority scheme was developed by an arrival priority queue. A dynamic adjustment of data transmission delay was also studied to improve the energy consumption and to prolong the network lifetime [11]. Authors focus on the dynamic adaptation of

the duty cycle based on feedback information concerning energy consumed by every packet delivery flow. In Wireless Body Area Network (WBAN), optimizing energy by a modulation method based on computing energy consumed was developed [12]. This scheme was specified by the IEEE-802.15.4 to improve the network lifetime. Also authors in [13, 14] was modified the sleep time in order to reduce energy consumption, in which they presented a cross-layer solution based on combined use of duty-cycling MAC protocol. They changed the activation of the antenna relatively on information coming from both MAC and network layers. In [15] a hybrid CSMA/CA-TDMA scheme to evaluate the congestion and the collision problem in the network was proposed. They used a Markov Decision Process as transmission strategies to access both the CAP and the CFP period. Proposed method used a queue status to evaluate congestion and provide an offered traffic to do not go beyond the channel capacity. Authors in [16] suggested an approach to evaluate the IEEE-802.15.4 standard during the CAP and the CFP period. These approaches looked forward to effectively allocate an adequate Guaranteed Time Slot (GTS) for the desired node. Based on the packet data length, duration of the slot will dynamically change. A Markov chain model is used to adjust the length and the start time of the GTS slot based on the length of packet. In articles [17] and [18], authors proposed a priority-based MAC protocol to evaluate the IEEE-802.15.4 performance. They dynamically allocated slots of time based on traffic priority information to reduce effectively the access delays. Improving the energy consumption was also achieved in [19] by introducing a priority level MAC to transmit data. A priority bit was added in the beacon frame to decide the type of data transmission.

Several method of energy optimization was developed in the literature. We have introduced a new scheme in WSN using the IEEE-802.15.4 technology communication between nodes. So, the aim of this work is to implement an adaptive

MAC algorithm for energy efficiency and traffic control enhancement. For the intended protocol, particular information about the situation of nodes must be gathered and transmitted to the Personal Area Network (PAN). Moreover, this information will be stored and then transmitted in the next super-frame. The transmission procedure will be scheduled according to traffic information and data packet transmission delay of each node. Therefore, the elasticity of the transmission procedure in this proposed contribution can improved energy consumption and also allow nodes to send data with low probability of collision. Thus, the proposed scheme used a hybrid transmission method which use both CSMA/CA and TDMA method for tow priority groups of nodes. This paper is structured as follow: Section 2 presented the control strategy of DAMT algorithm. Section 3 and 4 describe the TC-MAC based algorithm of the GTS reallocation. Next, experimental results are developed in section 5 and finally, section 6 concluded the paper.

## 2. Control strategy of the hybrid mechanism

### 2.1 traffic control mechanism

In this section, a brief description of the DAMT (Dynamic Adaptation Mechanism for Traffic) algorithm [21] is described. The proposed works classify nodes into two cluster types; first, author measured the traffic rate and calculated the time needed to transmit one data packet. Then, according that information collected after several simulations, they assume that nodes which have high traffic rate and random data packet transmission delay are considered as emergency nodes in group one. Those types of nodes will have the priority to access to the medium immediately without reservation of any GTS slots, by scheduling their data transmission using the CSMA/CA method during the CAP period. Those nodes will be classified later according to their queue length using a fuzzy logic rule as described and explained in [23]. The use of fuzzy sets allocated with a priority level guarantees a

deterministic power saving, consider the following:

- |       |  |
|-------|--|
| (i)   | Inputs parameters: Queue length and traffic rate   |
| (ii)  | Output parameter: Priority to access to the medium |
| (iii) | Rules:   |
|       | High priority → BE --, MacMaxCSMABackoffs --;      |
|       | Medium priority → BE = 2, MacMaxCSMABackoffs = 2;  |
|       | Low priority → BE ++, MacMaxCSMABackoffs ++;       |

In the fuzzy logic algorithm presented in [22], nodes are classified into three level of priority according to their queue length and their traffic rate. This mechanism dynamically adjusts the backoff exponent (BE) value by increasing its value or decreasing it depending on the priority level of nodes. Whenever nodes have a full buffer size and a high traffic rate, the value of BE should be decreased to minimize the time needed to access to the medium and vice versa. This mechanism is implemented into the CSMA/CA method of the NS-2 library. On the other hand the rest of nodes, that do not satisfy the proposed condition, are considered as normal nodes in the second group. The data transmission phase for the second type of nodes will be done only during the CFP period. The data transmission procedure is illustrated in Fig.1. The hole communication between nodes in group one and the PAN coordinator is done only during the CAP period, otherwise for nodes in group two the channel access and the reservation of GTS slots are done during the CAP period, however their data transmission is done during the CFP period using their reserved GTS slots. The PAN coordinator is the node in charge who broadcast beacon frames including all the necessary information including the priority type and the parameter presented the CAP length. After each operation an acknowledgment frame is delivered from either the PAN coordinator or nodes.

A hybrid use of both CSMA/CA and TDMA methods to transmit data is used to provide considerable guaranteed transmission. First step,

# 14<sup>th</sup> Annual Research Day

Organised by the Deanship of Scientific Research in Collaboration with the College of Engineering  
Research Centre

4<sup>th</sup> April 2019

we measured the traffic rate of each node and the time needed to transmit one data packet. This information will be sent to the PAN coordinator to be dealt later, to decide which priority group it is. An indicator of the priority of nodes is appended by adding one bit field into the beacon frame to schedule communication; this will be explained in the next subsection. According to the measured information, the PAN indicates that urgent data are considered as a high priority data packet when the bit is set to 1 and non critical data when it is set to 0. If this bit is set to 1, so transmission will be performed during CAP period, and if it is set to 0 then transmission will be performed during CFP period. If the measured traffic is greater than 50 Kbps and the time needed to transmit data packet cannot be estimated and it is variable from one node to another, in this case we mentioned that the data will be transmitted during the CAP period. When nodes are appreciated to have an unpredictable wakeup-sleep period, in case of having high traffic in the network, this may have more energy consumed in listening to the channel.

In the step number two, the transmission is decided to be in the CAP period, nodes are classified one more time according to their queue size and their traffic rate in the network. As already said, the modified CSMA/CA method is used to transmit data by adjusting the BE value in order to provide nodes that may have lost packets. Then in the step three, an incrementation of the CAP length period is done in order to prolong this period to support more slots. On the other hands, nodes with less priority will have a GTS slot reserved for data transmission, so we minimized the CAP length to avoid the problem that CFP period has not enough slots to transmit data packets. This adjustment can improve delay and energy consumption to not defer transmission in the next super-frame.

## 2.2 CAP length adjustment

The IEEE-802.15.4 is the most suitable MAC choice for optimizing the energy consumption

where he is flexible for any changes. To get information about the slot times duration in a super-frame, the duration is regularly expressed in numbers of symbols not in second. The 2.4 GHz PHY layer duration of 1 byte= 2 symbols = 32  $\mu$ s [23]. All nodes in the network are synchronized on a slotted time base. A slot frame is a collection of timeslots repeated in time. We define the time needed to transmit a successful data packet as TD. The PAN coordinator stores information about the traffic rate and TD. For high priority nodes data transmission is performed during CAP period. The PAN coordinator should not reserve any GTS slot for nodes that will send data using CSMA/CA mechanism and cancel any recommendation to send data during CFP period. The total length of the super-frame is unchangeable but a variation on the duty cycle is required to change the length of the active period. The active period depends on the SO parameter entered by the user, then according to the traffic condition it will be changed dynamically. Nodes which transmit their data during CAP period can increase the number of data packets transmitted due to the increase of the CAP length which can be calculated as given in equation 1:

$$L_{CAP}[s] = Nb_{slot} - B_{duration} - \sum_{n=1}^{Nb_{GTS}} \frac{LGTS}{Slot_{duration}} \quad (1)$$

Where  $n \in (1; NGTS)$

Where  $Nb_{slot}$  define the number of slots in a super-frame,  $B_{duration}$  define the beacon frame duration,  $Nb_{GTS}$  define the number of GTS generated in a super-frame,  $LGTS$  define the duration of one GTS and  $slot_{duration}$  define the duration time of one slot in the super-frame.

## 3. TC-MAC traffic classification

Maintain two columns of text throughout the writing of your paper, except for the title and abstract section.

To ensure the network stability, we are interested in the beacon mode of the IEEE 802.15.4. Indeed,

the goal is to reserve network resources using the GTS mechanism. Nodes are classified according to their traffic rate and the data packet delay using a fuzzy logic rule mechanism. We have defined for this fuzzy system two set of priority groups that will dynamically schedule data transmission during the contention active period or during the contention free period. A groups of nodes with an emergency data transmission send data during the first active period of the super-frame using the modified CSMA/CA mechanism presented in our previous work [ 22]. However, during the CFP period we are intended to develop a dynamic management of GTS to ensure a fairness allocation slots between nodes. We have defined a rigorous fuzzy system that admit traffic rate measurement and the time needed to transmit successfully one data packet as fuzzy input parameters. At each super-frame the PAN coordinator should collect information about all nodes in order to define a priority set groups. Input linguistic variable admit a triangular membership function however the output parameters will be presented using a singleton function.

Traffic rate  $\in$  (emergency, on demand, normal) (2)

Packet delay  $\in$  (random, continuous) (3)

A total number of possible combination arranged as a pair of these states is 6. For each of them we have to establish an appropriate state for the output fuzzy variable where P designed priority and NP mean that there is no priority, as shown in table 1:

**Table 1: Fuzzy rules base**

Packet_delay / Traffic	Emergency	On demand	Normal
Random	P	P	NP
continuous	P	NP	NP

This TC-MAC traffic control based MAC algorithm address the problem of IEEE-802.15.4 of the unfairness GTS allocation for high traffic network. However, the delay in DAMT algorithm hasn't been well improved, so for this reason we have improved the GTS allocation for nodes

according several conditions. In the proposed work we suppose that the PAN coordinator has allocated seven GTS for seven nodes, then each node desire to allocate another GTS it will share the first GTS allocated for the first incoming node in condition that they share the same specifications. This management is applicable for just 11 nodes in the network, more than 11 nodes the PAN coordinator decline every GTS reservation until all nodes accomplish their data transmission. The main aim of the TC-MAC algorithm is to reduce contention in CFP period and provide a fair chance for low traffic network. The classification of nodes is done for two groups of priority as presented in figure 1, nodes with high priority send their data during CAP period however the second type of priority of nodes are intended to send their data during the CFP.

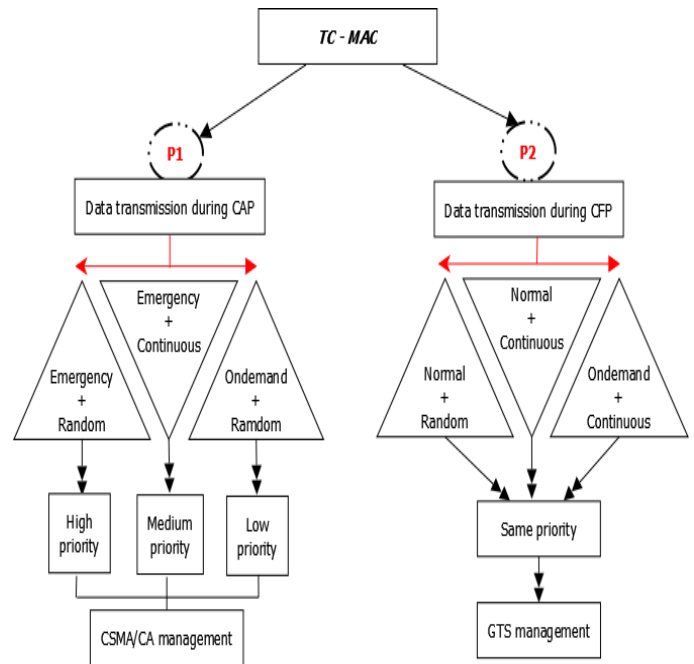


**Figure (1) TC-MAC implementation**

During the contention access period nodes are also classified into three groups of priority according their traffic rate and their queue length as explained in our previous work. Besides the second group of nodes transmit their data according the TC-MAC proposed algorithm by a dynamic GTS request allocation for the PAN

# 14<sup>th</sup> Annual Research Day

Organised by the Deanship of Scientific Research in Collaboration with the College of Engineering  
Research Centre

4<sup>th</sup> April 2019

coordinator. In this method, priority is assigned for nodes with different status of traffic rate and data transmission delay in order to improve the IEEE-802.15.4 standard and ameliorate the network life time.

## 4. GTS allocation scheme

The IEEE-802.15.4 standard presents an unfairness GTS allocation for nodes, in this section, the proposed scheme tried to address this problem by a new reallocation of GTS slots duration. To address the problem of the average delay processed in the proposed algorithm described in section 4, we address the CFP period by a management in the GTS slot allocation and the slot duration time. However, the rest of nodes are reorganized into two groups of priority according to the time needed to transmit one data packet. For periodic data transmission delay, we distinguished two range of the traffic rate as presented as follow:

$P1 = (Medium, Periodic) \text{ and } (Low, periodic)$  (4)

$P2 = (Low, Random)$  (5)

The proposed scheme deals with periodic data transmission delay and low traffic rate where nodes constantly gather information at periodic slot times. Nodes in this group of priority frequently transmit data in a periodic interval. This proposed scheme is adequate for remote sensing applications where nodes periodically sense and transmit data to the PAN coordinator, so the main aim of this work is to allow more nodes in the network to share GTS and avoid the unfairness in slot allocation. The basic method used to allocate GTS slot in the IEEE-802.15.4 standard is the method of First In First out (FIFO). The PAN coordinator allocates a maximum number of 7 GTS slot to nodes and it get quickly consumed in case of low traffic and hold them implicitly or explicitly deallocation. The problem that in several cases most nodes don't have data to be send in each super-frame in case that events transmission is uncommon. However, if the time of an implicit deallocation expire then other nodes in the network may be prevented to not allocate GTS due to the

unavailability of more slots in the contention free period, this take place for unfairness allocation in the GTS.

According to the traffic rate information for each sensor node, the PAN coordinator of the network preserves a fairness distribution of GTS between nodes. Hence, every node should identify to the PAN coordinator and send him additional information about the traffic rate and time needed to transmit one data packet. This scheme address nodes that are allocated a GTS and then they abandon it by an explicit or implicit deallocation.

In the IEEE-802.15.4 standard, the PAN coordinator award a maximum number of seven GTS for nodes by using the mechanism FIFO, these seven nodes maintain each reserved slot until holding it. The desired achievement is to allow the PAN coordinator assign more than seven GTS by a fairness distribution between nodes in the network and allow more than seven nodes to access to the contention free period. The goal of this scheme is allow more nodes to share communication in the same super-frame. Actually these groups of nodes has a low average packet arrival rate and they haven't data to be transmitted in each super frame, for this reason we have chosen to reallocate the GTS for another nodes. In this way, the PAN coordinator provides the last GTS to be used by the first six nodes. This can be ensured by a GTS reallocation test if the considerable GTS can be reused or not. Nodes that share the same GTS transmit their data during the contention free period until they share the same average arrival time and the average time needed to transmit one data packet, else node number one hold the GTS. For the next n super-frame this process is repeated and the PAN coordinator check the test with the node number 8 until it satisfy the required condition as shown in the algorithm number 1.

---

*Algorithm 1. GTS reallocation scheme*

**Begin**

$Nb_{GTS}$  = number of allocated GTS

**While** ( GTS request received = TRUE and node number  $\leq 11$  )  
**do**

**If** ( $Nb_{GTS} \leq 7$ ) **Then**

---

# 14<sup>th</sup> Annual Research Day

Organised by the Deanship of Scientific Research in Collaboration with the College of Engineering  
Research Centre

4<sup>th</sup> April 2019

```
Get nodes information
For (i=0; i<6; i++) do
GTS[i]= { GTS1,GTS2, GTS3,GTS4,GTS5, GTS6}
GTSmax= max GTS[i]
Return GTSmax
End for
If (GTS7 = GTSmax) && (GTSDirection = Transmit) Then
Return TRUE
Else Return FALSE
End If
Else drop GTS request
Repeat until (n+1)th super-frame
End if
End while
```

## 5. Experimental results

This paper models energy consumption for beacon-enabled time-slotted media accessing control cooperated with data scheduling in a cluster tree network containing 11 sensor nodes with an initial energy equivalent to 1000j. The hybrid access control mentioned earlier has been tested by simulations using the ns2 tool. We developed the simulator using the C++ language to evaluate and compare the performance of the IEEE-802.15.4 in low power consumption. The performance of the proposed scheme based on beacon-enabled MAC layer is compared with the IEEE-802.15.4 standard. The longest distance of the transmission range in one hop is 30m. To evaluate the performance of the power consumption and the total number of dropped packets.

Energy consumption is a critical issue in WSN. The comparison between the proposed algorithm and the DAMT algorithm and the IEEE-802.15.4 standard is shown in Fig. 3. This figure presented the energy consumption variation against traffic load. It depicts that the energy rise gradually as function of traffic load. For low traffic loads of 100 kbps, the maximum energy consumed is 10 J and this occurs in case of unprioritized network. On the other hand, prioritized network attains a consumed energy of 2J however the TC-MAC algorithm attain a value of 3J. As seen, the average energy consumption of the hybrid and the TC-MAC program are less compared to the

IEEE-802.15.4 standard unless the hybrid consumes well the power consumption.

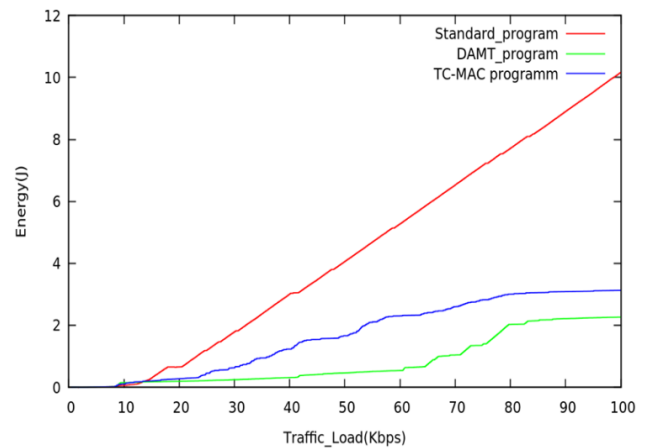


Figure (2) Average energy consumption

The end to end delay in the ns-2 definition is the difference of time between the moment at which the node transmitter generate a packet and the moment at which the receiver node receive successfully the same packet. To evaluate the efficiency of our proposed TC-MAC algorithm, a simulation has been done to trace the delay variation under different traffic load in the network.

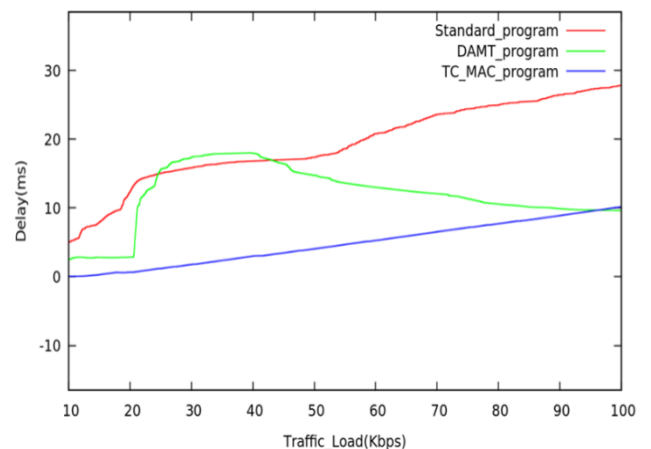


Figure (3). End to end delay variation

As we can see in figure 3 the end to end delay variation has been well optimized using the TC-MAC algorithm in comparison with the IEEE-

# 14<sup>th</sup> Annual Research Day

Organised by the Deanship of Scientific Research in Collaboration with the College of Engineering  
Research Centre

4<sup>th</sup> April 2019

---

802.15.4 and the DAMT algorithm. The classification of node to access the channel is well manipulated and it has reduced the wasted time for the communication between nodes and the coordinator.

## 6. Conclusions

Energy efficiency is a key issue in WSN. It is known that energy efficiency is a conflicting design objective. Hence, power control and rate adaptation need to be carefully considered used to achieve energy efficiency. Traffic rate adaptation to achieve energy efficiency is particularly a challenging task in MAC based IEEE 802.15.4 protocol. This is due to the inequality of channel access for different nodes. In this paper, a novel scheduling mechanism for data transmission packet delay and traffic rate management has been proposed in order to optimize energy consumption in WSN. Various methods of improving the network life time by optimizing energy consumption in WSNs have been discussed so far. An experimental real scenario, based on the IEEE-802.15.4 standard protocol, has been deployed in order to demonstrate benefits introduced by this approach. The self reorganization of nodes has well improved the network performance and has archived good results for the QoS. This reorganization is primordially based on the traffic in the network and according to this condition a GTS management based priority condition schedule the GTS allocation.

## References

- [1] Ramya, R., Saravana kumar G., Ravi, S., MAC Protocols for Wireless Sensor Networks. Indian Journal of Science and Technology, Vol 8(34), (2015) DOI: 10.17485/ijst/2015/v8i34/72318.
- [2] Korhan Cengiz, Tamer Dag, A review on the recent energy-efficient approaches for the Internet protocol stack. Journal on Wireless Communications and Networking, 2015:108

(2015).

- [3] Zhang, H., Cheng, P., Shi, L., Chen J., Optimal denial-of-service attack scheduling with energy constraint. IEEE Trans Autom Control 60(11), 3023–3028 (2015).
- [4] Jamalabdollahi, M., Zekavat, R., Seyed, A., Joint neighbor discovery and time of arrival estimation in wireless sensor networks via OFDMA. IEEE Sensors J. 15(10), 5821–5833 (2015).
- [5] Wang, H., Chi, X., Energy adaptive MAC protocol for IEEE 802.15.7 with energy harvesting. L. Optoelectron Lett. (2016) 12: 370. DOI:10.1007/s11801-016-6163-6.
- [6] Hoon Oh, Md Abul Kalam Azad, A Big Slot Scheduling Algorithm for the Reliable Delivery of Real-Time Data Packets in Wireless Sensor Networks. Wireless Communications, Networking and Applications, Lecture Notes in Electrical Engineering 348, (2016) DOI 10.1007/978-81-322 2580-5\_2.
- [7] Sreejith, V., Suriyadeepan, R., Anupama, K.R., Lucy, J., DS- MMAC: Dynamic Schedule based MAC for Mobile Wireless Sensor Network. (2016) DOI:10.1145/2851613.2851999.
- [8] Guerroumi, M., Pathan, AS.K. Derhab, A. et al: MMSMAC, A Multi-mode Medium Access Control Protocol for Wireless Sensor Networks with Latency and Energy-Awareness. Wireless Pers Commun DOI:10.1007/s11277-016-3726-6. DOI:10.1007/s11277-016-37266.
- [9] Wang, J., Ren, X., Chen, F. et al., On MAC optimization for large- scale wireless sensor network. Wireless Netw (2015) 22:1877. DOI: 10.1007/s11276-015-1073-2.
- [10] Subramanian, A.K. & Paramasivam, I. Wireless Pers Commun (2017) 92: 863. <https://doi.org/10.1007/s11277-016-3581-5>.
- [11] Chen, Z., Liu, A., Li, Z. et al.,

# 14<sup>th</sup> Annual Research Day

Organised by the Deanship of Scientific Research in Collaboration with the College of Engineering  
Research Centre

4<sup>th</sup> April 2019

---

Distributed duty cycle control for delay improvement in wireless sensor networks. Peer-to-Peer Network. Appl (2016). DOI: 10.1007/s12083-016-0501-0.

[12] Deepak, K. S., Babu, A. V., Energy consumption analysis of modulation schemes in IEEE 802.15.6-based wireless body area networks. Deepak and Babu EURASIP Journal on Wireless Communications and Networking. (2016) DOI 10.1186/s13638-016-0682-5.

[13] Luca Mainetti, Vincenzo, M., Luigi Patrono, HEC-MAC: A Hybrid Energy-Aware Cross-Layer MAC Protocol for Wireless Sensor Networks. International Journal of Distributed Sensor Networks. Article ID 536794, 12 pages (2015).

[14] Sherly, L., Puspha Annabel and Murugan, K., Energy-Efficient Quorum-Based MAC Protocol for Wireless Sensor Networks. ETRI Journal, 37(3) (2015).

[15] Rajesh, B. Shyamala, D., George, A., HYBRID CSMA/CA-TDMA BASED MAC PROTOCOLS FOR WIRELESS SENSOR NETWORKS. ARPN Journal of Engineering and Applied Sciences. 10(4) (2015).

[16] Bih-Hwang Lee, Eppy Yundra, Huai-Kuei Wu, M Udin Harun Al Rasyid, Analysis of superframe duration adjustment scheme for IEEE802.15.4 networks. Journal on Wireless Communications and Networking. 2015:103 (2015).

[17] Mohamed, B., Houria, R., Tahar, E., A Comprehensive Performance Study of the Contention Access Period of the Slotted IEEE 802.15.4. The International Conference on

Advanced Wireless, Information, and Communication Technologies (AWICT 2015).

[18] Sabin Bhandari, Sangman Moh, A Priority-Based Adaptive MAC Protocol for Wireless Body Area Networks. Sensors (2016), 401; DOI:10.3390/s16030401.

[19] Varsha, J., Shweta, A., Kuldeep, G., Energy Consumption Improvements by Priority based MAC Protocol for WSN. International Journal of Computer Applications® (IJCA) (0975 – 8887) National Seminar on Recent Advances in Wireless Networks and Communications, NWNC (2014).

[20] Tsung-Han Hsieh, Kuei-Ying Lin, Pi-Chung Wang, A Hybrid MAC Protocol for Wireless Sensor Networks. Proceedings of 2015 IEEE 12th International Conference on Networking, Sensing and Control (2015).

[21] Bouazzi, I., Bhar, J. and Atri, M. (2017) 'New CSMA/CA prioritisation based on fuzzy control mechanism', Int. J. Intelligent Engineering Informatics, Vol. 5, No. 3, pp.253–266.

[22] Imen B., Jamila B. and Mohamed A., Priority-based queuing and transmission rate management using a fuzzy logic controller in WSNs. ICT Express 3(2), 101-105 (2017).

[23] Imen Bouazzi, Jamila Bhar, Mohamed Atri. A Dynamic Adaptation Mechanism for Traffic Conditions in Wireless Sensor Network. Int. J. wireless personal communication. Issue 4, 2018.

# 14<sup>th</sup> Annual Research Day

Organised by the Deanship of Scientific Research in Collaboration with the College of Engineering  
Research Centre

4<sup>th</sup> April 2019

---

## Estimation of Carrier Frequency Offsets and Channel for SC-FDMA Uplink Systems

Muneer Parayangat., Thafasal Ijyas V. P., F. M. Suliman, Bushara. S. Elnoor

Department of Electrical Engineering, College of Engineering, King Khalid University,  
PO Box 394, Abha 61411 KSA.

Use subscripts for external affiliation.

E-mail address: mparayangat@kku.edu.sa

---

**Abstract:** In this paper, we propose a pilot-aided estimation technique for the joint estimation of carrier frequency offset (CFO) and quasi static channel for single carrier frequency division multiple access (SC-FDMA) uplink systems. The exact solution to this estimation problem requires a multidimensional search, which is highly computationally complex. Our proposed method makes use of space alternating generalized expectation maximization (SAGE) algorithm that replaces the multidimensional search with a series of one-dimensional searches. Hence, the proposed method is very much suitable for the practical implementation current and next generation wireless system. Simulation studies demonstrate that the proposed method gives a good estimation performance even with large number of users.

**Keywords:** SC-FDMA uplink, CFO, Channel estimation.

---

### 1. Introduction:

Wireless communication has become an rapidly growing segment of communication technology. There are several factors that influences exponential growth. The need for higher data rate and the immense requirement of QoS support have motivated the researchers to propose new theoretical models and develop the practical solutions to the problems arising in this area. The rapid growth of very large scale integration (VLSI) technologies over the past few decades also opened the way for this tremendous growth.

To achieve high throughput with great flexibility in wireless technologies the orthogonal frequency division multiplexing (OFDM) has been reinvented. The multiple access version of OFDM known as orthogonal frequency division multiple access (OFDMA) has evolved from OFDM as the most popular multiuser transmission technique. The OFDMA is multiuser version of OFDM has become a popular multi-carrier multiple access technique for high data

rate wireless communication systems because of its improved spectral efficiency, flexibility for QoS support and robustness to sustain in a frequency selective fading environment. However, the peak to average power (PAPR) problem in OFDMA systems is one of the challenges which may distort the transmit signal. But it can be solved by using the discrete Fourier transform (DFT) precoding to the transmit symbol. This version of OFDMA is called as single carrier frequency division multiple access (SC-FDMA). Frequency/timing synchronization, channel estimation and equalization are the key issues in OFDMA uplink transmission. Hence, the carrier frequency offsets (CFO) and the channel have to be estimated and to be compensated by using the suitable equalization techniques.

For mitigating the adverse effects of ICI in single user multi-carrier systems like OFDM, the methods that make use of frequency domain processing have been proposed in the existing literature. However, the interference causing factors such as CFOs and time channels can also

be estimated in time domain and can be used to mitigate their effects. In [1] an alternating projection-based estimator has been proposed for finding the CFO and residual timing error estimates iteratively. In [2], an iterative detection and frequency synchronization technique for OFDMA uplink is proposed. Joint ML estimation of CFO and channel using importance sampling is proposed in [3]. The method in [3] is guaranteed to converge to global optimum through ML search if initialized properly. In [4] and [5], blind estimation schemes for CFO estimation in OFDMA uplink are proposed. However, none of these methods addresses the channel estimation problem. Joint frequency offset and channel estimation using Gauss-Hermite integration is proposed in [6]. However, this approach is valid only for single-user systems.

Hence, there is need to address this problem of joint estimation of CFO and channels in SC-FDMA system. In this paper, we made use of the space alternating expectation maximization (SAGE) algorithm for achieving this task. Our proposed technique offers a very good estimation performance.

## 2. System Model

In this section we present the transmit and receive signal model for the SC-FDMA uplink system with CFO and channel impairments. It is assumed that the system is perfectly time synchronized.

### 2.1 Transmit Signal Model

We consider a burst structure for the transmit signal such that there are  $M$  SC-FDMA symbols in a frame. The preamble is used as the pilot symbol for each frame. It is assumed that the whole system consists of  $K$  users communicating with the base station receiver simultaneously. With these notions in mind, the received signal at the base station receiver is given as

$$y(n) = \sum_{k=1}^K \sum_{l=0}^{L-1} e^{\frac{j2\pi\epsilon_k n}{N}} h^k(l) x^k(n-l) + v(n) \quad (1)$$

Where we define

$$x^k(n-l) = CA[DFT\{X^k(i)\}] \quad (2)$$

Here  $DFT\{\cdot\}$  is the discrete Fourier transform operator and  $CA\{\cdot\}$ , is the function which perform carrier assignment operation according to the predetermined pseudorandom code. Mutually exclusive carriers are used in the carrier assignment scheme. The  $X^k(i)$  is the data symbol created by mapping the bits according to a constellation. Collecting all the  $N$  Samples in preamble and arranging it in the vector form, we obtain

$$\mathbf{y} = \sum_{k=1}^K \Psi(\epsilon_k) \mathbf{H}_k \mathbf{X}_k + \mathbf{v} \quad (3)$$

where  $\mathbf{H}_k$  is the channel matrix in time domain,  $\mathbf{v} = [v(0), v(1), \dots, v(N-1)]^T$  is the noise vector,  $\mathbf{y}$  is the received signal vector. Here  $\Psi(\epsilon_k)$  is the CFO matrix given by

$$\Psi_m(\epsilon_k) = \text{diag} \left( \left[ e^{\frac{j2\pi\epsilon_k}{N}(0+\tilde{m}(m))}, \dots, e^{\frac{j2\pi\epsilon_k}{N}(N-1+\tilde{m}(m))} \right]^T \right) \quad (4)$$

It is evident from (3) that the received signal is a superposition of signals from all active users. The problem of estimation can be formulated as

$$\hat{\Theta} = \underset{\Theta}{\text{argmax}} f(\mathbf{y}; \Theta) \quad (5)$$

Where

$$f(\mathbf{y}; \Theta) = \frac{1}{(\pi\sigma^2)^N} \exp\left(\frac{-1}{\sigma^2} \|\mathbf{y} - \Psi(\epsilon_k) \mathbf{H}_k \mathbf{X}_k\|^2\right) \quad (6)$$

However, we can rewrite the term  $\Psi(\epsilon_k) \mathbf{H}_k \mathbf{X}_k$  as  $\Psi(\epsilon_k) \mathbf{D}_k \mathbf{h}_k$ . By using this we obtain

$$\hat{\Theta} = \underset{\Theta}{\operatorname{argmax}} -\|\mathbf{y} - \Psi(\epsilon_k) \mathbf{D}_k \mathbf{h}_k\|^2 \quad (7)$$

The above problem mentioned in (7) can be solved by using SAGE algorithm as follows [7]

**Initialize:**

1.  $\epsilon_k^{(0)} = \operatorname{argmax}_{\epsilon} \mathbf{y}^H \Psi(\epsilon) \mathbf{P}_{\mathbf{D}_k} \Psi^H(\epsilon) \mathbf{y}$
2. **for**  $p=0, 1, \dots$ , do

$$u = 1 + (p)_K$$

Calculate:

$$\bar{\mathbf{y}}_p^k = \mathbf{y} - \sum_{u'=1, u' \neq u}^K \hat{\mathbf{y}}_{p-1}^{(u')}$$

$$\text{(where } \hat{\mathbf{y}}_{p-1}^{(u')} = \Psi(\epsilon_k^{u-1}) \mathbf{D}_k \mathbf{h}_k^{p-1}$$

$$\epsilon_u^{(p)} =$$

$$\operatorname{argmax}_{\epsilon} \bar{\mathbf{y}}_p^k{}^H \Psi(\epsilon) \mathbf{P}_{\mathbf{D}_k} \Psi^H(\epsilon) \mathbf{y}$$

$$\text{(where } \mathbf{P}_{\mathbf{D}_k} = \mathbf{D}_k (\mathbf{D}_k^H \mathbf{D}_k)^{-1} \mathbf{D}_k^H)$$

$$\mathbf{h}_k^p = (\mathbf{D}_k^H \mathbf{D}_k)^{-1} \mathbf{D}_k^H \Psi(\epsilon_u^{(p)})$$

**end for**

**Algorithm 1: Use of SAGE algorithm for joint estimation problem**

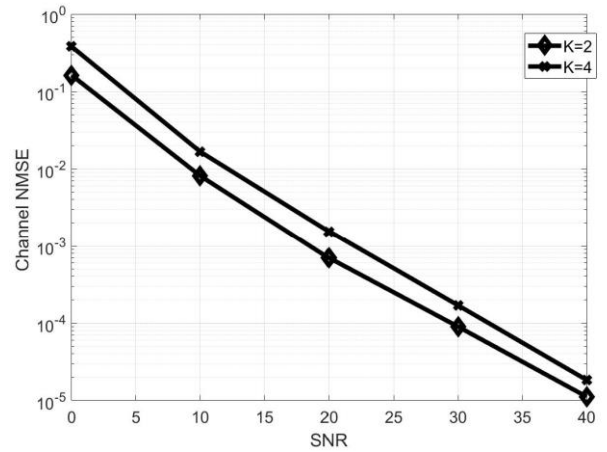
### 3. Simulation Results

In this section we provide the simulation results of the proposed estimation technique. We consider  $N = 256$ , the frame size  $M = 10$ . The data bits are mapped using the QPSK constellation. The multipath channel is assumed to be Raleigh fading channel with a length  $L = 6$ . The number of users which are active in the

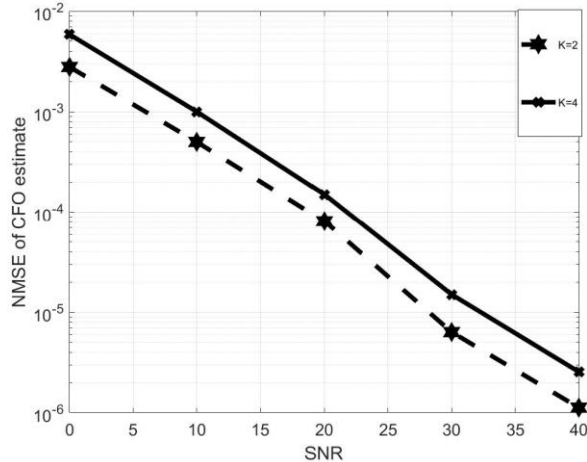
uplink transmission is  $K = 2, 4$ . The channel power delay profile is exponential with the significant path has 0 dB PDP.

Fig. 1 show the normalized mean square error performance (NMSE) of the proposed algorithm in estimating the channel. It is observed that the proposed technique offers a very good performance in estimating the channel in the presence of multiple users.

The NMSE performance of the proposed technique in estimating CFO with 2 and 4 active users in the uplink is shown in Fig. 2. It is to be noted that the NMSE performance obtained with  $N = 256$  is adequate for ensuring a good equalization



**Figure 1: NMSE performance of proposed estimator for channel estimation**



**Figure 2 NMSE performance of proposed estimator for CFO estimation**

performance for SNR's greater than 15 dB. The performance of the proposed technique at lower SNR's can be improved further by increasing the pilot length.

## 4. Conclusions

In this paper, we presented a pilot-aided estimation technique jointly estimating the CFO and channel for SC-FDMA uplink systems. Since the exact solution to this estimation problem requires a multidimensional search, we proposed the use of SAGE algorithm that replaces the multidimensional search with a series of one-dimensional searches. The proposed technique is very much suitable for the practical implementation. The results of the simulation studies illustrate that the proposed method offers a good estimation performance even with large number of users.

## References

- [1] M.-O. Pun, M. Morelli and C.-C. Kuo, "Maximum-likelihood synchronization and channel estimation for OFDMA uplink transmissions," *IEEE Trans. Commun.*, vol. 54, no. 4, pp. 726–736, Apr. 2006.
- [2] M.-O. Pun, M. Morelli and C.-C. Kuo, "Iterative detection and frequency synchronization for OFDMA uplink transmissions," *IEEE Trans. Wireless. Commun.*, vol. 6, no. 2, pp. 629–639, Feb. 2007.
- [3] R. Du, and J. Wang, "Novel blind CFO estimator for uplink interleaved OFDMA systems," *Internat. Journ. of Digital Content Tech. and its Appl. (JDCTA)*, vol. 6, no. 3, pp. 158-166, Feb. 2012
- [4] J. Chen, Y. Wu, Chan, and T. Ng., "Joint maximum-likelihood CFO and channel estimation for OFDMA uplink using importance sampling," *IEEE Trans. Veh. Tech.*, vol. 57, no. 6, pp. 3462-3470, Nov.2008
- [5] R. Du, and J. Wang, "Novel blind CFO estimator for uplink interleaved OFDMA systems," *Internat. Journ. of Digital Content Tech. and its Appl. (JDCTA)*, vol. 6, no. 3, pp. 158-166, Feb. 2012
- [6] R. Du, and J. Wang, "Novel blind CFO estimator for uplink interleaved OFDMA systems," *Internat. Journ. of Digital Content Tech. and its Appl. (JDCTA)*, vol. 6, no. 3, pp. 158-166, Feb. 2012.
- [7] Fessler and A. O. Hero, "Space-alternating generalized expectationmaximization algorithm," *IEEE Trans. Signal. Process.*, vol. 42, no. 10, pp. 2664-2677, Oct. 1994.

## Logic Based Approach for Analysis of Nucleotide Sequences in Typical Case

M. Abbas , H. Loukil

Department of Electrical Engineering, College of Engineering, King Khalid University,  
PO Box 394, Abha 61411 KSA.  
E-mail address: mabas@kku.edu.sa

**Abstract:** Analysis of Nucleotide Sequences is an important field to predict the behavior of different genus. The main contribution of the paper is proposing an efficient and a simple representation of DNA double helix structure in a typical case. The suggested representation is based on the logic concepts of digital computations. The suggested approach modifies the concept of DNA matrix representation for one strand to analyze the whole DNA double helix. This allows analyzing smoothly the structure of DNA presenting an efficient analysis for number of features such as DNA comparisons, determining the degree of similarity among DNA of different origins and the stability of the double helix. To verify the proposed work a case study about Influenza A virus H1N1, Swine Flu, is analyzed. A comparison is presented among the DNA of H1N1, and other types of Influenza A viruses based on Data collected from the online database GeneBank. The results of the case study using the proposed representation depict that H1N1 virus infects human is highly similar to H5N1 that infect avian. Another Study about the stability of the double helix of H1N1 virus is presented. This study depicts the ability of H1N1 virus to mutate over last seven years. These results are equivalent to results reported by WHO World Health Organization.

**Keywords:** DNA double helix, DNA comparison, double helix stability, matrix representation, H1N1 virus.

---

### 1. Introduction:

A DNA sequence or genetic sequence is a succession of letters representing the primary structure of a real or hypothetical DNA molecule or strand, with the capacity to carry information as described by the central view of molecular biology. The possible letters are A, C, G, and T, representing the four nucleotide bases of a DNA strand — adenine, cytosine, guanine, thymine — covalently linked to a phosphodiester backbone. In the typical case, the sequences are printed abutting one another without gaps, as in the sequence AAAGTCTGAC, read left to right in the 5' to 3' direction. Short sequences of nucleotides are referred to as oligonucleotides and are used in a range of laboratory applications in molecular biology. Sequences can be derived from the biological raw material through a process called DNA sequencing. A simple

structure of the DNA double helix is depicted in figure1.

Number of Methods is proposed to compare DNA sequences. Xiaoqiu Huang et al in [1] compare a DNA sequence with a protein sequence. They describe two methods for constructing an optimal global alignment of a DNA sequence and a protein sequence. The methods can rigorously process very huge sequences. S. Hiraoka et al in [2] compare DNA sequence based on amino acid similarity. They present an algorithm for DNA sequence comparison which translates the sequences most reliably and compares the translated sequences. The method enables us to find protein sequence similarity in DNA sequences even if we do not know the protein sequences which are coded in the DNA sequences. Arnau, Vicente et al in [3] presents fast comparison of DNA sequences by oligonucleotide profiling. They describe a program, called UVWORD, which determines the

number of times that each DNA word present in a sequence (target) is found in a second sequence (source), a procedure that we have called oligonucleotide profiling.

Other efforts are presented to study the stability of DNA double helix. Aditi Kanhere, et al. in [4] presents a novel method for prokaryotic promoter prediction based on DNA stability. Vollenweider HJ et al in [5] introduce a relationship between DNA helix stability and recognition sites for RNA polymerase. Breslauer KJ in [6] could predict DNA duplex stability from the base sequence. Darren A. Natale in [7] analyzed DNA helical stability accounts for mutational defects in a yeast replication origin. Andrew Krueger et al in [8] used Sequence-Dependent Basepair Opening in DNA Double Helix to focus on its stability. Erin Shammel Baker et al. in [9] could measure B-DNA Helix Stability in a Solvent-Free Environment.

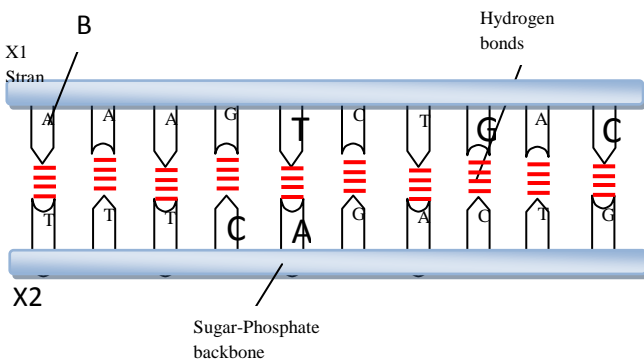


**Figure (1)** DNA double helix structure

The main contribution of this paper is to present a new and an efficient representation of the DNA double helix based on the concepts of matrixes and logic operations in digital computations. This representation enables us to simply compare two DNA duplex and analyzes its stability more efficiently.

The rest of the paper is organized as follow: section 2 represents the previous concept of Conversion of character-based DNA sequences to numerical Sequences, section 3 pioneers the proposed Logic based approach for analysis of typical DNA sequences, section 4 is a Case Study

about Influenza A virus H1N1, Swine Flu, using the proposed approach and section 5 conclusions and comments about the results of the case study.

## 2. Conversion of character-based DNA sequences to numerical Sequences

Mingjun Zhang et al in [10] proposed three methods to convert character-based DNA sequences into numerical sequences. One method is to use complex numbers. The second method is to use integer numbers. The third method is to convert DNA sequence into vectors. This paper focuses only on vector space analysis. In vector space analysis, numerical value based DNA sequences can be expressed as rows of a matrix [10-14]. Addition of such kinds of matrices can be regarded as DNA hybridization process. Scalar multiplication produces multiple copies of the sequences in a test tube. Consider the four DNA bases {A, T, G, C} as a vector, any DNA strand can then be expressed as a vector by a transfer matrix. For example, consider the DNA strand could be represented as X1 strand = AAAGTCTGAC, and X2 strand = TTTCAGACTG. Both of them are represented in separated matrixes as in figure 2 and figure 3.

$$X = \begin{matrix} & \begin{matrix} A & T & G & C \end{matrix} \\ \begin{matrix} 1 \\ 1 \\ 1 \\ 0 \\ 0 \\ 0 \\ 0 \\ 0 \\ 1 \\ 0 \end{matrix} & \begin{bmatrix} 0 & 0 & 0 & 0 \\ 0 & 0 & 0 & 0 \\ 0 & 0 & 1 & 0 \\ 1 & 0 & 0 & 0 \\ 0 & 1 & 0 & 0 \\ 0 & 0 & 0 & 1 \\ 0 & 1 & 0 & 0 \\ 0 & 0 & 1 & 0 \\ 1 & 0 & 0 & 0 \\ 0 & 0 & 0 & 1 \end{bmatrix} \end{matrix}$$

**Figure (2)** matrix structure for a single strand X1

$$X = \begin{matrix} & \begin{matrix} A & T & G & C \end{matrix} \\ \begin{matrix} 0 \\ 0 \\ 0 \\ 0 \\ 1 \\ 0 \\ 1 \\ 0 \\ 0 \\ 0 \\ 0 \end{matrix} & \begin{bmatrix} 1 & 0 & 0 & 0 \\ 1 & 0 & 0 & 0 \\ 1 & 0 & 0 & 0 \\ 0 & 0 & 1 & 0 \\ 0 & 0 & 0 & 1 \\ 0 & 1 & 0 & 0 \\ 0 & 0 & 1 & 0 \end{bmatrix} \end{matrix}$$

**Figure (3)** matrix structure for a single strand X2

This representation resembles the saving digits 1 and 0 in bits related to digital computations. As in digital concept the continuation of the pulse signifies 1 and not continuation signifies 0. It is obvious; each one strand is represented in one matrix. Digital operations could be used in the above mentioned matrix representation such as AND, OR and NOT operations. It is clear that, if you want to signify the whole DNA double helix you should operate with two matrixes. This may lead to more difficulty in analysis and causing errors. Next section introduces a new view of the double helix representing the structure in one matrix. Then use the suggested structure to analysis more easily number of features related to the double helix; DNA comparison, degree of similarity and DNA stability.

### 3. The proposed Logic based approach for analysis of typical DNA sequences

This section introduces a new representation of DNA double helix based on some modifications applied on the matrix

representation of one strand as depicted in section 2. Section 3.1 presents this modifications then section 3.2 uses the proposed representation to analyze some features of the whole DNA double helix such as DNA comparison and stability.

#### 3.1 A new vector representation of DNA double helix

In double strands each base in one strand is connected to its chemical bound base. For example A is bound to T and C is bound to G and vice versa as depicted in figure1. To represents the double strands it is important to modify the matrix of one strand to contain the double strands together. This modification starts by doubling the number of columns to be 8 columns with labels A1, A2, T1, T2, G1, G2, C1 and C2 , then the structure of the matrix will be as shown in figure 4.

$$\begin{matrix} & \begin{matrix} A1 & A2 & T1 & T2 & G1 & G2 & C1 & C2 \end{matrix} \\ \begin{matrix} 0 \\ 0 \\ 0 \\ 0 \\ 0 \end{matrix} & \begin{bmatrix} 0 & 0 & 0 & 0 & 0 & 0 & 0 & 0 \\ 0 & 0 & 0 & 0 & 0 & 0 & 0 & 0 \\ 0 & 0 & 0 & 0 & 0 & 0 & 0 & 0 \\ 0 & 0 & 0 & 0 & 0 & 0 & 0 & 0 \\ 0 & 0 & 0 & 0 & 0 & 0 & 0 & 0 \end{bmatrix} \end{matrix}$$

**Figure (4)** proposed structure of DNA double helix matrix

Now, let us fill the matrix with bases in figure1, starting from left to right. i) The first step is to represent base A in X1 strand and T in X2 strand. In first row put the element of A1 equal 1 and the element of A2 equals 0, this means the base A is exist in strand X1. Also, in first row put the value of element T1 to be equal 1 and the value of T2 to be equal 1 , putting both the values of elements related to T1 and T2 to be 1 means T base is exist in strand X2. Step2 and step3 are the same, where X1 strand contains the base A and the X2 strand contains the base T. So, the structure of the matrix after the third step is depicted in figure 5.

$$\begin{matrix} & \begin{matrix} A1 & A2 & T1 & T2 & G1 & G2 & C1 & C2 \end{matrix} \\ \begin{matrix} 1 \\ 1 \\ 1 \end{matrix} & \begin{bmatrix} 0 & 1 & 1 & 0 & 0 & 0 & 0 & 0 \\ 0 & 1 & 1 & 0 & 0 & 0 & 0 & 0 \\ 0 & 1 & 1 & 0 & 0 & 0 & 0 & 0 \end{bmatrix} \end{matrix}$$

**Figure (5)** proposed structure of DNA double helix matrix after the 3<sup>rd</sup> step

ii) Step no 4: to represent the base G in X1 strand, in the 4th row G1 value is equal 1 and G2 is equal 0. To represent the base C in X2 strand, C1 is equal to 1 and C2 is equal 1. the structure of the matrix after the 4th step is depicted in figure 6.

	A1	A2	T1	T2	G1	G2	C1	C2
1	1	0	1	1	0	0	0	0
2	1	0	1	1	0	0	0	0
3	1	0	1	1	0	0	0	0
4	0	0	0	0	1	0	1	1

**Figure (6)** proposed structure of DNA double helix matrix after the 3<sup>rd</sup> step

Rest of the steps should be as previous steps with the same rules, and then the complete matrix to represent the DNA double helix in figure 1 is represented in figure 7.

	A1	A2	T1	T2	G1	G2	C1	C2
1	1	0	1	1	0	0	0	0
2	1	0	1	1	0	0	0	0
3	1	0	1	1	0	0	0	0
4	0	0	0	0	1	0	1	1
5	1	1	1	0	0	0	0	0
6	0	0	0	0	1	1	1	0
7	1	1	1	0	0	0	0	0
8	0	0	0	0	1	0	1	1
9	1	0	1	1	0	0	0	0
10	0	0	0	0	1	1	1	0

**Figure (7)** complete matrix to represent the DNA double helix in figure 1

### 3.2 Using the proposed representation in analysis of DNA double helix

This section analyzes number of features related to the DNA double helix based on the vector representation of DNA proposed in section

3.1. these features are DNA comparisons, determining the degree of similarity and the stability of the whole DNA double helix. Next subsection explains in details how we can use the proposed representation of DNA in comparing two DNA double helixes.

#### 3.2.1 Comparing two DNA double helixes

To compare between two DNA double helixes, it is required to represent both of them as a matrix contains groups of 1's and 0's as presented in section 3.1. Figure 6 depicts that every row in the matrix contains three 1's in normal typical case. One of them represents the base in X1 strand and the others represent the base in X2 strand. This section proposed a new easy logic idea in comparing two DNA double helixes by applying the logic operation, AND, for each corresponding element in the two matrixes and preserve the results in one single matrix it represents the whole DNA. If the bases are the same, the result of AND operation will be three 1's in the whole DNA matrix but if the bases are different the result of AND operation will be two 1's. In this case, it is easy to distinguish the different bases by registering the rows contain two 1's.

```

Read number of rows of the matrixes (n)
for (i=0;i<n;i++)
{ for (j=0;j<8;j++)
{ x(i,j) : read the first sequence
y(i,j) : read the second sequence
z(i,j) = x(i,j) and y(i,j) } }
for (i=0;i<n;i++)
{ for (j=0;j<8;j++)
If (number of 1's in single row equals 2)
counter1 = counter1+1
Else
counter2 = counter2+1 } }
if counter1 = (n) then no similarity
counter2 = number of similar bases
Degree of similarity = counter2/(n)
Print (Degree of similarity)
    
```

**Figure (8)** proposed algorithm for comparing two double helixes

Figure 8 depicts the algorithm simulates the comparison operation using the proposed logic concept of AND operation. The proposed algorithm can measure the degree of similarity by counting the number of different bases divided by the total number of bases in the whole DNA double helix.

#### 4. Case Study: Influenza A virus H1N1 (Swine Flu)

This case study takes its data from the online database of the GenBank[16]. It is the NIH genetic sequence database, an annotated collection of all publicly available DNA sequences. There are approximately 85,759,586,764 bases in 82,853,685 sequence records in the traditional GenBank divisions and 108,635,736,141 bases in 27,439,206 sequence records in the WGS division as of February 2008. The complete release notes for the current version of GenBank are available on the NCBI ftp site. A new release is made every two months. GenBank is part of the International Nucleotide Sequence Database Collaboration, which comprises the DNA DataBank of Japan (DDBJ), the European Molecular Biology Laboratory (EMBL), and GenBank at NCBI. These three organizations exchange data on a daily basis [16]. GenBank contains the most recent data about different types of viruses of different species. For examples data about their organism, mol\_type, strain, serotype, host, segment, country from which data is collected, collection\_date, gene, codon\_start, the translation code and the DNA sequences. This case study focuses only on Influenza A virus H1N1 known as a Swine Flu. Because its data is recently collected and researchers are in badly need to discover its structure, its behavior to reach to a suitable vaccine that is under developed. During this case study the proposed algorithms in figure 8 and 9 are implemented using C# language.

#### 4.1 Comparing H1N1 DNA sequences with some Influenza A virus

This section applies the proposed algorithm in figure 8 for comparing the DNA double helixes. DNA sequences are collected from the Genebank and other different resources [16-22] about H1N1, H5N2, H10N4 and H5N1 infect human in addition H5N1 infects duck. The comparison are related to the genes (PB1) and (PB2) for 60 bases for every gene. The comparison data related to (PB1) gene is depicted in table1 and data related to (PB2) gene is depicted in table2.

**Table1: comparison data related to (PB1) gene for 60 bases**

Virus	H9 N2	H10 N4	H5 N1	H5N1( duck)	H5N1(h uman)
<b>Similarity to H1N1%</b>	91.6 6	28.3 3	31.6 6	89.66	25

Table1 depicts that H1N1 virus has DNA sequences similar to the virus H9N2 with percentage 91.66% and it is high percentage of similarity. There is also high percentage of similarity between H1N1 and H5N1 viruses reach to 89.66 %. Other viruses are far from similarity. This comparison is depicted in figure 10 all are related to (PB1) gene.

**Table 2: comparison data related to (PB1) gene for 60 bases**

Virus	H5 N1	H9 N2	H3N2	H2N2
<b>Similarity to H1N1%</b>	88. 33	35	90	35

Table 2 depicts that H1N1 virus has DNA sequences similar to the virus H5N1 with percentage 88.33% and it is high percentage of similarity. There is also high percentage of similarity between H1N1 and H3N2 viruses reach

# 14<sup>th</sup> Annual Research Day

Organised by the Deanship of Scientific Research in Collaboration with the College of Engineering Research Centre

4<sup>th</sup> April 2019

to 90%. H9N2 and H2N2 viruses both are similar with 35%. This comparison is depicted in figure 10 all are related to (PB2) gene. Both of comparisons in figures 9 and 10 depict that the proposed approach for comparing DNA sequences refers to H1N1 virus infect human is highly similar to H5N1 that infect avian.

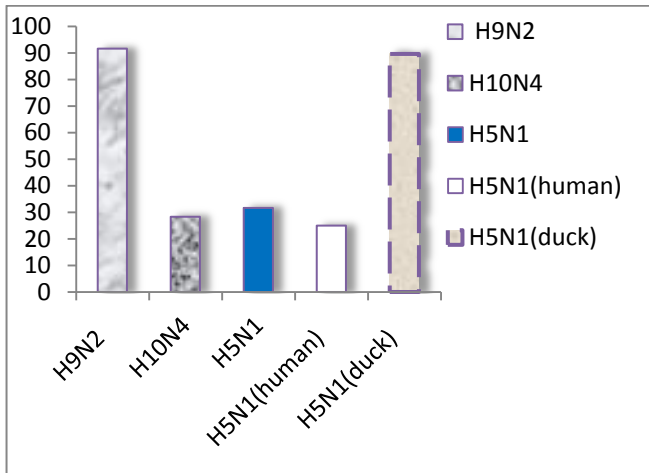


**Figure (9)** Degree of similarity to H1N1 related to (PB1) gene

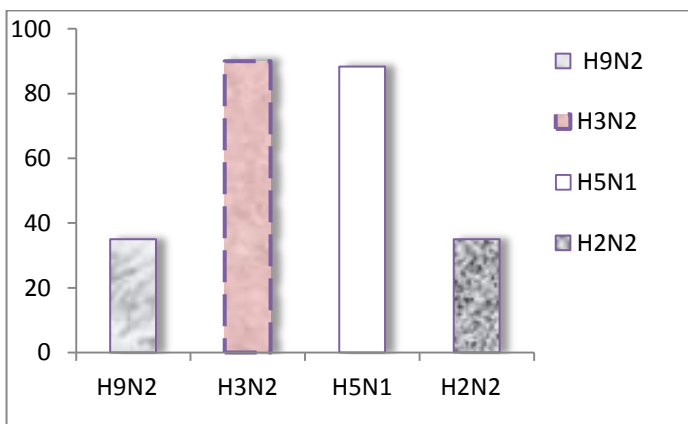


**Figure (10)** Degree of similarity to H1N1 related to (PB2) gene

These obtained results are the same as the universal results collected and reported from number of resources. WHO daily briefing on

H1N1 of Mexico and Worldwide cases, May 3, 2009 mentions that H1N1 behaves like H5N1 as both of them infect mostly younger population with ages less than 29 years old [23,24]. Both of them can be well put to control by the use of TAMIFLU vaccine.

## 5. Conclusions:

Representation and analyzing of DNA structure is a vital processes in predicting the behavior of different genus. This paper proposes a logic based approach for representing and analysis DNA sequences in typical case simply and efficiently. The proposed approach includes two algorithms; one for comparing two DNA sequences and the other for determining the degree of stability of the DNA double helix. To verify these algorithms a case study is analyzed concern H1N1 virus, swine flu, one of the most dangerous virus recently known. Data about its DNA sequence is existed in the online gene database GeneBank. The results of this case study depict that proposed approach performs its functions easily and efficiently without using labs or chemical interactions. The results are comparable with WHO reports say H1N1 behaves like H5N1 where as they have similar DNA sequences. The results of the case Study assure the instability of the virus DNA double helix related to data collected in 2009 from Mexico. In the same time WHO reports H1N1 virus starts to mutate in April 2009.

## References

- [1] Xiaoqiu Huang et al , "Comparing a DNA sequence with a protein sequence" , Oxford Journals , Life Sciences , Bioinformatics , Volume 12, Number 6 , Pp. 497 - 506, 1996
- [2] S. Hiraoka , "DNA sequence comparison based on amino acid similarity", <http://citeseer.ist.psu.edu/4998.html>

# 14<sup>th</sup> Annual Research Day

Organised by the Deanship of Scientific Research in Collaboration with the College of Engineering  
Research Centre

4<sup>th</sup> April 2019

- [3] Arnau , et al. "Fast comparison of DNA sequences by oligonucleotide profiling ", BMC Res Notes. February 28, 2008. doi: 10.1186/1756-0500-1-5.
- [4] Aditi Kanhere, et al., " A novel method for prokaryotic promoter prediction based on DNA stability", BMC Bioinformatics, January 2005
- [5] Vollenweider HJ, Fiandt M, Szybalski W: A relationship between DNA helix stability and recognition sites for RNA polymerase. *Science* 1979, 205:508-511.
- [6] Breslauer KJ, Frank R, Blocker H, Marky LA: Predicting DNA duplex stability from the base sequence. *Proc Natl Acad Sci USA* 1986, 83:3746-3750.
- [7] Darren A. Natale," DNA helical stability accounts for mutational defects in a yeast replication origin", *Proc. Nati. Acad. Sci. USA* Vol. 89, pp. 2654-2658, April 1992
- [8] Andrew Krueger et al," Sequence-Dependent Basepair Opening in DNA Double Helix", *Biophysical Journal* Volume 90 May 2006, p.p 3091–3099
- [9] Erin Shammel Baker et al."B-DNA Helix Stability in a Solvent-Free Environment", *American Society for Mass Spectrometry.*, p.p 1188-1195, March 12, 2007
- [10] Mingjun Zhang,et al."A Mathematical Formulation of DNA Computation", *IEEE Transactions On NanoBioscience*, vol. 5, no. 1, pp. 32-40, 2006.
- [11] L. Adleman, Molecular Computation of Solutions to Combinatorial Problems, *Science*, vol.266, pp. 1021-1024, Nov. 1994.
- [12] L. Adleman, On Constructing A Molecular Computer, *DNA Based Computers*, Eds. R. Lipton and E. Baum, DIMACS: series in Discrete Mathematics and Theoretical Computer Science, American Mathematical Society, pp. 1-21, 1996.
- [13] D. Bartel, and J. Szostak, Isolation of new ribozymes from a large pool of random sequences. *Science*, vol. 261, pp. 1411-1418, September 1991.
- [14] E. Baum, and D. Boneh,"Running dynamic programming algorithms on a DNA computer.' the 2nd DIMACS workshop on DNA based computers, pp. 141-147, 1996.
- [15] Dawei Li, "A subsequent study of visualized DNA sequence comparison based on NKS" NKS 2007 Conference & Minicourse, <http://www.wolframscience.com/conference/2007/presentations/DaweiLi.html>
- [16] <http://www.ncbi.nlm.nih.gov/Genbank,2-8-2009>
- [17] Centers for Disease Control and Prevention (CDC). Update: swine influenza A(H1N1) infections – California and Texas, April 2009. *MMWR Morb Mortal Wkly Rep* 2009;58(16):435-7.
- [18] G M Nava et al," Origins of the new influenza A(H1N1) virus: time to take action" , *Eurosurveillance*, Volume 14, Issue 22, 04 June 2009
- [19] Nila J. Dharan et al," Infections With Oseltamivir-Resistant Influenza A(H1N1) Virus in the United States",*The Journal Of the American Medical Association*, Vol. 301 No. 10, March 11, 2009, p.p 1034-1041
- [20] airo Gooskens et al," Morbidity and Mortality Associated With Nosocomial Transmission of Oseltamivir- Resistant Influenza A(H1N1) Virus", *JAMA*. 2009;301(10):1042-1046.
- [21] David M. Weinstock et al,"the Evolution of Influenza Resistance and Treatment", *JAMA*. 2009;301(10):1066-1069.
- [22] Li. D et al. Understanding SARS with Wolfram approach. *Acta Biochemical et Biophysical Sinica*. 2004; 36(1):1-10.
- [23] <http://www.who.int/csr/disease/swineflu/en,10-8-2009>
- [24] World Health Organization (WHO), Influenza-like illness in the United States and Mexico, "Epidemic and Pandemic Alert and

# 14<sup>th</sup> Annual Research Day

Organised by the Deanship of Scientific Research in Collaboration with the College of Engineering  
Research Centre

4<sup>th</sup> April 2019

---

Response (EPR)". 24 April 2009. Available  
from:

[http://www.who.int/csr/don/2009\\_04\\_24/en/index.html](http://www.who.int/csr/don/2009_04_24/en/index.html)

## Control Strategies for Liquid Level Control in Twin Tank System

Mohammad Fazle Azeem<sup>1</sup>, Hamid Naseem<sup>2</sup>, Muneer Parayangat<sup>1</sup>

<sup>1</sup>Department of Electrical Engineering, College of Engineering, King Khalid University,  
PO Box 394, Abha 61411 KSA.

<sup>2</sup>Department of Electrical Engineering, Yeungnam University, South Korea  
E-mail address: mazeem@kku.edu.sa

---

**Abstract:** Liquid Level control is one of the very basic but most important control strategies in most of the plants. A pump will experience cavitation if the liquid level inside the tank falls below a threshold value, which in turn will damage the pump and of course could cause a big problem to the entire plant operation. A twin tank system dynamic model has been developed. Control strategies starting from Propotional (P) control going through Propotional Integral (PI) control and finally Fuzzy logic control (FLC) has been implemented on the developed twin tank system. Modified Queen Bee based Genetic Algorithm has been applied to learn the tunable parameter of these controllers. The simulation results are interesting and encouraging.

**Keywords:** *Twin Tank System, Liquid Level Control, Fuzzy Control, Genetic Algorithm.*

---

### 1. Introduction:

The level control on interconnecting tanks is typical for processing and logistics industries as to manage their tank farms of various liquid feedstock, chemicals, products and by-products. It is part of the inventory control to prevent accumulation in the tanks. It is often needed to pump liquid from one tank to another. A pump will experience cavitation if the liquid level inside the tank falls below a threshold value, which in turn will damage the pump and of course could cause a big problem to the entire plant operation. The performance of reactor or bioreactor is highly influenced by the liquid level in the reactor or bioreactor. So, reactor/bioreactor can run at its optimum condition by controlling the liquid level. Controlling the liquid levels in tanks is not only to keep those levels constants, but such a control is mandatory strategy to ensure that the entire system can run safely (e.g., no tank will dry up or overflow), smoothly (e.g. no pump will break down due to cavitation) and profitably (e.g., a reactor tank will always perform at its optimum condition).

With these objectives dynamic model of twin tank system has been derived on the principle of conservation of mass flow. It is implemented in SimuLink and described in section 2. Section 3 confers about the implementation of control strategies, namely Propotional (P) control, Propotional Integral (PI) control, and Fuzzy Logic Control (FLC), on twin tank system. Section 4 elaborates Modified Queen Bee based Genetic Algorithm, which is applied to learn the tunable parameter of these controllers. The simulation results and discussion are presented in section 5. Finally the conclusions are relegated to section 6

### 2. Dynamic Model of Twin Tank System:

Twin-level tank system is shown in Fig. 1, which consists of no. 1 and 2 tanks, actuators, a pump, and a valve together with flow-rate and level sensors. The liquid is injected into tank1 with quantity of flow via controlling the voltage  $V_p(t)$  of inlet pump using pulse width modulating (PWM), and then flow from tank1 to tank2 with quantity of flow through the interconnecting

valve 'b', with the valve opening 100% and the discharge valve c opening is 75%.

The dynamic model is established by taking material balance around each tank. Liquid levels in tank1 and tank2 are  $L_1$  and  $L_2$ . The independent variable is the voltage  $V_p(t)$  to inlet pump. Now the dynamic model for each tank is derived as follows:-

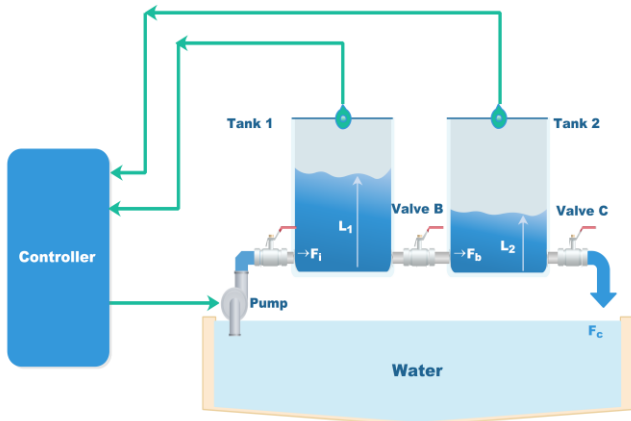


Figure (1) Twin Tank System with Controller

$$\dot{L}_1(t) = \frac{1}{A} [F_i(t) - F_b(t)] \quad \frac{\text{cm}}{\text{sec}} \quad (1)$$

where,

$F_i(t)$  = the pump flow rate  $\text{cm}^3/\text{sec}$

$F_b(t)$  = the flow rate ( $\text{cm}^3/\text{sec}$ ) from tank 1 to tank 2 through valve 'b'

$A$  = cross sectional area of tank 1 and tank 2 in  $\text{cm}^2$

$L_1(t)$  = water level in tank 1 in cm.

$$\dot{L}_2(t) = \frac{1}{A} [F_b(t) - F_c(t)] \quad (2)$$

where,

$F_c(t)$  = the flow rate ( $\text{cm}^3/\text{sec}$ ) from tank 2 through valve 'c'

$L_2(t)$  = water level in tank 2 in cm.

$$F_c(t) = a_c \cdot \sqrt{2g L_2} \quad (3)$$

$$F_b(t) = a_b \cdot \sqrt{2 \cdot g(L_1(t) - L_2(t))} \quad (4)$$

where,

$g$  = the acceleration due to gravity

Following dynamic model equations are obtained by substituting eq. (3) and (4) in eq. (1) and (2).

$$\dot{L}_1(t) = -\frac{a_b}{A_1} \cdot \sqrt{2 \cdot g(L_1(t) - L_2(t))} + \frac{K_p}{A_1} V_p(t) \quad (5)$$

$$\dot{L}_2(t) = \frac{a_b}{A_2} \cdot \sqrt{2 \cdot g(L_1(t) - L_2(t))} - \frac{a_c}{A_2} \sqrt{2g L_2(t)} \quad (6)$$

Equations (5) and (6) are being implemented in SimuLink and shown in Figure (2).

The system parameters are given in Appendix.

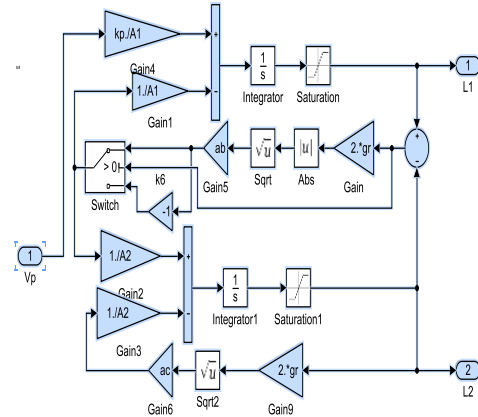


Figure (2) A SimuLink implementation of twin tank system.

### 3. Control Strategies:

#### 2.1 Proportional-Integral (PI) Control

The PI-control action is mathematically expressed as:

$$u(t) = K_P \cdot e(t) + K_I \int e(t) \cdot dt \quad (7)$$

Where,  $e(t)$  = set-point(t)-response(t); and

$u(t)$  = output of the controller.

$K_P$  = Proportional constant coefficient.

$K_I$  = Integral constant coefficient.

Only P-action is obtained by setting  $K_I = 0$ , in eq.(7). Figure(3) shows the P and PI control action implementation.

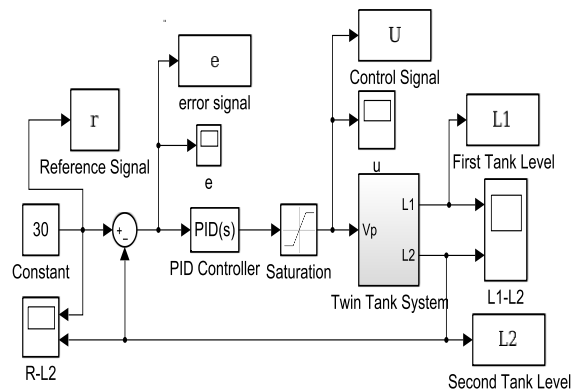


**Figure (3)** P and PI Control Implementation.

In the presented work the Proportional constant coefficient  $K_P$ , and Integral constant coefficient  $K_I$  for P-action and PI-action have been tuned using Modified Queen Bee based Genetic Algorithm and discussed in section 4.

### 2.2 Fuzzy Logic Control (FLC)

By FLC, we mean a control law that is described by a knowledge-based system consisting of IF-THEN rules with vague predicates and fuzzy logic inference mechanism. A typical rule of FLC is as follows:

IF  $e$  is **N** and  $ce$  is **P** THEN  $du$  is **Z**

The error  $e(k)$  and its change  $ce(k)$  as the input or antecedents, and change of control  $du(k)$  as the outputs or consequents of rule base.

where  $e(k) = \text{set-point}(k) - \text{response}(k)$ ;

and  $ce(k) = e(k) - e(k-1)$

FLC can be represented as:

$$du(k) = f[e(k), e(k-1)] \quad (8)$$

Where a rule base describes a nonlinear function  $f^*$ . Each of the rules of FLC is characterized with an IF part called antecedent and with a THEN part called consequent, thus FLC is a kind of state variable controller governed by a family of rules and fuzzy inference mechanism.

Equation (8) represents PD-type FKBC. In the case of PI-type FKBC the actual value of the controller output ( $u$ ) is obtained by:

$$u(k) = u(k-1) + du(k) \quad (9)$$

FLC control scheme for twin tank system is implemented as shown in Figure (4).

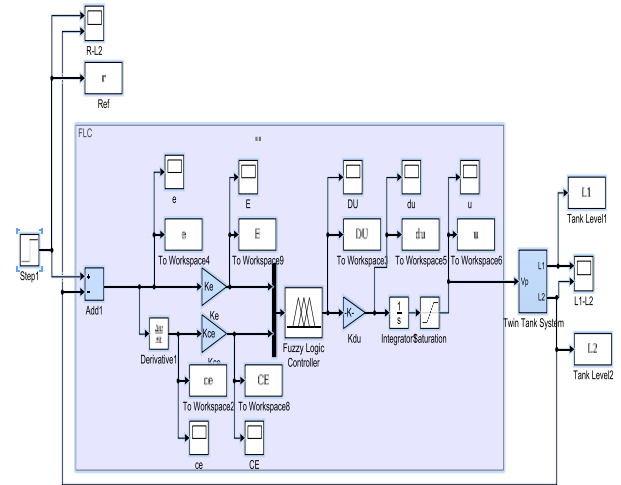


**Figure (4)** FLC Control Implementation.

The FLC implementation is discussed in section 2.3. In this work the scaling factors  $K_e$ ,  $K_{ce}$ , and  $K_{du}$  have been tuned using Modified Queen Bee based Genetic Algorithm and discussed in section 4.

### 2.3 Fuzzy Logic Control (FLC) implementation

For the design of FLC, the domain of  $e$ ,  $ce$  and  $du$   $[-1, +1]$  are partitioned into five Fuzzy sets (**NB**, **NS**, **Z**, **PS**, **PB**) by Gaussian membership functions (with variance 0.2123) as shown in Figure (5). The twenty five rules of FLC are listed as lookup table in Table 1. For ‘and’ an implication operation ‘min’ operator is used, while ‘max’ operator for ‘or’ and aggregation operation. Centroid method of defuzzification is applied.

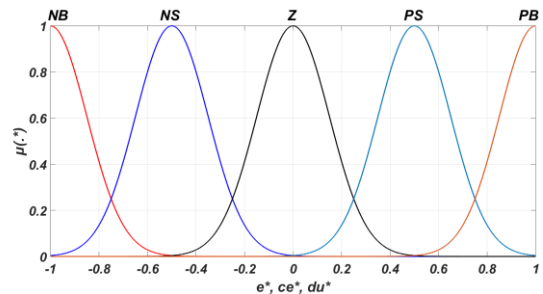


**Figure (5)** Partition of  $e$ ,  $ce$  and  $du$  by Gaussian membership functions.

**Table 1: 9 Rules of FKBC**

<b>ce*→</b>	<b>NM</b>	<b>NS</b>	<b>Z</b>	<b>PS</b>	<b>PM</b>
<b>e*↓</b>					
<b>NB</b>	<i>NB</i>	<i>NB</i>	<i>NS</i>	<i>NS</i>	<i>Z</i>
<b>NS</b>	<i>NB</i>	<i>NS</i>	<i>NS</i>	<i>Z</i>	<i>PS</i>
<b>Z</b>	<i>NS</i>	<i>NS</i>	<i>Z</i>	<i>PS</i>	<i>PS</i>
<b>PS</b>	<i>NS</i>	<i>Z</i>	<i>PS</i>	<i>PS</i>	<i>PB</i>
<b>PB</b>	<i>Z</i>	<i>PS</i>	<i>PS</i>	<i>PB</i>	<i>PB</i>

#### 4. Controller Parameters Learning:

An specific variant of Genetic Algorithm (GA) has been applied for learning/tuning of controller parameters, like Proportional constant coefficient  $K_p$ , Integral constant coefficient  $K_I$  for P-action and PI-action as well as scaling factors  $K_e$ ,  $K_{ce}$ , and  $K_{du}$  for FLC. The Genetic Algorithm is a probabilistic computer driven search and optimization technique modeled after the mechanics of genetic evolution. [41–42]. Unlike many classical optimization techniques, GA's do not rely on computing local derivatives to guide the search process, rather GA's perform random search. For this, all they need is an objective function. Reciprocal of the linear sum of Integral Time Absolute Error (ITAE) and Integral Absolute Error (IAE) is used as the objective function, called as fitness, to guide the GA based search process. The ITAE, IAE and the fitness function are defined by (10) and (11) respectively. GA's are also more likely to arrive at the global optima because they work on a population of points as opposed to conventional optimization techniques.

$$ITAE = \int_0^t t \cdot |e| \cdot dt$$

$$IAE = \int_0^t |e| \cdot dt \quad (10)$$

$$fitness = 1/(ITAE + \lambda \cdot IAE) \quad (11)$$

where,  $\lambda$  = a normalization constant ( $\lambda \in \mathbb{R}^+$ )

In general, a GA consists of three fundamental operators: reproduction (parent selection), crossover and mutation. GA's is started with a set of solutions (represented by chromosomes) called population, generated randomly, and the evolutionary process of reproduction, crossover and mutation are used to generate an entirely new population from the existing population. The reproduction operator selects good chromosomes in the population to form the mating pool. Selection of chromosome for parenthood can range from a totally random process to one that is biased by the chromosome fitness. The modified Queen bee evolution operators are discussed in subsection 4.1. Crossover operator is used to exchange genetic materials between the parents with the aim of obtaining better chromosomes. Two parent chromosomes are selected from the mating pool randomly and the crossover rate determines the probability of producing a new chromosome from the parents. A number of crossover operators are discussed in the literature. The crossover operator relevant to the investigations in this paper is detailed in subsection 4.2. The mutation operator is next applied. The mutation operator takes each child chromosome and randomly change some of its genes with a given mutation probability. Flipping a bit in the binary coded GA does mutation. While in non-binary coded GA, mutation involves randomly generating a new character in a specified position.

#### 4.1 Modified Queen Bee Evolution (Parent selection operator)

The queen bee algorithm is limited to a single pool (honeycomb). Author has another concept that bee algorithm should not be restricted to a single pool. In nature honeycombs grow around queen bee, and if any queen bee will born in a

honeycomb, she build another honeycomb by sharing the members from her parent honeycomb. The same concept is applied in proposing the modified queen bee algorithm. The schematic diagram of splitting of pools, generation by generation, with the availability of queen bee for modified bee genetic algorithm is shown in Figure (6). Since each member (solution) of the pool has to crossover with queen (most fitted solution) of the pool. After splitting the parent pool due to the birth of queen bee (next most fitted solution), above-mentioned mating process makes the specified population size of the pool. The new queen in a pool is identified if any solution has the fitness very close (say 98%) or above of the fitness of the mother queen. At the same time some of the beehives disappear due to some accidental process, i.e., death of queen bee, attack of bear/harvester in search of honey as food, storm etc. Only the best fitted beehives survive longer. This process is also imitated in the proposed genetic algorithm by limiting the number of pools. It is shown in the last stage of Figure (6). By limiting the six pools in a generation least fitted pools, i.e., pool 1 and pool 7 are disappearing from that generation.

In uniform crossover the gene selection is purely random. Each bit is crossed with some probability, typically one half. For each gene in the chromosome, one random value  $R$  is generated. If  $R$  is more than the probability, the corresponding bit in parent 1 is copied to child 2 and the corresponding bit in parent 2 is copied to child 1, otherwise the corresponding bit in parent 1 is copied to child 1 and the corresponding bit in parent 2 is copied to child 2.

In weighted based crossover operator gene selection is based on the weights assigned to the genes for crossover operation. This will guide GA to search for more new state space The Uniform crossover is a special case of weighted uniform crossover. In weighted uniform crossover, weights are assigned to each bit/gene in the chromosome according to the similarity of the test patterns in the population and weighted uniform crossover is performed which is based on some probability that depends on the weights of the parent bits. For example, two parents  $P1$  and  $P2$  are selected to produce two child chromosomes  $C1$  and  $C2$ . Each gene  $G_{i,1}$  in parent  $P1$  competes against the corresponding gene  $G_{i,2}$  of parent  $P2$ . If weight  $W_{i,1}$  is equal to  $W_{i,2}$ , the bits are crossed with a given probability as in uniform crossover. If  $W_{i,1}$  and  $W_{i,2}$  are different, both the child chromosomes are assigned the value of the lighter bit, i.e., bit with weight 0 as shown in Figure (7). The rules for Weight based crossover operator are shown in Table 2.

The Genetic Algorithm based on modified queen bee evolution is described in Algorithm 1. Various parameter values for GA are listed in Table 3.

Note that the population size for modified queen bee method is fifteen in a pool. In the beginning the number of solution, whose fitness has to be tested, is far less but within five generation it grows to specified number of solution as number of pools doubles in each generation. As the simulation progress number of pools reaches to its maximum number, i.e. nine, in turns the

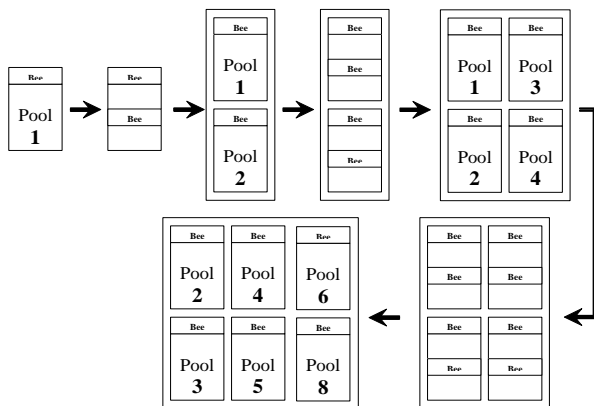


**Figure (6)** Schematic diagram of splitting of pools generation by generation in modified Queen bee evolution

## 4.2 Weighted Based Crossover Operator

# 14<sup>th</sup> Annual Research Day

Organised by the Deanship of Scientific Research in Collaboration with the College of Engineering Research Centre

4<sup>th</sup> April 2019

number of solution reached to one hundred thirty five, which is quit sufficient. The simulation is carried out for small size problem; it can be applied to large size problem too.

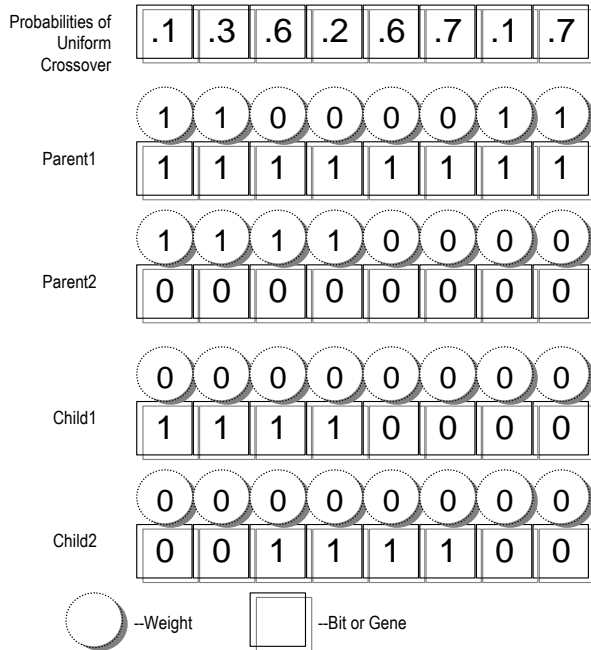


Figure (7) Schematic representation of weight base uniform crossover

Table 2: Rules For WCO

OPERATION	Bit/gene Weight of Parent 1	Bit/gene Weight of Parent 2
Same as uniform crossover	0	0
Assign bit of P1 to both C1&C2	0	1
Assign bit of P2 to both C1&C2	1	0
Same as uniform crossover	1	1

## Algorithm 1:

```

//t: generation//, //n: population size in a pool//,
//pl: number of pools//, //P: populations//,
//plmax: maximum number of pools//
//ξ: normal mutation rate//,
//pm: normal mutation probability//,
//p'm: strong mutation probability//,
//Iq: a queen bee//, //Im: selected bee//
1 t ← 0: pl(t) ← 1; initialize P{pl(t)}; evaluate P{pl(t)}
2 while 1 (not terminate condition)
3 do
4     t ← t+1
5     while 2 [pl(t)]
6     do 2
7         select P{pl(t)} from P{pl(t-1)}(*)
8         P{pl(t)}=[ Iq{pl(t-1)} , Im{pl(t-1)} ]
9         recombine P{pl(t)}; do crossover; do mutation (*)
10        for i=1 to n
11            if i ≤ (ξ×n)
12                do mutation with pm
13            else
14                do mutation with p'm
15            end if
16        end for
17        evaluate P{pl(t)}; search for new_ Iq{pl(t)}
18        if ( new_ Iq{pl(t)} found )
19            split the pool and new_pl(t) ← pl(t)+1
20        else
21            new_pl(t) ← pl(t)
22        end if
23        if (new_pl(t) > plmax)
24            pl(t) ← plmax (oldest pool deleted)
25        end if
26    end while2
27 end while1
    
```

Table 3: Values of GA Parameters

Parameters	Values
	Modified Queen bee
Crossover Probability (p <sub>c</sub> )	0.8
Normal Mutation Probability (p <sub>m</sub> )	0.01
Population Size	15
Individual bit length	10
Normal Mutation Rate (ξ)	0.6
Normal Mutation Probability (p' <sub>m</sub> )	0.4
Maximum Number of Pools	9

## 5. Simulation Results:

Parameters of P, PI, and FLC controller are tuned by GA with the objective to maximize the fitness. The learning has been performed for the reference level of liquid in tank2 = 30 cm. Figure(8) shows the learning pattern, i.e., fitness vs generation for all the controller parameters. It shows that FLC controller have the highest fitness value= $3.8836 \times 10^{-6}$  in its 40<sup>th</sup> generation of learning. The corresponding value of scaling factors  $K_e = 0.0498$ ,  $K_{ce} = 3.0059$ , and  $K_{du} = 1.8416$ .

On the other hand P-controller have the lowest fitness value= $1.9491 \times 10^{-6}$  in its 3<sup>rd</sup> generation of learning. The corresponding value of Propotional constant coefficient  $K_p = 1.9761$ . For PI-controller have the fitness value= $3.7202 \times 10^{-6}$  in its 49<sup>th</sup> generation of learning. This value is close to the fitness value of FLC controller. The corresponding value of Propotional constant coefficient  $K_p = 0.49956$ , and Integral constant coefficient  $K_I = 0.00509$ .

With the above tuned values of parameters for P, PI, and FLC control and reference level of liquid in tank2 = 30 cm, the responses of the twin tank system have recorded. The response of these three controllers for tank2 liquid level are shown in Figure(9). P-controller gives an 8% offset error, as usual, with settling time  $T_s \approx 298$ sec. A test has been conducted by increasing the value of  $K_p$ , which has reduced the offset value but at the same time it has increased the settling time, oscillation frequency for liquid level  $L_2$  and oscillation frequency and magnitude for generated control signal  $u(t)$  which is the input dc voltage  $V_p(t)$  to inlet pump. This high frequency oscillation is undesirable for stability of the system.

With PI controller offset has been removed but an overshoot is present in the tank2 liquid level with a value of 6.22cm (20.73%) with settling time for (2% error)  $T_s \approx 252.6$  sec.

FLC controller also has vanishes the offset error but but with no overshoot for the tank2 liquid

level with settling time for (2% error)  $T_s \approx 236.0$  sec.

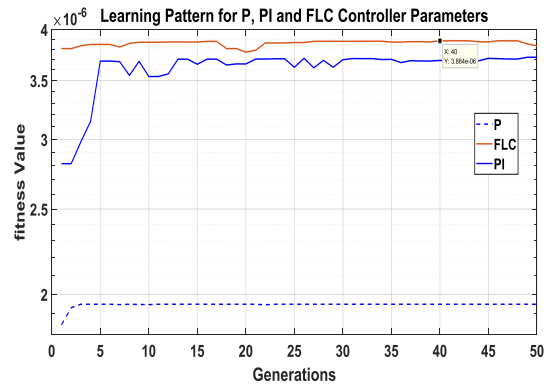


**Figure (8)** GA learning pattern for P, PI, and FLC controller Parameter

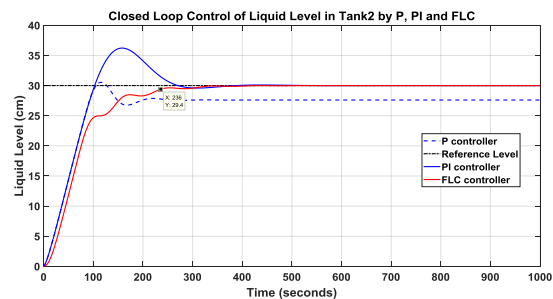


**Figure (9)** Closed loop control of liquid level in tank2 by P, PI, and FLC

The generated control signal  $u(t)$  by P, PI, and FLC control with reference level of liquid in tank2 = 30 cm is shown in Figure (10). Since the pump rating is 0-12 v (d.c.), the FLC and PI controller generate a smooth voltage signal in between 0-12 v. on the other hand P controller generates switching from 0 to 12 v in the beginning and later a smooth signal. The steady state control signal  $U_{ss}$  has been found as 5.0 volt for FLC and PI controller and 4.8 for P controller corresponding to the reference level as 30cm for tank2 liquid.

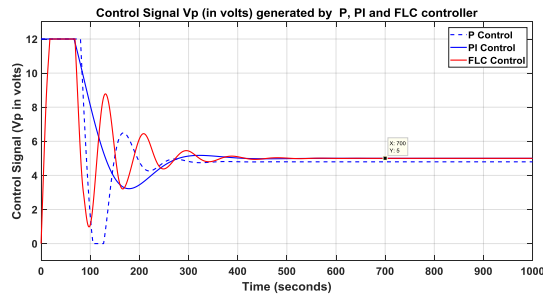


**Figure (10)** Control  $u(t)$  generated by P, PI, FLC

These controllers with the tuned parameters have been tested for variable reference liquid level of tank2. First the level has set to 30cm then increased to 40cm and finally reduced to 20cm. The responses are recorded and shown in Figure (11) and (12). These variable reference level test insures the functioning of these three controllers while preserving their performance. Since the obtained parameters of P, PI, and FLC controller are tuned for only one reference level of tank2 liquid (30cm), but they are preserving their performance for all the levels between 20cm~ 40cm.

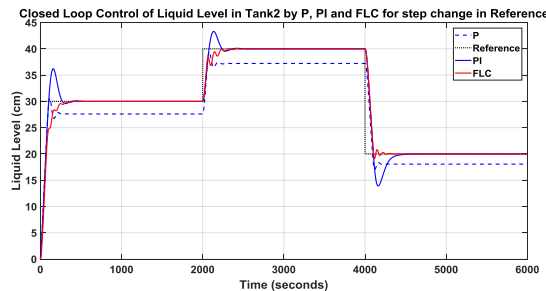


**Figure (11)** Closed loop control of liquid level in tank2 by P, PI, and FLC for step change in reference.

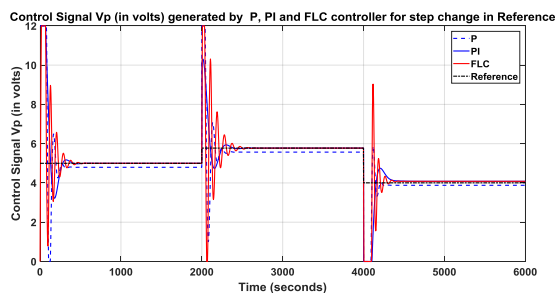


**Figure (12)** Control  $u(t)$  generated by P, PI, FLC for step change in reference

## 6. Conclusions:

Different modulation control strategies have been implemented for twin tank control system. Modified queen bee evolution based genetic

algorithm has been implemented for the tuning of P, PI, FLC controller parameters. Their performances have been compared. It is observed that FLC control outperform with P, and PI control in terms of offset error, peak overshoot and settling time. While PI control has been the best for control signal generation, but FLC control performance in this term is very close to PI control. In terms of control signal P control is the worst. In conclusion FLC control is the best among all discussed in the presented study.

## Acknowledgement

We are highly thankful to the King Khalid University and College of Engineering for providing this excellent platform of Research Day to present our research work.

## Appendix: Twin tank system parameters

Symbols	Significance	Value
$A_1, A_2$	Area of cross section of tank1 and tank2	1008.06 cm <sup>2</sup>
$L$	Height of tank1 and tank2	76 cm
$L_1, L_2$	Height of Liquid in tank1 and tank2	Variable
$a_b, a_c$	Area of cross section of valve 'b' and 'c'	$a_b = 0.7854$ cm <sup>2</sup> $a_c = 0.5891$ cm <sup>2</sup>
$K_P$	Inlet pump coefficient	114.30 cm/volt-sec
	Inlet Pump Rating	12v dc-2amp

## References

- [1]. Y. Fu and T. Y. Chai, "Nonlinear multivariable adaptive control using multiple models and neural networks," *Automatica*, vol. 43, no. 6, pp. 1101–1110, Jan. 2007.
- [2]. T. Y. Chai, L. F. Zhai, and H. Yue, "Multiple models and neural networks based decoupling control of ball mill coal-pulverizing systems," *J.Process Cont.*, vol. 21, no. 3, pp. 351–366, Mar. 2011.
- [3]. I. Markovsky and P. Rapisarda, "Data-driven simulation and control," *Int. J. control*, vol. 81, no. 12, pp. 1946–1959, 2008.

# 14<sup>th</sup> Annual Research Day

Organised by the Deanship of Scientific Research in Collaboration with the College of Engineering  
Research Centre

4<sup>th</sup> April 2019

---

- [4]. J. Helvoort, B. D. Jager, and M. Steinbuch, "Data-driven multivariable controller design using ellipsoidal unfalsified control," *IEEE Syst. Cont. Lett.*, vol. 57, no. 9, pp. 759–762, Sep. 2008.
- [5]. M. Ren, J. Zhang, and H. Wang, "Minimized tracking error randomness control for nonlinear multivariate and non-gaussian systems using the generalized density evolution equation," *IEEE Transactions on Automatic Control*, vol. 59, no. 9, pp. 2486–2490, 2014.
- [6]. X. Liu and Z. Gao, "Robust finite-time fault estimation for stochastic nonlinear systems with brownian motions," *Journal of the Franklin Institute*, 2016.
- [7]. J. Zhang, M. Ren, and H. Wang, "Minimum entropy control for nonlinear and non-gaussian two-input and two-output dynamic stochastic systems," *Control Theory & Applications, IET*, vol. 6, no. 15, pp. 2434–2441, 2012.
- [8]. K. J. Astrom and T. Hagglund, "Advanced PID control. ISA-The Instrumentation, Systems and Automation Society, 2006.
- [9]. R. K. Mudi and C. Dey, "Performance improvement of pi controllers through dynamic set-point weighting," *ISA transactions*, vol. 50, no. 2, pp. 220–230, 2011.
- [10]. T. Chai, S. J. Qin, and H. Wang, "Optimal operational control for complex industrial processes," *Annual Reviews in Control*, vol. 38, no. 1, pp. 81–92, 2014.
- [11]. J. Hu, Z. Wang, S. Liu, and H. Gao, "A variance-constrained approach to recursive state estimation for time-varying complex networks with missing measurements," *Automatica*, vol. 64, pp. 155–162, 2016.
- [12]. Y. Liu, H. Wang, and L. Guo, "Observer-based feedback controller design for a class of stochastic systems with non-gaussian variables," *IEEE Transactions on Automatic Control*, vol. 60, no. 5, pp. 1445–1450, 2015.
- [13]. J. S. R. Jang, "ANFIS: Adaptive-network-based fuzzy inference system," *IEEE Trans. Syst. Man Cybern.*, vol. 23, no. 3, pp. 665–685, May–Jun. 1993.
- [14]. Zadeh L. A., "Outline of a new Approach to the Analysis of complex systems and decision process", *IEEE Trans. Syst. Man. Cybern.*, vol. 3, no. 1, pp.28-44, 1973 & vol 15, pp. 15-30, 1979
- [15]. G. Caste llano, G. Attolico, and A. Distant, "Automatic generation of fuzzy rules for reactive robot controllers", *Robot. Auton. Syst.*, vol.22, pp. 133–149, 1997.
- [16]. L. X. Wang and J. M. Mendel, "Generating fuzzy rules by learning from examples", *IEEE Trans. Syst., Man, Cybern.*, vol. 22, pp 1414–1427, Feb. 1992.
- [17]. E.H. Mamdani and S Asian, "An experiment in linguistic synthesis with a fuzzy logic controller", *Int. J. Man-Mach. Stud.* vol.7, no.1, pp.1-13, 1975.
- [18]. Zadeh L.A., "Fuzzy sets", *Inf. Contr.*, vol 21. pp. 338-353, 1965.
- [19]. Holland J.H, "Adaptation in neural and artificial systems", *Univ. of Michigan press, Ann Arbor*, 1975.
- [20]. Davis, L, "A handbook of Genetic Algorithms", *Van Nostrand Reinhold, New York* 1990.
- [21]. D.E. Goldberg, "Genetic Algorithm in search, optimization and Machine learning", *Addison-Wesley* 1989.
- [22]. Bhuvanewari MC and Sivavandam SN, "Genetic Algorithm based Test Generation: An Analysis of Crossover Operators", *The Journal of The Computer Society of India*, vol. 32, No.1,
- [23]. Syswerda G, "Uniform crossover in Genetic Algorithms", in *Proc of the third international conference on Genetic Algorithms*, Schaffer, J (Ed); (Morgan Kauffman Publishers, Cambridge, MA, 1989), pp. 2-9.
- [24]. Sung Hoon Jung, "Queen bee evolution for genetic algorithms", *Electronics letters*, 20th March 2003, Vol. 36 No. 6 pp. 575-576. Online No.20030383, DOI: 10.1049/el:
- [25]. Cheong, F. and Lai, R, "On simplifying the automatic design of a fuzzy logic controller"; in *Proc. NAFIPS. 2002, Annual Meeting of the*

# 14<sup>th</sup> Annual Research Day

Organised by the Deanship of Scientific Research in Collaboration with the College of Engineering  
Research Centre

4<sup>th</sup> April 2019

---

North American, Fuzzy Information Processing Society, 2002, pp.481–487, 27-29 June 2002  
[26]. Rajni K. Mudi and Nikhil R. Pal, “A robust self-tuning scheme for PI- and PD-type

fuzzy controllers”. IEEE Trans. On Fuzzy Systems. 7(1). pp. 2—16, February 199

## Nonlinear Transformation for Improving Noise Robustness of Chaotic Signals

Thafasal Ijyas V. P., Muneer P., Fakher Eldin Mohamed Sulaiman,  
Bushara Salaheldin Bushara Elnoor<sup>1</sup>

<sup>1</sup>Department of Electrical Engineering, College of Engineering, King Khalid University,  
PO Box 394, Abha 61411 KSA.

---

**Abstract:** In this work, we propose that nonlinear transformations can increase the noise robustness of chaotic signals. Chaotic signals find application in secure communication. As is demonstrated in this work, an appropriate nonlinear transformation can improve the noise immunity of such signals. Thus, we can achieve the double benefits of security as well as better bit error rate (BER) performance using the technique proposed. We developed an interactive multiple model (IMM) estimator for the chaotic signals and also applied a hyperbolic tangent – hyperbolic arc tangent pair transformation to achieve encryption and noise immunity for the signals. The efficacy of the method is substantiated through simulation studies.

**Keywords:** *Chaos, Nonlinear estimation, IMM, BER, Secure Communication*

---

### 1. Introduction:

The last two decades have witnessed a flurry of research efforts for developing efficient chaos-based communication methods. Evolving from the theoretical results of Pecora and Carroll, who established that two identical chaotic systems starting from different initial conditions can synchronize [1], these efforts have now diversified into various theoretical and experimental directions. The phenomenon of chaos adduces several qualitative advantages to the communication issue. Due to the seemingly-random, deterministic behavior of chaotic signals, they can be used to spread information signals. This spreading of the signal spectrum provides us with many advantages like robustness against interference and noise, low probability of intercept etc. Chaotic signals can find application in Code Division Multiple Access (CDMA) systems due to the high degree of uncorrelatedness among the chaotic signals generated by the same system itself under varying initial conditions and parameters. The intricate dynamics of chaotic signals is generated from simple dynamical systems of low order. This

reduces the transmission system complexity and also makes it extremely difficult for unauthorized persons to access the messages transmitted.

Chaotic communication has come a long way from the initial breakthrough created by the Pecora – Carroll work in 1990 [2]. Recently, chaotic synchronization methods based on non-linear filters have evoked considerable interest in the communication field. These are based on the extended Kalman filter (EKF) and many other variants. It has been proved theoretically that EKF-based synchronization can outperform the conventional synchronization methods like drive-response method [1], unidirectional coupling [6] etc used in chaotic communication [3]. Also, EKF-based synchronization can be used for blind channel equalization [8], noise reduction, parameter estimation etc. There are newer versions of non-linear filters, which produce better results than the extended Kalman filter. Of specific mention is the interacting multiple model (IMM) approach [7, 11]. This method accounts for some of the best techniques for state estimation, where the underlying dynamics of the system is not

linear and consists of jumps between modes or corresponding models.

Conventional non-linear filters like EKF give poorer performance in cases where there is jump between models. Thus, IMM addresses a hybrid state estimation problem, where the state transition can be considered to be imbedded in a Markovian

jump between a set of models. This method is attractive in chaotic communication, where the chaotic model changes with the transmitted bit. The jump process between the different models is a Markov chain, with known transition probabilities. Though the IMM algorithm has been in use in target tracking for more than two decades now, its potential in communication has only been recently tapped. A recent work [13] on chaos-based communication utilizing the IMM algorithm sheds light on the advantages of this method over conventional EKF-based methods.

## 2. Problem Formulation:

This work primarily addresses the state estimation of discrete-time chaotic sequences generated by one-dimensional maps from the corresponding observations obtained over transmission through a noisy channel. We have developed a specific non-linear transformation method for chaotic sequences, which improves the security and noise robustness in chaotic communication.

### 2.1 System Model

A simplified block diagram of a chaos-based communication system is given in Figure 1. This could be an M-ary Chaos Shift Keying system in which each of the M-ary symbols is converted into a different discrete-time chaotic sequence of fixed length, say 50 or 100. The M-ary symbols are generated from the input binary stream data. The sequences used in this work are the symmetric tent map sequence which is represented as,

$$x(n+1) = a - 1 - a \times |x(n)| \quad (1)$$

The symmetric tent map turns chaotic for the parameter value range,  $1.5 < a < 2$ .

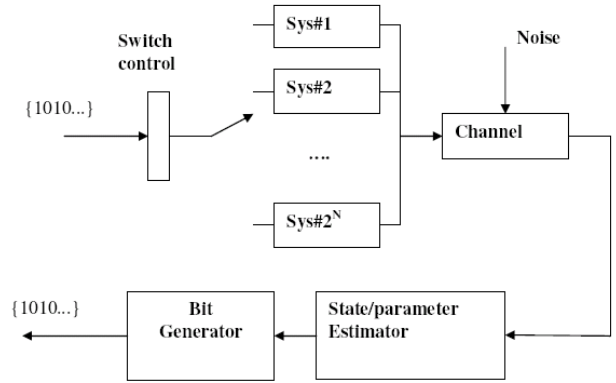


**Figure (1)** Block Diagram of a Chaotic Communication System.

In this work, each M-ary symbol is coded into a distinct chaotic sequence with a fixed parameter value. For example, in the single-bit modulation system implemented in this project, the symmetric tent map is chosen with  $a = 1.55$  for bit '0' and  $a = 1.75$  for bit '1'. The modulation of each bit into a chaotic sequence of length 20 is shown in Figure 2.

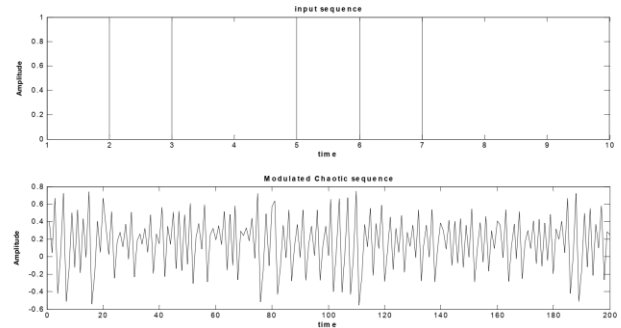


**Figure (2)** Chaotic Sequence for Symmetric Tent Map.

An AWGN channel is presumed and hence noise is added to this chaotic sequence. The estimator at

the receiver estimates the parameter values for each consecutive ‘N’ values of the chaotic time series corrupted by the noise.

## 2.2 IMM Estimator

Here, we make use of an IMM estimator for estimating the chaotic signal at the receiver side. The block diagram of the estimator is given in Figure 3.

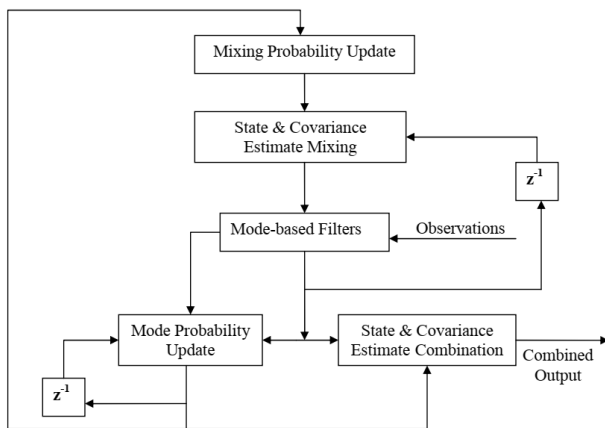


Figure (3) IMM Estimator

In the IMM method, the number of hypotheses at any time step ‘n’ is limited to ‘M’, the number of models instead of Mn. The ‘M’ different models are run as ‘M’ parallel non-linear estimation filters. Instead of directly feeding back the previous state and covariance estimates of each filter to itself, a weighted Gaussian mixture of the estimates of all the filters that can approximate the state density are calculated and fed back to each individual filter during each time step of the filter iteration.

## 2.3 A Nonlinear Transformation Method

In this work along with the development of the COF and UKF based IMM estimators for chaotic communication, a new nonlinear transformation method was also developed that is found to be useful in augmenting the noise robustness and security of a chaotic communication system. In the particular case discussed here, an arctanh

transformation is applied to the chaotic sequence at the transmitter side and a corresponding tanh transformation applied at the receiver side prior to estimation. The map used is the symmetric tent map itself. But this can be generalized to other maps also by either scaling this transformation to occupy the range of these maps or else by using other appropriate transformations.

## 3. Results and Discussion

The results for the EKF filter (state estimator, parameter estimator and IMM version) are shown in Figure 4.

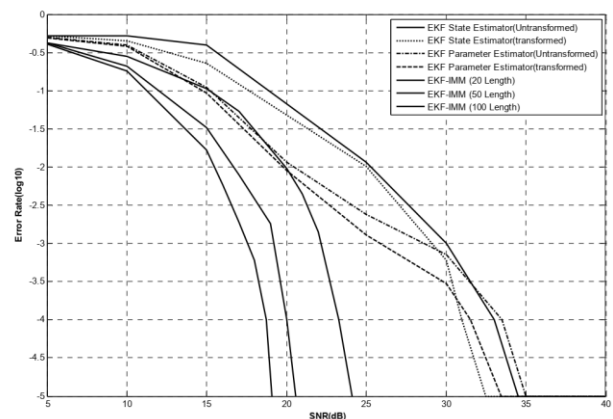


Figure (4) BER of the Proposed Method

We can see that the communication system with the non-linear transformation offers improved noise performance compared to the untransformed one in both cases. Also, the IMM version far outperforms the conventional EKF filters.

## 4. Conclusions:

In this work, we have developed a novel noise immunity enhancement technique for chaotic signals. This can have important applications in chaos-based systems for communication and control. The work is pioneering attempt to investigate the applications of non-linear transformations for the general class of non-linear signals.

# 14<sup>th</sup> Annual Research Day

Organised by the Deanship of Scientific Research in Collaboration with the College of Engineering  
Research Centre

4<sup>th</sup> April 2019

---

## References

- [1] L. Pecora, T. Carroll, "Synchronization in chaotic systems", *Phys. Rev. Lett.*, Vol. 64, pp. 821-823, 1990.
- [2] T. Yang, "A Survey of Chaotic Secure Communication Systems", *International Journal of Computational Cognition*, Vol. 2, No. 2, June 2004.
- [3] Henry Leung, Zhiwen Zhu, "Performance Evaluation of EKF-Based Chaotic Synchronization", *IEEE Trans. Circuits Syst. I*, vol. 48, pp. 1118-1125, 2001.
- [4] Kalman, R. E., "A New Approach to Linear Filtering and Prediction Problems," *Trans. ASME J. Basic Eng.*, 82, pp. 34-35, 1960.
- [5] Kalman, R. E. and R. S. Bucy, "New Results in Linear Filtering and Prediction Theory," *Trans. ASME J. Basic Eng.*, 83, pp. 95-108, 1961.
- [6] M. J. Ogorzalek, "Taming chaos—Part I: Synchronization," *IEEE Trans. Circuits Syst. I*, vol. 40, pp. 693–699, Oct. 1993.
- [7] T Söderström. "Discrete Time Stochastic Systems", Springer, London, Great Britain, 2002 Edition.
- [8] Zhiwen Zhu and Henry Leung, "Adaptive Blind Equalization for Chaotic Communication Systems Using Extended-Kalman Filter", *IEEE Trans. Circuits Syst.*, vol. 48, pp. 979–989, Aug. 2001.
- [9] S. J. Julier and J. K. Uhlmann, "A New Extension of the Kalman Filter to Nonlinear Systems", In *Proc. Of Aerosense: The 11th Int. Symp. On Aerospace/Defence Sensing, Simulation and Controls*, 1997.
- [10] Eric A. Wan and Rudolph van der Merve, "The Unscented Kalman Filter for Nonlinear Estimation", (Although an IEEE publication, journal not specified).
- [11] H. Ruan, E. Yaz and Tongyan Zhai, "Current Output Filter for the State Estimation of Stochastic Nonlinear Dynamic Systems," *International Journal on Innovative Computing, Information and Control*, Vol. 1, No. 2, pp. xx, 2005.
- [12] X. Rong Li and Vesselin P. Jilkov , "A Survey of Manoeuvring Target Tracking—Part V: Multiple-Model Methods", Department of Electrical Engineering, University of New Orleans, New Orleans, LA 70148, USA, *IEEE Transactions on Aerospace and Electronic Systems*: November 26, 2003.
- [13] Thuraiappah Sathyan and Thiagaligam Kirubarajan, "Markov-Jump-System Based Secure Chaotic Communication", *IEEE Trans.Circuits Syst. I*, vol. 53, No.7, pp. 1597–1609, July 2006.

# 14<sup>th</sup> Annual Research Day

Organised by the Deanship of Scientific Research in Collaboration with the College of Engineering  
Research Centre

4<sup>th</sup> April 2019

## Ratio of High-Extinction and Low Based Silica In Relation To Strictly Non-Blocking High Density Switches: a Review

Fakher Eldin M Suliman, Elfatih A. A. Elsheikh, Muneer P., Thafasal Ijyas

Department of Electrical Engineering, College of Engineering, King Khalid University  
PO Box 394, Abha 61411 KSA.

Correspondent E-mail: fmsuliman@kku.edu.sa

**Abstract:** In this study, we have inspected as a function of the number of laser pulses (from 500 to 2500) both morphological and optical properties of Nano metric Au NP deposited on 2D (silica and (100) Si) and 3D (silica NW switches) substrates by sup-picosecond ablation of an Au bulk target, Because of the different effective surface area, the morphology of the substrates influenced the number of laser pulses suitable to achieve a uniform coverage. The influence of the number of laser pulses on the NP size has been discussed based on a combined effect of structural surface modifications induced by residual thermal energy and re-deposition of the NPs produced by ablation presence. Moreover, the presence of droplets has been discussed as depending on the weak electron-phonon coupling of Au.

**Keywords:** High extinction ratio, silica nanowire, Nano particles, pulsed laser deposition

### 1. Introduction

The development of accurate, robust and selective sensors, that can be able to provide a real time monitoring of analyte elements, is a key tool for the advancement in many research and technology fields. Moreover, for this kind of sensors, the use of unconventional substrates like silica nanowire (NW) switches represents an interesting strategy to increase the sensitivity and selectivity of the sensor. In fact, a high surface-to-volume ratio and curvature features guarantee more sites available for adsorption than conventional bulk substrates and high density of hot spots. At the same time the use of this kind of substrates provides withstanding high temperatures (up to ~1000 °C) [1].

The decoration of NW switches with plasmonic nano particles (NPs) requires of growth/deposition methods of the metal nanostructures with control on their morphology, distribution, size and size-dispersion as well as density. To date, approaches allowing the deposition of plasmonic NPs on NW switches include wet chemical reduction methods, thermal evaporation, electron beam evaporation, ion

implantation, electro-deposition, sputtering, atomic layer deposition, electrophoretic deposition [chemical vapor deposition or chemisorption of pre-synthesized or in situ synthesized NPs], dewetting of thin metal films evaporated on the NWs, galvanic deposition-annealing and pulsed laser deposition (PLD). In general, non uniform coverage and size distribution as well as surface dispersion of the NPs result in the case of wet-chemical reduction or vapor phase deposition and dewetting of thin metal films. Moreover, thermal treatment is often required as a post-processing step to increase size and improve crystallinity of the NPs anchored over NWs. Instead, PLD could be advantageous for depositing substrate-immobilized plasmonic NPs because it is a clean method without need of surfactants or stabilizing agents in chemical synthesis and functionalization, presents a variety of experimental parameters that can be tuned and interplayed, and provides an enhanced adherence with reduced size dispersion and high growth rate. Indeed, the nature of the ablation process involves the production of very energetic particles and supersaturated fluxes of ablated materials that

# 14<sup>th</sup> Annual Research Day

Organised by the Deanship of Scientific Research in Collaboration with the College of Engineering  
Research Centre

4<sup>th</sup> April 2019

---

favor enhancement of the nucleation rate and the production of highly dense and uniform NP layers on different kinds of substrates, even at room temperature. By exploiting sub-picosecond time duration for the ablation of solid targets at laser intensities in the range of 1-10 TW/cm<sup>2</sup>, the generation of the NP is achieved directly within the ablation target and, leading to a narrower size distribution of the NP [2].

Moreover, the presence of different ablation regimes, such as photomechanical spallation, explosive boiling and fragmentation, should promote the arrival onto the substrate surface of NPs produced inside the target with a kinetic energy considerably higher than those involved in other approaches and capable of enhancing their adhesion to the silica NWs without the need of NP functionalization. Hence, energetic deposition flux combined with high curvature substrates (such as NWs) are expected to enhance the rate of surface redistribution and nucleation, improving the coverage of the substrates with NP. For comparison, annealing process is effective for changing size and size distribution of the NP by means of migration rate depending on the NW curvature changed by changing the diameter of the NW [3].

In this study we extend our previous investigation on the PLD deposition of Au NP deposited over NW switches turning from nanosecond to sub-picosecond ablation in order to inspect changes in the deposit features (NP morphology, growth evolution and distribution) and test the potentiality of the sub-picosecond regime in applications such as optical sensitive transducers [3].

## 2. Discussion

In Fig. 1, the high (a, b, c) and low magnification (d, e, f) FESEM images of the samples deposited with different number of laser pulses are presented. The most noticeable characteristic of the low magnification images is the appearance of a high density of large spherical droplets with diameters ranging from a few tens

of nm to few microns; in the high magnification micrographs, on the image background, smaller NP can be also observed whose density increases with the number of pulses. For 500 laser shots, the appearance of faint NP can be observed in the micrograph, whereas in the sample deposited with 1500 pulses the surface is already completely covered by well developed NP having a diameter of few nm. These results suggest that in the experimental conditions at least 1500 laser pulses have to be used to obtain a good Au NP coverage on 2D substrates [4].

Instead, the coverage of 3D substrates, such as the silica NWs used in this work and previous dewetting experiments, requires a larger number of laser pulses to obtain similar morphologies because of the increased surface deposition area. In fact, in order to uniformly cover silica NWs by Au NP, 2000 and 2500 laser shots were used (Fig. 2 a and b, respectively). From these images, it can be observed a shadow effect of the top of silica wires for the deposition of Au NP on deeper wires as well as the presence of the spherical droplets observed on the 2D substrates. However, the shadowed areas represent a small percentage of the overall exposed surface. In addition, the very energetic flux of ablated material promotes a better coverage of the NW [3].

The comparison between the Au coverage obtained at 2000 and 2500 pulses demonstrates that larger and more defined NPs form at higher number of pulses, having an average size of about 9 nm at 2000 pulses and 13 nm at 2500 pulses. Further increase of the NP size to about 21 nm and better NP separation are reached after thermal treatment at 500 °C for 10 minutes in N<sub>2</sub> flow, as demonstrated by the image in Fig. 2c that shows the morphology of the sample obtained with 2500 laser shots. This finding can be ascribed to increased rate of Au migration rate at high temperature that favors Ostwald ripening, i.e., growth of larger NP at the expense of the smaller ones.

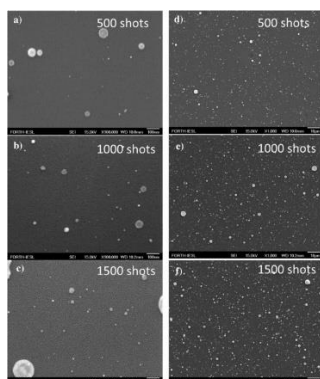


Fig. 1: Low (a, b, c) and high (d, e, f) magnification FESEM images of the samples deposited with 500 (a, d), 1000 (b, e) and 1500 ((c, f)) laser shots on (100) Si substrates.

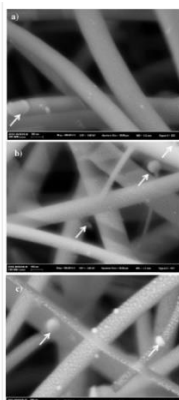


Fig. 2: High magnification FESEM images of the samples deposited on silica NWs with a number of laser pulses of (a) 2000, (b) 2500 and (c) 2500 after a thermal treatment at 500 °C for 10 minutes in N<sub>2</sub> flow. The arrows point at some of the spherical droplets formed in the target and transferred to the substrate.

The observed increase in the mean size of Au NPs for increasing number of ablation pulses is consistent with other reports in the literature and relates to the enhanced absorbance of gold following femtosecond laser ablation at high fluences with a large number of pulses at high fluence [3]. Under such experimental conditions, the increase in the mean size of Au NPs can be attributed not only to pure cumulative effects proper of multishot ablation, but also the change of the target morphology that leads to an increase in the density of NPs generated within the target.

The presence of circular droplets with dimension from tens of nm up to few  $\mu\text{m}$  (Fig. 1) deserves a dedicated discussion and can be related to the above mentioned residual thermal energy remaining in the bulk metal sample irradiated with multishot high fluence short-pulse laser [4]. As matter of facts, the formation of these structures under sub-picosecond laser irradiation could be unusual since the process is usually described as “melting-free” indicating a negligible warming up and damage of the material surrounding the laser spot as compared to nanosecond-laser ablation.

Instead, careful inspection of the surface morphologies of metal targets irradiated with ultra-short pulses indicates the presence of heat affected zones, even if much less extended with respect to the case of nanosecond laser ablation. This fact demonstrates the existence of residual thermal energy in the metal after the laser shot with the formation of a liquid phase, responsible of material rearrangement and its further ejection as molten droplets by ablation recoil stresses. Traces of molten material were also observed upon the transition from the low-fluence to the high-fluence regime and by the observation of large droplets (tens of nanometers) in the high-fluence regime of femtosecond laser ablation of Ni targets. In the case of Au, heat effects (such as the formation of an amorphous phase following the cooling down of the molten phase by fs-laser heating) were observed experimentally after the femtosecond laser irradiation. It is worth noticing that in femtosecond ablation of metals the electron-phonon coupling strength, which is the rate of the energy transfer from hot electrons to the lattice, plays an important role in the melting process. In fact, the ablation of metals with weak electron-phonon coupling (such as Au) can be accompanied by the formation of molten regions within the volume of the irradiated target that may result in the expulsion of the molten material, even in femtosecond laser ablation. Droplets, that are neither large NP nor agglomerates of NP, and NP result from different

# 14<sup>th</sup> Annual Research Day

Organised by the Deanship of Scientific Research in Collaboration with the College of Engineering  
Research Centre

4<sup>th</sup> April 2019

mechanisms that can be explained by target stress confinement [4].

Weak electron-phonon coupling can involve partial stress confinement regime, meaning that expansion of the overheated region of the target can occur while the lattice thermal energy is still increasing (i.e., before the complete equilibration between the temperature of hot electrons and lattice temperature following laser energy transfer to the target material). In the case of Au, most of the energy is transferred to the lattice within 15–35 ps, whereas complete equilibration between the hot electrons and the lattice takes up to 30–50 ps. It is known that the condition of stress confinement requires that the maximum value between the pulse duration (500 fs in our experiments) and the characteristic time of the energy transfer from electrons to lattice (15–35 ps) is shorter than the acoustic time  $t_s = L_s/C_s$ , where  $L_s$  is the diffusive/ballistic electron penetration depth and  $C_s$  is the speed of sound in the target material. Accounting for  $L_s \sim 100$  nm and  $C_s = 3240$  m/s in bulk Au, the stress confinement condition is satisfied for our irradiation conditions, with a laser pulse duration of 500 fs.

However, the effective heating depth can be larger than  $L_s$  depending on the strength of the electron-lattice coupling. Heat transfer in depth first by ballistic electron transport ( $\sim 100$  nm for gold) and then by thermal conduction favored by weak electron-phonon coupling implies waste of the laser delivered energy remaining as residual thermal energy in the metal following laser ablation [5]. On the other hand, femtosecond laser irradiation of a target with thickness larger than the ballistic penetration depth is characterized by temperature gradients leading to different ablation regime (photomechanical spallation, explosive boiling and fragmentation) depending on the depth. These effects could explain the appearance of the spherical droplets observed on Fig. 1. In Fig. 3 it is reported the optical extinction spectra determined from the measured transmission (T) spectra as  $\ln(1/T)$ , in the range 300 to 800 nm, as

a function of number of laser shots. It can be clearly observed how the SPR peak red shifts and increases in intensity and broadens with the number of laser shots used for the gold target ablation. The evolution of the SPR band can be seen in a more quantitative way in Fig. 4 where both the peak position (left-hand side axis) and the corresponding extinction values (right-hand side axis) are reported as function of the number of laser shots. The data are extracted from the spectra shown in Fig. 3 after the background subtraction aiming to remove the contribution of the interband transitions, and through a Gaussian fit of the resulting ‘baselined’ curves. It is worth noting that the SPR signal appears even for the sample obtained with the lowest number of laser shots, with a center position at  $\sim 550$  nm, that is close to values commonly associated with isolated spherical Au NP. The SPR band redshifts with the number of laser shots and mostly increases linearly in intensity with the laser shots, as reported for ns-pulses, coherently with the increase in the metal content of the samples. Interestingly, the SPR redshift is accompanied also by a band broadening mostly ascribable to the increase on the Au NP density and the subsequent effects related to NP, dipole-dipole as well as higher-order multipolar interactions. For samples produced with a number of laser shots greater than 2000, the optical response of the sample switches over to that one of a continuous film and the band related to the SPR it is not defined at all. In fact, with the increase of the NP size and the inherent reduction of interparticle distance, the SPR wavelength decays almost exponentially. Indeed, in Fig. 5 it is reported the variation of the fractional plasmon shift, defined as the ratio between the band width (full width half maximum, FWHM),  $\Delta\lambda$ , and the peak position,  $\lambda_{SPR}$  related to the SPR band, as a function of the NP gap/diameter ratio,  $\ell$ . The latter represents the ratio between the estimated inter-particle separation and the average diameter, and it can be calculated from the exponential decay defined by the plasmon ruler equation :

$$\Delta\lambda/\lambda_{SPR} = a \exp(-l/\tau)$$

Where  $a$  is the amplitude and  $\tau$  is the decay constant, and the values obtained from the exponential fit are  $0.26 \pm 0.05$  and  $0.5 \pm 0.2$ , respectively. For comparative aims, the corresponding laser shots for the ablation of the gold target are reported in the Fig., thus demonstrating that, when it increases, the separation between the NPs and then the strength of the interparticle electromagnetic coupling decreases with respect to the intraparticle plasmonic restoring potential. Indeed, in the framework of the dipolar coupling model [6], it is generally acknowledged that the enhanced electric field confined near the surface of the particles decays approximately to zero for ratios about 2.5 times (gap-to-diameter).

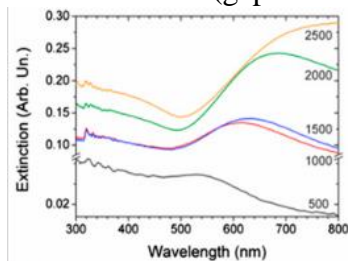


Fig. 3. Optical extinction spectra of the Au NP deposited on silica glass as a function of the laser shots as labeled close to each graph.

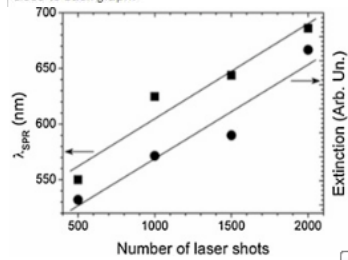


Fig. 4. SPR peak position,  $\lambda_{SPR}$ , (left-hand side) and corresponding extinction (right-hand side) values as a function of the number of laser shots. Each pair of values has been obtained from a Gaussian fit of the background (interband transition contribution [35]) subtracted extinction spectra shown in Fig. 3. The continuous lines are linear fits of the experimental data.

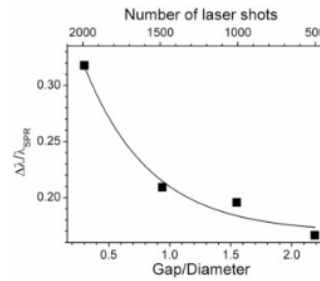


Fig. 5. Evolution of the fractional plasmon shift as calculated from the values shown in Fig. 4, simulated by an exponential decay (solid line) relationship with the gap/diameter ratio for Au NP pairs as obtained from the morphological analysis. The fit is carried out following the plasmon ruler equation [58] with the values. The correspondent number of laser shots for the ablation of the gold target is shown.

The optical characterization of the samples deposited on silica NWs are reported in Fig. 6a where the corresponding reflectivity spectra are shown in the 400–800 nm spectral range for the samples obtained with 2000 and 2500 laser pulses before and after thermal annealing (at 500 °C for 10 minutes in dry N<sub>2</sub> flow). It is also worth noting that the inverse of the reflectivity profile of a representative sample with metal decorated silica NWs, reported in Fig. 6b, has the peculiar feature of the Au localized SPR (LSPR) extinction coefficient. This behavior can be well described by the recent model of diffuse optical reflectors, which successfully predicts the optical behaviour of Si and GaAs NWs [4].

This model demonstrates that in the spectral range where the NWs are absorbing, the reflectivity,  $R$ , is inversely proportional to the wire absorption coefficient,  $\alpha$ , according to the relationship  $R \cong 1/N\alpha d$ , where  $N$  can be roughly assumed as the number of NWs that the incoming light encounters and  $d$  the absorption length. In our case, since the silica NWs are transparent in the investigated spectral range, the total absorption of our system is only determined by the LSPR absorption of the NPs immobilized on the wires, and  $N$  is roughly the number of NP that interact with the propagating light. Hence LSPR peaks for metal NP immobilized on silica NWs can be detected by spectral reflectance measurements [7].

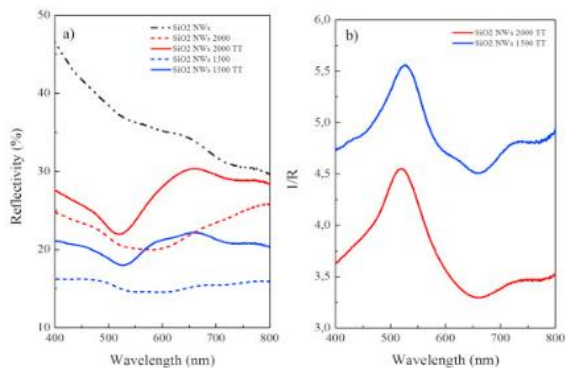


Fig. 6. (a) Reflection spectra of silica NWs covered with Au NP by using 2000 and 2500 laser pulses before and after thermal treatment (TT) at 500 °C for 10 minutes in dry N<sub>2</sub> flow; (b) reciprocal of the reflection spectra of silica NWs covered with Au NP by using 2000 and 2500 laser after the thermal treatment.

### 3. Conclusion

In this study, we have inspected as a function of the number of laser pulses (from 500 to 2500) both morphological and optical properties of Nano metric Au NP deposited on 2D (silica and (100) Si) and 3D (silica NW switches) substrates by sup-picosecond ablation of an Au bulk target. Because of the different effective surface area, the morphology of the substrates influenced the number of laser pulses suitable to achieve a uniform coverage. The samples deposited on silica NWs and subjected to a thermal treatment in order to promote a dewetting process demonstrated an effective increase of the NP average size from about 9 nm and 13 nm, for the sample deposited with 2000 and 2500 pulses, respectively, up to an average size of about 21 nm and the consequent enlargement of the antiparticle distance. All the samples presented the SPR peak characteristic of the Au NP, making them suitable for sensing applications, although a further optimization of the deposition process is necessary in order to improve the NP size distribution/dispersion. The influence of the number of laser pulses on the NP size has been discussed based on a combined effect of structural surface modifications induced by residual thermal energy and re-deposition of the NPs produced by ablation presence. Moreover, the presence of droplets has been discussed as depending on the weak electron-phonon coupling of Au.

### Acknowledgements

The author would like to express his gratitude to King Khalid University, Saudi Arabia for providing administrative and technical support.

### References

1. Fackenthal, R., Kitagawa, M., Otsuka, W., Prall, K., Mills, D., Tsutsui, K., ... & Hush, G. (2014, February). 19.7 A 16Gb ReRAM with 200MB/s write and 1GB/s read in 27nm technology. In *Solid-State Circuits Conference Digest of Technical Papers (ISSCC), 2014 IEEE International* (pp. 338-339). IEEE.
2. Ji, S., Reusch, D., & Lee, F. C. (2013). High-frequency high power density 3-D integrated gallium-nitride-based point of load module design. *IEEE Transactions on Power Electronics*, 28(9), 4216-4226.
3. Bakkum, D. J., Frey, U., Radivojevic, M., Russell, T. L., Müller, J., Fiscella, M., ... & Hierlemann, A. (2013). Tracking axonal action potential propagation on a high-density microelectrode array across hundreds of sites. *Nature communications*, 4.
4. Cubukcu, M., Boule, O., Drouard, M., Garello, K., Onur Avci, C., Mihai Miron, I., ... & Gaudin, G. (2014). Spin-orbit torque magnetization switching of a three-terminal perpendicular magnetic tunnel junction. *Applied Physics Letters*, 104(4), 042406.
5. Dong, D., Cvetkovic, I., Boroyevich, D., Zhang, W., Wang, R., & Mattavelli, P. (2013). Grid-interface bidirectional converter for residential DC distribution systems—Part one: High-density two-stage topology. *IEEE Transactions on Power Electronics*, 28(4), 1655-1666.
6. Van Uden, R. G. H., Correa, R. A., Lopez, E. A., Huijskens, F. M., Xia, C., Li, G., ... & Okonkwo, C. M. (2014). Ultra-high-density spatial division multiplexing with a few-mode

# 14<sup>th</sup> Annual Research Day

Organised by the Deanship of Scientific Research in Collaboration with the College of Engineering  
Research Centre

4<sup>th</sup> April 2019

---

- multicore fibre. *Nature Photonics*, 8(11), 865-870.
7. Whitaker, B., Barkley, A., Cole, Z., Passmore, B., Martin, D., McNutt, T. R., ... & Shiozaki, K. (2014). A high-density, high-efficiency, isolated on-board vehicle battery charger utilizing silicon carbide power devices. *IEEE Transactions on Power Electronics*, 29(5), 2606-2617.

# 14<sup>th</sup> Annual Research Day

Organised by the Deanship of Scientific Research in Collaboration with the College of Engineering  
Research Centre

4<sup>th</sup> April 2019

## Evaluating Flexible Manufacturing System using Combinatorial Approach

Mohamed Rafik Noor Mohamed Qureshi<sup>1</sup>

<sup>1</sup>Department of Industrial Engineering, College of Engineering, King Khalid University,  
PO Box 394, Abha 61411 KSA.  
E-mail address: mrnoor@kku.edu.sa

**Abstract:** Manufacturing system has been evolving rapidly because of the leaping change in technology. The flexible manufacturing system (FMS) has been adopted by manufacturers for gaining the cutting edge in the manufacturing world. FMS consisting of units like Computer Numerical Control (CNC) machine, Robots / Automated Guided Vehicle (AGV) that are interfaced and work under server control. Using FMS, the speed of factory operations increases tremendously. It also raises production and productivity to become competitive. However, buying such a system offers many hurdles hence a manager needs a decision support model which help in FMS acquisition based on its technical, operational and corporate objectives. In the research work, a performance evaluation framework based on combinatorial approach has been provided.

**Keywords:** *Analytic Hierarchy Process (AHP), Combinatorial approach, Flexible manufacturing System (FMS), Performance evaluation of FMS.*

### 1. Introduction:

Flexible manufacturing system (FMS) has been revolutionarily replaced the traditional production systems in order to have a cutting edge in manufacturing market. The leaping changes in manufacturing system have put the manufacturers in better competitive positions in averting fierce competition. FMS is able to provide agility and flexibility. It has been preferred because of its versatile capability to machine high strength temperature resistant (HSTR) materials with ease. It provides high material removal rate (MRR) to shorten the lead time to market. Thus, FMS provides the much-needed merits over the traditional manufacturing process. The fast changes in machining technology have also compelled to change from traditional machining to computer integrated machining. The direct numerical control (DNC) and computerized numerical control (CNC) machines have been part and partial of the manufacturing system.

Higher production and productivity may be achieved using FMS as it has tremendous

manufacturing capability. FMS reduces shop-floor inventory drastically and supports higher inventory turnover [1]. However, FMS also pose some challenges as it needs high initial system capital cost that restricts it's functionality due to the system hardware expandability i.e. physical/hard reconfiguration becomes difficult [1]. FMS needs revisiting on its huge infrastructure resources, employee productivity, production volume, order positioning etc. Thus, the decision to acquire FMS poses lot of challenges to management. In order to acquire the right FMS, management must look for right decision making. A MCDM based AHP-TOPSIS may be adopted in decision-making and optimizing. AHP will benefit the comprehensive performance evaluation whereas TOPSIS will optimize selection among the available alternatives. Based on the above premises, research has been undertaken with the following two-fold objectives:

1. To prepare combinatorial two-phase AHP-TOPSIS methodology for the FMS selection.

# 14<sup>th</sup> Annual Research Day

Organised by the Deanship of Scientific Research in Collaboration with the College of Engineering  
Research Centre

4<sup>th</sup> April 2019

2. To provide a systemic illustration for the FMS selection case problem.

The remainder of the paper is organized as follows: in the next section a FMS selection framework along with main criteria has been documented, which is followed by a review of the FMS selection literature. A MCDM based AHP-TOPSIS is briefly discussed along with a case problem illustration. Later on, evaluation and comparison of various FMS has been carried out using MCDM based AHP-TOPSIS. Later on, significant along with managerial implications are discussed.

## 2. Literature Review:

On reviewing FMS selection literature, it has been found that selection issue became the focus area for many researchers. Researches on FMS evaluation and its selection are found in the area of FMS system selection, AGV selection, Robot selection, AS/RS selection, Material handling equipment selection etc.

Shamsuzzaman et al. [2] developed FMS selection model using FAHP. Rao [3] applied a digraph and matrix methods in evaluating FMS. AHP was proposed in the FMS selection [4], followed by FDEA/AR methodology [5] and FMCDM [6]. Raj et al. [7], employed AHP selecting advanced manufacturing system. An integration data envelopment analysis (DEA) and AHP was also used [8]. FMS selection was carried out using an improved compromise ranking method [9]. A combinatorial mathematics-based decision-making [10], and grey relation under uncertainty [11] is also found in FMS selection. Preference selection index (PSI) [12] has been applied in FMS selection. Rao & Singh [13] applied Euclidean distance-based integrated approach in evaluating FMS. MACBETH method has been used for the evaluation and selection of a FMS alternative [14]. Preference ranking methods for FMS selection has also been used [15] followed Fuzzy Hybrid Decision Model using GRA-TOPSIS [16].

From the comprehensive review of the literature, it may be concluded that MCDM based

two-phase AHP-TOPSIS methodology hasn't been applied in FMS selection. Hence present research will be proved to be significant for practicing managers in manufacturing area looking for selecting a FMS.

## 2.2 Framework for FMS Selection

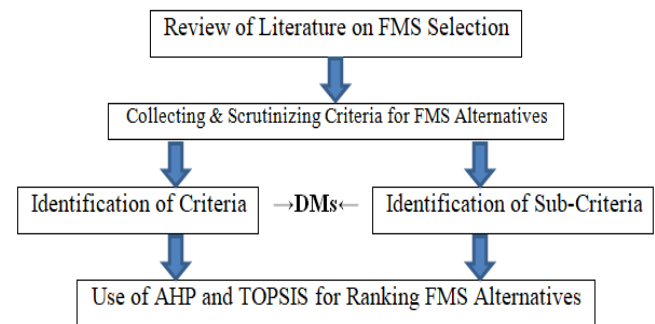


**Figure (1) Framework for FMS selection**

Based on the detailed review of literature, main criteria have been identified for FMS selection problem. A framework for FMS selection is constructed which shown in Figure (1). The main criteria selected for FMS selection also influence the economic cost of the FMS system. The collected criteria and sub-criteria for the FMS selection have been studied carefully for further performance analysis. Three Decision Makers (DMs) having experience of more than 10 years in the area of manufacturing system have been consulted to seek their opinion on performance evaluation of criteria. The main criteria and sub-criteria are documented as under.

### 2.3 Main Criteria

**2.3.1 Line Efficiency:** It is the ratio of total workstation time to the product of cycle time and the available workstations.

**2.3.2 Performance:** The performance of FMS is a significant factor as it enhances production and productivity.

**2.3.3 Process:** It influences FMS utility tremendously.

**2.3.4 Volume:** Profit is directly linked with the production.

# 14<sup>th</sup> Annual Research Day

Organised by the Deanship of Scientific Research in Collaboration with the College of Engineering  
Research Centre

4<sup>th</sup> April 2019

---

2.3.5 *Configuration control*: It maneuvers the overall FMS functioning.

## 2.4 Sub-Criteria

2.4.1 *Machine Utilization*: IT helps in increasing the line efficiency and depends upon the available inventory.

2.4.2 *Reduced Labour*: It influences the production and overall productivity.

2.4.3 *Set-Up Time*: The line efficiency is governed by set-up time.

2.4.4 *In-Process Inventory*: FMS performance is supported by in-process inventory to avoid large hold-ups for shortages of work materials.

2.4.5 *Production Lead-Time*: Right selection of FMS provides the least production lead-time.

2.4.6 *Part Mix*: It depends upon the FMS Precision parameters like size of the table, buffer pallets, ATC, Transport software, etc.

2.4.7 *Design Change Accommodation*: Modified and new production process depends upon the flexibility in design change accommodation.

2.4.8 *Scheduling and Control*: It influences the production volume and influenced CNC software, System control, and Computer Interfacing.

2.4.9 *Ease of Operation*: It leads to higher production and depends upon the table, buffer pallets, ATC. System control, Transport Software, and Loading.

2.4.10 *Routing Flexibility*: It enhances the production volume in case of maintenance and breakdown.

2.4.11 *Production Capacity*: It directly affects the volume and has the high influence of ATC.

2.4.12 *Capacity Growth*: It affects the production volume and depends upon the Transport Software, System control, Robot loader and Computer Interfacing.

2.4.13 *Delivered Accuracy*: It depends upon the configuration control. It is influenced by the table, and buffer pallets, ATC and Manufacturing system.

2.4.14 *Manufacturing Precision*: It affects the configuration control. It is governed by FMS

Precision parameters and Manufacturing system (Manufacturing control).

2.4.15 *Design Complexity*: It influences Configuration control.

## 3. Combinatorial Approach of Two-Phase AHP-TOPSIS methodology

Main-criteria and sub-criteria do play a vital role in the selection of. The criteria and sub-criteria selection have significant influence on the FMS selection. MCDM based AHP may be employed for the criteria weights. Similarly, TOPSIS may also be used in the ranking of sub-criteria. A MCDM based methods are utilized in evaluating goals, objectives and ranking problems. An integrated AHP and TOPSIS approach [17], has been applied in the present research.

A complex decision problem having multiple levels of a hierarchy can be resolved by AHP. IT contains the main goal, criteria and sub-criteria and the alternatives arranged from top to bottom in the systematic hierarchy. A pair-wise technique is applied using the expert opinion of DMs. The AHP procedure is described as follows [18]:

**Step 1: Decomposition**: Structuring the decision problem into a hierarchy with the help of DMs.

**Step 2: Comparative Judgments**: The various pair-wise matrixes may be prepared using the judgement of DMs. The pairwise decision matrix depends upon the selection of suitable comparison using Saaty's scale. It provides the opportunity of selecting 1, 3, 5, 7, and 9, and intermediate values of 2,4,6,8 during a pairwise comparison. The Saaty's scale may be applied where 1 refers to "equally important," 3 denotes "slightly more important," 5 equals "strongly more important," 7 represents "demonstrably more important" and 9 denotes "absolutely more important." Also, 2, 4, 6, and 8 are used for intermediate values. This yields an  $n \times n$  comparison matrix A as shown in equation (1).

$$A = [a_{ij}]_{n \times n} = \begin{bmatrix} a_{11} & a_{12} & \dots & a_{1n} \\ a_{21} & a_{22} & & a_{2n} \\ \vdots & \vdots & \ddots & \vdots \\ a_{n1} & a_{n2} & \dots & a_{nn} \end{bmatrix}$$

$$= \begin{bmatrix} a_{11} & a_{12} & \dots & a_{1n} \\ 1/a_{12} & a_{22} & & a_{2n} \\ \vdots & \vdots & \ddots & \vdots \\ 1/a_{1n} & 1/a_{2n} & \dots & a_{nn} \end{bmatrix} \quad (1)$$

Where normalization may be obtained through the equation (2).

$$a_{ij}^* = \frac{a_{ij}}{\sum_{i=1}^n a_{ij}} \quad (2)$$

For all  $j = 1, 2 \dots n$ .

Weight calculation is made using the equation (3)

$$w_{ij} = \frac{\sum_{j=1}^n a_{ij}^*}{n} \quad (3)$$

For all  $i = 1, 2 \dots n$ .

After a decision-making matrix is prepared, the priority weights of the criteria are ascertained through the maximum Eigenvectors and Eigenvalues using the equation (4) & (5) respectively.

$$A \cdot w = \lambda_{\max} \cdot w \quad (4)$$

$$\lambda_{\max} = \sum_{j=0}^n a_{ij} \frac{w_j}{w_i} \quad (5)$$

Where,  $w$  is Eigenvector and  $\lambda_{\max}$  is the largest Eigenvalue, of matrix  $A$ .

**Step 3: Consistency Check:** In AHP consistency of decision making is very essential. Each decision matrix may be tested for its consistency using the equations (6) and (7), Consistency index ( $CI$ ) is a measure of the inconsistencies of pair-wise comparisons and can be calculated using the equation (6):

$$CI = \frac{\lambda_{\max} - n}{n - 1} \quad (6)$$

Where  $\lambda_{\max}$  is the largest Eigenvalue of the pair-wise comparison matrix and  $n$  is the rank of the matrix. Consistency ratio ( $CR$ ) should be less than 0.1, for acceptable judgement [18], which can be derived using the equation (7).

$$CR = \frac{CI}{RI} \quad (7)$$

Wherein Random Index ( $RI$ ) is obtained based on the value of  $n$  from the Table 1.

**Table 1: Random Index Values [18]**

RI	0.00	0.00	0.52	0.89	1.11	1.25	1.35	1.40	1.45	1.49
----	------	------	------	------	------	------	------	------	------	------

**Step 4: Synthesis of Priorities:** Pair-wise matrices will give weights of each main-criterion, sub-criteria in respect to its goal. Thus relative weights of the main criteria and sub-criteria are obtained later can be used as input data for selecting the best alternatives in TOPSIS.

TOPSIS is a technique to find an ideal solution in similarity. It has a positive ideal solution (PIS) and a negative-ideal solution (NIS) in a geometrical (i.e. Euclidean) sense. The TOPSIS approach is described as follows:

**Step 5: Calculation of the normalized decision matrix.** The normalized value  $r_{ij}$  is calculated using the equation (8):

$$r_{ij} = \frac{f_{ij}}{\sqrt{\sum_{j=1}^J f_{ij}^2}} \quad j = 1, 2, 3, \dots, J;$$

$$i = 1, 2, 3, \dots, n \quad (8)$$

**Step 6: Calculation of the weighted normalized decision matrix.** The weighted normalized value  $v_{ij}$  is calculated using the equation (9):

$$v_{ij} = w_i^* r_{ij} \quad j = 1, 2, 3, \dots, J;$$

$$i = 1, 2, 3, \dots, n \quad (9)$$

Where  $w_i$  is the weight of the  $i$ th attribute or criterion, and  $\sum_{i=1}^n w_i = 1$

**Step 7: Determination of the ideal and negative-ideal solution:** The ideal and negative ideal solution may be obtained using the equations (10) and (11):

$$A^* = \{v_1^*, \dots, v_n^*\} = \{(max v_{ij} \mid i \in I'), (min v_{ij} \mid i \in I'')\} \quad (10)$$

$$A^- = \{v_1^-, \dots, v_n^-\} = \{(min v_{ij} \mid i \in I'), (max v_{ij} \mid i \in I'')\} \quad (11)$$

Where  $I'$  is associated with benefit criteria, and  $I''$  is associated with cost criteria.

**Step 8: Calculation of the separation measures:** Using the  $n$ -dimensional Euclidean distance, the separation distances from PIS and NIS may be obtained.

The separation of each alternative from the ideal solution is calculated using the equation (12):

$$D_j^* = \sqrt{\sum_{i=1}^n (v_{ij} - v_i^*)^2},$$

$$j = 1, 2, 3, \dots, J. \quad (12)$$

n	1	2	3	4	5	6	7	8	9	10
---	---	---	---	---	---	---	---	---	---	----

Similarly, the separation from the negative ideal solution is calculated using the equation (13):

$$D_j^- = \sqrt{\sum_{i=1}^n (v_{ij} - v_i^-)^2}, \quad j = 1, 2, 3, \dots, J \quad (13)$$

**Step 9:** Calculation of the relative closeness to the ideal solution or Closeness Coefficient (CC). The Closeness Coefficient is calculated using the equation (14):

$$CC = C_j^* = \frac{D_j^-}{D_j^* + D_j^-}, \quad j = 1, 2, 3, \dots, J \quad (14)$$

The higher value of the Closeness Coefficient indicates a higher preference of that alternative.

### 4. Illustration of Actual Case problem for FMS Selection:

A hypothetical case of selecting a FMS system for a manufacturing unit has been presented for illustration.

**Step 1: Decomposition:** Structuring the decision problem into a hierarchy with the help of decision makers, group decision or survey technique.

The significant main-criteria and sub-criteria of the FMS selection are identified. A systematic AHP hierarchy is prepared shown in Figure (2).

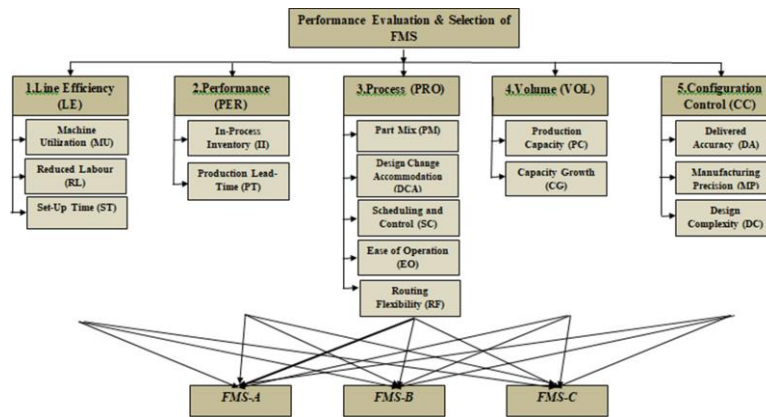


**Figure (2): FMS Hierarchical Structure**

**Step 5-8:** Calculation of the separation measures: Calculation of the separation measures: After calculating the normalized matrix, the weighted decision matrix is arrived.

Using formula the ideal positive and negative solution is calculated. The ideal Euclidean distance for the benefiting criteria must be near to the PIS. Similarly, non-benefiting criteria or the cost criteria of must be away from the PIS or near. The ideal Euclidean distance for the benefiting criteria must be near to the PIS. Similarly, non-benefiting criteria or the cost criteria of must be away from the PIS or near to NIS. The various separation distances may be obtained by using the equations (12) and (13), thus various separation distances for each FMS alternative may be obtained, the same are depicted in Table 1.

**Step 9:** Calculation of the relative closeness to the ideal solution or Closeness Coefficient (CC).

Using the equation (14) the closeness coefficient of the various FMS alternatives may be obtained. The FMS alternative having larger CC value may be preferred (Table 2).

**Table 1: Results of Positive and Negative Extreme ( $D_j^*$  and  $D_j^-$ )**

Alternatives	$D_j^*$	$D_j^-$
FMS1	0.112	0.311
FMS2	0.192	0.281

# 14<sup>th</sup> Annual Research Day

Organised by the Deanship of Scientific Research in Collaboration with the College of Engineering Research Centre

4<sup>th</sup> April 2019

FMS3	0.195	0.316
------	-------	-------

**Table 2: Results of a two-phase AHP and TOPSIS methodology**

FMS1	FMS1	FMS2	FMS3
$C_j^*$	0.3597	0.6824	0.6170
Ranking	3	1	2

## 5. Sensitivity analysis:

The sensitivity analysis demonstrates the effect and stability of criterion's weight on FMS selection. Each criterion's weight is interchanged with another criterion's weight to verify the effect of on the five main criteria and respective relative closeness to the ideal solution  $C_j^*$  is calculated. The sensitivity analysis of output is represented in Figure (3).

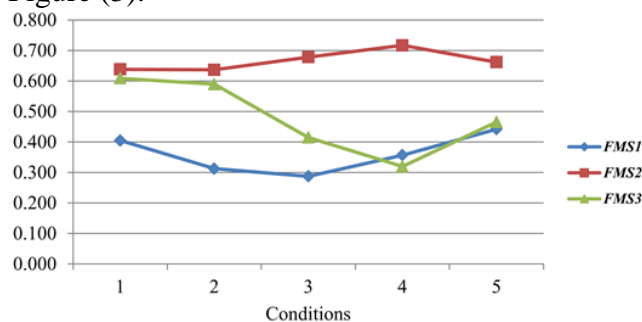


**Figure (3): Sensitivity analysis**

## 6. Results:

Management has a great deal of confusion while selecting a potential FMS. Hence a MCDM based AHP and TOPSIS methodology may prove vital in such a situation. The results of MCDM based two-phase AHP-TOPSIS approach, implemented to FMS selection problem, results in the  $C_j^*$  values as 0.679 0.613 and 0.359 in *FMS-A*, *FMS-B* and *FMS-C* order. Hence, the relationship of  $FMS-B > FMS-C > FMS-A$  (where '>' means 'preferred to') may be obtained. Thus

it shows that the *FMS-B* is preferred over *FMS-C* and *FMS-A*.

## 7. Conclusions:

The present research provides MCDM based two-phase AHP-TOPSIS approach in FMS selection. The FMS selection obtained in order of preference is *FMS-A*, *FMS-B* and *FMS-C*.

In the present work, the sensitivity analysis has also been carried out to verify the obtained results. It is concluded that *FMS-B* is the best alternative for the present hypothetical case.

## References

- [1] H.A. ElMaraghy, Flexible and reconfigurable manufacturing systems paradigms. Int j of flexible manufacturing systems. 17 (2005)261–276.
- [2] M.Shamsuzzaman, A.M.M. Sharif Ullah, & E.L.J.Bohez, Applying linguistic criteria in FMS selection: fuzzy-set-AHP approach. Integrated manufact systems. 14 (2003) 247–254.
- [3] R.V.,Rao, A decision-making framework model for evaluating flexible manufacturing systems using digraph and matrix methods. The Int J of Adv Manuf Tech, 30(2006)1101–1110.
- [4] E. Çimren, B. Çatay, E. Budak, Development of a machine tool selection system using AHP. The Int J of Adv Manuf Techn. 35(2007) 363–376.
- [5] S.-T.,Liu, A fuzzy DEA/AR approach to the selection of flexible manufacturing systems. Comp & Ind Engg. 54(2008), 66–76.
- [6] A.Bhattacharya, A.Abraham, P.Vasant, FMS selection under disparate level-of-satisfaction of decision making using an intelligent fuzzy-MCDM model. In Fuzzy Multi-Criteria Decision Making. (2008.). 263–280.
- [7] Raj, T. et al., An AHP approach for the selection of Advanced Manufacturing System: a case study. Int J of Manuf Research. 3(2008)471–498.
- [8] K.Rezaie, S.N.Shirkouhi, S.M.Alem, Evaluating and selecting flexible manufacturing systems by integrating data envelopment analysis

# 14<sup>th</sup> Annual Research Day

Organised by the Deanship of Scientific Research in Collaboration with the College of Engineering  
Research Centre

4<sup>th</sup> April 2019

---

and analytical hierarchy process model. In Modelling & Simulation, Asia Int Conf. (2009)460–464.

[9] R.V.Rao, Flexible manufacturing system selection using an improved compromise ranking method. Int J of Ind and Systems Engg. 4(2009) 198–215.

[10] R.V. Rao, M. Parnichkun, Flexible manufacturing system selection using a combinatorial mathematics-based decision-making method. Int J of Prod Research. 47(2009) 6981–6998.

[11] P.R. Dhal, S.Datta, S.S. Mahapatra, Flexible Manufacturing System selection based on grey relation under uncertainty. International J of Services and Oper Manag. 8(2011)516–534.

[12] K.D. Maniya, M.G.Bhatt, The selection of flexible manufacturing system using preference selection index method. Int J of Ind and Systems Engg. 9(2011) 330–349.

[13] R.V. Rao, D. Singh, Evaluating flexible manufacturing systems using Euclidean distance-

based integrated approach. Int J of Decision Sciences, Risk and Manag. 3(2011) 32–53.

[14] P.Karande, S.Chakraborty, Evaluation and selection of flexible manufacturing systems using MACBETH method. Int J of Services and Oper Manag. 16(2013)123–144.

[15] P. Chatterjee, S.Chakraborty, Flexible manufacturing system selection using preference ranking methods: a comparative study. Int J of Ind Engg Computations. 5(2014) 315–338.

[16] S.Yang, X.Xu, M.Yang, G.Li., Fuzzy Hybrid Decision Model for FMS Evaluation and Selection based on GRA-TOPSIS Method. Int J of Fuzzy Systems and Adv Applic 1(2014)80–91

[17] A.T. Gumus, Evaluation of hazardous waste transportation firms by using a two step fuzzy-AHP and TOPSIS methodology. Expert Systems with Applications. 36(2009) 4067–4074.

[18] T.L. Saaty, How to make a decision: the AHP. Interfaces. 24(1994)19–43.

# 14<sup>th</sup> Annual Research Day

Organised by the Deanship of Scientific Research in Collaboration with the College of Engineering  
Research Centre

4<sup>th</sup> April 2019

---

## Gripping Task Performance Evaluation by Varying Grip Span and Stroke Rotation

Zulqarnain Mallick<sup>1</sup>, Mohammed Sadique Khan<sup>2</sup>, Shaik Dawood Abdul Khadar<sup>3</sup>

<sup>1,2,3</sup>Department of Industrial Engineering, College of Engineering, King Khalid University,  
PO Box 394, Abha 61411 KSA.  
E-mail address: zuahmad@kku.edu.sa

---

**Abstract:** Investigations in this study were conducted on two-handle tools where gripping with torqueing were involved like pliers, scissors etc. The present study was designed to evaluate the combined effect of posture and grip span on discomfort for combined gripping with torqueing task. Experimental investigations conducted for constant grip force (50N), two levels of the frequency of exertion (10 exertions per minute), two levels of stroke rotation (30° & 60°) and three levels of grip span (4.7cm, 6.0cm, & 7.3cm). Twelve participants performed task for all experimental treatments for 5 minutes to record the perceived discomfort score on 100mm VAS. Results revealed that grip span was significant on discomfort. It was also noticed that lowest discomfort was found at 60° stroke rotation and 6cm span.

**Keywords:** *Discomfort; Grip span; Gripping with torqueing task; stroke rotation*

---

### 1. Introduction:

The Grip span is an important factor to maximize grip performance and/or reduced risk of WMSDs in designing hand tools with two handles [1]. Grip span can also influence force exertion and rotation of forearm during hand tool users. Among other design parameters, grip span has also been treated as a critical factor for reduced risk of WMSDs as well as performance of workers [2, 3].

Many researchers have attempted to obtain optimal grip span of two-handle tools for gripping task. One of the studies was Eksioglu [4], in which evaluation of grip span effect on maximum voluntary isometric grip force, EMG activity and subjective discomfort was performed. They reported that the relative optimum grip span range is TCLm -2.5 to TCLm -2 where TCLm termed as one's modified thumb crotch length. In another study, Hoozemans and Dieën [5] determined the validity of linear regression model using EMG activities of forearm muscles to predict handgrip forces for isometric gripping tasks at different levels of grip width. They

concluded that EMG-handgrip force model was minimally affected by grip width. However, Lee et al. [6] evaluated effects of five level of grip span on subjective rating of comfort and found that grip span was significantly affected on subjective rating of comfort.

It was also found in literature that stroke rotation is significantly effected on discomfort where stroke rotation meant for rotation of forearm with gripping till end of stroke. Bano et al. [7] evaluated effect of stroke rotation on discomfort for screw driving task and found that stroke rotation significantly affected discomfort. In a similar study for a gripping combined with torqueing task, Bano et al. [8, 9] evaluated discomfort at different levels of stroke rotation and reported that discomfort was significantly affected by stroke rotation.

After literature review, it was found that there was lack of study investigated effect of posture and span on discomfort for task of gripping/ torqueing/ combination of both. Therefore the purpose of present study was to correlate the effect of posture and grip span on discomfort for

# 14<sup>th</sup> Annual Research Day

Organised by the Deanship of Scientific Research in Collaboration with the College of Engineering Research Centre

4<sup>th</sup> April 2019

gripping with torqueing task. The Null hypothesis for the present study was as follows:

“there was no main and interaction effect of stroke rotation and grip span on discomfort score”.

## 2. Methodology:

### 2.1 Experimental Design

A 2 (stroke rotation) x 3 (grip span) full factorial design was used for analysis of variance (ANOVA) with a significance level of 0.01. Perceived discomfort was the dependent variable and the symptoms of discomfort could include numbness, warmth, cramping, pulling, soreness, fatigue aching, tenderness, pressing or pain [10, 11].

The two levels of stroke rotation were 30° & 60° as per the study of Bano et al. [7,8,9] and three levels of grip span were taken as 4.7, 6.0, and 7.3cm in line with the studies [5,12,13] with constant grip force of 50N and frequency of exertion at 10 exertion/minute. Participant performed repetitive upper limb exertions for 5 minutes at all levels of independent variables. Experiment was conducted in a random order for every participant.

### 2.2 Participants

A total of 12 male undergraduate students were participated in the study. All the participants were right handed and none were reported musculoskeletal disorders in their upper extremity. The averages (standard deviation) of age, weight, height, palm hand length, Maximum grip force were  $\mu= 21.67$ years ( $\sigma=2.19$ ),  $\mu= 62.93$ kgs ( $\sigma=6.64$ ),  $\mu= 171.8$ cm ( $\sigma=5.66$ ),  $\mu= 188.8$ mm ( $\sigma=5.58$ ), and  $\mu= 375$ N ( $\sigma=56.19$ ).

### 2.3 Apparatus

A rig was designed in which wheel with handle was integrated at a fixed platform (Fig.1). The

handle returned back to its starting position with the help of spring which was attached to the rod of the rig. A 360° range protector and pointer were fixed on the rig to monitor and control the stroke rotation.

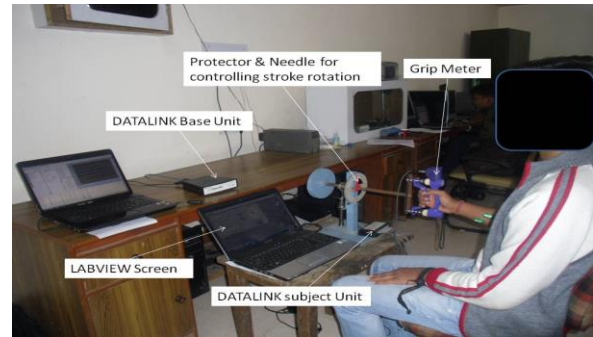


Figure (1) Experimental setup

A digital grip force Dynamometer (Model: Precision Dynamometer G200; Make: Biometrics Ltd. UK) was used to control the grip force and grip span according to treatment. Grip meter was directly interfaced to the DataLINK using cable H2000 (Make: Biometrics Ltd. UK). DataLINK was connected with the Laptop. Out of range effort levels were alarmed using different colours and a buzzer.

A code was written in LabVIEW 10 to provide different information for the experimenter and the participant. The screen had levels of stroke rotation and grip span on screen according to the assigned treatment (Fig. 2). It also had an analogue clock with three hands, two fixed and one moving. When a moving hand overlapped first fixed hand participant started to rotate their forearm in supine direction till it reached second fixed hand.

# 14<sup>th</sup> Annual Research Day

Organised by the Deanship of Scientific Research in Collaboration with the College of Engineering Research Centre

4<sup>th</sup> April 2019

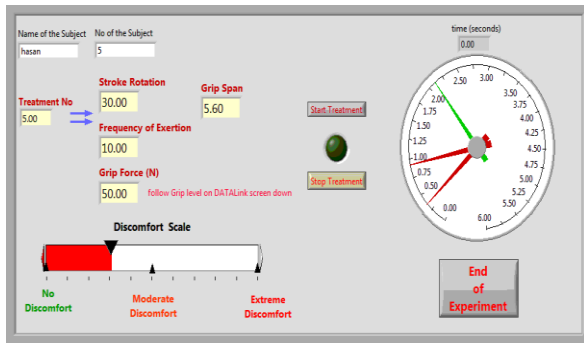


Figure (2) LabVIEW Screenshot

## 2.4 Procedure

After giving prior consent, participant was provided with a brief description of procedure and rules involved in the experiment. A participant sat on a chair with neutral forearm angle and elbow flexed at 90° without upper arm adduction. Experimenter set the span according to level displayed on screen prior to each treatment. Participant exerted 50N grip force on dynamometer and rotated their forearm in supine direction for assigned stroke rotation (30°/60°) for one second then released; rested for 5 seconds. The time for each experimental exercise was controlled by glowing green light bulb at the end of each experimental exercise. The participant was asked to record discomfort on 100mm Visual Analogue Scale which was displayed on computer screen. A rest of at least 5 minutes was provided between treatments or till participant reported no feeling of discomfort.

## 3. Results and Analysis

Summary of the discomfort score is presented in Table 1. It showed that stroke rotation 60° had less mean discomfort as compared to 30°. For both levels of stroke rotation, lowest mean discomfort was found at middle grip span i.e. 6cm.

Table 1: Summary of discomfort at different variables

Stroke rotation	Grip span	Discomfort
30°	4.700	5.12
30°	6.000	4.78
30°	7.300	5.65
Mean		5.18
60°	4.700	4.95
60°	6.000	4.41
60°	7.300	5.02
Mean		4.79

Further univariate ANOVA was applied on data and found grip span was highly significant on discomfort. Stroke rotation and interaction effect were not significant. When graphically it was noticed in Fig. 3, showed almost slightly higher level of mean discomfort for stroke rotation 30° than 60° at all levels of grip span. Almost no difference in discomfort was observed for both stroke rotations at span 4.7cm and difference increased further as grip span increases.

Table 2: Summary of ANOVA

Source	Type III Sum of Squares	Degree of freedom	Mean Square	F-value	Sig. (p-value)
SR	2.720	1	2.720	3.114	0.082
GS	6.667	2	3.334	3.817	0.027
SR * GS	0.673	2	0.337	0.386	0.682
Error	57.640	66	0.873		
Total	1859.24	72			

# 14<sup>th</sup> Annual Research Day

Organised by the Deanship of Scientific Research in Collaboration with the College of Engineering Research Centre

4<sup>th</sup> April 2019

Corrected Total	67.700	71			
-----------------	--------	----	--	--	--

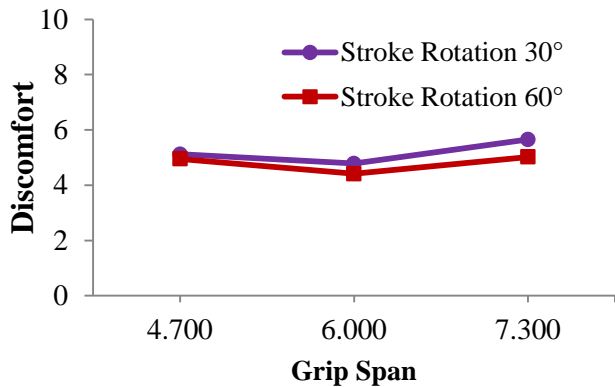


Figure (3) Interaction effect of discomfort due to grip span and stroke rotation

## 4. Discussions:

Gripping with torqueing task was mostly used in industries especially in hand tool such as assembly task, wood cutting, meat cutting etc. However, in past researches very few studies [14] evaluated discomfort on combined effect of gripping with torqueing exertions with three levels of forearm rotation and concluded forearm rotation was significant on discomfort. Bano et al. [8, 9] examined discomfort for combined gripping with torqueing exertion and reported stroke rotation was statistically significant on discomfort. They also concluded that stroke rotation 60° was most comfortable among other stroke rotations 30° and 45°. In screwing task, Bano et al., [7] found stroke rotation had significant effect on discomfort. Other researchers revealed that forearm rotation had significant effect on discomfort in repetitive task [10, 15], torqueing task [16, 17, 18]. The present results found stroke rotation was not significant on discomfort but lower discomfort was recorded at 60° stroke rotation. The present findings were slightly similar to past results of Bano et al., as lower discomfort reported at 60° stroke rotation. The risk of WMSDs in assembly tasks depended

on stroke rotation which was used in accomplishing the cycle of task element. Therefore, control of stroke rotation may play an important role in industrial task especially hand tool users for reduced risk of WMSDs.

The present study found that grip span was significant on discomfort and least discomfort was found at 6cm than other two spans, 4.7cm and 7.3cm. Lee et al. [6] evaluated effect of grip span on subjective comfort rating and found that grip span was highly significant. They conducted an experiment on five grip span 45, 50, 55, 60 and 65mm and found that 50mm and 55mm grip span were most comfortable. Eksioglu [4] reported that span had significant effect on subjective rating in terms of comfort. They considered nine spans (TCL (thumb crotch length) - 4 to TCL) and concluded that span wider or narrower discomfort was increased whereas TCL-2 (middle one) was an optimum grip span. Findings of present study also revealed that discomfort score was increased as grip span more or less. Therefore, present results supported the previous findings.

## 5. Conclusions:

The aforementioned results showed grip span was significant on discomfort during combined gripping with torqueing task. Whereas, stroke rotation was not significant on discomfort and low Discomfort was found at 60° stroke rotation. The trend of discomfort for larger span was found to be first decreases then increases i.e. at 6cm (middle level) minimal discomfort recorded. It was also observed that most comfortable posture for gripping with torqueing task was found to be 60° stroke rotation at 6cm span. It seems to be very useful and hopefully that will reduce the risk of WMSDs if considered while designing tools or tasks.

## References

# 14<sup>th</sup> Annual Research Day

Organised by the Deanship of Scientific Research in Collaboration with the College of Engineering  
Research Centre

4<sup>th</sup> April 2019

- 
- [1] S.W. Meagher, "Tool design for prevention of hand and wrist injuries," *Journal of Hand Surgery*, vol. 12 (A), pp. 855–857, 1987.
- [2] C. Fransson and J. Winkel, "Hand strength: the influence of grip span and grip type," *Ergonomics*, vol. 34, pp. 881–892, 1991.
- [3] J. R. Blackwell, K.W. Kornatz, and E.M. Heath, "Effect of grip span on maximal grip force and fatigue of flexor digitorum superficialis," *Applied Ergonomics*, vol. 30, pp. 401-405, 1999.
- [4] M. Eksioglu, "Relative optimum grip span as a function of hand anthropometry," *International Journal of Industrial Ergonomics*, vol. 34, pp. 1-12, 2004.
- [5] M. J. M. Hoozemans and J. H. V. Dieën, "Prediction of handgrip forces using surface EMG of forearm muscles," *Journal of Electromyography and Kinesiology*, vol. 15, pp. 358-366, 2005.
- [6] S. J. Lee, Y. K. Kong, B. D. Lowe, and S. Song, "Handle grip span for optimising finger-specific force capability as a function of hand size," *Ergonomics*, vol. 52, no. 5, pp. 601-608, 2009.
- [7] F. Bano, Z. Mallick, and A. A. Khan, "Effect of grip, stroke rotation and handle size on discomfort for screwing task," *International Journal of Human Factors and Ergonomics*, vol. 1, no. 4, pp. 390-407, 2012.
- [8] F. Bano, Z. Mallick, and A. A. Khan, "The effect of stroke rotation and frequency of exertion on discomfort in gripping task," in *International conference on Automation and Mechanical systems*, Lingayas University, Faridabad, India, 21st -22nd March, 2013a.
- [9] F. Bano, Z Mallick, and A. .A. Khan, "The effect of self pace cycle time for combinations of grip force and stroke rotation," in *2nd International Conference on Emerging Trends in Engineering & Technology*, April12, 13, 2013, 12th -13th April, 2013b.
- [10] A. A. Khan, L. W. O’Sullivan, and T. J. Gallwey, "Effects of combined wrist deviation and forearm rotation on discomfort score," *Ergonomics*, vol. 52, no. 3, pp. 345-361, 2009a.
- [11] M. L. Lin, R. G. Radwin, and S. H. Snook, "A single metric for quantifying biomechanical stress in repetitive motions and exertions," *Ergonomics*, vol. 40, pp. 543-558, 1997.
- [12] J. P. M. Mogk and P. J. Keir, "The effects of posture on forearm muscle loading during gripping," *Ergonomics*, vol. 46, no. 9, pp. 956-975, 2003.
- [13] J. P. M. Mogk and P. J. Keir, "Prediction of forearm muscle activity during gripping," *Ergonomics*, vol. 49, no. 11, pp. 1121-1130, 2006.
- [14] P. Mukhopadhyay, T. Gallwey, and L. W. O’Sullivan, "Effect of grip force and shoulder abduction angles in repetitive clockwise forearm pronation/supination," In: *Proceedings of the International Annual Occupational Ergonomics and Safety Conference*, Munich, 2003.
- [15] A. A. Khan, L. O’Sullivan, and T. J. Gallwey, "Effects of combined wrist flexion/extension and forearm rotation and two levels of relative force on discomfort," *Ergonomics*, vol. 52, no. 10, pp. 1265-1275, 2009b.
- [16] P. Mukhopadhyay, L. W. O’Sullivan, and T. J. Gallwey, "Estimating upper limb discomfort level due to intermittent isometric pronation torque with various combinations of elbow angles, forearm rotation angles, force and frequency with upper arm at 90° abduction," *International Journal of Industrial Ergonomics*, vol. 37, pp. 313-325, 2007a.
- [17] P. Mukhopadhyay, L. W. O’Sullivan, and T. J. Gallwey, "Effects of upper arm

# 14<sup>th</sup> Annual Research Day

Organised by the Deanship of Scientific Research in Collaboration with the College of Engineering  
Research Centre

4<sup>th</sup> April 2019

---

articulations on shoulder-arm discomfort profile in a pronation task," Occupational Ergonomics, vol. 7, pp. 169-181, 2007b.

[18] L. W. O'Sullivan and T. J. Gallwey, "Forearm torque strengths and discomfort

profiles in pronation and supination," Ergonomics, vol. 48, pp. 703-721, 2005.

# 14<sup>th</sup> Annual Research Day

Organised by the Deanship of Scientific Research in collaboration with the College of Engineering  
Research Centre

4<sup>th</sup> April 2019

## Application of Phase Change Materials in Transportation of Temperature Sensitive Products

C Ahamed Saleel<sup>1</sup>, Irfan Anjum Badruddin, T M Yunus Khan and Sarfaraz Kamangar

Department of Mechanical Engineering, College of Engineering, King Khalid University,  
PO Box 394, Abha 61411 KSA.  
E-mail address<sup>1</sup>: aveetil@kku.edu.sa

**Abstract:** Ability of storage and release of thermal energy within the prescribed temperature range allow various PCMs suitable for thermal packaging in transportation of temperature sensitive products especially food stuffs. Use of PCMs in thermal packaging ensures intact delivery of above mentioned products from manufacturer to end user by keeping it in the specified temperature limits. Usual temperature range for these type of products are between  $-80^{\circ}\text{C}$  and  $+40^{\circ}\text{C}$  and the most of them are in the range of  $2^{\circ}\text{C}$  to  $8^{\circ}\text{C}$ . PCMs with specific phase change temperature are appropriately selected to ensure the temperature range of the products during its logistics. This paper propose a conceptual study on various types of PCMs that can be considered in thermal packaging by discussing the salient attributes like availability and bio-degradability apart from its thermo-physical properties. The study concludes by proposing few PCMs that change the way of present thermal packaging designs and ensure that its use result in compact light weight freight designs that outperform their counterparts.

**Keywords:** Phase Change Materials, Temperature sensitive products, thermal packaging and thermal energy storage.

### 1. Introduction:

The major contributor to total greenhouse gas (GHG) emissions in the world is commercial food sector. The GHG emission share of the components of commercial food sector such as agriculture and food processing is much lower than the food transportation sector, where in diesel engine-driven refrigeration units are widely used. The figure 1 shows the proportion of energy used by the different components of commercial food sector [1].



Figure 1. Proportion of energy used by the different components of commercial food sector

Figure 1 ascertain that packaging and transportation together constitutes 16% of total energy, hence any endeavour to minimize the

energy consumption is highly appreciated. Use of renewable energy is escalated due to the fast depletion of conventional energy sources coupled with its ill effects posed to the environment. Widely used conventional refrigerants used in a diesel engine-driven refrigeration units installed in lorries and trucks that transport temperature sensitive products/food stuff also cause global warming and ozone layer depletion. Even though the solar powered refrigeration system is posed as the best alternative, intermittent nature of solar energy during transportation significantly limited its use in long run. Thus, it requires new options to be explored to maintain the desired temperature during transportation of temperature sensitive products especially food stuffs. Phase change materials (PCM) can act as a new thermal energy storage/release facility which can be applied in transportation of temperature sensitive products.

The exhaust gas and noise emissions of diesel engine driven refrigerators present in Lorries and

# 14<sup>th</sup> Annual Research Day

Organised by the Deanship of Scientific Research in collaboration with the College of Engineering Research Centre

4<sup>th</sup> April 2019

trucks can be considerably lessened by the use of PCMs. The results of scientific simulations reveal that for an outside temperature of 30 degree Celsius, a duration of 5 hours with the desired temperature limits may be easily obtained with the PCM packaging. Certain international standards should be followed with regard to transportation of food stuff especially in temperature limits or temperature inside the container [2, 3] and are shown in Table 1 and Table 2 for chilled and frozen food products. Generally, during transportation of food stuff, it is categorized as chilled and frozen. Chilled foodstuff should be maintained below -18 degree Celsius whereas frozen foodstuff should be between 0 and 5 degree Celsius. As an example, readymade food stuff should be maintained between 2 and 8 degree Celsius during its transportation.

Table 1. Transport temperature requirements of chilled foodstuff [2, 3]

## 2. Selection of PCM

PCMs typically used in thermal packaging are usually grouped by their chemical makeup (“organic” or “inorganic”), with the most common being organic. Organic PCMs, which are oil-based, have the  $(CH_2)_n$  group that provides their high latent heat. It can be identified that the specific attributes of a “perfect” PCM for packaging are: Phase change temperature in desired range, sharp melting/freezing point, high latent heat of fusion (solid to liquid), non-toxic & non-carcinogenic, commercially available at low cost, should not react with and/or act as a solvent for packaging materials, landfill disposable and/or waterway disposable, biodegradable, low/non-flammable (high flash point, low vapor pressure), non-corrosive, good stability upon thermal cycling (no super-cooling), limited volumetric expansion/contraction upon freeze/thaw

## 3. Applications

Various applications of PCM in transportation of temperature sensitive products are detailed in two categories (i) already in the market and (ii) in research. Due to inherent thermal inertia, PCM provides the opportunity of adequate protection (thermal) during transportation of abovementioned goods and can be used during storage. Applications of PCM varied from cooked food, beverages, solid food, blood derivatives, pharmaceutical goods and electronic devices/circuits. The PCMs are widely used in following applications: (i) Food industry: hotel trades, transport, ice-cream, etc. (ii) Medical applications: operating tables, transport of blood, cold therapies and (iii) Industrial cooling methods: re-gasification terminals. Table 3 shows various PCMs suitable in chilled and frozen food packaging.

Figure 1 shows the commercially available container to transport temperature sensitive food is made available SOFIGRAM [7] with PCM having melting points of 0 degree Celsius, -15 degree Celsius and -20 degree Celsius (Figure 2).



Figure 1. Gel packs of SOFIGRAM [7].

Isothermal water bottle-Quenchua (figure 2) is another application that has been commercialized. The most interesting feature is that it can be recycled easily. The PCM is impregnated in between the two walls. The idea is quite novel and may be used for various other fields, such as isothermal maintenance of fresh drinks like champagne, wine, soft drink, etc.

# 14<sup>th</sup> Annual Research Day

Organised by the Deanship of Scientific Research in collaboration with the College of Engineering Research Centre

4<sup>th</sup> April 2019



Figure 2. Isothermal water bottle with PCM as active part

In most of the catering industries, meals are cooked or food stuffs are frozen in a point and should be transported to various customer destinations. PCM containers shown in figure 3 and 4 could be used to avoid breaking the cold chain during transportation of smoked salmon, precooked meals, milk products, ice-creams and many other food stuffs. The companies like Rubitherm, Climator and Teap PCM are about to commercialize the same [8].

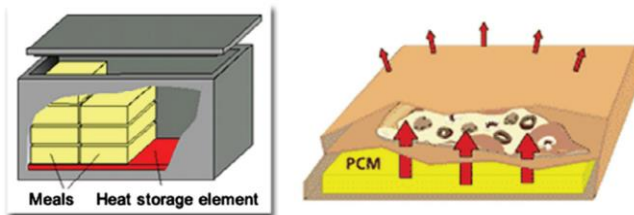


Figure 3. Concept of catering applications [8].



Figure 4. Different PCM containers [8]

Transportation of human blood and organs in medical sector by PCM container is conceptual stage and is shown in figure 6. and organs. Other PCM applications in medical field is use of cold or hot pads to alleviate local pain in the human body.



Figure 5. PCM containers to transport human blood and organs PCM [8].

## 4. Conclusions

This paper gives insight to possibility of application of PCMs in thermal packaging during transportation of temperature sensitive products with an emphasis on desired temperature range and various attributes in its selection. PCM-based transportation/food packaging is in conceptual stage and gaining interest from researchers and few PCM based containers are developed by industry due to its potential to provide safety and quality benefits without damaging the product/environment. Biodegradable PCM based containers will have a major market share and will change the way that packaging of food is designed. Smart food packaging will be flourished by the application of PCMs, bestowing prospects to better gratify quality and cost concerns for both consumers and retailers.

# 14<sup>th</sup> Annual Research Day

Organised by the Deanship of Scientific Research in collaboration with the College of Engineering  
Research Centre

4<sup>th</sup> April 2019

---

## References

- [1] Executive Summary: Environmental Footprint Literature Review Food Transportation, State of Oregon, Department of Environmental Quality
2. Lämpöhallittavien elintarvikkeiden kuljetusopas, L. Luoto, 2007, Yleinen Teollisuusliitto, in Finnish
- [3] <http://www.carriertransicoldeurope.com>
- [4] Chalco-Sandoval W, Fabra MJ, López-Rubio A, Lagaron JM (2015a) Optimization of solvents for the encapsulation of a phase change material in polymeric matrices by electro-hydrodynamic processing of interest in temperature buffering food applications. *Eur Polym J* 72:23–33. <https://doi.org/10.1016/j.eurpolymj.2015.08.033>
- [5] Wi S, Seo J, Jeong S-G et al (2015) Thermal properties of shape-stabilized phase change materials using fatty acid ester and exfoliated graphite nanoplatelets for saving energy in buildings. *Sol Energy Mater Sol Cells* 143:168–173. <https://doi.org/10.1016/j.solmat.2015.06.040>
- [6] Chen J, Ling Z, Fang X, Zhang Z (2015) Experimental and numerical investigation of form-stable dodecane/hydrophobic fumed silica composite phase change materials for cold energy storage. *Energy Convers Manag* 105:817–825. <https://doi.org/10.1016/j.enconman.2015.08.038>
- [7] <http://www.sofigram.com>
- [8] <http://www.rubitherm.com>

# 14<sup>th</sup> Annual Research Day

Organised by the Deanship of Scientific Research in collaboration with the College of Engineering  
Research Centre

4<sup>th</sup> April 2019

SL. No	Food Products [Chilled]	Temperature (°C)
1	Fresh fish (in ice- excluding live ones)- shellfish and crustaceans	+2
2	(i) Readymade and cooked dishes/foods such as fresh pastries, pastry creams, egg foods and sweet serving dishes (ii) Offal (iii) Meat [Raw and Cooked]-pre-packaged for consumer use (iii) Fermented, untreated, unpasteurized or non-sterilized milk, fresh cream, cottage cheese and curd (iv) Offal	+3
3	Poultry, rabbit and gane	+4

Table 1. Transport temperature requirements of chilled foodstuff [2, 3]

Table 2. Transport temperature requirements of frozen food products [2, 3]

SL. No	Frozen Food Products	Temperature (°C)
1	Ice cream and ice	-25
2	(i) Foodstuff - frozen (ii) Foodstuffs-fishery	-18
3	Edible fats and Butter	-14
4	Egg foodstuffs, rabbit, and poultry	-12
5	Meat	-10

Table 3 PCMs appropriate in food packaging

PCM	Phase transition temp/melting point	Application	References
Inorganic Salts( <u>HS 33N</u> , <u>HS 26N</u> , <u>HS 23N</u> , <u>HS 18N</u> , <u>HS 15N</u> , <u>HS 10N</u> , <u>HS 7N</u> , <u>HS 3N</u> ,	-34 to +1°C	Frozen/Chilled Food Packaging	-----
Rubitherm (RT 4)	- 1.5 °C	Smart packaging Food	Chalco-Sandoval et al. [4]
Coconut oil//Exfoliated graphite nano-platelets shape-stabilized PCMs	26.93/14.95 °C	Refrigerated foodstuffs	Wi et al. [5]
Dodecane	- 9.6 °C	Storage system for food	Chen et al. [6]
Polyurethane	2-8°C	Food Transportation	---
(i)Salt Hydrates (inorganic): Salt·nH <sub>2</sub> O-	8-18°C	Food packaging	-----

# 14<sup>th</sup> Annual Research Day

Organised by the Deanship of Scientific Research in collaboration with the College of Engineering  
Research Centre

4<sup>th</sup> April 2019

---

K <sub>2</sub> HPO <sub>4</sub> ·6H <sub>2</sub> O (ii) Hexanoic Acid			
--	--	--	--

# 14<sup>th</sup> Annual Research Day

Organised by the Deanship of Scientific Research in collaboration with the College of Engineering  
Research Centre  
4<sup>th</sup> April 2019

## Strain Rate Sensitivity of a superelastic NiTi Shape Memory Alloy after Hydrogen Immersion

FEHMI GAMAOUN<sup>a</sup>, AMIR KESSENTINI<sup>a</sup>, NABIL BEN KAHLA<sup>b</sup>

<sup>a</sup> Department of Mechanical Engineering, College of Engineering, King Khalid University,  
PO Box 394, Abha 61411 KSA.

<sup>b</sup> Department of Civil Engineering, College of Engineering, King Khalid University,  
PO Box 394, Abha 61411 KSA.  
fgamaoun@kku.edu.sa

**Abstract:** In this work, we will be interested in studying the susceptibility of Ni-Ti superelastic archwires to the strain rates during tensile testing after hydrogen absorption. Hydrogen immersion is performed at a current density of 10A/m<sup>2</sup> from 2 to 12h in 0.9W% NaCl solution and aged for 24h at room temperature. NiTi specimens underwent one cycle of loading-unloading under an imposed stress value of 700MPa. During stress loading, strain rates from 10<sup>-6</sup> /s to 5.10<sup>-2</sup>/s have been achieved. After 8h of electrolytically hydrogen charging, a delay fracture has been detected in the tensile strain rate range of 10<sup>-5</sup>/s to 10<sup>-4</sup> /s. In contrast, no embrittlement has been detected for the strain rate higher than 10<sup>-3</sup> /s. Nevertheless, after 12h of immersion and annealing for 24h at room temperature, the fracture occurs in the beginning of the plateau of the reverse martensite transformation for all the studied range of strain rate. These results show that for a range of critical amounts of diffused hydrogen, the mechanical behaviour of the Ni-Ti superelastic alloy is strongly related to the strain rate during the tensile test. Furthermore, it has been shown that this reduction in the superelastic property occurs for low values of strain rate contrary to the case of ordinarily metal alloys. This behavior is attributed to the interaction between the diffused hydrogen and the thermo-mechanical aspect of both the nucleation and the growth of the martensitic domains.

**Key words:** *Ni-Ti Superelastic Alloy; Hydrogen; embrittlement; Strai*

### Introduction

Ni-Ti Shape Memory Alloys (SMA) were introduced as an alternative material for the production of metallic orthodontic, particularly on the posterior segment of the arch [1]. The reason underlying the use of such a wires becomes essentially from its unique shape memory effect, superelasticity and biocompatibility in the human body [2, 4]. Moreover, this material presents excellent mechanical properties and a very high resistance to corrosion for a long term applications [5]. The superelastic behavior outcomes from the reversible transformation from an austenite parent phase to a martensitic phase under loading and

unloading [6, 7]. Nevertheless, the mechanical properties of Ni-Ti superelastic alloys will be altered notably after a few months of working in the oral cavity [8]. It has been proved that the most important environment factor for the degradation of the alloy is the hydrogen adsorption, caused by fluoride acid, which is contained in toothpastes and prophylactic agents [8-14].

The effect of hydrogen embrittlement on SMA in Ni-Ti superelastic alloy was considered under different electrolytically hydrogen charging conditions. Indeed, the effect of hydrogen on the mechanical behavior of this material was studied after hydrogen immersion using different

# 14<sup>th</sup> Annual Research Day

Organised by the Deanship of Scientific Research in collaboration with the College of Engineering

Research Centre

4<sup>th</sup> April 2019

---

solutions as the fluoride solution [15] or the 0.9 W% NaCl aqueous solution [8]. It is known that after a few hours of immersion at about 25°C, the mechanical properties of the Ni-Ti superelastic alloy are degraded due to the absorbed hydrogen. This latter property is marked by a significant decrease of the tensile strength and the appearance of a brittle fracture in the stress-induced martensite transformation step [16].

Limited research has been conducted on the effect of strain rate on the mechanical properties, through tensile tests, of the Ni-Ti alloy. Ng et al. [10]; Pieczyska et al. [11]; He et al. [12] have shown that the austenite-martensite transformation is a thermomechanical phenomenon. This behavior is attributed to the formation and growth of the macroscopic domains of the martensite during loading. Moreover, the space and the width between the bands are related to the value of the strain rate. For high values of strain rates, the number of domains is high and the variant spacing is restricted in the specimen. In fact, during the plateau of austenite-martensite transformation, new martensite variants are generated and the applied stress drops. In addition, an instantaneous local temperature increases around the front-domain of the martensite bands because of the released heat during growth [13, 14]. As the applied strain rate is low, the applied stress during the tensile test help to the growth of the martensite variants, not to the nucleation of new ones [13]. However, for higher strain rates, the critical stress for martensite nucleation is reached at many points of the specimen. As a result, the number of obtained domains is important. Then, to further understand the hydrogen degradation of the alloy after hydrogen absorption, the effect of the strain rate during the tensile tests of the Ni-Ti must be examined.

The aim of this study is to investigate the effect of the strain rate on the mechanical properties of the superelastic NiTi alloy to the strain rate after hydrogen-charging. The

susceptibility to hydrogen damage has been examined by tensile tests of charged specimens in the parent phase.

## Materials and methods

---

The 50.9 (at%) Ni–49.1(at%)Ti is used in this study. The phase transformation temperatures of the heat treatment material have been obtained from the Differential-Scanning-Calorimetry (DSC) test. At room temperature, the material has a fully austenitic structure with an austenite transformation finish temperature  $A_f = -2$  °C. Rectangular specimens with 0.64 x 0.43 mm<sup>2</sup> with 20 mm of nominal length have been used during the tensile tests. Uniaxial-tensile loading and unloading tests have been performed on a standard Instron mechanical-testing 5566-type machine with a load cell of 10 kN. To study the loading rate effect on the mechanical behavior of the Ni-Ti alloy, strain rates from  $10^{-6}$  s<sup>-1</sup> to  $5 \cdot 10^{-2}$  s<sup>-1</sup> have been used. The hydrogen charging of the specimens has been carried in an aqueous 0.9% NaCl solution at a current density of 10 A/m<sup>2</sup> for various periods of immersion from 2h to 12h at 25°C. Specimens have been aged for one day at room temperature in air to have a uniform distribution of the absorbed hydrogen [6].

## Results and discussion

---

The engineering tensile stress–strain behavior of the Ni-Ti wire at six strain rates is represented in Figure 1. These strain rates correspond to extension rates from  $10^{-6}$  to  $5 \cdot 10^{-2}$  s<sup>-1</sup>. For the low strain rate between  $10^{-6}$  and  $10^{-4}$  s<sup>-1</sup>, the tensile curve is characterized by an elastic loading of the austenite phase, followed by a “a plateau” at almost a constant load of introducing martensite, and then an elastic deformation of the martensite phase. The critical stress for the austenite-martensite transformation increases from 360 MPa to about 400 MPa for strain rates from  $10^{-6}$  to  $10^{-4}$  s<sup>-1</sup>. However, for the higher strain rates, between  $10^{-3}$  and  $5 \cdot 10^{-2}$  s<sup>-1</sup>, the critical stress reaches 500 MPa for  $5 \cdot 10^{-2}$  s<sup>-1</sup> and the slope hardness of the austenite-martensite transformation increases with the rise of the strain

rate. Moreover, we notice that the high strain rates are characterized by a decrease in the total deformation after one cycle with an imposed stress of 700 MPa; and the material conserves its superelastic performance. P. Schlosser et al. [17] showed that the more the strain rate is low, the more the sample temperature during tensile testing goes up due to the released latent heat during the stress-inducing nucleation and growth of the martensite phases. Consequently, the critical stress of the austenite-martensite transformation increases and the archwire has a low number of martensite variants and large bands.

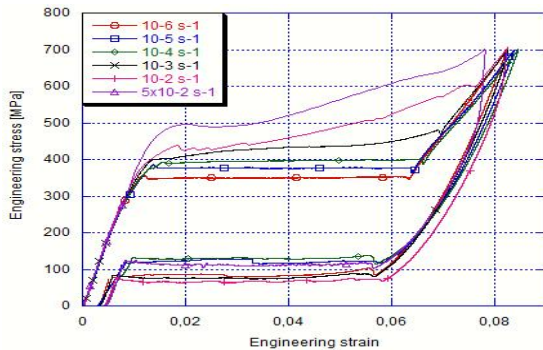


Figure 1: Typical engineering tensile curves of the superelastic Ni-Ti alloy before hydrogen-immersion for a strain rate range between  $10^{-6}$  and  $5 \times 10^{-2} \text{ s}^{-1}$ .

After hydrogen immersion with a current density of 10A/m<sup>2</sup> and ageing for one day at 25°C, the critical stress for the austenite-martensite increases with the rise of the hydrogen-charging time. In addition, after hydrogen immersion from 2h to 7h, the superelastic NiTi wire conserves its superelastic behavior, and there was not any embrittlement detected between  $10^{-6}$  and  $5 \times 10^{-2} \text{ s}^{-1}$  of strain rates, during loading. Besides, the critical stress for the austenite-martensite transformation becomes more important compared to the same strain rate of loading for the non-immersed alloy. This increase in the value of the critical stress of introducing martensite is endorsed to the effect of hydrogen diffusion which acts as an obstacle for

the nucleation and growth of the martensite bands [6, 17]. Between 8 and 10 hours of hydrogen immersion and ageing for one day in air at room temperature (Figure 2), an remarkable behavior of the archwire at the studied strain rates appears during tensile loading. Indeed, for the strain rates below  $10^{-4} \text{ s}^{-1}$ , an premature fracture has been detected. This embrittlement is localized in the plateau of introducing martensite bands and the fracture rises with the decrease in the strain rate. Yokoyama et al. [19] showed that the fracture in a brittle manner of the superelastic Ni-Ti alloy appeared in the austenite-martensite transformation process. This embrittlement was considered to be linked to the ingress of hydrogen into the solid, likely in the lattice defects, which blocks the martensite transformation and acts as an obstacle for the austenite-martensite transformation during loading.

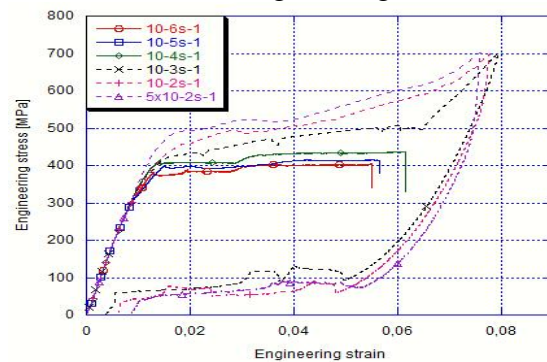


Figure 2: Tensile curves of the superelastic Ni-Ti alloy after 8 h of hydrogen-immersion showing the hydrogen embrittlement for strain rates equal to and lower than  $10^{-4} \text{ s}^{-1}$ .

For higher values of strain rates, higher than  $10^{-3} \text{ s}^{-1}$ , there was not any embrittlement and the specimens show a superelastic behavior. These samples show a higher critical stress for introducing martensite and a reduction in the total strain compared to the as-received archwire after one cycle of loading and unloading with the imposed stress of 700 MPa. For a longer period of immersion of 12h of hydrogen immersion and ageing for one day in air at room temperature, the Ni-Ti SMA arch fractures in a brittle way near the critical stress of introducing martensite for all the

studied range of strain rate (Figure 3). These outcomes emphasize that after this period of immersion, the ingress of hydrogen causes an embrittlement of the Ni-Ti SMA arches in all values of the strain rate.

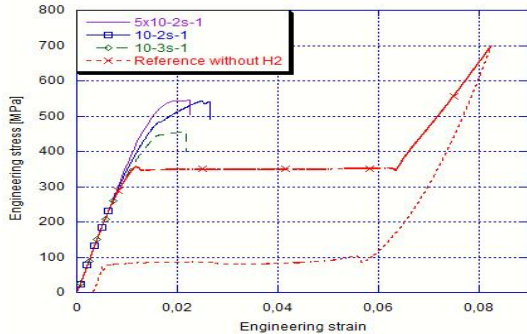


Figure 3: Typical engineering stress–strain curves of the superelastic Ni–Ti alloy after 12 h of hydrogen-charging.

Upon tensile testing after electrolytically hydrogen immersion in 0.9% NaCl solution, the superelastic Ni–Ti material often fails and this premature fractures is related to the stress-induced austenite-martensite transformation [6–7]. Particularly, these embrittlement, strongly linked to the introducing martensite phase, happen after a critical hydrogen-charging time and for a tensile strain rate of about  $10^{-3} \text{ s}^{-1}$  [18]. In our study, however, no premature fracture has been detected under an applied strain rate higher than  $10^{-3} \text{ s}^{-1}$ ; while, for the same immersion time, the embrittlement come out for the strain rate lower than  $10^{-4} \text{ s}^{-1}$ . These findings obviously emphasis that the hydrogen ingress time into the archwire is not necessarily the only main parameter when taking into account the hydrogen fracture of the superelastic Ni-Ti SMA archwire.

After hydrogen immersion for more than 8h showed that, for strain rates lower than  $10^{-4} \text{ s}^{-1}$ , once the first martensite variants is nucleated in the plateau of introducing martensite phase, the temperature of the entire specimen goes up compared to the initial room temperature. This rise in temperature is caused by the martensite bands growth and the heat transfer from the front of the austenite-martensite interface during

growth. For that reason, the critical stress of introducing new martensite bands becomes more important and the applied stress during the monotonic tensile test serves to coerce the growth of the existing bands, and not to the nucleation of new ones. On the other hand, after hydrogen immersion in 0.9% NaCl solution, it is possible that the trapped diffused hydrogen at lattice defects [19] strongly blocks the martensite variants to grow; Thus, the transformation process cannot conquer the obstacle induced by the trapped amount of hydrogen, and the premature fracture appears to occur during the plateau of introducing martensite. For strain rates higher than  $10^{-3} \text{ s}^{-1}$  and after hydrogen immersion during 8 and 10 hours and ageing at  $25^\circ\text{C}$  for one day, we presume that the amount of diffused hydrogen into the NiTi archwire is not enough to block the nucleation of the martensite bands; and the time to transfer the latent heat is very limited. Consequently, the applied stress past the critical needed stress for introducing the martensite bands conducts to the nucleation of new martensite variants instead of the growth of the existing ones. As a result, the new martensite variants present a large number and small domain spacing, and the materials keep their superelastic behavior. Nonetheless, after a hydrogen-immersion time above 12 hours, the diffused hydrogen is considered sufficient to hinder the nucleation of the martensite transformation bands, and then, the embrittlement happens just after the critical stress for introducing the martensite for all the studied strain rate range between  $10^{-6}$  and  $5.10^{-2} \text{ s}^{-1}$ .

To recapitulate, we have shown that after electrolytically hydrogen immersion in 0.9% NaCl solution, the mechanical behaviour of the Ni-Ti SMA alloy strongly depends on the value of strain rate during the monotonic tensile test. After 8h of hydrogen immersion, an embrittlement was detected in the tensile strain rate lower than  $10^{-4} \text{ s}^{-1}$ . However, there was not any premature fracture detected for the strain rate higher than  $10^{-3} \text{ s}^{-1}$ . Nevertheless, after half-day

# 14<sup>th</sup> Annual Research Day

Organised by the Deanship of Scientific Research in collaboration with the College of Engineering

Research Centre

4<sup>th</sup> April 2019

of hydrogen immersion and ageing for one day at 25°C, the fracture occurs at the beginning of the plateau of introducing martensite on for all the studied strain rate range. In addition, it was mentioned that this embrittlement happens for low values of the strain rate contrary to the case of ordinary steel. This behaviour is considered as linked to the interaction between the trapped hydrogen into the alloy and the thermo-mechanical aspect nucleation and growth of the martensitic bands, which strongly depend on the loading strain rates.

## References

- [1] L. S. Castleman, S. M. Motzkin, F. P. Alicandri, and V. L. Bonawit, Biocompatibility of nitinol alloy as an implant material, *J. Biomed. Mater. Res.*, 10, (1976) 695.
- [2] P.H. Lin, H. Tobushi, K. Tanaka, T. Hattori, M. Makita, Pseudoelastic Behaviour of TiNi Shape Memory Alloy Subjected to Strain Variations, *J. Intell. Mater. Syst. Struct.* 5 (1994) 694.
- [3] N. Sharma, T. Raj, and K. Kumar, Applications of nickel titanium alloy, *J. Eng. Technol.*, 5, (2015) 1.
- [4] Biscarini A, Campanella R, Coluzzi B, Mazzolai G, Trotta L, Tuissi A, et al. Martensitic transitions and mechanical spectroscopy of Ni<sub>50.8</sub>Ti<sub>49.2</sub> alloy containing hydrogen, *Acta Mater.*, 51 (2003) 573.
- [5] R. Sarraj, W. E. Letaief. T. Hassine, F. Gamaoun, Modeling of rate dependency of mechanical behavior of superelastic NiTi alloy under cyclic loading, *Int J Adv Manuf Technol.*, 100, 9-12 (2019) 2715.
- [6] K. Yokoyama, T. Ogawa, K. Asaoka, J. Sakai, M. Nagumo, Degradation of tensile strength of Ni–Ti superelastic alloy due to hydrogen absorption in methanol solution containing hydrochloric acid, *Mater. Sci. Eng. A* 360 (2003) 153.
- [7] F. Gamaoun, M. Ltaief, T. Bouraoui, T. Ben Zineb, "Effect of hydrogen on the tensile strength of aged Ni-Ti superelastic alloy, *J. Intell. Mater. Syst. Struct.* 22 (2011) 2053.
- [8] Ogawa, T, Yokoyama, K, Asaoka, K, Sakai, J (2006) Hydrogen in trapping states innocuous to environmental degradation of high-strength steels. *Mater. Sci. Eng. A* 422 (2006) 218.
- [9] K. Yokoyama, T. Eguchi, K. Asaoka, M. Nagumo, Effect of constituent phase of Ni–Ti shape memory alloy on susceptibility to hydrogen embrittlement, *Mater. Sci. Eng. A* 374 (2004) 177.
- [10] K.L. Ng, Q.P. Sun, Stress-induced phase transformation and detwinning in NiTi polycrystalline shape memory alloy tubes, *Mech. Mater.* 38 (2006) 41.
- [11] E.A. Pieczyska, S.P. Gadaj, W.K. Nowacki, Phase-transformation fronts evolution for stress- and strain-controlled tension tests in TiNi shape memory alloy, *Exp. Mech.* 46 (2006) 531.
- [12] Y.J. He, Q.P. Sun, Macroscopic equilibrium domain structure and geometric compatibility in elastic phase transition of thin plates, *Int. J. Mech. Sci.* 52 (2010) 198.
- [13] X.H. Zhang, P. Feng, Y.J. He, T.X. Yu, Q.P. Sun, Experimental study on rate dependence of macroscopic domain and stress hysteresis in NiTi shape memory alloy strips, *Int. J. Mech. Sci.* 52 (2010) 1660.
- [14] Y.J. He, Q.P. Sun, Rate-dependent domain spacing in a stretched NiTi strip, *Int. J. Solids Struct.* 47 (2010) 2775.
- [15] K. Otsuka, X. Ren, Physical metallurgy of Ti–Ni-based shape memory alloys, *Prog. Mater. Sci.* 50 (2005) 511.
- [16] J.A. Shaw, Simulations of localized thermo-mechanical behavior in a NiTi shape memory alloy, *Int. J. plast.* 16 (2000) 541.
- [17] P. Schlosser, H. Louche, D. Favier, L. Orgéas, Image processing to estimate the heat sources related to phase transformations during tensile tests of NiTi tubes, *Strain* 43 (2007) 260.
- [18] K. Yokoyama, M. Tomita, K. Asaoka, J. Sakai, Hydrogen absorption and thermal

# 14<sup>th</sup> Annual Research Day

Organised by the Deanship of Scientific Research in collaboration with the College of Engineering

Research Centre

4<sup>th</sup> April 2019

---

desorption behaviors of Ni–Ti superelastic alloy subjected to sustained tensile-straining test with hydrogen charging, *Scr. Mater.* 57 (2007) 393.

[19] K. Yokoyama, M. Tomita, J.Sakai, Hydrogen embrittlement behavior induced by dynamic martensite transformation of Ni–Ti superelastic alloy, *Acta Mater.* 57 (2009) 187

---

# 14<sup>th</sup> Annual Research Day

Organised by the Deanship of Scientific Research in Collaboration with the College of Engineering  
Research Centre  
4<sup>th</sup> April 2019

---

## Strengthening Mechanisms of Metal Matrix Composites

VINEET TIRTH<sup>1</sup>

<sup>1</sup>Department of Mechanical Engineering, College of Engineering, King Khalid University,  
PO Box 394, Abha 61411 KSA.  
E-mail address: vtirth@kku.edu.sa

---

**Abstract:** This article presents the physical and metallurgical parameters, which affect the distribution of the discontinuous reinforcements in the matrix of metals or alloys with empirical relationships to predict the strengthening of composites fabricated by liquid state processing. The strengthening mechanisms have been predicted using classical continuum model and the factors affecting the load and stress distribution are also discussed explicitly to design and control the mechanical properties of the metal matrix composites within the desirable range. The interaction between the reinforcement and the dislocations have been mathematically modeled to predict the behavior of composites during elastic deformation. The mathematical models and the empirical relationships suggested in this article will help the researchers and industries to design the discontinuously reinforced composite materials developed by liquid metallurgy and to control the distribution of reinforcement and strengthening of the matrix.

**Keywords:** Metal Matrix Composites; Strengthening of Composites; Dislocations; Plastic Deformation.

---

### 1. Introduction:

A diversity of fabrication methods have been developed in past four decades to augment the microstructure and obtain desirable properties of metal matrix composites. These processing techniques are reviewed from time to time by the researchers [1-5]. Common processing routes include; gravity, pressure, compocasting, and rheocasting, mechanical mixing, powder processing, deposition, friction processing etc. Most of these processes include introduction of pre-fabricated particulate or fibrous reinforcement externally, in the matrix of metal or alloy. In such composites, the size of the reinforcement is typically of the order of 10-100 microns and are often referred to as macro composites. However, to obtain the composites with fine reinforcement, of the order of 1 micron or lesser, reaction synthesis is employed. The matrix material in metal matrix composites (MMCs) may be solid; in the form of powder, film or sheet; liquid, in the form of molten metal or alloy and; vapor, in the

form of superheated molten metal atomized to generate a spray. The schematic representation of different processing routes of MMCs is displayed in Figure (1).

### 2. Materials and Methods:

#### 2.1 Materials

In this article, The composites have been prepared with commercial 98.5% pure  $\alpha$ -Al (1,1,1) as the matrix and ceramic dispersoids of laboratory grade active Al<sub>2</sub>O<sub>3</sub> particles of size range ~100 microns as the reinforcement with a fixed weight percent of 7%.

#### 2.2 Experimental Procedure

The metal matrix composites were developed using stir casting at stirring speed of 800 rpm, temperature of 750 °C and using a pitched blade stirrer. Figure (2) shows the photo of the stirrer and Figure (3) shows the schematic diagram of the stir casting set-up.

# 14<sup>th</sup> Annual Research Day

Organised by the Deanship of Scientific Research in Collaboration with the College of Engineering  
Research Centre  
4<sup>th</sup> April 2019

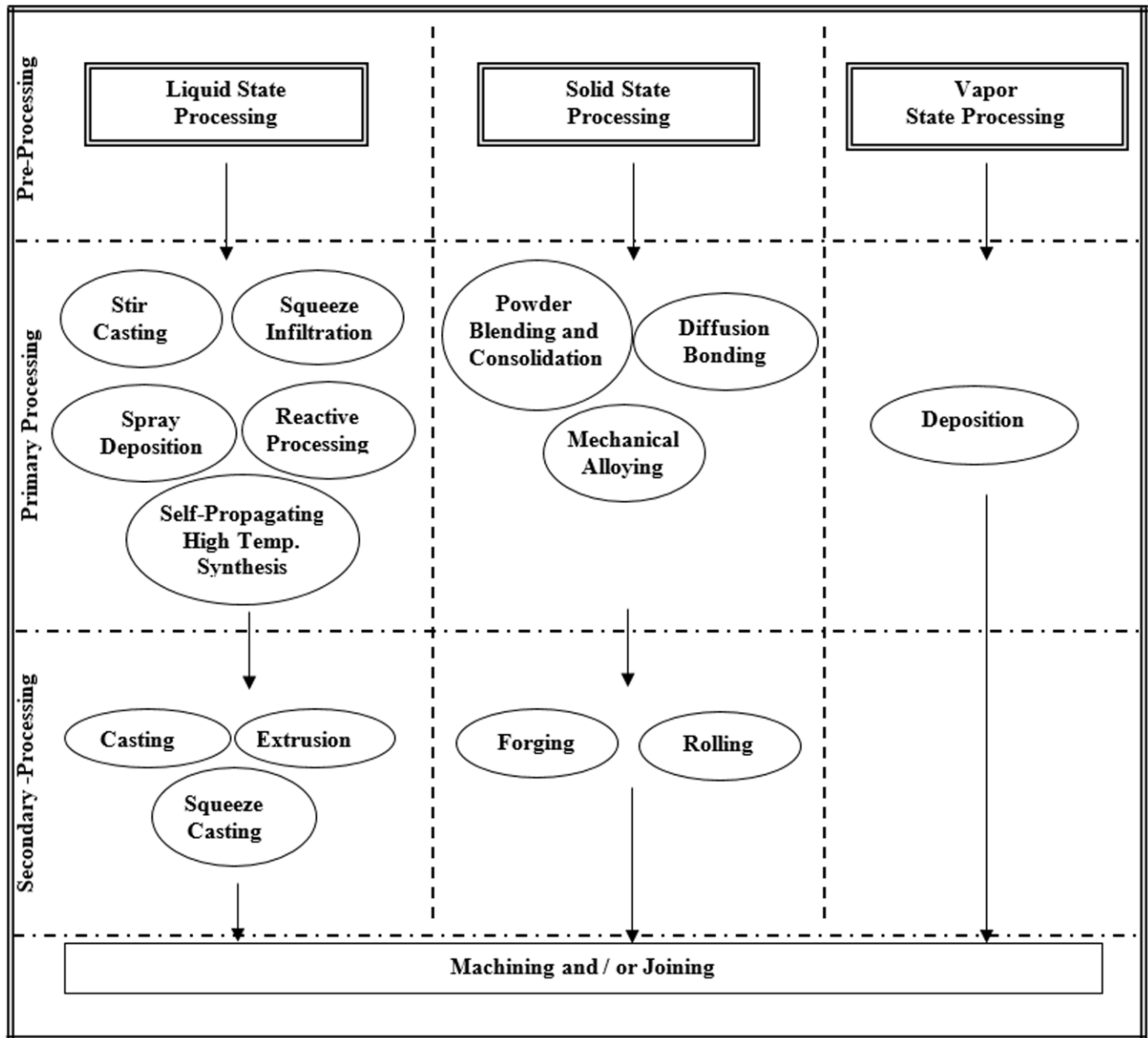


Figure (1). Processing routes of MMCs [2].

The density of the composites was measured by Archimedes principal and the porosity was determined by the difference in volume of the composite and the sum of the volumes of the matrix and the reinforcement.

## 3. Results and Discussion

### 3.1 Properties of composites

For prediction of elastic properties of a two phase composite, two simple limiting models of rule of mixtures are generally used [6-7]. The first one represents an iso-strain condition of the two phases and predicts the upper limit of the Elastic

modulus of the composite, which is given in Eq. (1).



**Figure (2)** Photo of pitched blade stirrer used in the study.

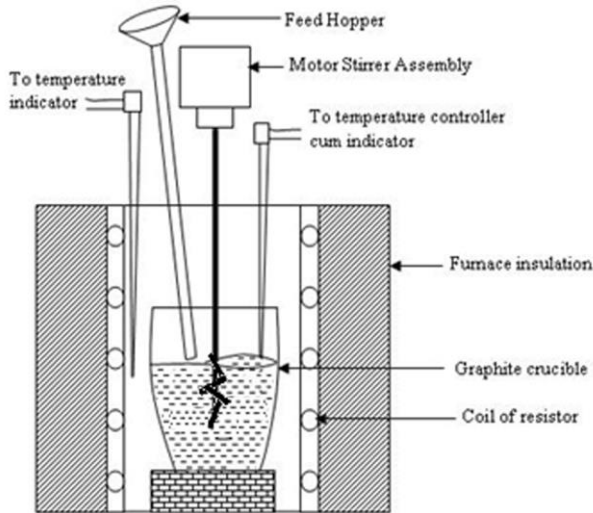


**Figure (3)** Schematic diagram of the Stir casting set-up used to develop the MMCs.

$$E_c = E_f V_f + E_m V_m \quad (1)$$

Where,  $E_m$ ,  $E_c$ , and  $E_f$  are the Elastic modulus of the alloy matrix, composite, and reinforcement respectively, and  $V_m$  and  $V_f$  are the volume

fractions of the matrix and reinforcement. The other expression given in Eq. (2) represents an iso-stress condition of the two phases and predicts the lower limit estimate of the Elastic modulus.

$$E_c = \frac{E_f E_m}{E_f V_m + E_m V_f} \quad (2)$$

The rule of mixture has been found most appropriate for the composites with continuous reinforcements. However, it has also been modified for the composites of discontinuous reinforcement and is expressed by Eq. (3).

$$E_c = \frac{(1 + 2 A q V_f) E_m}{1 - q V_f} \quad (3)$$

Where,  $A$  is the aspect ratio ( $l_p/d_p$ ) of the particle, represented by Figure (4) and  $q$  may be estimated by Eq. (4).

$$q = \frac{E_f / E_m - 1}{E_f / E_m + 2A} \quad (4)$$

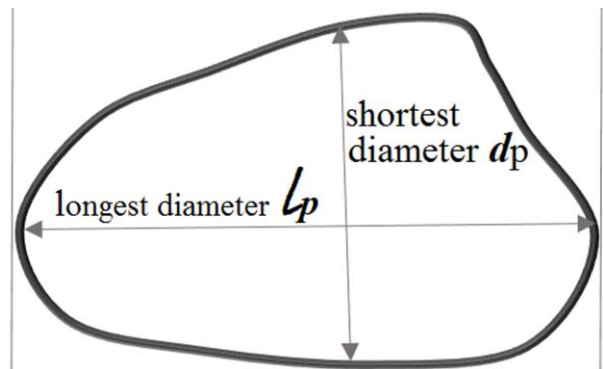


**Figure (4)** Aspect ratio of particle.

### 3.2 Strengthening of composites

Numerous strengthening mechanisms have been proposed for discontinuously reinforced composite materials [8-12].

The strength of a composite is dependent on the plastic behavior of its phases. Beyond the elastic limit of a composite, the matrix deforms plastically while the strengthening phase may

deform elastically under the stress concentration imposed by virtue of its continuity with the matrix. Thus, the strength of a particulate composite is to be considered from two different angles such as, the composite having deformable or non-deformable particles in the matrix [13]. In presence of the deformable particles, the composite may undergo an extensive plastic deformation. The stress necessary to impart extensive ductility to these composites is identical to the flow stress of the dispersed phase under the stressed state in the composite. Thus, the stress initiating gross plastic flow is independent of the volume concentration of the particles and their mean free path. The yield stress of the composite,  $\sigma_{yc}$  under a matrix constraint sufficient to develop stresses to deform the particle is expressed by Eq. (5) [6].

$$\sigma_{yc} = [(G_m G_p b)/c]^{1/2} \quad (5)$$

Where,  $G_p$  and  $G_m$  are the shear moduli of the particle and matrix respectively,  $b$  is Burger's vector of the dislocation pile up against the particle and  $c$  is a constant. The yield strength of composite containing non-deformable particles may be expressed by Eq. (6).

$$\sigma_{yc} = [(G_m G_p b)/c \lambda_1]^{1/2} \quad (6)$$

where,  $\lambda_1$  is the inter-particle spacing, expressed by Eq. (7) [7].

$$\lambda_1 = d_o [\sqrt{(2\pi/3V_f)} - \sqrt{(8/3)}] / 2 \quad (7)$$

Where,  $d_o = \sqrt{(3/2)}(l)$ , and  $l$  is the mean linear intercept of a random particle distribution and,  $V_f$  is the particle volume fraction.

Mileiko (1969) [14] was the first who developed a theory correlating the strength and ductility of two ductile components to the mechanical properties of the composite with fibers as reinforcement. It is based upon the application of plastic instability criteria to the composite. The criteria is applied under the following assumptions; (i) the bond between the fiber and the matrix is ideal so that there exists equal strain in both the phases; (ii) the flow stress

of the composite can be estimated by the law of mixture and; (iii) the relationship between the stress and strain of both the composite and the components follows a power law, expressed by Eq. (8).

$$\sigma_c = k_f \varepsilon_c^n \quad (8)$$

Where,  $\sigma_c$  is the stress,  $\varepsilon_c$  is the strain, and  $k_f$  and  $n$  are constants.

### 3.2.1 Classical Composite Strengthening (Models of Continuum)

Classical (continuum) composite models are based on the assumption that there exists a load transfer and sharing mechanism between the matrix and the reinforcement, which undergoes a non-plastic deformation. Based on the same assumption, in shear-lag theory the transfer of load transpires from the matrix and the reinforcement having high aspect ratio by means of shear stresses developed at the matrix-reinforcement interfaces. A modified shear-lag theory also explains the transfer of load at the ends of the reinforcement to predict the composite yield stress, given in Eq. (9) [15].

$$\sigma_{yc} = \sigma_{ym} V_f \left[ 1 + \frac{(L+t)A}{4L} \right] + \sigma_{ym} (1 - V_f) \quad (9)$$

Where  $\sigma_{yc}$  and  $\sigma_{ym}$  represent the yield stress of the composite and the un-reinforced alloy matrix,  $t$  and  $L$  represents the reinforcing particulate lengths parallel and perpendicular to the applied stress respectively,  $A$  is the aspect ratio of particulate and,  $V_f$  is the volume fraction of particulates. In case of an equiaxed reinforcement particulate, Eq. (9) may be reduced to Eq. (10).

$$\sigma_{yc} = \sigma_{ym} (1 + \alpha V_f) \quad (10)$$

Where  $\alpha$  is a constant which has different values as reported by researchers given hereunder:

$$\alpha = 1/2 \quad [15]$$

$$\alpha = 4(DZ)^2/\pi^2 \quad [16]$$

Where  $Z$  is the average of reciprocal of section diameter of the plane and  $D$  is the average size of the particle.

# 14<sup>th</sup> Annual Research Day

Organised by the Deanship of Scientific Research in Collaboration with the College of Engineering  
Research Centre

4<sup>th</sup> April 2019

$\alpha = -0.3$  [16-17] in steel with dual phase.

It is noteworthy that the Eq. (10) is linear however, the increase in  $\sigma_{yc}$  in marginal in response to the increase in the volume fraction of the particle.

### 3.2.2 Dispersion Strengthening; Orowan Strengthening

Another possible explanation of the observed strengthening of particulate reinforced Aluminum based composite is based on the Orowan theory. The moving dislocations can adjust and bypass the reinforcement particulates, which are difficult to penetrate, leaving a footprint called Orowan loop. For polycrystalline materials,  $\sigma_{yc}$  of the composite may be estimated by Eq. (11), called as Orowan relationship.

$$\sigma_{yc} = \frac{0.83M G b \ln(2r_s / r_o)}{2\pi\sqrt{1-\nu} \lambda} \quad (11)$$

Where  $\lambda$  represents the average interparticle separation over the plane of slip,  $G$  represents shear modulus,  $M$  is a factor called Taylor factor,  $b$  is burger vector,  $\nu$  is the poisson's ratio,  $r_o$  is cut-off radius, and  $r_s$  is effective particulate radius.

### 3.2.4 Effects of dislocation density

It is a well known phenomenon that the dislocations are generated in the composites during solidification and also during heat treatment due to the difference in the thermal expansion coefficient between the reinforcement particulates which are often ceramic and the metallic matrix. The thermal expansion coefficient of the later is much higher than the former. A few examples of such composites are Al-Al<sub>2</sub>O<sub>3</sub>, Al-SiC, Al-MgO etc. The same philosophy is applicable to the fibers and platelets. With the increase in the number of dislocations, the dislocation density increases leading to an increase in the strength of the composite. The strength of the matrix (or

composite) hence is a function of the dislocation density, which in turn depends on the strength of the matrix, the amount of reinforcement and their size [18].

### 3.2.5 Multiple Dislocations-Models of Particle Interaction

The metallic materials are normally polycrystalline with a single phase. Their yield stress  $\sigma_{yc}$  is phenomenally proportionate to the diameter of the grain,  $d_g$ , represented by the universal Hall-Petch expression given in Eq. (12).

$$\sigma_{yc} = \sigma_o + \frac{K_y}{\sqrt{d_g}} \quad (12)$$

In Eq. (12),  $K_y$  is the resistance of the grain boundary to slip also called as Hall-Petch gradient. The values of  $K_y$  at ambient temperature are; (i) for face-centered cubic (fcc), of the order of 0.05-0.1 MPa-m<sup>1/2</sup>; (ii) for body-centered cubic (bcc) metals, 0.3-1.8 MPa-m<sup>1/2</sup>. A factor  $\sigma_o$  is used to rationalize the internal back stresses and the stress resistance due to friction, during the gliding motion of dislocation.

## 4. Conclusions:

The theories of particle incorporation, rejection and the strengthening of the composites have been reported and discussed in this article. Some theories have been applied to validate their applicability on the Al-7%Al<sub>2</sub>O<sub>3</sub> composites prepare din this study. Following conclusions are drawn from the study.

1. The rule of mixture has been found most appropriate for the composites with continuous reinforcements and for discontinuous reinforcement, it is still valid after little modification.
2. In presence of the deformable particles, the composite may undergo an extensive plastic deformation.
3. The stress initiating gross plastic flow is independent of the volume concentration of the particles and their mean free path.

# 14<sup>th</sup> Annual Research Day

Organised by the Deanship of Scientific Research in Collaboration with the College of Engineering  
Research Centre

4<sup>th</sup> April 2019

4. With the increase in the number of dislocations, the dislocation density increases leading to an increase in the strength of the composite.

## Acknowledgement

Authors thankfully acknowledge the support provided by Deanship of Scientific Research, and College of Engineering, King Khalid University, Abha-Asir, Kingdom of Saudi Arabia to complete the research work.

## References

- [1] D.B. Miracle, Metal Matrix Composites-From Science to Technological Significance, *Composites Science and Technology*, 65, (2005) 2526-2540.
- [2] T.W. Clyne, Metal Matrix Composites: Matrices and Processing, *Encyclopedia of Materials: Science and Technology*, A Mortensen (ed.) Elsevier, (2001) 1-14.
- [3] M.J. Koczak and M.K. Premkumer, Emerging Technologies for the In-Situ Production of MMCs, *JOM*, 45 (1), (1993) 44-48.
- [4] S.C. Tjong and Z.Y. Ma, Microstructural and Mechanical Characteristics of In-Situ Metal Matrix Composites, *Mater. Sci. Engg.*, 29, (2000) 49-113.
- [5] L. Froyen and J. De. Wilde, 'In-situ Synthesis, A Alternative Way to Produce Materials', *Mater. Sci. Forum*, 437-438, (2003) 141-144.
- [6] L.J. Broutman and R.H. Krock, *Modern Composites Materials*, Addison-Wesley Publishing Co., Inc., (1967) 7,8,481,486.
- [7] G.Le Roy, J.D. Embury, and G. Edward, A Model of Ductile Fracture Based on the Nucleation and Growth of Voids, *Acta Metall.* 29, (1981) 1509-1522.
- [8] R.J. Arsenault, Strengthening of Metal Matrix Composites Due to Dislocation Generation Through CTE Mismatch, In 'Metal Matrix Composites: Mechanisms and Properties', Edited by Everett, R.K. and Arsenault, R.J., Academic Press Inc., San Diego, CA, USA, (1991) 101-132.
- [9] R.J. Arsenault, L. Wang, and C.R. Feng, Strengthening of Composites due to Microstructural Changes in the Matrix, *Acta Metall. Mater.*, 39, (1991) 47-57.
- [10] V. Tirth, Dry Sliding Wear Behavior of 2218 Al-Alloy-Al<sub>2</sub>O<sub>3</sub>(TiO<sub>2</sub>) Hybrid Composites, *J. Tribol.* 140 (2), (2018) 021603 1-9.
- [11] V. Tirth, S. Ray, M. L. Kapoor, Effect of Squeeze Pressure on Aging and Mechanical Properties of AA2218-5 Wt. Pct. Al<sub>2</sub>O<sub>3</sub> (TiO<sub>2</sub>) Composites, *Metall. Mater. Trans. A Phys. Metall. Mater. Sci.* 40A, (2009) 1246-1254.
- [12] V. Tirth, A. Algahtani, E.R.I. Mahmoud, Tribological Characterization of Stir Cast 2218 Alloy-5%-Alumina-Titania Hybrid Microcomposites Developed by Liquid Forging, *Mater Express.* 8(6), (2018) 475.
- [13] P.K. Ghosh and S. Ray, Effect of Porosity and Alumina Content on the Mechanical Properties of Compocast Aluminium Alloy-Alumina Particulate Composite, *J. Mater. Sci.*, 21, (1986) 1667-1674.
- [14] S.T. Mileiko, The Tensile Strength and Ductility of Continuous Fiber Composite, *J. Mater. Sci.*, 4(11), (1969) 974-981.
- [15] R.M. Aikin Jr. and L. Christodoulou, The Role of Equiaxed Particles on the Yield Stress of Composites, *Scripta Metallurgica et Materialia*, 25, (1991) 9-14.
- [16] P.R. Prasad, S Ray., J.L. Gaindhar and M.L. Kapoor, Mechanical Properties of Al-10% Cu Alloy Particulate Composites, *Scripta Metallurgica*, 19 (1985) 1019-1022.
- [17] S.K. Nath, S. Ray and M.L. Kapoor, A Single-Particle Model for Theoretical Estimation of Tensile Strength of Two-Phase Metals, *Metals Materials and Processes*, 14 (3), (2002) 241-254.

# 14<sup>th</sup> Annual Research Day

Organised by the Deanship of Scientific Research in Collaboration with the College of Engineering  
Research Centre

4<sup>nd</sup> April 2019

---

- [18] R.M. Aikin, The Mechanical Properties of In-Situ Composites, Jr. of Mat. Science, 49(8), (1997) 35-39.



**Abha 61411 P.O. Box 394 Tel: +966 17 241 8816**

**Website: [www.engineering.kku.edu.sa](http://www.engineering.kku.edu.sa)**

**Email: [eng-coll@kku.edu.sa](mailto:eng-coll@kku.edu.sa)**